Ex Vivo and *In Vitro* Investigation of Biodegradable Magnesium-Gadolinium Implants

Dissertation
zur Erlangung des akademischen Grades eines
Doktors der Naturwissenschaften (Dr. rer. nat.)
der Christian-Albrechts-Universität zu Kiel

vorgelegt von
Diana Krüger
aus
Jerewan, Armenien

2023

Betreuer: Prof. Dr. Regine Willumeit-Römer
Zweitgutachter: Prof. Dr. Martin Müller
Dissertationsdatum: 14.12.2022

Declaration of Authorship

I, Diana KRÜGER, declare that this thesis titled, "*Ex vivo* and *In vitro* Investigation Of Biodegradable Magnesium-Gadolinium Implants" and the work presented in it are my own. I confirm that:

- This work was done wholly while in candidature for a research degree at Helmholtz Center Hereon.
- No parts of this thesis has previously been submitted for a degree or any other qualification at this University or any other institution.
- Where I have consulted the published work of others, this is always clearly attributed.
- Where I have quoted from the work of others, the source is always given. With the exception of such quotations, this thesis is entirely my own work.
- I have acknowledged all main sources of help.
- Where the thesis is based on work done by myself jointly with others, I have made clear exactly what was done by others and what I have contributed myself.

Ich, Diana KRÜGER, erkläre hiermit, dass

- die Abhandlung, abgesehen von der Beratung durch die Betreuerin oder den Betreuer nach Inhalt und Form die eigene Arbeit ist,
- die Arbeit bei keiner weiteren Stelle im Rahmen eines Prüfungsverfahrens vorgelegen hat, veröffentlicht wurde oder zur Veröffentlichung eingereicht wurde
- die Arbeit unter Einhaltung der Regeln guter wissenschaftlicher Praxis der Deutschen Forschungsgemeinschaft entstanden ist.

Signed: _____

Date: _____

Abstract

Biodegradable magnesium-based implants are playing an increasingly important role in the area of orthopaedic implants as they eliminate the need for a second surgery to remove the implant, consequently reducing the chance of patients' harm as well as the financial burden. They aim to replace permanent implants. Not only the alloying elements and alloy preparation procedure, but also the implant machining are important aspects influencing the implant's performance. There is a need for degradable magnesium-based implants to be fully characterized in terms of microstructure, corrosion performance *in vitro* and *in vivo* due to the implants' performance differences in these different environments. The implants' degradation rate and homogeneity characterization has to be completed before they can be approved for further clinical testing. Additionally, the *in vivo* experiments provide information on the implant's osseointegration into the host tissue. Two magnesium gadolinium alloys (Mg-5 weight% Gd and Mg-10 weight% Gd) in the shape of M2 screws have been investigated with regards to their microstructure and their degradation performance over 1 - 56 days period *in vitro via* both weight loss and volume loss measurements. Investigations were performed *via* optical microscopy, scanning electron microscopy / backscatter electrons microscopy, electron backscatter diffraction and micro computed tomography (µCT). *Ex vivo* analysis on the same Mg-xGd alloys at 4, 8, 12 weeks was performed *via* synchrotron radiation µCT and histology towards their degradation performance in Sprague Dawleys' tibia and bone-to-implant interaction. In order to gain knowledge about the bone-to-implant interaction parameters bone-to-implant-contact area and bone volume density around the implant have been investigated. Additionally, *in situ* synchrotron radiation µCT imaging of the implant failure during the increase of force on the implant was performed (push-out experiments). Titanium and PEEK implants were analyzed as reference materials. For the *ex vivo* experiments, overall 60 animals were chosen for the implantation of four implant materials. Comparisons with *in vitro* experiments of the same implants are performed for the time points 4 and 8 weeks. Moreover, the potential of high-resolution synchrotron radiation µCT is used to non-destructively determine the degradation behaviour of a 3D data. As a result, for instance, it is possible to determine the pitting factor of the 3D implant or to investigate the degradation variation on the different areas of the implant's thread. Also, the influence of the microstructure on the implant's localized degradation is determined in this work. The latter could make the prediction on the implants *ex vivo* stability from the *in vitro* experiments possible.

In vitro investigations suggested Mg-10Gd to be more suitable as load bearing implant alloy than Mg-5Gd. It is due to its lower degradation rates, its more homogeneous microstructure and degradation performance and also due to its weaker texture. *Ex vivo* investigations reveal, that Mg-5Gd alloys degrade faster and more inhomogeneously than Mg-10Gd. Additionally, both Mg-xGd alloys showed bone-to-implant contact comparable to golden standard Ti implants. In contrast, the PEEK implants revealed a much lower bone-to-implant contact for all investigated time points than Mg-xGd and/or Ti implants. After detailed exploration and correlation

of *in vitro* and *ex vivo* results, it is suggested that both Mg-xGd alloys are suitable as materials for bone implants.

Zusammenfassung

Orthopädische Implantate aus biodegradierbaren Magnesiumlegierungen gewinnen in der Medizin immer mehr an Bedeutung, mit dem Ziel, die vorhandenen permanenten Implantate bei temporären Anwendungen zu ersetzen. Nicht nur die Legierungselemente und Legierungspräparation spielen eine große Rolle für das Degradationsverhalten solcher Implantate, sondern auch die Implantatherstellung. Die maschinelle Bearbeitung der Implantate zur Schraubenform, ist unter anderem, ein wichtiger Aspekt dabei. Um sowohl den Einfluss solcher Prozessierungsschritte auf den Abbau des Implantats zu untersuchen, als auch die allgemeine Tauglichkeit des Implantats für den Einsatz im Körper zu testen, ist eine umfassende Analyse der Mikrostruktur des Gefüges und des Degradationsverhaltens, der Degradationsgeschwindigkeit und -homogenität, *in vitro* und *ex vivo* von großer Bedeutung. Die *ex vivo* Experimente geben zusätzliche Information über die Osseointegration des Implantats in dem Knochen. Im Rahmen dieser Arbeit wurden zwei Magnesium-Gadolinium-Legierungen (Mg-5 Gew.% Gd und Mg-10 Gew.% Gd) in Form von M2 Schrauben *in vitro* untersucht. Immersionsexperimente wurden in einem Zeitraum zwischen 1 bis 56 Tagen durchgeführt. Es wurden die Mikrostruktur und das Degradationsverhalten der Schrauben analysiert, wobei hierfür Lichtmikroskopie, Rasterelektronenmikroskopie im Elektronenrückstreubeugung-Modus und Mikrokomputertomograpie benutzt wurden. Die gleichen Legierungen wurden auch *ex vivo* im Bezug auf ihr Degradationsverhalten und Osseointegration untersucht. Dafür wurden die Schrauben für 4, 8 und 12 Wochen im Rattenknochen *in vivo* degradiert. Um Erkenntnisse über die Osseointegration zu gewinnen, wurden Parameter wie Knochen-zu-Implantat-Kontakt und die Menge des Knochenvolumens in der Umgebung des Implantats untersucht. Ferner wurden *in situ* Lastexperimente, auch Push-Out Experimente, durchgeführt. Dabei wurden definierte Kräfte auf die Implantate ausgeübt und gleichzeitig 3D Synchrotronstrahlung-Mikrotomographiebilder aufgenommen. Die *in vitro* Analysen wurden *via* Massen- und Volumenverlust durchgeführt. Die *ex vivo* Proben wurden durch Mikrokomputertomographie mit Synchrotronstrahlung analysiert und die Ergebnisse mit den Ergebnissen der histologischen Untersuchungen verglichen. Als Referenzmaterialien wurden Ti- und PEEK-Implantate ebenfalls implantiert und untersucht. Außerdem wurde das Potential der Synchrotronstrahlung µCT-3D-Daten zur Analyse des Degradationsverhaltens benutzt. Als Ergebnis, konnten zum Beispiel Pitting Faktor oder die Variation der Degradationsmenge an den 3D-Datensätzen in verschiedenen Teilen des Implantatgewides analysiert werden. Ebenfalls wurde nach einem Zusammenhang zwischen der oberflächennahen Mikrostruktur der Implantate und ihr lokales Degradationsverhalten *in vitro* gesucht. Dies könnte helfen, das *ex vivo* Degradationsverhalten der Implantate vorherzusehen.

Die Ergebnisse der *in vitro* Analysen zeigten, dass Mg-10Gd-Implantate eine homogenere Mikrostruktur, langsamere Degradationsgeschwindigkeiten und eine homogenere Degradationsstruktur aufweisen als Mg-5Gd-Implantate. Zusätzlich

verfügen die Mg-10Gd-Implantate über eine schwächere Textur als Mg-5Gd-Implantate. Somit würde sich die, durch die Belastung entstandene, auf das Implantat wirkende Kraft, homogener in Mg-10Gd verteilen als in Mg-5Gd. Auch *ex vivo* Analysen bestätigen die Tendenz der langsameren Degradation der Mg-10Gd-Schrauben im Vergleich zu Mg-5Gd-Schrauben. Beim Vergleich von *in vitro* und *ex vivo* Degradationsgeschwindigkeiten, bauen sich die *ex vivo* Schrauben langsamer ab. Darüber hinaus zeigten die Implantate der Mg-xGd-Legierungen eine gute Knochenintegration, vergleichbar zu der von Titanimplantaten. Dahingegen wiesen die PEEK-Implantate zu allen Zeitpunkten eine wesentlich niedrigere Knochenintegration als Mg-xGd- und Titanimplantate auf.

Nach einer ausführlichen Untersuchung und Korrelation der *in vitro* und *ex vivo* Ergebnisse, zeigten sich die Mg-xGd Materialien geeignet für den Einsatz als Knochenimplantate.

Acknowledgements

First, I would like to thank my supervisor Prof. Dr. Regine Willumeit-Römer for giving me the apportunity to work on the current project. Also, I am grateful for her scientific and personal support, advice and help throughout the doctoral thesis.

Further, I am thankful Prof. Dr. Rainer Adelung, Prof. Dr. Franz Faupel and Pr. Dr. Martin Müller for being in the board of examiners.

Moreover, I want want to thank my additional supervisors and colleagues, like Berit, Florian, Julian, Björn, Paria, all other colleagues from DESY and Geesthacht, for their time and voluable support at any time. Special thanks to Berit for proof-reading my work.

And of course, also a special thanks to my beloved family and friends, who were supporting me mentally day and night.

Thank You All Very Much!

Contents

List of Abbreviations

α-MEM	α- **M**odified **E**agle's **M**inimum **E**ssential **M**edium
Al	**A**luminium
ASTM	**A**merican **S**ociety of **T**esting and **M**aterials
ATP	**A**denosine **T**ri**P**hosphate
BIC	**B**one **I**mplant **C**ontact
BMU	**B**asic **M**ulticellular **U**nit
BV/TV	**B**one **V**olume to **T**otal **V**olume
Ce	**Ce**rium
CV	**C**oefficient of *V*ariation
DAMP	**D**anger **A**ssociated **M**olecular **P**attern
DC	**D**endritic **C**ell
DESY	**D**eutsches **E**lektronen-**S**ynchrotron
DMEM	**D**ulbecco's **M**odified **E**agle's **M**edium
DNA	**D**eoxyribo**N**ucleic **A**cid
DR	**D**egradation **R**ate
EH2	**E**xperimental **H**utch **2**
Eu	**E**uropium
FBS	**F**etal **B**ovine **S**erum
Fe	Iron
GBCA	**G**adolinium **B**ased **C**ontrast **A**gents
Gd	**G**adolinium
HBSS	**H**ank's **B**alanced **S**alt **S**olution
ISO	**I**nternational **O**rganization for **S**tandardization
Li	**L**ithium
Lu	**L**utetium
MDD	**M**ean **D**egradation **D**epth
Mg	**M**agnesium
MRI	**M**agnetic **R**esonance **I**maging
mRNA	**M**essenger **R**ibo**N**ucleic **A**cid
NSF	**N**ephrogenic **S**ystemic **F**ibrosis
PBS	**P**hosphate **B**uffered **S**aline
PEEK	**P**oly**E**ther**E**ther**K**eton
PET	**P**oly**E**thylene-**T**erephthalate
PF	**P**itting **F**actor
PMMA	**P**oly**M**ethyl**M**eth**A**crylat
REE	**R**are **E**arth **E**lement
SAXS	**S**mall-**A**ngle **X**-ray **S**cattering
SBF	**S**imulated **B**ody **F**luid
SEM	**S**canning **E**lectron **M**icroscopy
SOP	**S**tandard **O**perating **P**rocedure
SRμCT	**S**ynchrotron **R**adiation μ **C**omputed **T**omography
Ti	**T**itanium

VL	**V**olume **L**oss
XRD	**X**-**R**ay **D**iffraction
Y	**Y**ttrium

Chapter 1

Motivation and Objectives

1.1 Aim of this Work - Investigation of Biodegradable Magnesium Implants

Depending on different applications, e.g. orthopaedic, oral/dental, cardiovascular, implants can be made from different materials to result in the desired properties [1]. The materials mostly used as temporary implants nowadays are non-degradable metals, ceramics, polymers or composites [1].

In contrast to permanent implants, e.g. joint implants, which are supposed to stay in the patient for decades, implants meant for temporary bone support, such as screws, plates or nails, have to be removed after healing [2]. Keeping the permanent implants in the body can lead to complications especially in case of children, since permanent implants could compromise their growth [2].

To avoid this costly and risky implant removal procedure it is desired to use implant materials, which would degrade during the healing period [3]. This also prevents the possible release of toxic metallic ions and/or particles through corrosion or wear processes, hence preventing the possible inflammatory cascades, thus reducing the biocompatibility and cause tissue loss [4]. Also the stress shielding effect would be reduced, which leads to reduced stimulation of new bone growth and remodeling, and thus decreases the implant stability [4].

The requirement of biodegradation is fulfilled either by biodegradable polymers or biodegradable metallic implants. It has been proven, however, that the mechanical and degradation properties of biodegradable polymeric implants significantly decrease in physiological environments, thus limiting them as load bearing implants [5]. In addition to available zinc or iron-based metallic degradable implants, magnesium (Mg) alloys are showing optimal strength, adjustable corrosion rate and adjustable compliance [6]. Released Mg^{2+} ions do not cause cellular toxicity in the body if below a critical concentration and are expelled along with urine [7]. In addition, Mg is essential to the human metabolism as a cofactor of many enzymes and facilitates tissue-healing [1].

The high degradation rate under physiological conditions is the major limitation of Mg and can cause a reduction in the mechanical integrity of the implant before the bone or tissue is sufficiently healed. Rapid production of hydrogen gas as a result of too fast degradation can lead to the formation of gas bubbles around the implant, which causes separation of tissue layers and delays the healing of the tissue [8] (necrosis of surrounding tissue might be the result). In the worst case, the evolution of the gas bubbles may block the blood stream, which can be lethal [9]. An additional undesirable effect of rapid degradation is the pH increase in localized areas next to the implant, which is harmful for the cells [2]. Thus, the degradation

rate of Mg implants must be such that the cells can synthesize and deposit an extracellular matrix for their own support and function before the structural integrity of the implant is compromised.

Since pure Mg doesn't provide sufficient strength for load bearing applications, alloying elements are added such that the mechanical properties of the alloys are suitable for implant applications. By alloying, the implant's density, elastic modulus and yield strength can be tailored close to those of human bone [1]. The investigation of the synergetic effect of mechanical loading and *in vivo* corrosion are very important in the context of Mg implants being applied as load bearing implants. Depending on the Mg alloy, the latter can be a reason for sudden implant cracking or failure, due to stress corrosion cracking and corrosion fatigue [10].

It has been shown that through addition of rare earth elements (REE), specifically gadolinium (Gd), to the high purity Mg matrix (5-10 weight percentages [wt.%] Gd) the corrosion resistance of the alloys' mechanical properties are improved [11]. Such alloys exhibited sufficient strength and toughness and, thus, could be well used as biodegradable load-bearing alloys [10, 12]. One of the important effects of REE on the corrosion resistance of Mg is the so-called "scavenger effect". It is an effect, where the influence of impurities in Mg, like iron (Fe), is eliminated due to the formation of the intermetallic phases between the REE and the impurity [13, 14]. The toxicity of Gd is still a concern because of its unknown health impact [13, 14]. Additionally, it has been found that Gd accumulates in animal organs [13]. However, in other studies it has also been demonstrated that the toxicity of Gd is within the acceptable level and that Mg-xGd alloys can be considered as good candidates in medical applications [15–17]. It has been shown, that Mg-10Gd retains its cytocompatibility and could even improve osteoblast-induced mineralization [18], and that the cells grown on Mg-10Gd develop and generate healthy cellular structures that allow them to have a good adhesion to the surface [19]. So, by providing the essential requirements, like initial mechanical stability, a suitable corrosion rate and ensuring the biocompatibility, Mg-xGd alloys are a possible choice as implant materials [20].

The most typical corrosion types of Mg are galvanic, intergranular, pitting or crevice corrosion, which occur in physiological environments [21, 22]. Since the irregular, localized pitting corrosion may lead to implant failure [23, 24], an alloy that tends to pitting corrosion should be excluded from being considered as implant material. Such implants could fail before the bone is sufficiently healed. There is literature on the *in vitro* experimental results on the implant itself [25], but the combination of *ex vivo*, *in vivo* and *in vitro* quantitative investigation of degradation homogeneity of potential pin or screw fixation implants, are missing. To the best of our knowledge, up to now information only on the pitting behaviour of the used implant's bulk material is available [26].

The focus of this work is to characterize the degradation of Mg-xGd alloys screws through several experiments and various analysis methods. The analysis of the *in vitro* and *in vivo* performance of two Mg-xGd implants with 5 and 10 wt% Gd based on high-resolution synchrotron radiation micro computed tomography (SRμCT) are presented here. In this regard the connection of the microstructure (SEM, BSEM, OM) of the alloys and their degradation behavior was investigated. Mass loss experiments are the most common experiments of the biodegradation rate investigation. Although it provides clearly defined data about the degradation rate, it doesn't provide information on the degradation homogeneity [27]. This work suggests to combine mass loss experiment and volume loss measurements from μCT to gain full information about the degradation rate and the homogeneity. Short and long time *in vitro* immersion tests (1-56 days) were performed in two different immersion

media. A comparison of weight loss and volume loss for the quantificationof the degradation rate was performed.

In this work the potential of SRμCT to determine degradation performance of Mg-xGd alloys, as well as its influence on the implants osseointegration is demonstrated [28]. Utilizing SRμCT was also possible to assess the bone microstructure from *ex vivo* experiments. The degradation rate (*DR*), mean degradation depth (*MDD*), pitting factor (*PF*), bone to implant contact (*BIC*), bone volume fraction (*BV/TV*) have been investigated in explants of rat tibia. The Mg-5Gd and Mg-10Gd implants were implanted for 4, 8 and 12 weeks and investigated, using a non-destructive 3D imaging technique. As comparison, screws of titanium (Ti) and polyetheretherketon (PEEK) have been implanted. Furthermore, the influence of microstructure variation on localized degradation at implant screws was determined. In addition, new ways of assessing this behavior is presented, e.g. by studying the degradation in terms of a crest to root ratio for implant screws. The latter can be useful in the prediction of the implant's performance in the certain area of the bone *in vivo*.

Additionally, a comparison of the *ex vivo* and *in vitro* degradation behaviour at 4 and 8 weeks of Mg-xGd alloys was performed.

To gain insight into the implants performance under load, which will be the case for a real implant in the body, load experiments on the *ex vivo* samples were carried out. The bone-to-implant interface of the explants were investigated using a customized push-out device under static load conditions. A precondition for the push-out experiment was, that the longitudinal axis of the screw is parallel to the loading direction. Since the positioning of the screw in the bone didn't fulfill this precondition just by explantation, custom made sample holders had to be developed and 3D printed for each sample separately. The information about the maximum force gave insights into the failure mechanisms of the bone-implant interface. Different forces, depending on different healing times, hence different osseointegration stages and therefore different forces needed for breaking the interface were expected [29]. The 3D tomographic images in connection with all the other data sets, like histology data and SAXS, which were investigated in co-projects, shed light on the implant's failure mechanism.

Aiming to gain scientific information on the *in vivo*, *in vitro* degradation performance of the Mg-xGd alloys and the bone response, the technical issues have also been solved in scope of this work. Speifically, an automatic image processing and semi-automatic 3D image analysis was developed, making the quantitative analysis of the degradation performance possible. Part of the semi-automated segmentation was developed in a masters thesis that I co-supervised ("Investigation of the corrosion of magnesium alloy Mg-10Gd implants using tomographic methods on *ex vivo* samples").

Overall, my work has contributes to 8 publications funded by the project Synchroload (BMBF project number 05K16CGA) in cooperation with Project MgBone (BMBF project number 05K16CGB)). A list of publications can be found in chapter 7.

Chapter 2

Theoretical Background

2.1 Bone - Fracture and Healing

"The skeleton, out of sight and often out of mind, is a formidable mass of tissue occupying about 9% of the body by bulk and no less than 17% by weight. The stability and immutability of dry bones and their persistence over the centuries, and even millions of years after the soft tissues have turned to dust, gives us a false idea of bone during life. Its fixity after death is in sharp contrast to its ceaseless activity during life." [Cooke 1955]

The skeleton of all higher vertebrates consists mainly of bone [30]. Bone protects the internal organs, while simultaneously supporting the body structure. Moreover, it provides space for haematopoiesis (the formation of blood cellular components) in the bone marrow and performs the function of an attachment site for the muscles enabling mobility [31, 32].

Being a part of the connective tissue, bone, also called osseous tissue, has a large amount of two different types of matrix materials, organic (protein - collagen) and inorganic (minerals - hydroxyapatite). The organic material is similar to other connective tissues, as it includes some amount of collagen and elastic fibers. These give the strength and the flexibility to the tissue. Mineral salts, mostly where calcium phosphate is included, make up most of the inorganic matrix, which are the reason for the tissue hardness. In case of inadequate amounts of organic material in the matrix the tissue would break. On the other hand in case of a lack of inorganic material the matrix tissue would bend too easily.

The bone structure is illustrated in figure 2.1. White and Folkens [33] report that all the bones of the adult skeleton consist of two basic structural components: compact and spongy bone. The compact, or cortical bone, which consists of osteons, is the solid and dense bone. It is making up the walls of bone shafts and on external bone surfaces. The Haversian canals, which are in the middle of the osteons, consist of blood vessels, nerves and lymphatic vessels. The Haversian canals are surrounded by rings of lamellae and the hollow areas between the lamellae are the lacunae. The osteocytes (the cells that lie within the fully formed bone) are placed in the lacunae. At joints the compact bone is covered by cartilage and is called subchondral bone. In contrast, the spongy bone is porous, lightweight and has the structure of a honeycomb. It is under protuberances where tendons attach, in the vertebral bodies, in the ends of long bones, in short bones, and sandwiched within flat bones. This spongy bone is also called cancellous or trabecular bone.

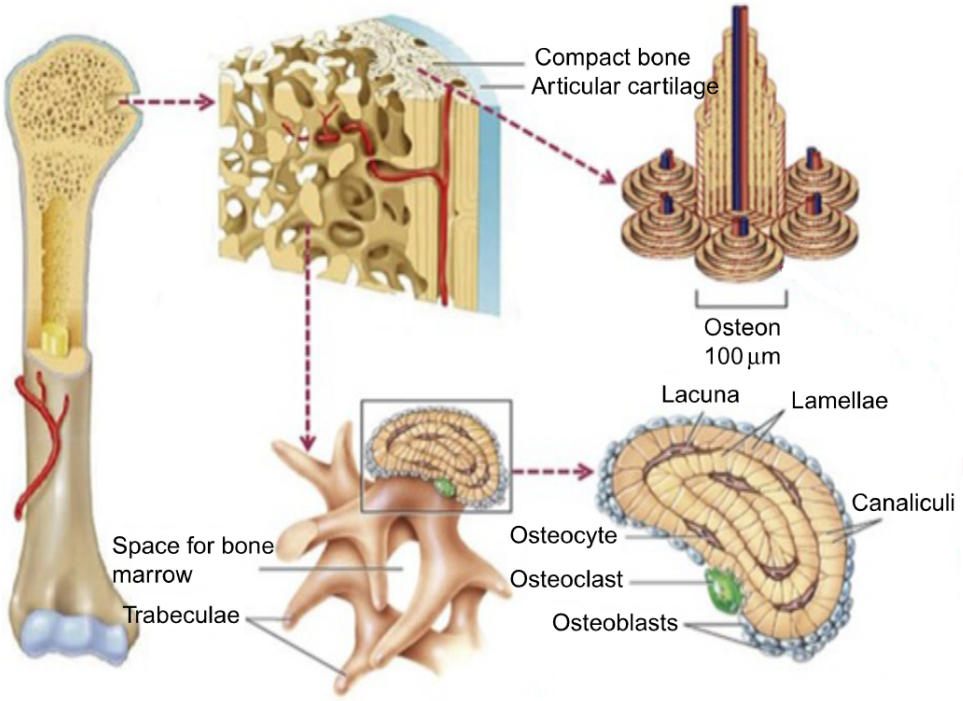

FIGURE 2.1: Bone structure: the compact, dense bone is placed on the outside of the bone. Inside is the spongy, porous bone with web-like trabeculae. Compact bone consists of osteons, blood vessels, nerves, and lymphatic vessels are going through (central Haversian canal) the middle of the osteons. These Haversian canals are surrounded by rings of lamellae. The hollow areas between the lamellae are lacunae, which are connected to each other *via* microchannels, called canaliculi. Visible are also the osteocytes in the lacunae, the bone removing osteoclalts, and the bone building osteoblasts. Image with permision from [34]

Bone is the major supportive tissue. White and Folkens [33] mention bone as one of the strongest weight bearing biological materials, being simultaneously a very lightweight material. During running human bones at the knee joint bear forces, which are nearly five times the weight of the entire body.

Once the force acting on the bone extends the ultimate tensile strength, the bone is going to break. In general, the bone fractures are categorized by the 1) position of the bone ends (non-displaced or displaced), 2) completeness of the fructure (incomplete or complete), 3) orientation of the fructure (linear or transverse) and 4) penetration of skin (compound or simple). In addition it may be fragmented [35].

In some cases is it enough to have a plaster cast around the fractured bone to hinder the movement such that the bone healing process can take place. However, if there is a movement of the broken bone parts towards each other, a surgical fixation on the bone with screws or plates is needed for the proper healing.

Depending on the condition present at the injured tissue there are different extents of the cortex, the periosteum, the bone marrow and the external soft tissue being involved in the healing process [36]. These conditions might be the level of growth factors, hormones, nutrients, pH, oxygen tension, the electrical environment, and the mechanical stability of the fracture [37].

There are two general types of fracture healing processes: direct (primary) and indirect (secondary). In the case of the direct healing process, the healing takes place without presence of a callus, either with "contact healing" (when the gap between the

bone ends is less than 0.01 mm) or "gap healing" (when the gap between the bone ends is between 800 µm and 1 mm) [38, 39]. This process takes place only after rigid surgical fixation, or in case with a partial crack in the bone, a so-called "unicortical" fracture, where the remaining bone holds everything rigid. But most common is the indirect, secondary bone healing process. John Hunters (1728-1793) frame of fracture healing process divides it in three main groups: 1) the inflammatory phase, 2) the reparative phase and 3) the remodeling phase. An approximate period of time of the fracture healing stages is presented in figure 2.2 [40].

1) The **inflammatory process** is a trauma response that includes three different stages:
1.1) hematoma stage: Following injury, the vascular disruption leading to acute necrosis occurs and local acidosis and hypoxia of bone, periosteum, bone marrow and soft tissues takes place. The activation of thrombotic factors follows, resulting in blood clot formation in fracture site. Hematoma is the source of signaling molecules that have the capacity to initiate cascades of cellular events that are critical to fracture healing [41]. Osteocytes deprived of nutrition at the fracture ends die and play a passive role in the repair process;
1.2) inflammatory stage: Macrophages and other immune cells (like monocytes, lymphocytes and leucocytes) are brought to the fracture site and are essential in secreting pro-inflammatory cytokines [42]. Mainly, they affect the induction of extracellular matrix synthesis, the angiogenesis stimulation. Moreover, they have a chemotactic effect on circulating immune, mesenchymal cells and the recruitment of endogenous fibroblasts [43]. Activated platelets release growth and differentiation factors to the induction of ossification;
1.3) granulation tissue stage: In this stage the following organization of hematoma takes place; capillary buds grow from endosteal circulation. Hereby, the damaged material is being removed, the dead calcified bone resorbed, macrophages activated. Simultaneously, the modulation of undifferentiated mesenchymal cells into chondroblasts, osteoblasts and fibroblasts takes place. The temporary tissue is replaced by fibrocartilage.

2) The **reparative phase** is generally improved by micromovement and stopped by fixation [44]. Here, the osteoprogenitor and undifferentiated mesenchymal cells are integrated into the callus tissue, which will be differentiated into skeletal cells afterwards . In this phase one of the following two processes take place:
2.1) The intramembranous ossification stage: The bone is build directly without the formation of a transitional cartilage tissue.
2.2) The endochondral ossification stage: It takes place next to the fracture and consists of two processes. During the first process, called chondrogenesis, the mesenchymal cells are recruited, attached and proliferated. Here, they are differentiated into growth cartilage while angiogenesis takes place. The second process, which partially overlaps with the first one, is the endochondral ossification. It is a sequence of cartilage calcification, cartilage removal and bone formation.

3) The last phase, the **remodeling phase** also consists of two processes in order to replace the freshly built bone with actual, lamellar bone tissue. At the same time the callus size is being reduced and the normal vascular supply ensured.
3.1) In the first process the basic multicellular unit (BMU) replaces the woven bone with the lamellar one and the callus between the ends of compact bone with new osteons. These are aligned parallel to the compression and tension stress and strain, which arise from mechanical use or muscle forces [45].
3.2) In the second process the external surface of bone is remodeled with osteoclasts (bone removing cells) and osteoblasts (bone building cells).

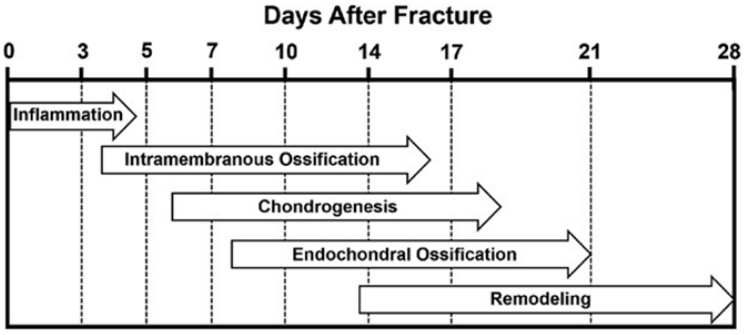

FIGURE 2.2: Stages of fracture healing in rodents subjected to internally stabilized experimental long bone fractures, as described by Bonnarens and Einhorn [48]. Image with permission from [40].

This third phase takes place between 1 and 4 years. As a result, the bone strength is returned to its initial strength and the chance of re-fracture decreases [46, 47].

2.2 Implants

To preserve anatomic shape, restore function and obtain rapid healing without any local and/or general complications, nonsurgical and surgical treatments are applied [49–51]. Examples for nonsurgical treatments are bracing with plastic apparatus and immobilization with casting. External or internal fracture fixations are indicated as surgical treatments.

The materials of which the medical implants are engineered from are biomaterials, namely ceramics, polymers or metals. The definition of a biomaterial can be taken from International Union of Pure and Applied Chemistry: "A biomaterial is a material exploited in contact with living tissues, organisms, or microorganisms" [52]. According to other definitions: "A biomaterial is any matter, surface or construct that interacts with biological systems" [53] or "Biomaterials are generally synthetic, nonliving materials for therapeutical (e. g. implants) and diagnostical use in medicine and direct contact to biological tissue. Thus, they are in chemical, physical and biological interaction to the biological systems (cells, extracellular matrix, body fluids, etc.) and must fulfill biocompatible properties – with long-term reduction of negative influence (inflammation, immunological, toxicological, mutagenic, allergic, etc.) to the surrounding tissue" [54].

An overview about the requirements for biomaterial for implants is described in [55]. The general requirements towards the internal fixation devices made of biomaterials are offering a suitable mechanical environment for fracture healing, sufficient strength, biocompatibility and, in the case of non-biodegradable implants, corrosion resistance. Known non-degradable implant materials, which fulfill the requirements to be called a biomaterial, are cobalt–chrome (CoCr) alloys, stainless steel and titanium (Ti) alloys. They are mostly being used as internal fixation [51]. In addition to Mg, tungsten (W), zinc (Zn) and iron (Fe) are described as metals, which can degrade in physiological environments [56].

2.2.1 Surgical Implants for Fracture Fixation - Screws

There are four main categories of internal fracture fixation devices: 1) plates and screws, 2) external fixation, 3) intramedullar devices (rods or nails), 4) wires and

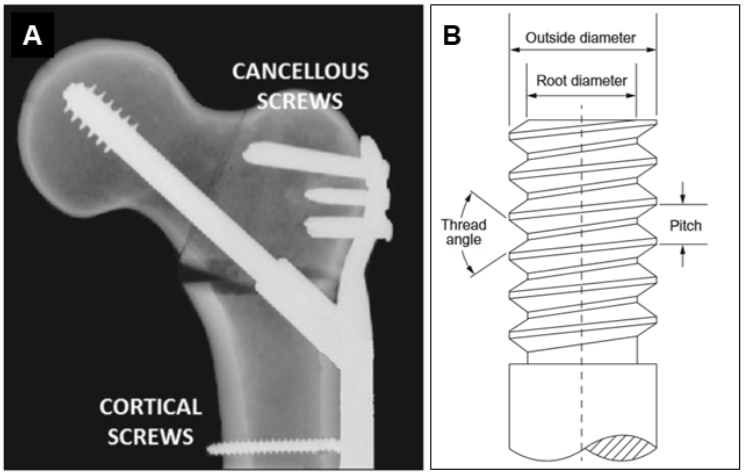

FIGURE 2.3: A) Radiographs showing cortical and cancellous screws for fracture fixation in proximal femur. Image with permission from [58]. B) Schematic of a typical screw thread with several bone describing parameters. Image with permission from [57]

cables [57]. Exemplary internal fixation screws are shown in figure 2.3A.

Bone screws, being the most widely used orthopedic fracture fixation devices, must be strong and secure enough to allow early mobilization of the injured part, as well as the entire patient. Thus, for an increase in the contact area and in the stability between fragments as well as a decrease of the stress on the implant, compression is used whenever possible [57, 59]. The attachment of plates or the provision of interfragmental compression is performed with the help of screws. Simultaneously, during the healing process, a prevention of displacement and a support of the fragments is taking place [59].

There are several types of screws in different sizes for this purpose. The typical parameters of a surgical screw are presented in figure 2.3B. The difference between a cortical and a cancellous bone screws is in the depth of the thread , in the number of threads and the depth of the screw. The threads of a cortical screw are more in count and are lower than the ones of cancellous screws. Since the cancellous screws have greater thread depth, thus increased surface area, hence they provide improved hold than the cortical screws [57, 60].

2.2.2 Non-Biodegradable Permanent or Temporary Implants

The mechanical properties of bones don't match well with the ones of most the bioimplant materials [61]. A comparison of the mechanical properties can be found in table 2.1 [62].

The mismatch of the mechanical properties may cause stress shielding, which is the reduction in bone density (osteopenia) occuring when the the typical stress experienced by bone is removed by an implant [63]. This could lead to aseptic loosening [64] for example. In case of stainless steel, where the oxide of stainless steel becomes conductive [65, 66], it can also stimulate an inflammatory response. All the mentioned potential complications in connection with implants are of extra importance of course in the case of implantations for children.

After the fracture has healed most non-degradable implants remain in the body, which often causes, next to the above mentioned reactions, discomfort and makes a second, implant removal surgery necessary. The need of the second implant removal

TABLE 2.1: Some mechanical properties of chosen materials [62]

Tissue/Material	Density (g/cm^3)	Compressive strength (MPa)	Tensile strength (MPa)	Elastic Modulus (GPa)
Natural Materials				
Arterial wall	-	-	0.5 - 1.72	0.001
Collagen	-	-	60	1.0
Collagen (Tar tail tendon)	-	-	-	3.75 - 11.5
Cancellous bone	1.0 - 1.4	1.5 - 9.3	1.5 - 38	0.01 - 1.57
Cortical bone	1.8 - 2.0	160 Trans. 240 Long.	35 Trans. 283 Long.	5- 23
Magnesium Alloys				
Pure magnesium	1.74	20 - 115	90 - 190	45
AZ31 (Extruded)	1.78	83 - 97	241 - 260	45
AZ91D (Die cast)	1.81	160	230	45
Other metal alloys				
Cobalt-Chrome Alloys	7.8	-	450 - 960	195 - 230
Stainless Steel	7.9	-	480 - 620	193 - 200
Titanium Alloys	4.4	-	550 - 985	100 - 125
Ceramics				
Synthetic-Hydroxyapatite	3.05 - 3.15	100 - 900	40 - 200	70 - 120
Alumina Ceramics (Al2O3 80%-99%)	3.30 - 3.99	2000 - 4000	-	260
Polymers				
Polymethylmethacrylate (PMMA)	1.12 - 1.20	45 - 107	38 - 80	1 8 - 3.3
Polyethylene-terephthalate (PET)	1.31 - 1.38	65 - 90	42 - 80	22 - 35

surgery has been discussed in detail in [67]. The solution of this problem is the development of biodegradable implants.

2.2.3 Biodegradable Temporary Implants

Biodegradable implant materials include natural / synthetic polymers and hydrolyzable metals [68]. There are several benefits when choosing a biodegrabale implant over a non-biodegradable one. The main ones are: 1) temporary sufficient mechanical support, due to mechanical properties more similar to the ones of bone [61], 2) decrease of health care costs, postoperative inflammatory reactions and patient morbidity due to avoidance of a second, implant removal surgery [67], 3) potential inherent repair, *via* osteoinduction. Osteoinduction is the process by which new bone formation (osteogenesis/ossification) is induced. [61, 69, 70].

The aim of a biodegradable orthopedic implant is to support the fracture structure, first by having an adequate strength. The bone healing process should then be accompanied by not too fast degradation process of the implant - not before the bone healing occurs. Hereby, the load would gradually be transferred from the implant to the healing tissue. During the implant degradation the break down products should be well tolerated by the host without any mutagenic or immonogenic tendencies and incorporated into the normal biochemical and cellular physiological processes [71].

After implantation of the surgical device, an immediate host response begins, which consists of the general bone healing processes (described in 2.1). In case of biodegradable implants, the extent of these processes highly depends on the degradation products and degradation kinetics [68]. Additionally, the host response affects the degradation process, which results in further changes in the morphology, structure, mechanical properties, consequently, the performance of the implant. A disadvantage of degradable polymers over degradable metals is polymers causing a "foreign body reaction" [72]. The degradation of polymers creates an acidic pH environment, which then enhances formation of osteoclasts and diminishes the formation of osteoblasts [61, 73].

Basic requirements to biocompatible, biodegradable implants are the non-toxicity of degradation products and a good solubility, thus they can be easily extracted from the body with urine. These requirements are fulfilled by Mg implants [4, 74].

2.2.3.1 Magnesium and its Alloys

Magnesium (Mg) Mg occurs naturally only in combination with other elements, where it has a +2 oxidation state. The metal, a so-called free element, which can be produced artificially, is highly reactive. It was discovered by chemist Humphery Davy in 1808 [75], is a shiny gray solid, has the atomic number 12, and is in the second group in the periodic table and belongs to the alkaline earth metals. It is one of the light metals with a density of 1.74 g/cm^3. In the earth's crust Mg is the 8th most abundant element, in the universe the 9th and due to its ion's high solubility in water, it is the 3rd most abundant element dissolved in seawater [76]. When being exposed to the air a process called passivation takes place. As result of it the Mg is covered by an oxide layer, which partially inhibits its reactivity. Information on Mg degradation products and their influence on the body can be found in [77].

Overall, it has been found that Mg is a co-factor for more than 300 enzymatic reactions, where it is crucial for adenosine triphosphate (ATP) metabolism [78–80]. There are 21-28g of Mg in the body of an adult, where 60% of it is in the bone, 30% in the muscles, 19% in the soft tissue and 1% in the extracellular matrix [80]. Thus, Mg is very important for all the steps of replication and transcription of deoxyribonucleic acid (DNA), translation of messenger ribonucleic acid (mRNA) and is necessary for the energy balance of the cells [81]. The kidney is the organ, which mostly regulates the concentration of Mg. But also parathyroid hormone, vitamine D and calcitonin adjust the mount of Mg in the body [81, 82]. A low level of Mg in the body, Mg deficiency (hypomagnesemia), is an electrolyte disturbance, the reasons for which may be alcoholism, diarrhea, increased urinary loss, low dietary intake, poor absorption from the intestines and diabetes mellitus [83–85]. Symptoms of Mg deficiency could be tremor, muscle spasms, poor coordination, loss of appetite, personality changes, and nystagmus, whereby the complications may include seizures or cardiac arrest [83]. On the other hand, the symptoms of hypermagnesemia are confusion, weakness, decreased breathing rate, and decreased reflexes [83]. In this case the complications could include low blood pressure and cardiac arrest [83, 86].

Since most of total Mg in the body is stored in the bone it serves as a reservoir of exchangeable Mg useful to maintain physiological extracellular concentrations of the cation. One third of it is located in the cortical bone either on the surface of hydroxyapatite or in the hydration shell around the crystal [7, 87, 88].

The larger amount of Mg in bone is probably saved as an integral part of the hydroxyapatite crystal and the result of its release is the resorption of bone. Besides, apart from its importance in the structural role in the crystals, Mg is essential to all living cells, including osteoblasts and osteoclasts [87].
In the case of hypomagnesemia the influence of parathyroid hormone on the bone is being locked, thus osteoclasts are being reduced and as a result the stability of the bone is also being reduced [80]. On the other hand, in case of hypermagnesemia, during which the osteoblasts show a high activity, an unwanted bone shortening and thickening [89, 90] is observed.

During degradation the metal is gradually degraded *via* an electrochemical reaction with their environment. Hereby, it is possible that the material loses its functionality [91].

The main reaction partner of Mg and its alloys in the living organism is the water. The redox reaction with its anodic and cathodic reactions is shown below:

Anodic reaction: $Mg(s) \rightarrow Mg^{2+} + 2e^-$
Cathodic reaction: $2H_2O + 2e^- \rightarrow H_2(g) + 2OH^-$
The overall reaction is then: $Mg(s) + 2H_2O \rightarrow Mg^{2+} + 2OH^- + H_2(g)$

Mg hydroxide and gaseous hydrogen are formed on the material surface as result of reaction between the Mg and the water from the body fluids [80, 91–93].

The produced hydrogen in the cathodic reaction increases the pH of the local environment to more basic [92, 93], which is harmful for the cells [2] and in case of a fast degradation the amount of the formed hydrogen might overrun the amount of hydrogen, which the organism can resorb, thus gas bubbles arise [70].

In theMg degradation process the formed magnesium hydroxide layer would serve as degradation retarder, but it also has a positive effect on the bone regeneration process [94, 95]. However, this protective magnesium hydroxide layer is being dissolved to accelerate the degradation process if there is too high chloride concentration (higher than 30mmol/L) in the plasma. Thereby, the chloride ions react with the magnesium ions to water soluble magnesium chloride [93]: $Mg(OH)_2 + 2Cl^- \rightarrow MgCl_2 + 2OH^-$.
The result of this process could be the extremely localized corrosion, leading to small, but with the time increasing holes on the implant [4].

On the other hand Yang, Hort, Willumeit, and Feyerabend [96] found out, that the accelerative influence of those chloride ions on the degradation is being weakened by the protein layer, which arises on the surface of the implant right after the implantation. The amino acids are able to bind to the Mg^{2+} cations, hence keeping them in the solution and reducing the degradation rate [97].

Willumeit, Feyerabend, and Huber [98] showed *in vitro*, that CO_2, which is a part of the bicarbonate buffer system, also plays an important role in the degradation process. A concentration of the CO_2 above 5% in the degradation solution forms magnesium carbonate as another degradation product: $Mg + H_2CO_3 \rightarrow MgCO_3 + H_2$.

Although, depending on the conditions, the mentioned $Mg(OH)_2$ is one ot the main crystalline degradation product of Mg and its alloys upon exposure to aqueous media, it is not the only product to be expected [99, 100]. Previously, during an *in vivo* study Xu, Yu, Zhang, Pan, and Yang [94] found magnesium containing calcium on the surface of Mg-Mn-Zn alloy. During the *in vitro* degradation of magnesium rare earth alloys a complex product with the general formula $(Mg, Ca)_x(PO_4)_y(CO_3)_z(OH)_I$ was found [100, 101]. Also, many authors reported the formation of magnesium carbonates during the degradation of pure magnesium in different aqueous media [97, 100, 102].

However, not just the physiological environment has an influence on the degradation rate of Mg or Mg alloys, but also the processing parameters of the implants play an important role.

Impurities, like Fe, Si, Cu and Ni [103] play a very important role in the degradation rate of pure Mg. Because of the extraction process it is not possible to achieve 100% pure Mg, thus the typical impurities in Mg are iron, nickel, copper and beryllium [80]. Acting as galvanic cells in the material they increase the degradation process [92].

It has been shown, that implants with porous or rough surfaces degrade faster than the ones with smooth surfaces [104, 105]. Several studies revealed, that alloys with smaller grain sizes degrade faster than the ones with bigger grain sizes [106–108]. On the other hand more recent investigations have been showing that the grain size doesn't have any significance influence on the degradation rate [109].

Rare Earth Elements (REE), in particular Gadolinium(Gd)

Very early after their discovery it was found that REE possess antimicrobial, antiviral, anticarcinogenic and anticoagulant properties [110]. Nowadays, there are investigations on the potential usability of these metals in the therapy after incineration, diagnosis and therapy of tumors and in the therapy of hyperphosphataemia [80, 110, 111].

However, depending on the application as well as on the species, its sex and body weight, these metals can be very toxic to the adult body [111]. Feeling of unwellness, difficulties during breathing, apathy and even sedation are described as symptoms of intoxication [112].

The lanthanoids have big similarities with calcium. Because of their similarity regarding their atomic size, it is possible that lanthanoids by mistake replace calcium in several areas, like the replacement of the calcium in the calcium channels (ion channels, which are selective permeability to calcium ions) [110]. The latter would lead to the blockade of the channel [80, 110, 111].

Additionally, it has been shown that lanthanoids can react *in vitro* with a lot of cell organelles, with the cell proteins and enzymes, but can also penetrate into the healthy cells [80, 111].

Gadolinium (Gd) is a REE and a lanthanoid. There are a lot of advantages and disadvantages associated with the usage of Gd in medicine. Although Gd based contrast agents (GBCA) are the most widely used contrast agents for magnetic resonance imaging (MRI) since their introduction into clinical practice in 1988 [113], its toxicity is still a topic for discussions. For example, at the neurons, the free Gd ions (Gd^{3+}) can lead to direct release of neurotransmitters. The result of this could be the wrong reaction of the "stress response pathways" and later the wrong protein folding [80, 114], leading to different diseases [115].

To avoid its toxic influence Gd is being used in its stable state, in combination with chelatcomplexes. Unfortunately the stability of this complex is well understood just in the *in vitro* experiments, but there are complications in *in vivo* cases. As the result of repeated GBCA usage in high dose there are symptoms like skin thickening, hair loss and eschar formation occurring. An additional complication is the nephrogenic systemic fibrosis (NSF), which mostly arises in the case of patients with an advanced kidney failure [116, 117]. Here, the release of free Gd^{3+} is occurring as a result of de-chelation because of very long elimination times of the complex from the body. Hence, there are some types of GBCA, which are not allowed for use in patients with kidney failure [118]. In a mouse model it has been shown that in case of high amount of GBCA insertion into the body Gd agglomerates in the liver, kidney and spleen [80]. Additionally, a sign of an inflammatory reaction was detected *via* over-expression of inflammatory cytokines in the lung and kidney, and an increase of lymphocytes and granulocytes in the blood [80]. From the histological point of view there were morphological changes in the liver tissue, thickened walls of alveolus in the lungs and atrophy of the glomerulus and tubular ephitelium in the kidney [114].

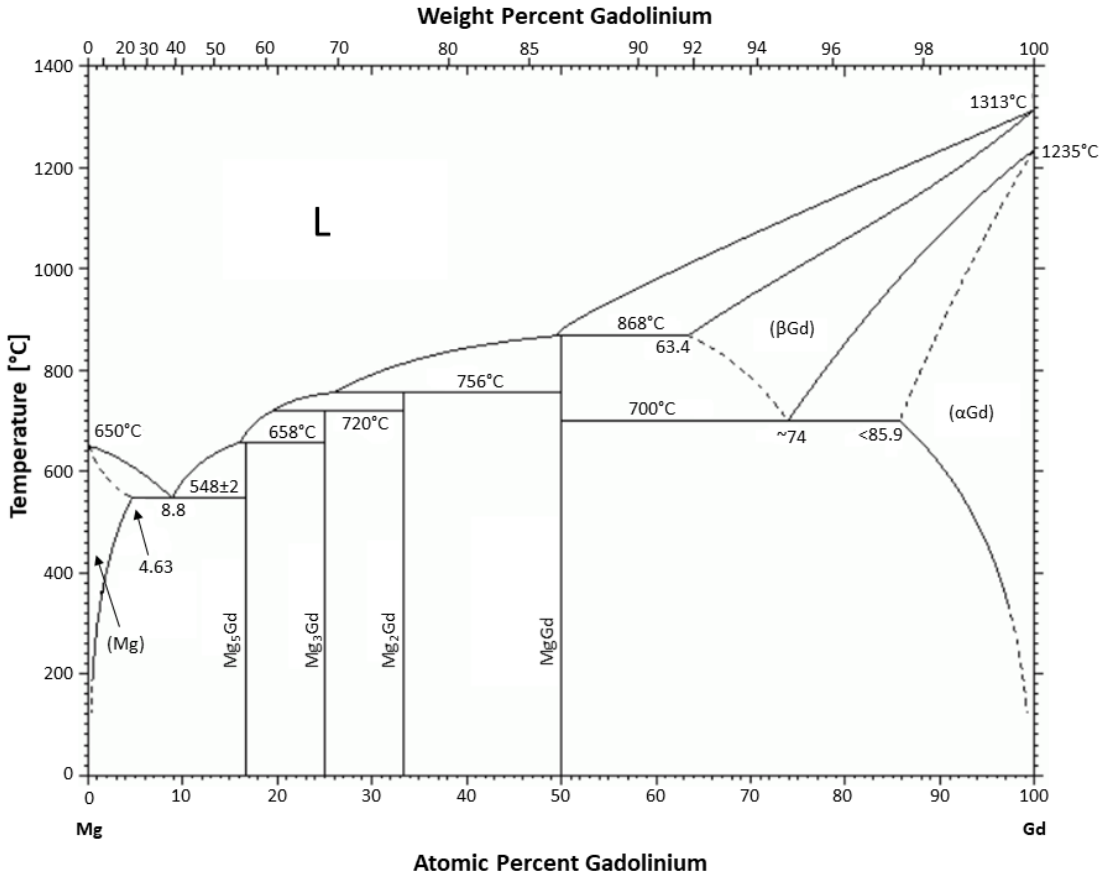

FIGURE 2.4: Mg-Gd phase diagram [121].

Magnesium-Gadolinium Alloys

Depending on the amount of their valence electrons, hence their solubility in Mg, the REE can be divided into two groups: Cer- (Li to Eu) group and Y- (Y and Gd to Lu) group. The solubility of the Y-group elements in Mg is much higher, than the one of the Cer-group elements and the Y-group elements are better precipitation hardening elements [119, 120].

Figure 2.4 from [122] represents the equilibrium phase diagram for the Mg-Gd binary system. There are four main binary compounds: Mg_5Gd, Mg_3Gd, Mg_2Gd and MgGd, which are formed by peritectic reactions [122]. On the Mg side there is one eutectic equilibrium and one eutectoid equilibrium connected with two allotropic forms of Gd (β-Gd $\rightarrow$ α-Gd + MgGd). Mg_5Gd is the real composition of the compound and its stoichiometric formula is $Mg_{45}Gd_{11}$ [121]. The eutectic temperature is ca. 542° C and there is 40.4 wt.% Gd in the composition. There is a relative high solid solubility of Gd in Mg with a maximum of ca. 24 wt.% at 542 °C and around 4 wt.% and 6 wt.% at 200 °C and 300 °C, respectively.

Addition of REEs to the high purity Mg matrix results in promising biodegradable Mg alloys since they exhibit sufficient strength and toughness, so they could be well used as load-bearing alloys [12]. Especially in Mg-xGd alloys significant solid solution strengthening effects have been observed. Additionally, from a biocompatibility point of view Gd is conserved as relatively acceptable additive in low concentrations and is indicated to have anticarcinogenic properties [12, 123]. It has also been indicated, that the cells grown on the Mg-10Gd alloy generated healthy

cellular structures that allowed them to have a good adhesion to the surface [19]. Mg-10Gd has been tested *in vivo* and *in vitro* by Marco *et. al.* [124] over a short time period of up to 7 days. Myrissa *et. al.* [125] and Galli *et. al.* [126] tested Mg-10Gd *in vivo* over a time period of 12 weeks. Myrissa *et. al.* [125] implanted pins transcortically and Galli *et. al.* [126] implanted screws into the femur of rats. Myrissa *et. al.* [125] reported an initial low degradation rate without gas bubbles, but afterwards a very fast degradation rate with high amount of gas bubbles visible. After 12 weeks implantation nearly a complete dissolution of the implant in the bone was observed. This would not be acceptable for a fracture fixing implant, since it should provide structural stability at least for 12 weeks [125, 127]. On the other hand Galli *et. al.* [126] concluded that Mg-10Gd showed a degradation behavior appropriate for bone formation and stable degradation layer. The different outcomes of experiments may be arising from different microstructures, differences in the implants production and manufacturing, place of implantation and different imaging modalities [126].

2.2.4 Types of Material Testing: *In Vivo*, *Ex Vivo* and *In Vitro* Tests

The experiments, which investigate the progress of metal corrosion in a corrosive environment, as well as other factors, which could influence the corrosion, are the immersion tests. They are the most simple and economical ways to measure the corrosion ability of the material.

Gonzalez et al. [128] reviewed the types of immersion tests: static, semi-static and dynamic. The importance of the immerion test type and the immersion medium composition on the degradation result are also summerized by Gonzalez et al. [128].

To be used as implants, Mg and its alloys have to go through tests, which are defined by the International Organization for Standardization (ISO 2009) and/or American Society of Testing and Materials (ASTM 2003). Thereby, for the *in vitro* degradation testing immersion solutions like sodium chloride solutions, simulated body fluid (SBF), Hank's balanced salt solution (HBSS), phosphate buffered saline (PBS) are used. The modified Eagle's minimum essential medium (MEM), Dulbecco's modified Eagle's medium (DMEM), Alpha modified Eagle's minimum essential medium (α-MEM)) are recommended for the study of the degradation behaviour and mechanisms, to obtain a comparable degradation behaviour to *in vivo* conditions. [129]. However, the degradation *in vivo* is much more complex, hence it is difficult to compare the results of those of experiments.

Several studies show that the *in vitro* degradation rate is higher than the *in vivo* one, sometimes they are even inverse, so that from the result of an *in vitro* experiment no conclusions about the *in vivo* result can be drawn [130–132]. It is still a challenge to find the matching *in vitro* experimental conditions to make it comparable to *in vivo* [56, 91].

One possibility to obtain insight into the *in vitro* and *in vivo* (respectively *ex vivo*) degradation is the usage of micro-computed tomography technique, which principles are summerized in the next section.

2.3 Micro-Computed Tomography (µCT)

Being derived from the Greek, the term tomography means "to cut" and the term computed refers to use of a mathematical reconstruction algorithm, which combines the projections into slices of the object's cross section [133].

µCT is a very important method in non-destructive 3D characterization and materials evaluation [134], since the difference in X-ray absorption between regions with dissimilar atomic numbers or densities in the investigated object is visualized [135]. X-rays can be generated either in the laboratory (in X-ray tubes) or at synchrotron radiation (SR) sources [136]. Depending on different factors like sample size and composition, required spatial and contrast resolution or scanning time and volume, the choice of the optimal method is being made [137].

The first step of computed tomography is the recording of two-dimensional X-ray images of an object from various angles (2D projections). The second step is the digital three-dimensional (3D) image reconstruction, which results in a 3D image of the object. It makes the multidirectional examination of an area or volume of interest possible, but also permits dimensional, volumetric, or other more advanced measurements to be made [138–140].

Depending on the atomic number of the element and the X-ray energy, there are different interactions taking place between the specimen and the X-ray [133]. The elastic scattering and photoelectric effect are the dominating effects and they modify the incident X-ray beam intensity and direction for low-energy X-rays. Additionally, Compton scattering also affects the X-rays passing through the specimen when using X-rays at higher energies. The idea of the tomographic reconstruction is to compare the incident and exit beams, whereby the most widely used form of µCT principal is based on the X-ray absorption contrast revealed by differences in the linear attenuation coefficient μ. However, changes in other signals also can be used for reconstruction: refractive index (phase contrast), crystallographic structure (X-ray diffraction contrast), elemental distribution (fluorescence contrast), particle size and shape (scattering contrast), and local atomic environments (e.g., X-ray absorption near-edge structure, XANES). The main steps of acquiring the projections always include the following: a beam is propagating from the X-ray source through the sample onto the detector, whereby the sample is being rotated either to 180° or 360°. The principle of the X-ray absorption is presented in figure 2.5 [133]. It briefly gives an idealized 2D example on the X-ray absorption principle depending on the materials thickness and linear attenuation coefficient.

Having an incident X-ray intensity of I_0, after being transmitted through a homogeneous sample with the thickness t it changes to intensity I [133]. This is expressed with the Beer-Lambert law

$$I = I_0 e^{-\mu t} \tag{2.1}$$

The linear attenuation coefficient μ [cm^{-1}] is defined as in equation (2.2). It depends on the number and type of atoms traversed by the beam. Under the conditions of moderate energy range and away from the absorption edges, $(\mu/\rho) \approx Z^4\lambda^3$ whereby Z is the atomic number and λ is the X-ray wavelength. In the case that the specimen consists of i elements, the effective attenuation coefficient $< \mu >$ is calculated taking into account the weight fraction w_i, mass attenuation coefficient $(\mu/\rho)_i$, and density ρ through [133]

$$< \mu >= \sum_i w_i (\frac{\mu}{\rho})_i \rho \tag{2.2}$$

Since equation 2.1 describes the integrated effect of a uniform sample on the

beam, but the idea of CT is to determine μ_i of material i for each position within a sample, the equation 2.3 [133] is used.

$$\sum_i \mu_i \Delta t_i = ln(I_0/I) \tag{2.3}$$

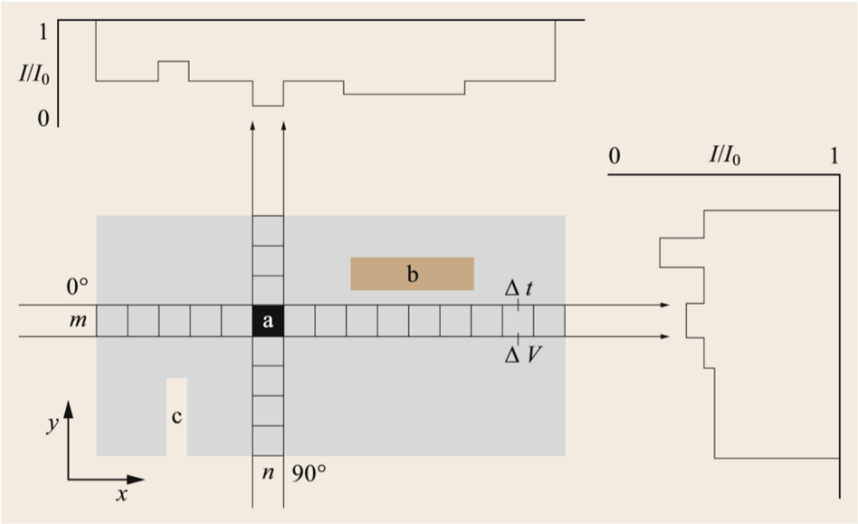

FIGURE 2.5: Principle of X-ray absorption: Presented are the X-ray absorption profiles for two views through an idealized specimen. $\Delta\, t$ is the thickness of the voxel ΔV. For both views the ratio I/I_0 is shown schematically, ranging from 1 (corresponds to no absorption since outside of the sample) to 0 (depending on the material: the darker the gray, the more absorbing the corresponding material). Exemplary, the voxels through the row m and at view 0° and along column n at view 90° are shown. Accordingly, the highest absorbing material is the single voxel a, which results a narrow decrease in I/I_0 in both views. Image with permission from [133].

The image reconstruction is the mathematical process, which generates tomographic images from X-ray projection data.

There are two major categories of reconstruction methods: analytical and iterative reconstruction. The most widely used analytical reconstruction method is the filtered backprojection (FBP), because of its computational efficiency and numerical stability [141]. Here, a 1D filter on the projection data is applied before it is being backprojected (2D or 3D) onto the image space [141]. Following three steps are applied

1. Radon tansformation of the projection profile
2. Application of high-pass filter, or ramp filter, to eliminate blurring (star-like artifacts), which occures during the iterative constructive interaction of the projections. Afterwards the filtered projection profiles are transformed back.
3. Backprojection of the projection profile.

2.3.1 Laboratory µCT

X-ray tubes are the most common radiation sources in analytical and quality laboratories, due to their accessibility, relative cheapness and good results [142]. All laboratory µCT devices consist of an X-ray source, a stage to hold the specimen, which

is being images and a detector / camera. Depending on the X-ray source and the detector, there are four scanner hardware configurations: pencil, fan, parallel and cone beam geometries (figure 2.6 [133]). In two of the geometries a beam collimation is taking place, which is the narrowing and direction of the beam before it reaches the object of investigation [133].

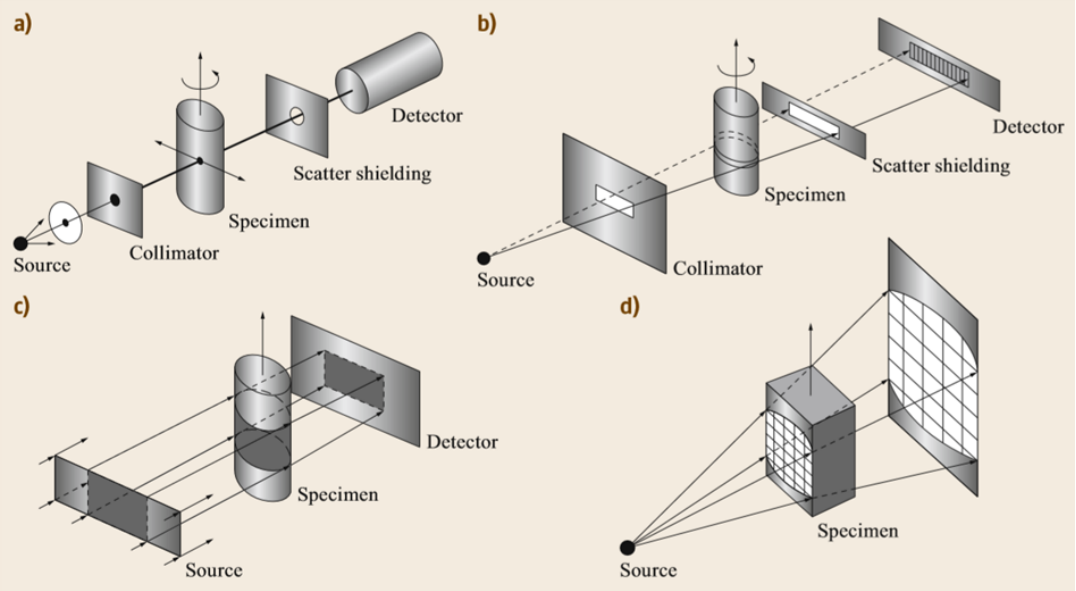

FIGURE 2.6: Schematically presentation of laboratory µCT scanner geometries: a) Pencil beam, b) Fan beam, c) Parallel beam, d) Cone beam. Image with permission from [133].

Figure 2.7 presents a schematic of the X-ray generation in a laboratory X-ray tube. A polychromatic radiation is generated within a tube source. Firstly, the filament material is being heated up, which enables the electrons to be released from it (thermionic emission). Due to the applied voltage between the filament (cathode) and the metallic target (anode) the electrons are being accelerated towards the anode. As soon as the electrons reach the target the Bremsstrahlung is being produced. The Bremsstrahlung is the continuous spectrum of X-rays chatacteristic for each target material, which is being generated when the electron is being decelerated. There are two disadvantages of this process: i) the X-rays are emitted in all directions, thus limiting the amount of X-rays that will actually be emitted toward the specimen and ii) only a limited amount of the original energy is converted to X-rays energy, resulting in the conversion of the residual energy into thermal energy. Adjusting the maximum energy, which is the peak voltage, kVp and the current (µA) the user of a laboratory µCT scanner has some freedom of producing different imaging conditions [133].

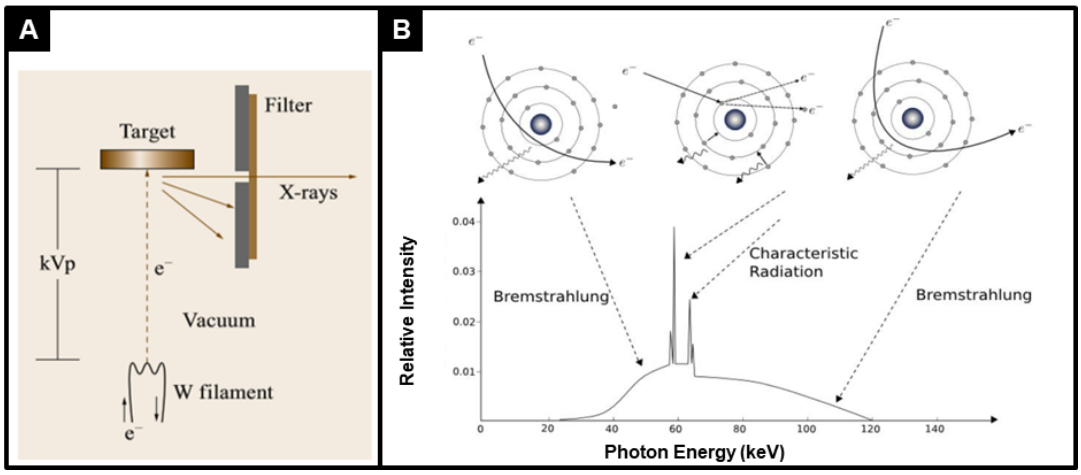

FIGURE 2.7: A) Schematically illustration of an X-ray tube source. The filament is heated up, so the free electrons can be accelerated towards the target material *via* a certain electric field. When the electrons are slowed down by the target material, the Bremsstrahlung and the characteristic radiation are being produced. After filtering some of the produced radiation the X-rays can be used for imaging. Image with permission from [133]. B) X-ray spectrum of a tungsten X-ray tube. The peaks correspond to the characteristic radiation of tungsten and the continuous part of the spectrum represents the Bremsstrahlung. Image with permission from [143]

2.3.2 Synchrotron Ratiation µCT (SRµCT)

The SR sources offer high brilliant X-rays on an almost routine basis with the advantage of the X-rays' high intensity, its high collimation (small divergence of the beam), and its tunable wavelength [142]. In contrast to the laboratory µCT X-ray sources, X-rays from the synchrotron source are generated in a large circular particle accelerator, a storage ring [133], where controlled assemblies of magnets are used to steer the particles. The particles (electrons or positrons) are accelerated in a circular path and their energy is maintained [133]. High vacuum conditions minimize the loss of particle energy due to deflection. A very simplified exemplary sketch of a synchrotron radiation storage ring is presented in figure 2.8.

In such a ring alternating magnetic fields are put together to bending magnets, wigglers and undulators, which force the electrons / positrons to a sinusodial trajectory, whereby the output radiation is being enhanced [144]. In the present radiofrequency cavities the particles are being accelerated, hence their energy loss is being compensated [144].

The most important advantage of synchrotron radiation over a laboratory X-ray source is the brilliance of the synchrotron radiation. The brilliance of the storage ring is the number of photons per time interval (s), per source size (mm^2), per opening angle ($mrad^2$), per 0.1% spectral bandwidth [144]. It describes the brightness and the angular spread of the beam. The higher the brilliance the more detailed investigation of the material is possible. As shown in figure 2.9 the brilliance of the emitted radiation beam has been enhanced over the last years. The above mentioned magnetic arrays, bending magnets, wigglers and undulators, make it possible to enhance the flux and the brilliance of the photon beam of the synchrotron source radiation in comparison to laboratory based sources.

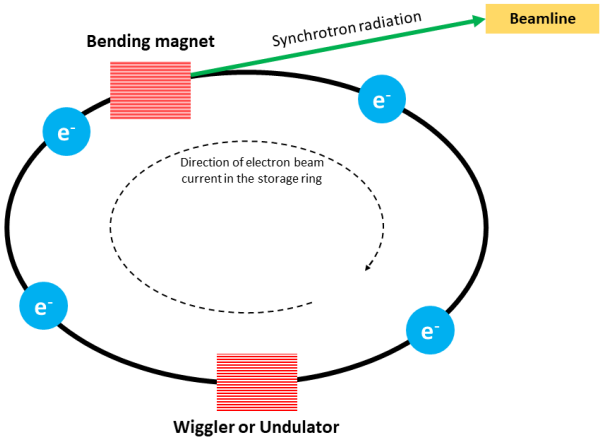

FIGURE 2.8: Storage ring of a synchrotron radiation as sketch. The storage ring, which is a circle of an appropriate radius, consists of curved and straight sections. The curved sections are within the dipole magnets and the straight sections are between them. After electron bunches being injected into the storage ring, they can be bended *via* bending magnets and emit radiation. To increase the intensity of synchrotron radiation a series of bending magnets is being lined up to a so called wiggler and the eletron beam is forced through it. The same principle of enhancing the radiation intensity is working *via* more modern undulators instead of wigglers. Also the undulators consist of periodic arrangements of dipole magnets deflecting the electron beam sinusoidally, but they differe from wigglers by themagnitude of the magneti strength. Devices producing the undulator radiation have low fields and short magnetic periods [145].

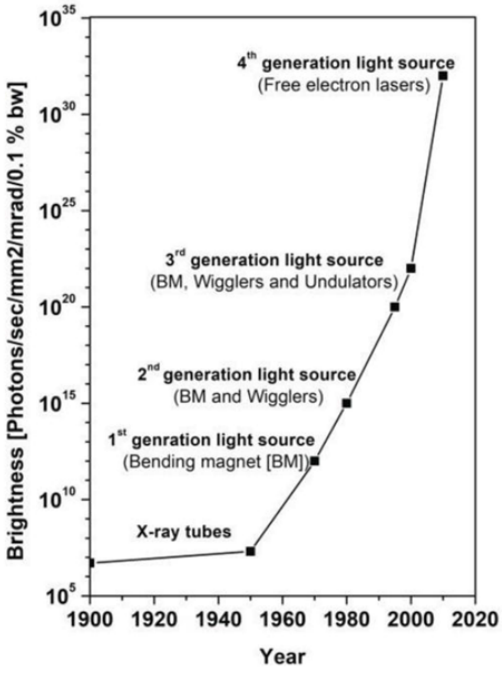

FIGURE 2.9: Brilliance of emitted radiations of different technical sources [146]. Although the main mission of the bending magnet is to circulate the elektrdeon beam in a closed path, it is also the primary source of the synchrotron radiation. Through the years, due to evolution of further insertion devices like wigglers and later undulators the brilliance of the synchrotron radiation electron beam was enhanced.

The Deutsches Elektronen-Synchrotron (DESY) in Germany, Hamburg, operates one of the world's brightest, third generation storage-ring-based X-ray radiation sources PETRA III, where the imaging beamline P05 is located [147].

A sketch of the P05 beamline at DESY, PETRA III, which is being operated by the Helmholtz-Center Hereon is presented in figure 2.10. The wide energy range of 5-50 keV makes the investigation of different materials possible. Tompgraphic scan times of ca. 15 minutes without loosing the high density resolution can be reached [147].

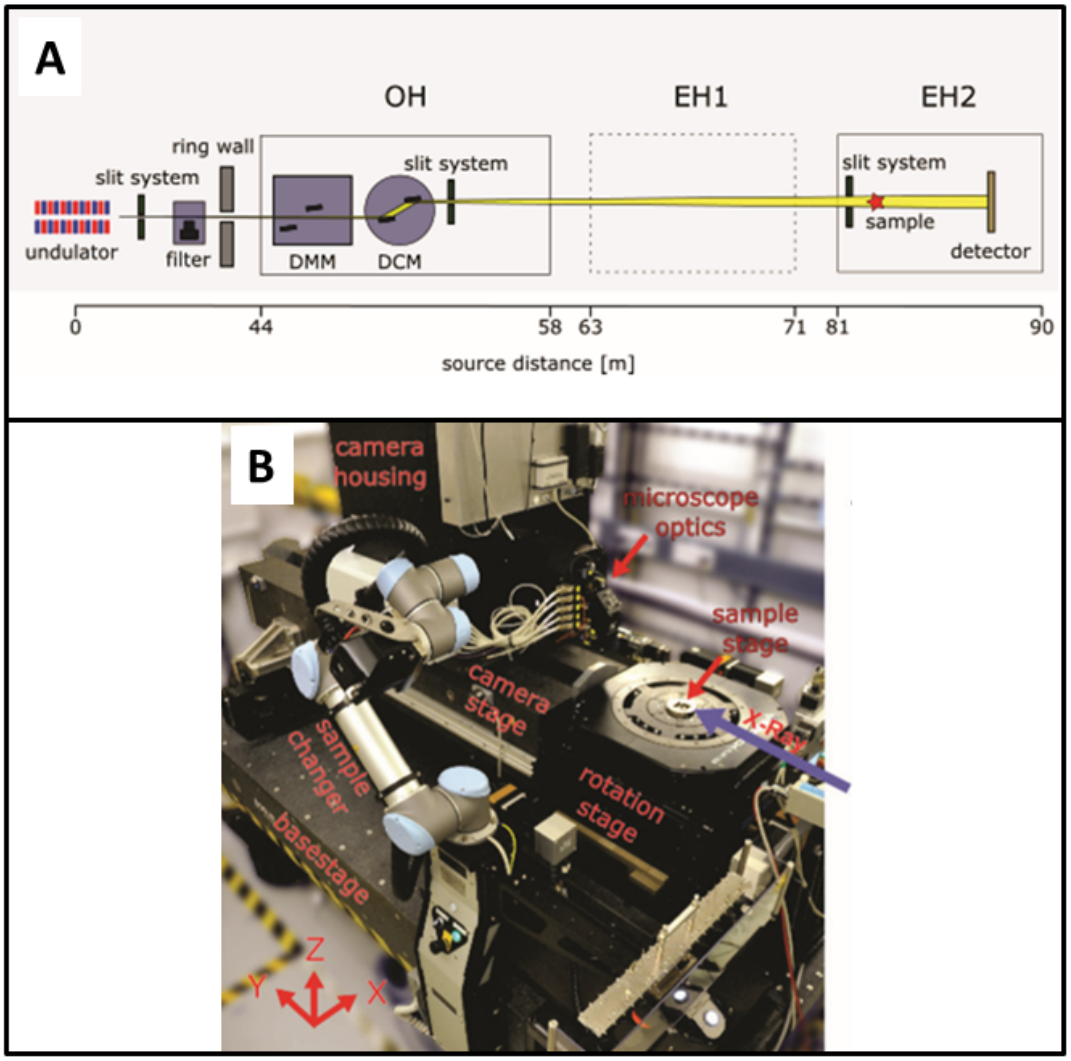

FIGURE 2.10: Sketch of P05 beamline at DESY: A) An undulator, slits and filters, an optics hutch (OH, consisting of a double crystal monochromator and a double multilayer monochromator), the first experimental hutch (EH1, used for nano tomography) and the second experimental hutch (EH2, used for µCT) are in the beamline, B) Inside of EH2: four spatial motion stages (base, rotation, camera and sample stages), a microscope system (consisting of two cameras), sample changer and a slit system are visible [147]

2.4 Image Processing: Filters, Segmentation, Registration, Resampling

The result of tomographic image reconstruction provides a 3D data set, consisting of 2D greyscale slices. Prior to all quantitative analysis some image processing, like image filtering, segmentation, registration and resampling are required.

Filters

Most of the reconstructed 3D tomographic data need some image processing prior to the quantitative analysis. In contrast to qualitative analysis, for the quantitative one a very clear separation of the grey values of different objets in the image is needed. Hence any kind of noise or image artifact can act as an analysis inhibitor. To reduce the noise of the image and improve its quality filters are used [148]. There are linear and nonlinear algorithms used for filtering the images. Examples for linear filters are mean filter, gaussian, derivative, gradient, lowpass or highpass filters. Nonlinear filtering algorithms are used for example in median filter, min and max filters, entropy or kuwahara filters.

In this work, depending on the image quality only mean and median filters are used. The mean filter is the simplest filter, which performs average smoothing on an image. Thereby each pixel in the image is replaced with the mean of the pixels that surround it, depeding on the chosen amount of the filtering pixels [148]. In contrast, in the case of the median filter, each pixel in the image is replaced with the median of the pixels that surround it. Instead of smoothing the whole image like in the case of the mean filter it sharpenes the edges by enhancing them. A comparison of the effect of both, mean and median filters on an image can be found in figure 2.11.

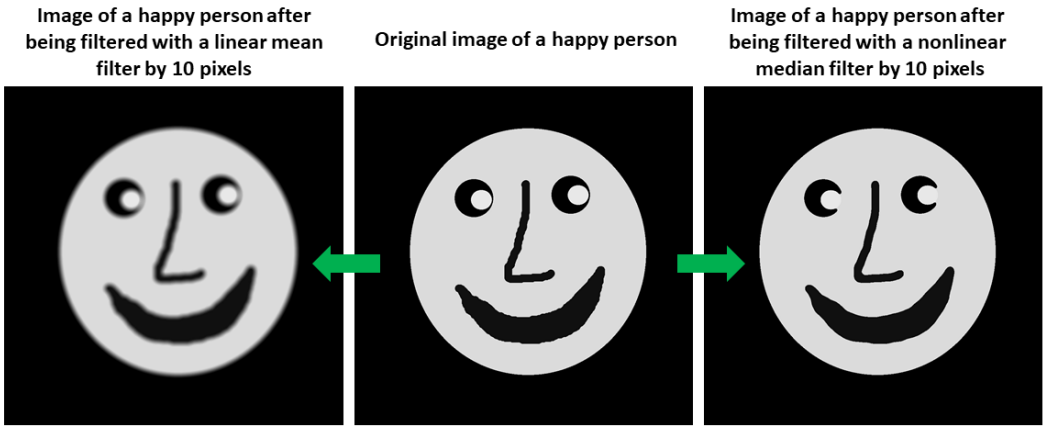

FIGURE 2.11: Comparison of mean and median filters. In the middle is the original image without any filters applied. On the image on the left side is the result of the original image being filtered by a mean filter with a pixel size of 10. In constrast, on the right side is the same original image after being filtered by a median filter with the pixel size of 10. The differences of both filtering methods are well visible on the edges of the mouth, eyes and the nose.

Segmentation

After an appropriate image filtering the segmentation of the image can be performed. Segmentation is the grouping of voxels belonging to the same object or area of the image. If the linear attenuation coefficient distribution of two objects are very different a simple global thresholding technique can provide a successful segmentation result [133]. An example of a thresholding segmentation can be found in figure 2.12. Thresholding is the simplest method of image segmentation, which can be used to create binary images from a grey scale image by selecting a threshold value [149]. From the histogram of the original image the threshold value is chosen once to separate the two side objects from the background and the third bigger object and in the second case the third object is separated from both side objects and

the background. In this case only the intensity of the pixel is the deciding criterion for the pixel to be assigned to the one other the other object.

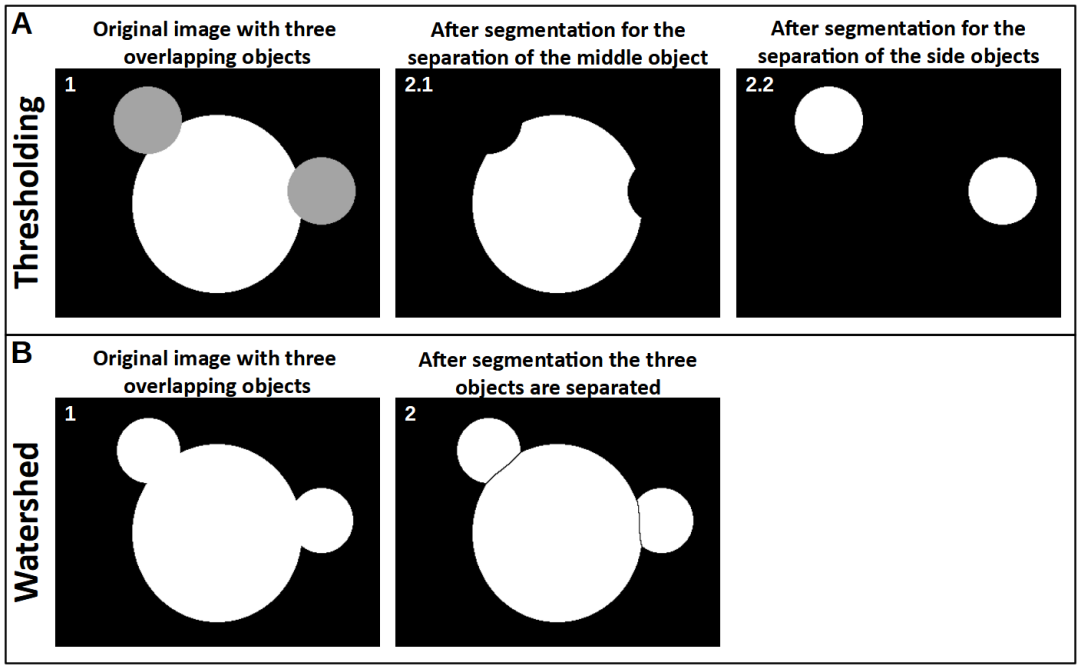

FIGURE 2.12: Example of thesholding (A) and watershed (B) segmentations using software Fiji (ImageJ). For the thresholding segmentation, based on the histogram of the original image, the pixels with same grey values are grouped (2.1 and 2.2). In the first thresholding step the middle object is seprated from the other two smaller obects and the background. In the second thresholding step the two smaller objects having the same grey values are separated from the background and the bigger object in the middle. As a results of the watershed segmentation there is a watershed line, which separates all three objects from each other.

Another prominent segmentation methods is the watershed segmentation. It is a region-based segmentation method. Hereby the image is regarded as a topographic landscape with ridges and valleys [150]. After a user defines at least one marker, also called "seed point", the algorithm grows the marker usind morphological watershed transformaiton. Thereby the valleys are filled with water (growing of the seed points) as long as they have the first contact to each other. These first contact points create the watershed line and also the object separation line [151]. The "seed point" for the growing also can be set by some algorithms automatically. An example of a watersehd segmentation can be found in figure 2.12.

Image Registration and Resampling

In order to be able to compare or integrate the data obtained from different measurements the image registration is needed. It is a procedure, which determines the parameter values for a rigid body transformation for matching the image with the reference image [152]. There are two classes of algorithms: intensity-based and feature-based [153]. Intensity-based algorithms compare intensity patterns of the "moving" and the "fixed/target" images *via* correlation metrices. In contrast, the feature-based methods find correspondences/matches between the both images (points, lines or contours). A very simple sketch of a rigit registration is presented in figure 2.13.

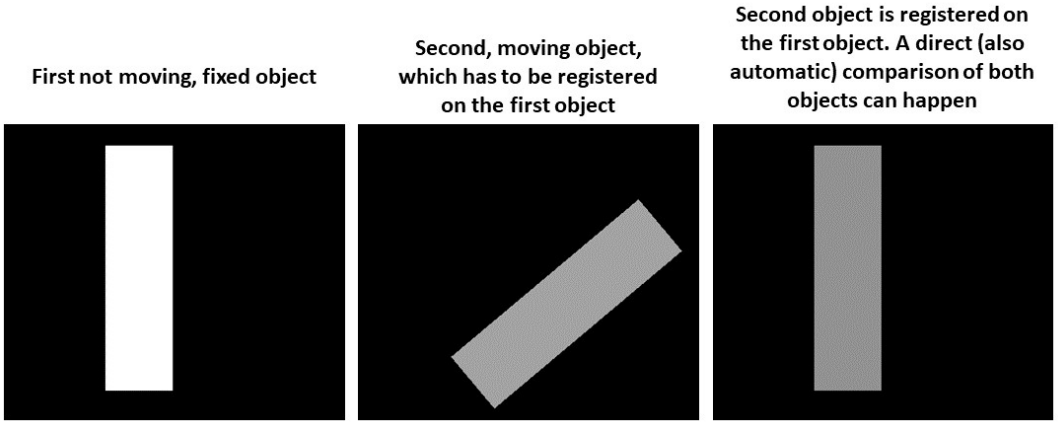

FIGURE 2.13: Sketch of a rigit registration of the object in the second image on the object of the first image. In the third image the second object has the same orientation as the fixed, source object from the first image.

In the abovementioned literature all the types of registration and their algorithms are well described [153]. The next step of registration is the image resampling, which is the actual transformation of the object from one image grid to another.

Following segmentation and potentially image registration, quantitative parameters pertaining to the sample morphology can be obtained.

This will be outlined in detail for biodegradable Mg-xGd implants in the material and methods section.

Chapter 3

Materials and Methods

3.1 Materials and Samples

The following description of materials and methods has been published in large parts in [154] and [155], hence some sections here are copied or paraphrased from the publications. Material manufacturing took place as stated in [154]:

"Two Mg alloys with 5 and 10 weight% (wt.%) Gd (Mg-5Gd, Mg-10Gd) were investigated in the current study. Melting and casting were performed by permanent mold direct chill casting using Ar + 3 vol.% SF_6 as shielding gas in the induction furnace (Nabertherm). 5 or 10 wt.% Gd was added to the Mg melt at 700 °C and stirred for 20 min with a rotation speed of 150 min^{-1}. The molten materials were then poured into a permanent steel mold (diameter 110 mm, height 230 mm), which was preheated up to 680 °C, and kept for 15 min. Afterwards the ingots were cooled down by water quenching. They were solution heat treated (T4) at 525 °C for 6 h and cooled down by water quenching. Indirect extrusion was performed with an extrusion ratio of 84 to the final diameter of 12 mm. A ram speed of 0.7 mm/s for Mg-5Gd and 0.52 mm/s for Mg-10Gd and a temperature of 400 °C were used for extrusion. From the extruded bars rods with a diameter of 3 mm were cut *via* wire electrical discharge cutting. Finally, screws were machined by turning and by milling the slit head (4 mm length, 2 mm in diameter, thread M2 and a 0.5 mm x 0.5 mm slotted screw head).

For both experiment, *in vitro* and *ex vivo*, the same alloys were used. In the *ex vivo* experiments Ti and PEEK were used as reference materials. Ti and PEEK screws purchased from Promimic AB (Mölndal, Sweden). Additionally, *in vitro* experiments were performed on pure Mg, Mg-5Gd and Mg-10Gd pins. The pins of Mg-5Gd and Mg-10Gd samples were prepared from the same material rod as the screws. The dimensions of the pins: diameter = 2 mm, length = 4 mm."

3.2 Degradation Experiments

3.2.1 *In Vitro* Experiments

In vitro immersion tests were performed on screws and pins. The immersion tests of the screws was described in [154]:

"Immersion tests were performed on screws of both alloys over a (i) short time spans (1, 3, 6, 7 and 9 days) and over 2 longer time spans ((ii) 7, 14, 21 and 28 days and (iii) 28, 56 days) as a results of semi static immersion experiment. For experiments (i) and (ii) degradation medium α- Minimum Essential Medium (α-MEM; Thermo Fisher Scientific GmbH, Darmstadt, Germany) + 10% Fetal Bovine Serum (FBS; PAA Laboratories, Linz, Austria) + 1% Penicillin/Streptomycin (Thermo Fisher Scientific GmbH, Darmstadt, Germany) was used. For experiment (iii) the

α-MEM was replaced with DMEM (Dulbecco's Modified Eagle's Medium) to compare the implant's degradation behavior in these two media. The immersion test was performed under cell culture conditions (37 °C, 5% CO_2, 20% O_2, 95% relative humidity). To avoid saturation the medium was changed every 2-4 days. At each medium change pH and osmolality measurements were performed. The amount of samples used for the weight loss and volume loss measurements per time point can be found in table 3.1. The small number of samples with 1-2 samples per time point and material are acceptable in this case, since the experiments are running over several time points, so the outliers are going to be detected."

TABLE 3.1: Number of samples used for *in vitro* investigation per measurement time point [154]

	Weight loss	Volume loss
experiment (i)	1	1
experiment (ii)	1	2
experiment (iii)	2	2

In vitro experiments were performed also on Mg-5Gd (screws and pins (n=4)), Mg-10Gd (screws (n=8) and pins (n=4)) and pure Mg (only pins (n=4)) over two month time period (4, 12, 23, 51 days). The experiment was executed as following: same immersion solution was used and the same semi-static conditions were applied as for the screws. At each measuring day the samples were taken out of the immersion solution, dried and tomographed with the degradation layer. Afterwards they were inserted into the immersion solution again. The degradation layer was only removed after the last measurement time point. Unfortunately, due to technical problems during the experiments and image acquisition the image quality was very often not sufficient enough for a proper analysis. Hence, the results were not further analyzed and are not presented nor discussed. Some of the µCT images from this experiment can be found in appendix D.

3.2.2 *Ex Vivo* Experiments

The animal experiments were performed by project partners at the Malmö University in Lund, in particular by Dr. Silvia Galli as stated in [155]:

"The animal experiments were conducted after ethical approval by the ethical committee at the Malmö/Lund regional board for animal research, Swedish Board of Agriculture, with the approval number DNR M 188-15. Sixty Sprague Dawley male adult rats with an average weight of 300 gr were selected for this experiment. The rats were housed in cages of 2 or 3 animals each for at least 2 weeks before the beginning of the experiment. The implantation protocol followed was described in [156]. In brief, general anesthesia was adiministrated before starting the surgical procedures and consisted in an intraperitoneal dose of Fentanyl 300 µg/kg + Dexmedetomidin 150 µg/kg. After shaving and disinfection of the rats' legs (chlorhexidine ethanol solution 0.5 mg/ml, Klorhexidinsprit; Fresenius Kabi, Uppsala Sweden), local anesthetic was injected in the tibial area (1 ml xylocain, Aspen Nordic, Ballerup, Denmark) and a full thickness flap was created. The tibia metaphysis was exposed and an osteotomy was drilled with a 1.4 mm round bur and then enlarged with a cylindrical bur of 1.6 mm diameter, under constant irrigation with sterile saline. After tapping, the screws were inserted with a manual screwdriver, one in each leg. Each rat received either 2 Mg-based screws (one Mg–10Gd and one Mg–5Gd) or two

non-Mg screws (PEEK and Ti), with random allocation. In total, 30 screws for each material were implanted in 60 rats. After screw insertion, the flaps were sutured. The rats received an analgesic dose of Buprenorfin of 0.01–0.05 mg/kg (Temgesic, Indivior Europe Limited, Dublin, Irleand). The rats free to move in the cages and were fed *ad libitum*. After 4, 8 and 12 weeks of healing, the rats were euthanized (10 rats per healing time) with a lethal dose of anesthetic. The legs were dissected and bone was exposed around the implant area. The implants with bone around were explanted using a trephine bur of 6 mm diameter. The bone-implant blocks were fixed in 70% ethanol for at least 1 day and were then dehydrated in a graded series of ethanol. The samples were critically point dried.

The number of *ex vivo* samples per time point and material is summarized in table 3.2. "

TABLE 3.2: Number of samples used for *ex vivo* and histology investigation per measurement time point and analysis method [155]

	SRμCT			Histologically		
	4 weeks	8 weeks	12 weeks	4 weeks	8 weeks	12 weeks
Mg-5Gd	9	11	6	10	11	6
Mg-10Gd	8	9	8	7	10	9
Ti	5	8	8	9	9	10
PEEK	9	10	9	10	10	9

3.3 Imaging Methods

In addition to the μCT analysis, investigations with optical microscopy (OP) and scanning electron microscopy (SEM) have been executed to obtain detaild information on the material microstructure. In this section the chosen parameters and the analysis procedures are described. Sample preparation and microstructure analysis took place as stated in [154].

3.3.1 Microstructure Analysis

The following section has been published in [154].
"Bulk material and screws were cold embedded in an epoxy resin (Demotec 30®, Demotec Demel e.K, Nidderau, Germany), manually grinded and polished for the microstructure analysis. The grinding process was performed from 500 to 2500 grit SiC sandpapers. The polishing was performed in two steps. First by using SiO_2 (OP-STM Cloeren Technology GmbH, Wegberg, Germany) with water (H_2O), H_2O-free lubricant (ethylene glycol to ethanol in parts of 10:7) and natriumhydroxid (NaOH) for approximately 5 min. Second by using H_2O-free SiO_2 (OPSTM Cloeren Technology GmbH, Wegberg, Germany), diamond particle suspension with 0.25 μm particle size with H_2O-free lubricant (ethylene glycol to ethanol in parts of 10:7) for 15-20 min.

Optical Microscopy (OM) After etching the samples by picric acid solution [157], observation of the microstructure was performed using an optical microscope (Leica DMI5000 M). The calculation of the grain sizes was performed on the bulk material, in longitudinal (extraction direction) and transversal direction of extrusion as well as on transversal sections of the screw *via* the linear intercept method. The analysis

software “analySIS Pro” (version 5, Olympus Soft Imaging Solutions GmbH, Münster, Germany).

Scanning Electron Microscopy (SEM) Figure 3.1 shows the areas chosen for the investigation of the microstructural differences between the bulk (210x195 µm^2) and surface near area of the screw, within the crests (310x200 µm^2) and the roots (310x200 µm^2) in particular.

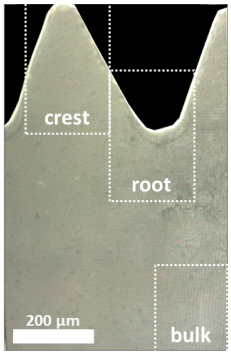

FIGURE 3.1: Exemplary areas of bulk, crests and roots on a Mg-5Gd screw for the EBSD measurements [154]

EBSD (SEM: Zeiss Crossbeam 550, EBSD detector: Oxford Symmetry) measurements were performed on one screw per material (1.5 pitches of the screws, whereby a pitch is the distance from the crest of one thread to the next crest). The features of the deformed microstructures were studied by analyzing boundary characteristics and misorientation among neighboring measuring points (pixel size or “step size” = 0.4 µm). The kernel average misorientation (KAM), which represents the average misorientation between each pixel and its nearest neighbors, was calculated to study the subgrain structures. These are indicators of the strain locally accumulated at the corresponding area." [154]

3.3.2 Degradation Analysis

The following section has been published in [154].
"Prior to immersion testing or the implantation the screws were imaged using a laboratory µCT (Phoenix Nanotom GE inspection and sensing technologies, Wunstorf, Germany) at an operating voltage of 100 kV at 70 µA current (binned pixel size: ≈ 2.5 µm).

The parameters of all µCT imagings are presented in table 3.3 [154].

TABLE 3.3: µCT imaging parameters [154]

Parameter	Laboratory µCT: Nanotom	SRµCT: IBL P05, DESY	TOPO-TOMO beamline, KARA
Amount of projections	2700	1201	3000
Exposure time	1000 ms	300 ms	14.3 ms
Energy	-	25-30 keV	white beam-peak at 16 keV
Current	70 µA	-	-
Voltage	100 kV	-	-
Voxel size	2.5 µm	2.6 µm	2.4 µm

1. ***In Vitro* imaging**
   After the immersion tests and removal of the degradation layer by chromic acid treatment, the degraded screws from immersion test (ii) have been imaged either at the imaging beamline (IBL) P05, which is operated by the Helmholtz-Center Hereon, at the PETRA III storage ring at DESY (energy: 25-30 keV, binned pixel size: $\approx$ 2.6 µm) or at the TOPO-TOMO beamline of the KARA synchrotron facility at the Karlsruhe institute of technology (KIT) (energy: 16 keV, binned pixel size: $\approx$ 2.4 µm). The degraded screws from test (iii) have been imaged using the laboratory µCT after removal of the degradation layer. Depending on the image quality the segmentation was either performed on the original dataset or after an application of a filter. The chosen image filters, filter parameters, segmentation software and method are presented in table 3.4. After segmentation, all registration and resampling was performed in Avizo version 9.4.2 (Thermo Fisher Scientific, Waltham, MA), resulting in a final data voxel size of 5 µm.

   TABLE 3.4: Segmentation methods and used softwares [154]

Experiment	i, ii, iii	i, ii	iii
Immersion time	0 time point	1-9 days, 7-28 days	28-56 days
Tomography device/ pixel size [µm]	Nanotom / 2.5	DESY, IBL P05 / 2.6, KIT / 2.4	Nanotom / 2.5
Denoising	No filter	Non-local means [158, 159]	Mean 3D
Denoising parameters	-	sigma=15, smoothing factor=1	3x3x3
Segmentation method/ software	Threshold/ Fiji (ImageJ) [157]	Watershed/ Avizo version 9.4.2 (Thermo Fisher Scientific, Waltham, MA)	Threshold/ Fiji (ImageJ)

   Prior to the analysis the z-axis of the 3D data was aligned parallel to the longitudinal axis of the screw, for an example of a transverse view see figure 3.6.

2. ***Ex Vivo* Imaging**
   Imaging of the critically point dried explants was performed at the Helmholtz-Center Hereon operated beamline P05 at the PETRA III storage ring, DESY, at a photon energy of 20 keV in absorption contrast mode with a field of view of 3.8 mm x 2.0 mm. We have determined the spatial resolution *via* an mtf edge scan to 3.7 µm in the original recorded projections at an effective pixel size of 1.25 µm and obtained a voxel size of 2.5 µm at two times binning in the final reconstructed volume. We performed quasi-continuous recordings of tomographic data by acquiring 1800 equally spaced projections over a rotation of 360°. " [154]

3.3.3 Histology

After SRµCT imaging, the explants were used for the histology analysis. It was performed by Dr. Silvia Galli. The detailed description of the performance and the results can be found in [155] (publication also attached in appendix A).

3.4 Image Processing and Analysis

In order to perform quantitative analysis on the acquired µCT images from *in vitro* and *ex vivo* experiments image processing was necessary. The image processing and analysis were extensive parts of this work and are more precisely explained in the current section.

3.4.1 Segmentation, Registration, Resampling

Since the processing of the 3D µCT images can be a highly time consuming and difficult an image processing and segmentation workflow was developed. It is divided into three parts, consisting of segmentation, registration and resampling of i) not corroded screw (screw after degradation in the animal with the degradation layer), ii) corroded screw (the residual screw after the removal of the degradation layer) and iii) mineralized bone.

Image analysis steps, which are going to be described in the following SOP are presented in the process charts (figures 3.3, 3.4 and 3.5). In all three segmentation steps, the data sets, which are marked yellow are being exported, but again imported and reused in a different or same software. All the data sets colored with other colors are being exported and are only partly being reused in the following steps.

The summary and the result of the registration, resampling and segmentation of the pre-implantation screw and the *ex vivo* data is presented in figure 3.2. These subfigures are going to be referenced in the workflows.

In this work the data segmentation with the help of the workflow is adressed as semi-automatic segmentation. Although the semi-automatic segmentation was less time consuming in contrast to the manual segmentation, it is still very slow (2 to 3 days depending on the image quality). Hence, to make the analysis of over 100 datasets possible an automatically segementation approach was found. For the training of the machine learning approach, a certain amount of already segemented data were needed as input. Therefore, the semi-automatically segmented datasets have been used as input data for the machine learning approach for the segmentation of all tomographed data [160, 161].

3.4.1.1 Segmentation Workflows

The segmentation of the acquired data mainly consists of three different segmentations: segmentation of the not corroded screw, segmentation of the corroded screw and the segmentation of the bone. All three steps will be explained in the current section.

Step 1 of 3: Segmentation of "not corroded screw"

In the following the segmentation of the not corroded screw is described, which is visualized in the flowchart in figure 3.3. The step by step instruction can be found in appendix E. First the preimplantation screw is being segmented *via* thresholding and the *ex vivo* data are being converted into 8 bit and filtered in Fiji. Afterwards, the screw from the filtered *ex vivo* data is being roughly segmented manually in Avizo and registered and resampled on the segmented preimplantation screw. To ensure the same orientation of all implants from all datasets a reference screw is used with a certain orientation for the registration and resampling. After the registration and resampling of the screw (not corroded screw) from the *ex vivo* data and the whole *ex vivo* data itself, the borders of the implant from the *ex vivo* data and the preimplantation screw should have nearly the same dimension.

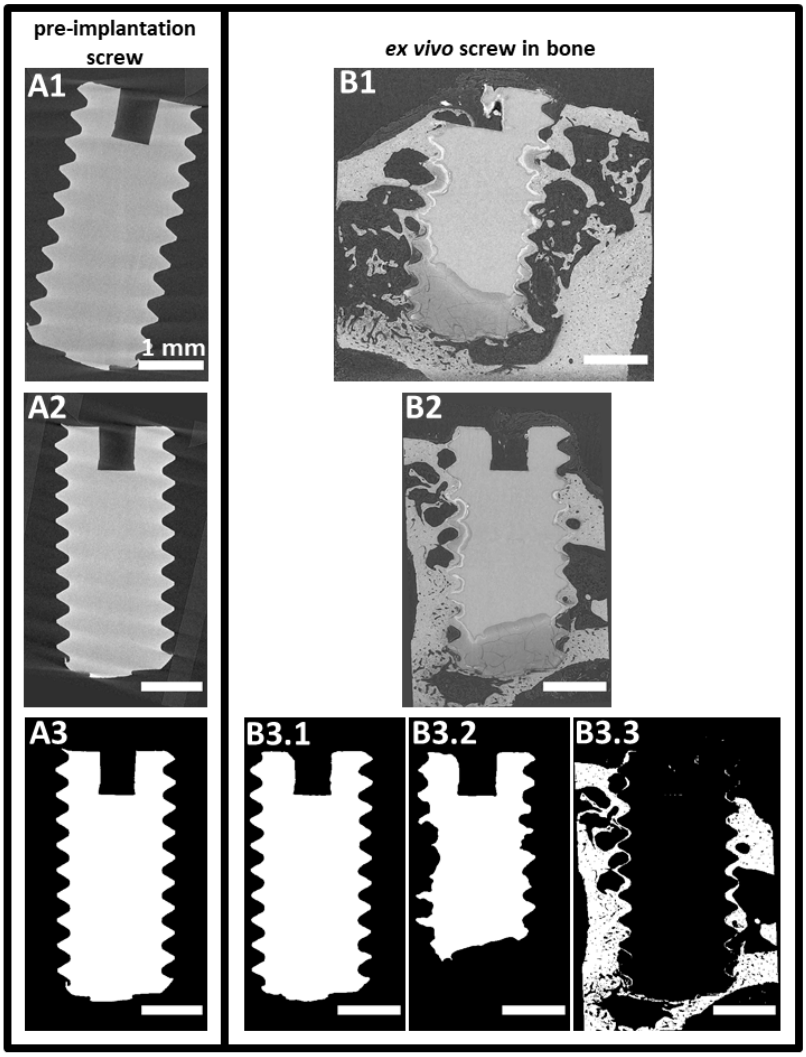

FIGURE 3.2: Short summary of the in workflow presented image registration and segmentation steps. Mg-5Gd pre-implantation screw, which A1) has been tomographed at laboratory µCT device, A2) registered and resampled, A3) segmented *via* threshold. *Ex vivo* data of the same screw after 12 weeks *in vivo* degradation B1) being tomographed at SRµCT beamline P05 (at PETRA III), B2) registered and resampled, B3.1) *via* watershed segmented residual screw with the corrosion layer (=not corroded screw), B3.2) *via* watershed segmented residual screw, B3.3) *via* thresholding segmented bone. Scale bar is the same for all images = 1 mm.

Step 2 of 3: Segmentation of "corroded screw"

The result from the first segmentation step, the not corroded screw, is segmented into the residual screw and the corrosion layer in Avizo by watershed. The flowchart for this segmentation can be found in 3.4. The step by step instruction can be found in E.

Step 3 of 3: Segmentation of "bone"

The last segmentation step is the segmentation of the bone, which is being performed in Fiji *via* thresholding. The flowchart for this segmentation can be found in 3.5. The step by step instruction can be found in E.

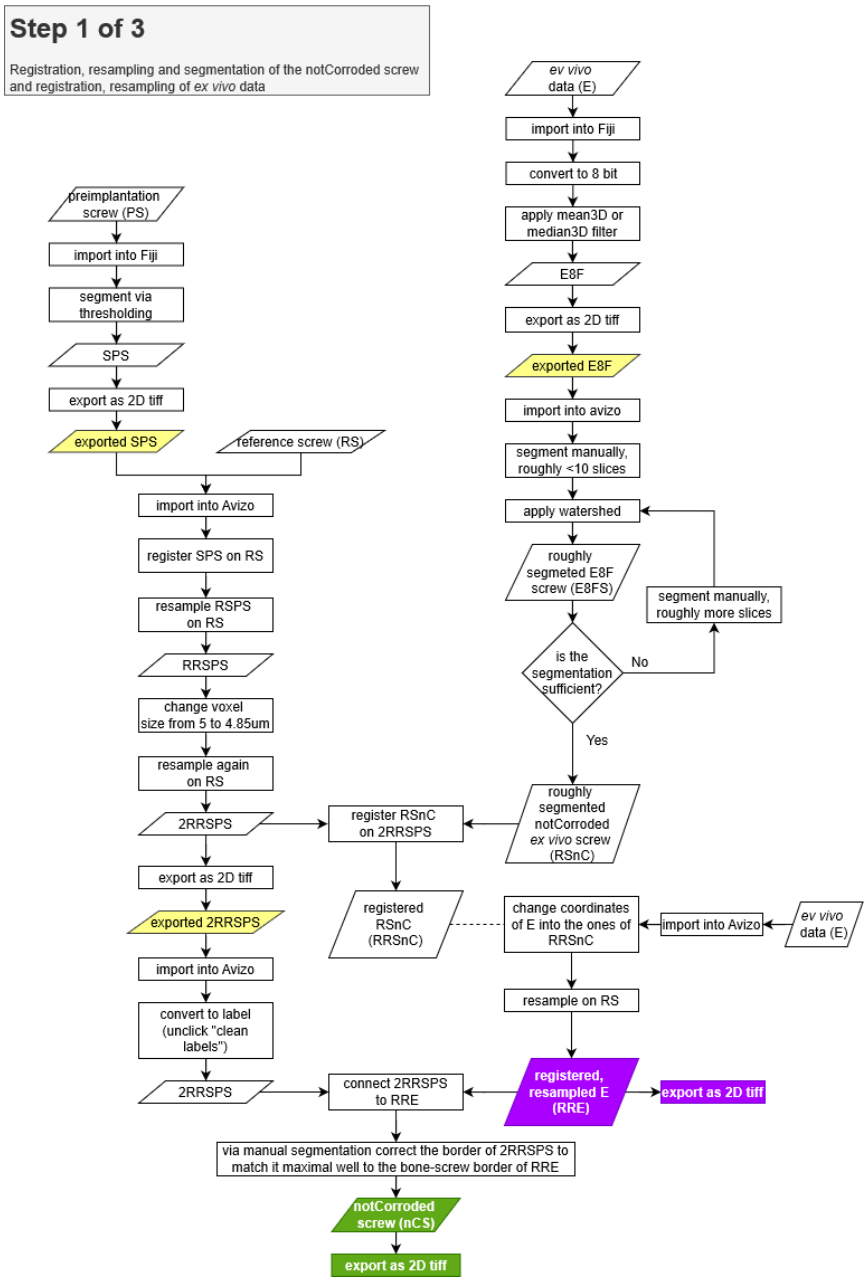

FIGURE 3.3: First step of the image analysis: registration, resampling and segmentation of the pre-implantation screw. Registration and resampling of the *ex vivo* data and segmentation of the not corroded screw (= residual screw + corrosion layer). Yellow colored data are the exported data, which are being again imported and used in the current workflow step. Green and purple colored data are the exported data, which will be imported and used in the second and third workflow steps. Green colored data is also the final result of the segmentation, which is exported and used in the further analysis. Abbreviations: PS = preimplantation screw, SPS = segmented preimplantation screw, RS = reference screw, RSPS = registered segmented preimplantation screw, 2RRSPS = twice resamples registered segmented preimplantation screw, E = *ex vivo* data, E8F = *ex vivo* 8 bit converted and filtered data, E8FS = screw from the *ex vivo* 8 bit converted and filtered data, RSnC = roughly segmented not corroded screw from the *ex vivo* data, RRSnC = registered roughly segmented not corroded screw from the *ex vivo* data, RRE = registered resampled *ex vivo* data, nCS = not corrded screw (which is the residual screw with the corrosion layer). Used softwares are Fiji and Avizo. The voxel size change from 5 to 4.85 µm is due to the voxel size differences of the data tomographed at the laboratory and SRµCT, which is explained in the subsection 4.3.5.

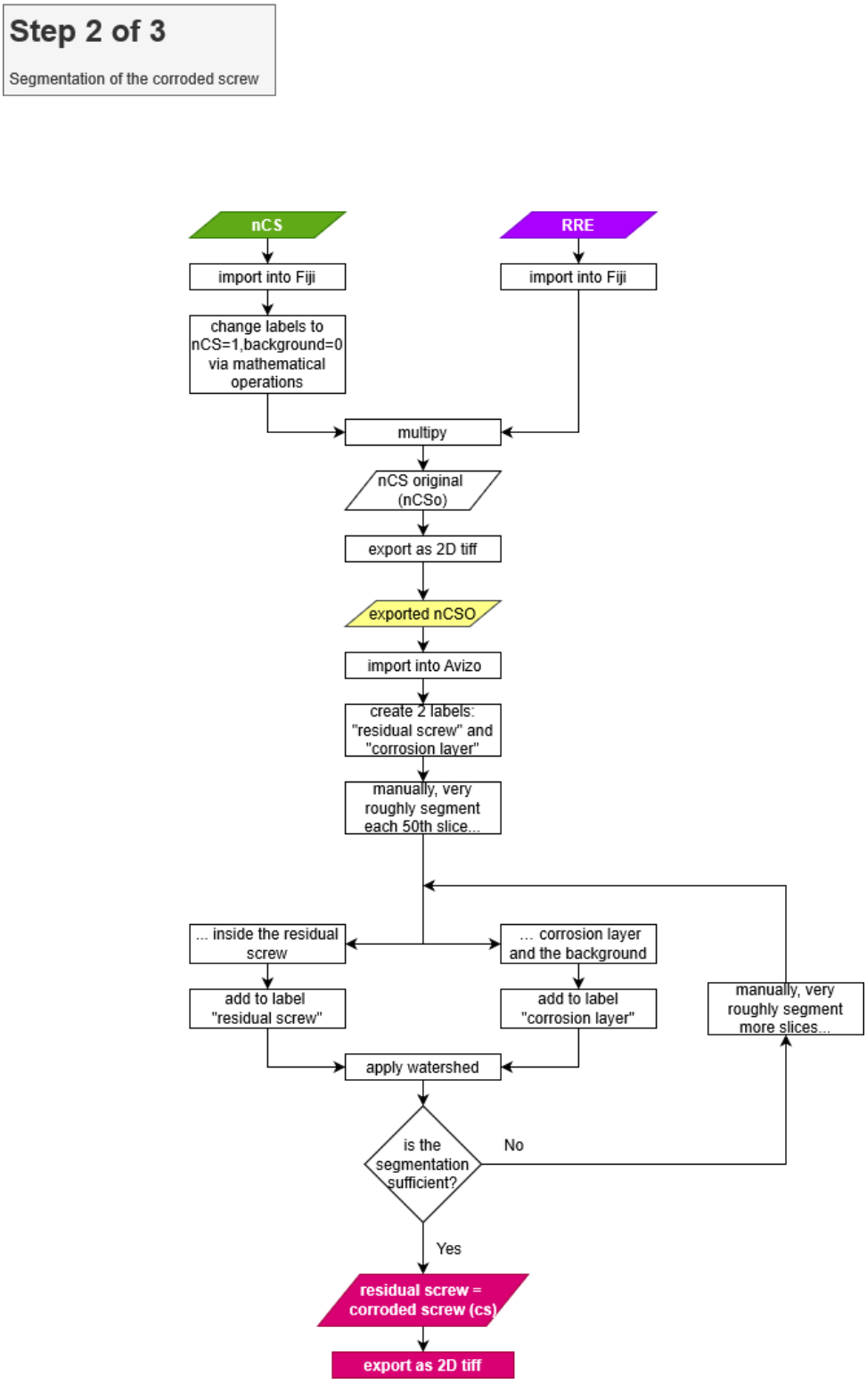

FIGURE 3.4: Second step of the image analysis: segmentation of the *ex vivo* corroded screw (= residual screw). Yellow colored data is the exported data, which is being again imported and used in the current workflow step. Green and purple colored data are the exported data from first workflow step, which are imported into and used in the current workflow step two. Magenta colored data are the final result of the segmentation, which is exported and used in the further analysis. Abbreviations: nCS = not corrded screw (which is the residual screw with the corrosion layer), RRE = registered resampled *ex vivo* data, nCSo = not corroded screw from the original *ex vivo* data, cs = corroded, residual screw without the corrosion layer. Used softwares are Fiji and Avizo.

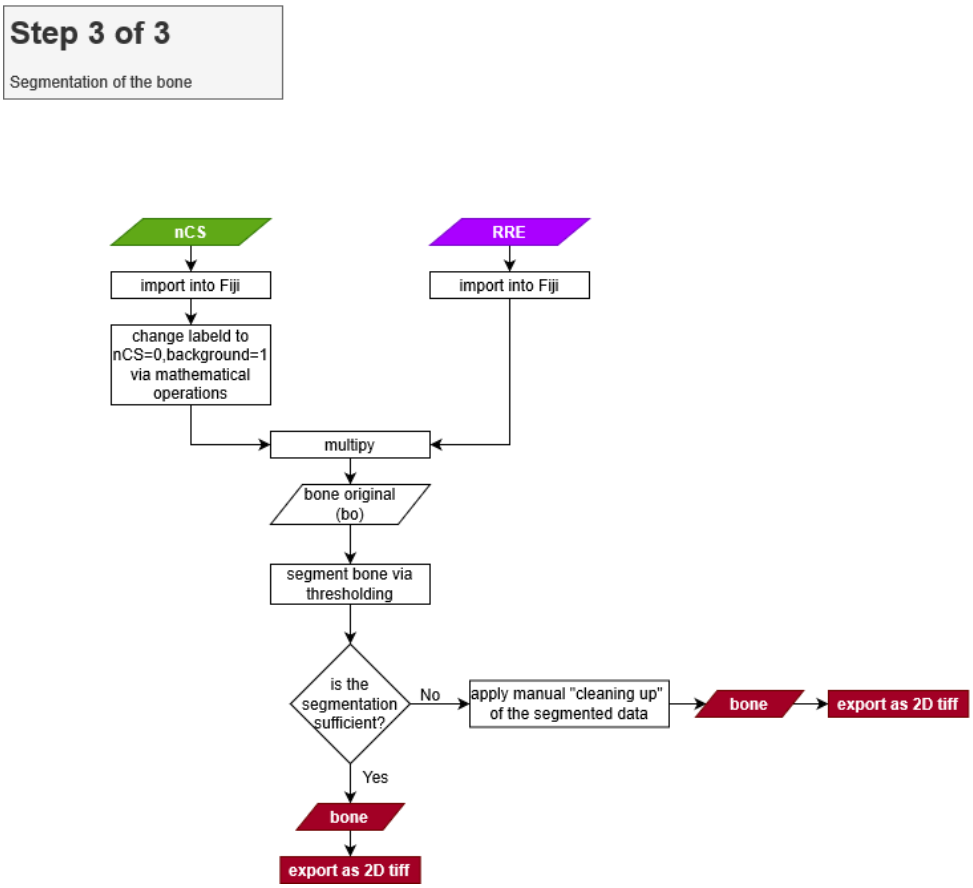

FIGURE 3.5: Third step of the image analysis: segmentation of the *ex vivo* bone. In green and purple colored data are the exported data from first workflow step, which are imported into and used in the current workflow step three. In magenta colored data is the final result of the segmentation, which is exported and used in the further analysis. Abbreviations: nCS = not corrded screw (which is the residual screw with the corrosion layer), RRE = registered resampled *ex vivo* data, bo = bone from the original *ex vivo* data. Used software is Fiji.

3.4.2 Image Analysis

As segmentation result of *ex vivo* data the labels presented in figure 3.6 are obtained. The lable bone is not existing in the *in vitro* data.

The quantitative data analysis is feasible after image segmentation, registration and resampling. The analysed parameters can be categorized in 5 groups:

1. parameters characterising implant's microstructure
2. parameters analysing the implant's degradation rate
3. parameters describing the implant's degradation homogeneity
4. parameters analysing extend of the implant's integrity into the surrounding tissue
5. parameters describing the homogeneity of implant's integration into the surrounding tissue

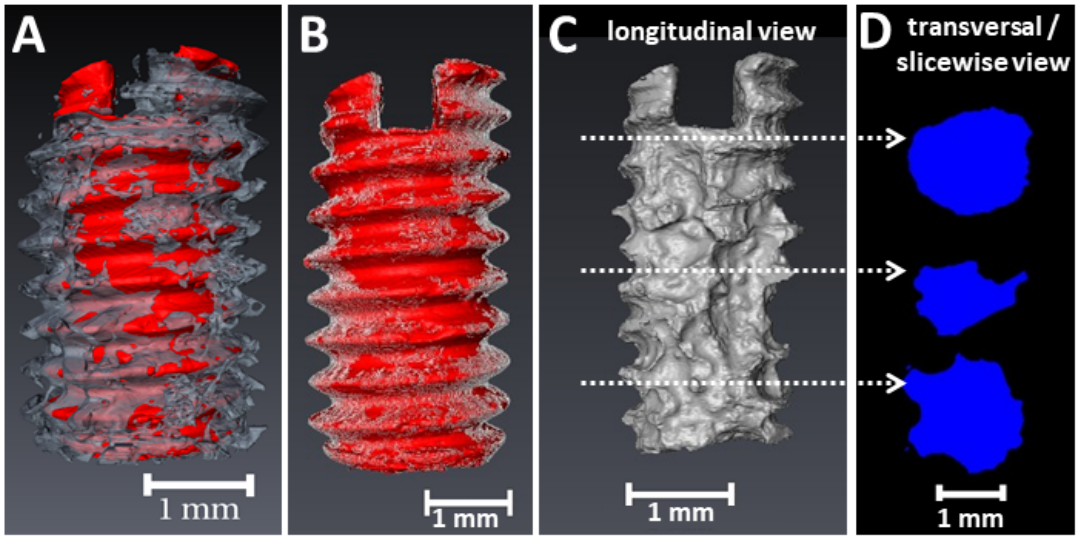

FIGURE 3.6: 3D volume renderings of Mg-10Gd screws after 8 weeks *in vivo* degradation. A) Implant (red) with 200 µm of surrounding bone; B) Visualization of the *BIC* (white) over the total area of the implant (red); C) 3D volume rendering of the longitudinal and 3 exemplary transversal views sections of the residual metallic screw (degradation layer removed) [155].

The selected parameters for analysis are presented in table 3.5. The 3D character of the data makes it possible to analyse parameters both in 3D and in 2D. Thereby, a statistical analysis of even one sample is achievable. Also, a comparison between the same parameter analysed in 3D and in 2D is enabled. *DR* and *MDD* were only calculated in 3D, *difference layer* (layer between the preimplantation and corroded screw) only in 2D and *PF* in 3D and in 2D. Same formulae of the 3D calculations were used in 2D calculations on each slice, resulting in statistical mean and standard deviation values for one sample.

TABLE 3.5: Analysis dimensions of parameters [155]

	Parameter	Dimension	
	Experiment	*in vitro*	*ex vivo*
1	Global Degradation Rate (*GDR*)	3D	3D
2	Degradation Rate (*DR*)	3D	3D
3	Mean Degradation Depth (*MDD*)	3D	3D
4	*Volume loss*	2D	2D
5	Pitting Factor (*PF*)	3D and 2D	3D and 2D
6	Crest/Root ratio	2D	-
7	Bone to Implant Contact (*BIC*)	-	3D and 2D
8	Bone volume fraction (*BV/TV*)	-	3D and 2D

3.4.2.1 Gd-rich Particles

The following section has been published in [154]. The high image quality of SRµCT data made it possible to detect the amount, size and the distribution of the Gd-rich particles in the Mg-xGd implants. "To segment the Gd-rich particles of 3D tomographic images automatic thresholding in Fiji followed by a removal of 1 pixel large

particles (Avizo version 9.4.2 (Thermo Fisher Scientific, Waltham, MA)) was performed. On the segmented 3D tomographic data, a 3D distance transform was applied in Fiji [162]. As a result each pixel of the image was labeled with the distance to the nearest obstacle pixel. After fitting a Poisson distribution to the histogram of the transformed images, the minimum distance between two Gd-rich particles was determined. On 3D tomographic segmented images the Feret diameter of the particles was calculated in order to investigate the size of the particles in Fiji."

3.4.2.2 Degradation Rate (*DR*), Global Degradation Rate (*GDR*), Mean Degradation Depth (*MDD*)

In this work the degradation velocity is described *via* three parameters: degradation rate (*DR*), global degradation rate (*GDR*) and mean degradation depth (*MDD*). The calculation of each of them is described in detail below.

1. **Degradation Rate (*DR*)** The following section has been published in [154].
   "The *DR* at certain immersion time periods was calculated once through (1) weight loss (WL) measurements *via* weighing the screws before immersion and after removal of the degradation layer with chromic acid and through (2) volume loss (VL) measurements, based on µCT measurements *via* calculation of the screw volume before immersion and after removal of the degradation layer. It has to be mentioned, that the WL experiments were performed only for the *in vitro* experiments. For WL and VL measurements, the degradation rate was calculated using equation 3.1 [163]:

$$DR[mm/a] = \frac{\Delta m}{A \cdot \rho \cdot t} = \frac{\Delta V}{A \cdot t} \tag{3.1}$$

   where Δm denotes the sample weight loss, ΔV the sample volume loss, A the initial surface area, ρ the material density ($\rho_{(Mg-5Gd)}$ = 1.81 g/cm^3 , $\rho_{(Mg-10Gd)}$ = 1.87 g/cm^3), and t the immersion time. For the weight loss measurements a high precision balance (MYA 2.4Y Microbalance, Radwag Balances and Scales, Radom, Poland) was used. The volume from the µCT investigations were calculated with softwares ImageJ (Fiji) [164] and Avizo version 9.4.2 (Thermo Fisher Scientific, Waltham, MA). For the WL calculations the surface area of the screws was assumed to be the same for all screws theoretically calculated (A = 0.4125 cm^2), for the VL measurements the surface area of each screw was calculated with Avizo."

2. **Mean Degradation Depth (*MDD*)** The following section has been published in [154].
   "In order to be able to directly calculate how much is the shrinkage of the implant after certain degradation time the parameters *MDD* is used very often. The *MDD* for each immersion time was calculated based on equation 3.1 [163]:"

$$MDD[\mu m] = DR \cdot t \tag{3.2}$$

3. **Global Degradation Rate (*GDR*)** The following section has been published in [154].
   "By fitting a straight line to the *MDD* values, the slope of the fitted line was calculated and defined as the global degradation rate (*GDR* [mm/a]). The coefficient of determination (R^2), which is a measure of the proportion of variance

of a predicted outcome [165], was determined for the fitted *GDR*s. It reveals how well a linear regression model fits the experimental results, whereby the value 1 would correspond to a perfect fit of the data to the regression line."

3.4.2.3 Degradation Homogeneity: Pitting Factor (*PF*), *Difference/Volume Loss Layer*, Crest to Root Ratio

The homogeneity of the implant degradation is described in 3D (*via* 3D pitting factor) and in 2D (*via* 2D pitting factor, *difference/volume loss layer* and the *crest/root ratio*). In the following section their calculation is reported.

1. **Pitting Factor (*PF*)** The following section has been published in [154].
   "*PF* (in 3D and 2D), *difference layer* in 2D and *crest/roots ratio* were selected as analysis parameters describing the degradation homogeneity. These are described in more detail in following and were performed on samples degraded between 7-56 days (experiment(ii) and (iii)).

   The calculation of *2D-PF* mean and standard deviation for each sample was performed *via* equations 3.3 and 3.4 respectively, where N is the amount of analyzed slices.

$$2Dmean PF[a.u.] = \overline{PF} = \frac{1}{N}\sum_{i=1}^{N} PF_i \tag{3.3}$$

$$2DstdPF = \sqrt{\frac{1}{N-1}\sum_{i=1}^{N}(PF_i - \overline{PF})^2} \tag{3.4}$$

   where PF_i is the *PF* calculated as in equation 3.5 for each slice i of the chosen volume of interest (VOI) [166]:

$$PF_i[a.u.] = \frac{DP_i}{MDD_i} \tag{3.5}$$

   In equation 3.5 DP_i is the deepest pit and MDD_i is the mean degradation depth of each slice, see figure 3.7C. Note that this calculation is only possible for the slices where the degradation layer did not reach the center of the screw.

   For the calculation of the *3D-PF* in the equation 3.5 the DP [µm] is the deepest pit of the whole 3D implant chosen among all slices of the VOI and *MDD* is the one from the whole 3D implant calculated from the tomographic data with equation 3.2."

2. ***Difference/Volume Loss Layer (Diff. Layer)***
   The following section has been published in [154].
   "The volume difference between before and after immersion of each slice along the longitudinal axis of the screw in voxels was calculated (3.6). Here, *ncs* = not corroded screw, *rs* = residual screw (3.7)."

$$2Ddiff.layer_i = (voxels_{ncs} - voxels_{rs}) \cdot voxelsize^3 \tag{3.6}$$

3. **Crest/Root Ratio**
   The following section has been published in [154].

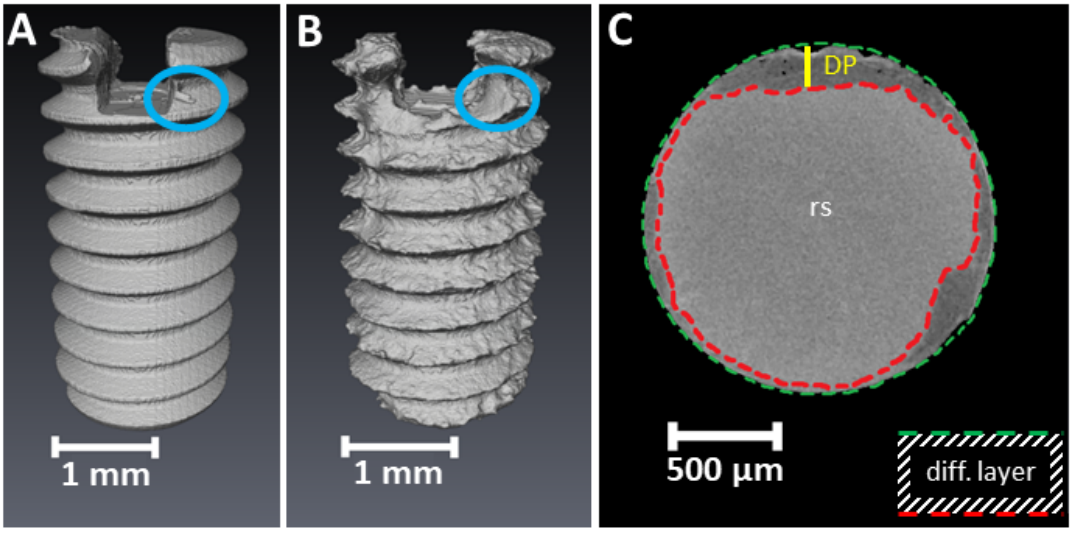

FIGURE 3.7: Exemplary visualization of not corroded and corroded Mg screws A) Mg-5Gd screw before immersion/degradation (ncs = not corroded screw): 3D volume rendering after segmentation, B) Mg-5Gd screw after 56 days *in vitro* degradation. Screw after degradation and removal of degradation layer (rs=residual screw): 3D volume rendering after segmentation, C) Screw after degradation and before removal of degradation layer: A representative slice from the middle of screw before degradation layer removal. Green line – border between the preimplantation screw and the background; red line – separates the degradation layer from the residual, not degraded material, the layer between the green and red lines – difference layer; yellow line – deepest pit (DP) of this slice [154]

"In order to analyze the height variations of the degradation layer depending on its location the 3D image of the difference layer was mapped to a 2D height profile. For the latter a Fiji script was implemented (appendix F). Here the height of surface was encoded as a grey value whereas the positions on the screw surface are given by x and y. Figure 3 shows a 2D height profile of a not corroded Mg-5Gd screw (3.8A) and difference layer (3.8B) of the same screw after 56 days *in vitro* degradation. After transformation of the 3D images of the difference layer into 2D images, the ratio of difference layer at the crest areas divided by the amount of difference layer at the roots areas (equation 3.7) was calculated.

$$\frac{Crest}{Root} = \frac{G_{A_{crests}}}{G_{A_{roots}}} = \frac{\sum_{i=1}^{N} G_{A_{crests_i}}}{\sum_{i=1}^{N} G_{A_{crests_i}}} \tag{3.7}$$

where $G_{A_{crest_i}}$ and $G_{A_{root_i}}$ represent the sum of the grey values in one crest and root area, respectively (figure 3.8B). The grey values represent the thickness of the difference layer. The determination of crests and roots was performed semi-automatically; the first crest area was determined manually (dimensions of A: a = 43 µm, b = 365 µm, α = 77°) and all following all crests and roots were defined automatically."

3.4.2.4 Implant Integration into the Surrounding Tissue: Bone to Implant Contact (*BIC(t)*), Bone Volume Fraction and Bone Area (*BV/TV(t)*)

The extend and homogeneity of the implant's integration into the surrounding tissue is quantified *via* calculation of the amount and distribution of the bone to implant

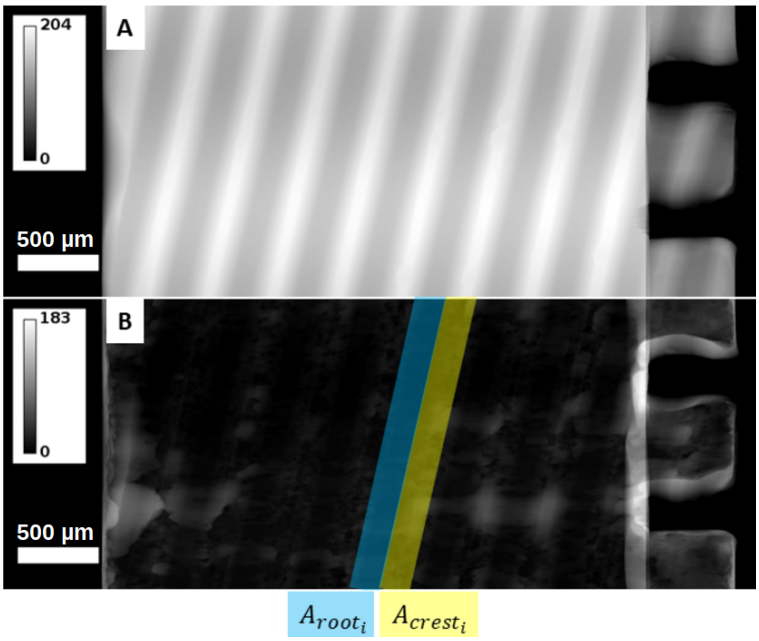

FIGURE 3.8: 2D image of Mg-5Gd screw imaged using µCT A) before degradation (not corroded screw), B) difference layer as defined in 3.6, after 56 days *in vitro* degradation; the colorbar in the images shows the image depth in pixel [154]

contact area and the amount of the bone, which surrounds the implant.

1. **Bone to Implant Contact of Tomographic Data *BIC(t)***
   The following section has been published in [155].
   "In order to characterize how well the implant is integrated into the bone, the *BIC(t)*, which is the contact of the not corroded screw with the surrounding bone, was calculated according to equation 3.8 (see figure 3.6B for visualization).

$$3D - BIC[\%] = \frac{\#surface\ voxels\ of\ implant\ in\ contact\ with\ bone}{\#total\ surface\ voxels\ of\ ncs} \tag{3.8}$$

   To determine the contact voxels, the not corroded screw was dilated once (Fiji) and added to the label bone. The overlapping voxels were defined as in contact. "

2. **Bone Volume Fraction of Tomographic Data *(BV/TV(t))***
   The following section has been published in [155].
   "In order to evaluate differences in the amount of bone formed around the implants and to observe if there is a difference of it depending on the distance from the screw, the *BV/TV* was calculated in three different regions of interest (ROIs) around the screws [167]. The thread depth of those M2 screws is 250 µm, hence the analysed ROIs consisted of volumes of 100 µm (very close to the screw surface), 200 µm (a little smaller than thread depth) and 300 µm (a little larger than the thread depth) enlargements from the implant surfaces (figure 3.6A). To define the three subvolumes, first the pre-implantation screw was dilated 20 times, 40 times and 60 times, respectively then added to the label bone and the not dilated pre-implantation screw was subtracted. The overlapping region of the dilated bone and the original bone was defined as

BV = bone volume. Equation 3.9 was used for the *BV/TV* calculation in each area, with TV = total volume of the ROI.

$$3D - \frac{BV}{TV}[\%] = \frac{\#voxels\ of\ bone\ volume}{\#voxels\ of\ total\ volume\ of\ the\ VOI} \tag{3.9}$$

The quality of SRµCT data gives sufficient contrast between non-mineralized and mineralized bone, which enables the additional quantification of the non-mineralized bone. In figure 3.9B it is possible to detect the newly formed, non-mineralized bone, which exhibits the same structure as the mineralized one, but less contrast to the background due to lower X-ray absorption [168]. Due to the low contrast between the background and the non-mineralized bone the segmentation couldn't be performed automatically. Since the semi-automatically segmentation (*via* the region growing algorithm in Avizo) of this non-mineralized bone was very time consuming, it was performed exemplary only on three Mg-10Gd samples after 12 weeks degradation .

The broken degradation layer on the threads of the implant is well visible in figure 4.8B. Some pieces of the figure degradation layer, which have fallen apart, have been fully integrated into the bone and are visible in 3.9B. These parts of the degradation layer do not count in the label degradation layer and might falsify the results. To have an insight on the amount of the broken degradation layers, integrated or not into the bone, three Mg-10Gd implants after 12 weeks were segmented semi-automatically *via* the region growing algorithm in Avizo version 9.4.2)."

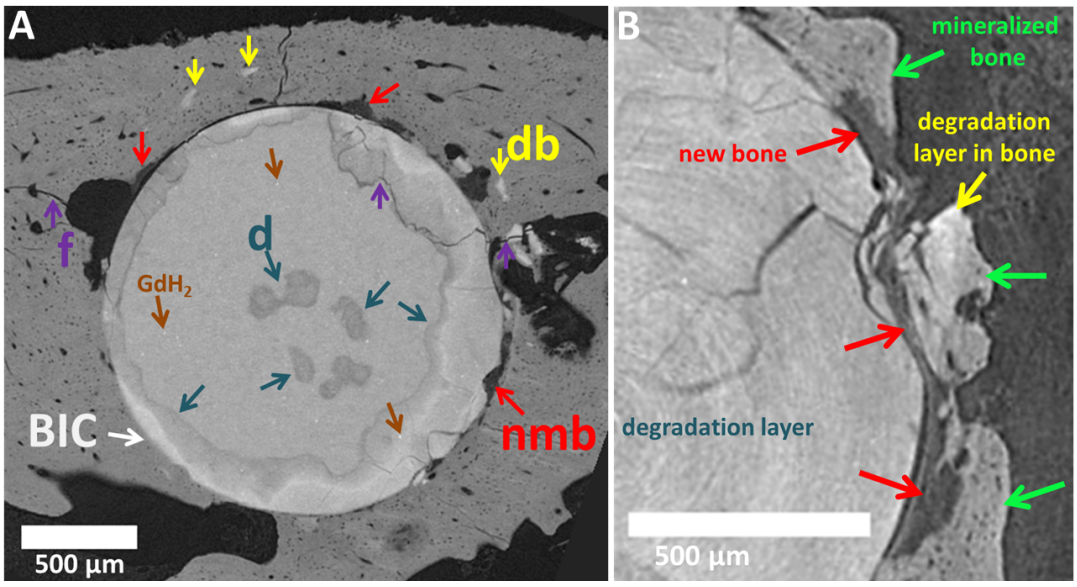

FIGURE 3.9: A and B) Two different Mg-10Gd implants after 12 weeks *in vivo* degradation; f=fracture, db=degradation layer in bone, nmb=non-mineralized bone (newly formed bone), d=degradation layer. [155]

3.4.2.5 Comparison of *In Vitro* with *Ex Vivo* Results

The following section has been published in [155]. "Comparison of results from *ex vivo* and *in vitro* have been performed. The *ex vivo(p)/in vitro(p)* ratio (where the p

stands for the compared parameter) calculation was performed for the results at 4 and 8 weeks degradation time periods, as both experiment types were performed for these time periods. Each for *ex vivo(p)* and *in vitro(p)* the mean value of the calculation is taken, since there were different amounts of samples in both experiments."

3.4.2.6 Correlations and Statistical Analysis

The following section has been published in [155]. "To measure the variation of the *PF* and *diff. layer* over the whole sample along its longitudinal axis the coefficient of variation (CV) of the *PF* for each sample was calculated *via* division of the *2D-mean PF* (equation 3.3) by the *2D-std PF* (equation 3.4) and *2D-mean diff. layer* by the *2D-std diff. layer* of each sample respectively [169].

The means, medians and standard deviations of all analyzed parameters were calculated for each group. To measure the variation of the *PF*, *volume loss* and *BIC* over the whole sample along its longitudinal axis the CV [169] of the pitting factor for each sample was calculated *via* division of the *2D mean PF* by the *2D std PF*, *2D mean volume loss* by the *2D std volume loss* and *2D mean BIC* by the *2D std BIC* of each sample respectively. The *CV PF*, *CV volume loss* and *CV BIC* are considered as investigated parameters indicating the degradation homogeneity. Pearson's R correlation (linear correlation) was used to calculate the dependency between the parameters investigated, assuming normal distribution of the data (in MATLAB R2019b). *BIC* calculations obtained with histology and SRµCT were compared using a pair Person correlation (a pair being the results of the calculation with the two methods on the same sample).

The mean values of all the 2D and 3D parameters for each group (material per each time point) were compared using 2-way analysis of variance ANOVA multiple comparison test in MATLAB R2019b (The MathWorks Inc., USA). Multiple testing correction was performed using the Bonferroni adjustment method [170]. A p-value below 0.05 was considered statistically significant."

3.4.3 Various Influence Factors on Analysis Results

During the image processing several factors were identified, which had an influence on the final analysis result. Hence, the most relevant were investigated.

1. Person-Dependent Segmentation Differences
   In the following, to investigate how big the segmentation differences could be if segmented by different persons, three slices have been segmented once by M.Sc. student Paria Werner, once by Diana Krüger.

2. Manual vs. Workflow Segmentation
   To determine how strongly the segmentation influences the analysis parameters, the analysis was applied on the same data set, once segmented semi-automatically (using the described workflow, section 3.4.1.1) and once by segmenting manually. Although it is difficult even by eye to determine some image areas, it is assumed, that the manual segmentation is the more precise segmentation. After the segmentation has been finished, those data sets have been analyzed regarding following parameters: *DR MDD, 3D-BIC, 2D-BIC, CV BIC, 3D-BV/TV, 2D-BV/TV, CV BV/TV, 3D-PF, 2D-PF, CV PF*.

3. Variation of Dimensions when Tomographed *via* Different µCT Devices
   The pre-implantation screws were tomographed at laboratory µCT and the *ex*

vivo data were tomographed with the SRµCT at the P05 beamline. Due to the use of different µCT devices during the registration process a dimensional dissimilarity of the same screw tomographed before and after implantation was discovered. Hence, a metal ball (with real physical diameter of Xmm) was tomographed in both devices to determine the difference in the sample's dimensions occurring due to the different image acquisition devices. The metal ball tomography settings on the Nanotom were taken the same as for the tomography of the preimplantation screws: voltage = 100 kV, current = 70 µA, voxel size $\approx$ 2.7 µm. The metal ball tomography settings of the P05 beamline were chosen the same as for the tomography of the *ev vivo* samples: energy = 30keV, binned voxel size $\approx$ 1.3 µm.

4. Influence of Object's Geometry on the Results
Two objects were created in order to see how big the influence of the implants geometry on the analyzed parameters is: a cylinder and a cuboid with the following dimensions: h = 4 mm, a = b = 2 mm. Both objects were shrunk by 250 µm for an homogeneous degradation. Parameters like *MDD*, mean corrosion layer (*MCL*) and *3D-PF* were analyzed. The *MDD* was calculated *via volume loss* and the *MCL* was calculated slicewise, by averaging the degradation layer depth over all slices of the object. The measurement happens *via* a self-implemented Fiji-script through all slices along the length of the object. Hence, the *MCL* is the more accurate measurement as the usually calculated *MDD*.

5. Influence of Various Image Processing Steps on the Analysis Result
To obtain more correct segmentation, several image processing steps, like smoothing, shrinkage or growing were applied to the segmented data. The influence of the data smoothing, growing shrinking with different parameters on the analysis parameters *DR*, *3D-PF*, *3D-BIC* and *3D-BV/TV* was investigated in Avizo. All applied processing variations are presented in table 3.6. Therefore three samples were explored: Mg-5Gd and PEEK explants after 12 weeks *ex vivo* degradation and Mg-10Gd screw after 8 weeks *in vitro* degradation. The analysis was not applied on a Ti implant due to the time consuming processing and the assumption, that the influence of the processes could be the same as in case of the non degradable PEEK implant. Figure 3.10 presents an exemplary schematics of the image processing Nr. 7 from table 3.6. On the segmented not corroded screw two operations were applied:

   (a) The screw was grown in 3D with the pixel size of 1.
   (b) Afterwards the screw was smoothened in 3D with the pixel size of 3.

   The different procedures were applied on the not vorroded screw and on the bone as presented in table 3.6. Overall 22 different procedure combinations were applied. Afterwards the processed labels were analyzed and the magnitude of the processing influence on the analysis parameters was calculated.

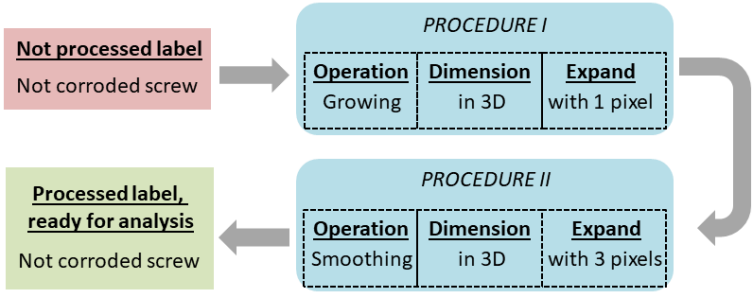

FIGURE 3.10: Exemplary schematics of image processing before image analysis: corresponds to processing Nr. 7 from table 3.6. Input data is the not corroded screw. On this data two procedurs are being applied: growing and smoothing. The outcome is the processed not corroded screw, which will be used in the further analysis.

TABLE 3.6: Operations smoothing, growing or shrinking on the already segmented labels before the image analysis. The operations were applied either on label "not corroded screw" or on "bone". *Pixel size of the applied procedure

Nr.	Label	Operation I	Dimension I	Expand* I	Operation II	Dimension II	Expand* II
1	not corroded screw	smoothing	3D	3	-	-	-
2	not corroded screw	smoothing	3D	3	smoothing	3D	5
3	not corroded screw	smoothing	3D	5	-	-	-
4	not corroded screw	smoothing	2D longitudinal	5	-	-	-
5	not corroded screw	smoothing	2D transversal	5	-	-	-
6	not corroded screw	growing	3D	once	-	-	-
7	not corroded screw	growing	3D	once	smoothing	3D	3
8	not corroded screw	growing	3D	twice	-	-	-
9	not corroded screw	growing	3D	twice	smoothing	3D	3
10	not corroded screw	growing	2D longitudinal	once	-	-	-
11	not corroded screw	growing	2D longitudinal	once	smoothing	3D	5
12	not corroded screw	growing	2D longitudinal	twice	-	-	-
13	not corroded screw	growing	2D longitudinal	twice	smoothing	3D	5
14	bone	growing	2D longitudinal	once	-	-	-
15	bone	growing	2D longitudinal	twice	-	-	-
16	bone	growing	3D	once	-	-	-
17	bone	growing	3D	twice	-	-	-
18	bone	shrinkage	2D longitudinal	once	growing	2D longitudinal	once
19	bone	shrinkage	2D longitudinal	once	-	-	-
20	bone	shrinkage	2D longitudinal	twice	-	-	-
21	bone	shrinkage	3D	once	-	-	-
22	bone	shrinkage	3D	twice	-	-	-

3.5 Push-Out Experiments

In order to gain insight on the quality of the implant integration into the surrounding tissue *in situ* push-out experiments were designed on fresh explants of all four materials. To make sure the samples are right positioned in the experimental setup sample holders for each sample had to be prepared. The preparation of the sample holder is presented in the following subsection. The explants with the sample holders were placed into the custom-made load frame, which is presented in [160]. To ensure that the explants did not dry out, they were covered with parafilm. First, the explants were tomographed without force, afterwards a sequence of increasing the applied force and performing a tomographic scan was executed. Simultaneously, reconstructions of the tomography images were performed to detect the occurrence of cracks in the bone, corrosion layer and/or interface of bone and corrosion layer. The increase of the applied force was taking place until either a detachement of the

implant from the surrounding bone, or a bone/screw failure occured. Some preliminary results from the push-out experiments are presented in [160].

The overall number of the samples studied with push-out testing is shown in table 3.7.

TABLE 3.7: Number of samples planed for *in situ* push-out experiments per implant material time point and material

	4 weeks	8 weeks	12 weeks
Mg-5Gd	6	5	8
Mg-10Gd	8	6	7
PEEK	6	6	6
Ti	6	6	6

3.5.1 Modification of Sample Holders for Push-Out Experiments

For each *ex vivo* sample a holder was developed and 3D printed, leading to an alignment of the screw longitudinal axis parallel to the load axis. The sample holders have been initially designed by Dr. Berit Zeller-Plumhoff. Further modifications of the holder design have been applied by myself. The detailed modified SOP can be found in the end of this subsection.

Prior to the holder preparation the fresh, frozen explants were being tomographed roughly with voltage of 120 kV, current 47 µA, just 400-900 images and a voxel size of ca. 6-7.5 µm (maximum 10 minutes tomography for each explant was reached by limiting the exposure time) at the laboratory nanotom. During this rough tomography process the explants were kept frozen by keeping the explants in an environment filled with dry ice.

Figure 3.11 represents the two iterations of the sample holder. In the first version the *ex vivo* sample was being placed into the holder in a way, that the implant was being pushed on its slit (figure 3.11A). Since on the other side of the implant it was mostly completely covered by bone, by pushing on the implant in this direction, the screw was not being pushed-out of the bone but into the bone. To correct this, the sample holder was modified in a way, that the screw is being pushed on the opposite end (not the slit end) (figure 3.11B).

The modified sample holder consists of two parts: top and the bottom (figure 3.11C) and the precise attachment of these both is ensured *via* designation on both parts (visible in figure 3.11B). After preparation of the 3D data they were 3D printed (Polyjet or Stereolithography with materials Watershed XC 11122 and MJP 3600 Max (Visijet Crystal)). To make the explant to match perfectly into the sample holder the small gaps between the sample holder and the explant were designed to be filled with modelling resin for highend casting (easyformLC from DTAX, Ettlingen, Germany) and hardened *via* UV-curing lamp (Dental 1500MW Curing Light Zahnarzt Polymerisations lampe 5W whitening lamp - Black) through designed empty cylinders in the bottom half of the holder (figure 3.11D). In the modified version, to be able to push on the screw, first the bone covering the screw from the top had to be removed. This was performed with a dental drill.

The step-by-step instruction for the sample holder preparation can be found in appendix G.

The first step is to make a very fast µCT image of the fresh sample and segment the screw and the surrounding bone in Fiji. The segmented screw from the *ex vivo*

data and the *ex vivo* data are being registered and resampled on the reference screw. The reference screw itself is already centered into the middle of the sample holder's top and bottom part. Hence the result of the registration and resampling is the right orientation of the *ex vivo* data in the sample holder. *Via* a customized sample holders are prepared for each individual *ex vivo* sample.

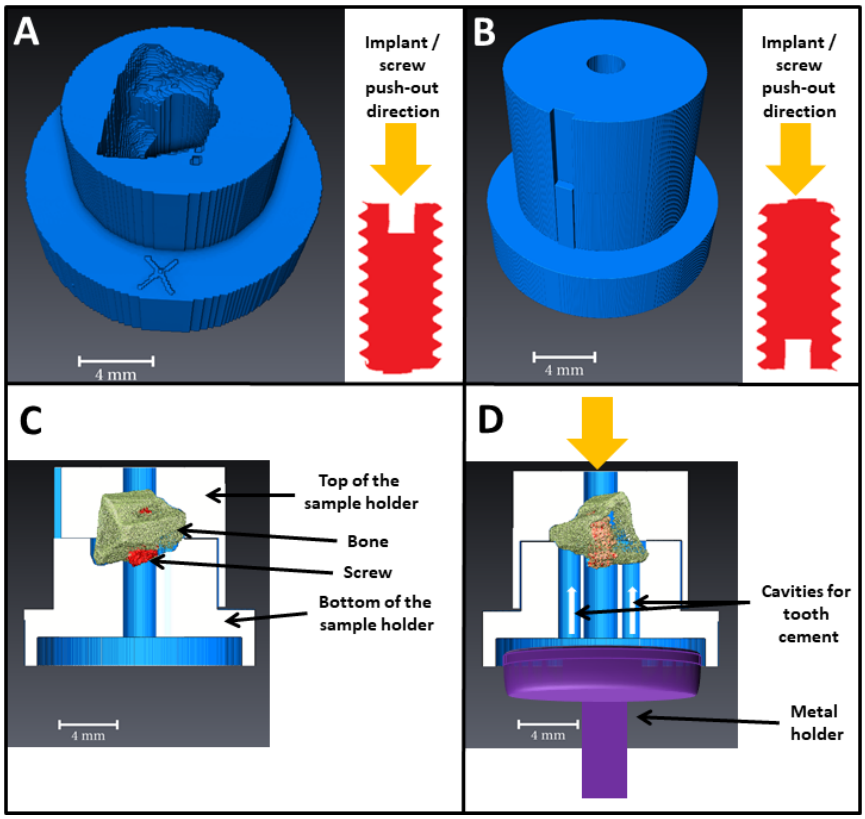

FIGURE 3.11: A) 3D volume rendering of the "old" sample holder; B) 3D volume rendering of the modified, "new" sample holder consisting of the bottom and the top part; C) XZ-ortho slice of the modified sample holder with the 3D volume rendering of the *ex vivo* bone and the implant; D) YZ-ortho slice of the modified sample holder with the 3D volume rendering of the *ex vivo* bone and the implant, additionally marked the push out pin direction(orange arrow), tooth cement filling empty cylinders and the bottom sample holder-holder pin(purple)

Chapter 4

Results

4.1 *In Vitro* Experiments

All the results analysis described in the following sections have been published in large parts in [154] and [155], hence some sections here are copied or paraphrased from the publications. Values to all diagrams and significance analysis can be found in the appendix B.

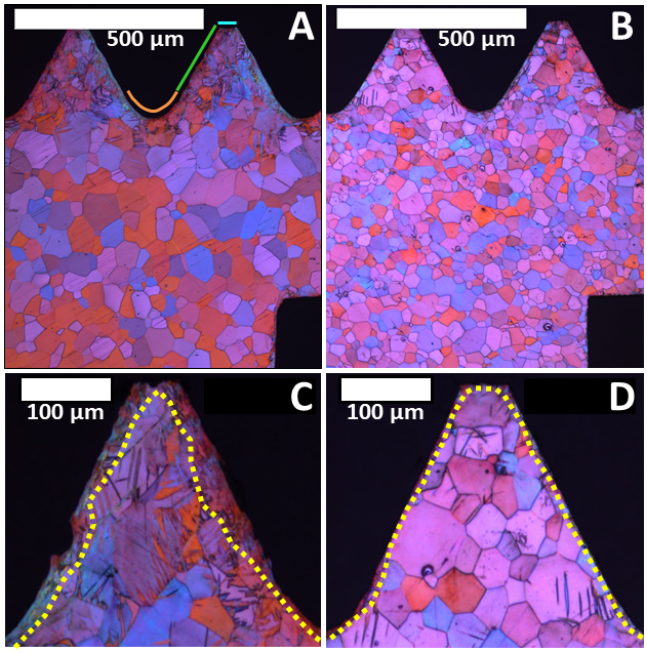

FIGURE 4.1: Polarized optical micrographs of Mg-5Gd (A, C) and Mg-10Gd (D, B) screws, respectively. Markers in A): orange - area of root, green - area of flank, blue - area of crest, C) and D) yellow line separates the deformed layer from not deformed one [154]

4.1.1 Macro- and Microstructural Analysis

The following section has been published in [154]. "The microstructure of Mg-5Gd and Mg-10Gd screws, obtained from polarized optical micrographs, are shown in figure 4.1. Mg-5Gd displays overall larger grain sizes (51.78 ± 10.91 µm) and less homogeneous grain size distribution, whilst the average grain size of Mg-10Gd is significantly smaller (26.67 ± 1.30 µm) and more homogeneously distributed.

The deformation layer is defined as the near-surface region of the screw, where the machining process has influenced the microstructure and where no clear grain boundaries can be identified (see figure 4.1C,D). Three threads (six flanks, three

crests and three roots – exemplarily marked in figure 4.1A) of one screw of each alloy were analyzed towards the deformation layer thickness. As displayed in table 4.1, there is no noticeable difference between the deformation layer thicknesses in the roots of both alloys. By contrast, Mg-5Gd reveals a deformation layer nearly 2.5 times as deep as Mg-10Gd on the crests and flanks of the threads.

Optical microscopy images reveal a large number of twins in the near-surface region of the threads in Mg-5Gd screws in comparison to Mg-10Gd screws.

TABLE 4.1: Deformation layers thicknesses of processed Mg-xGd alloys in different areas of the screw [154]

Deformation layer thickness [µm]	Mg-5Gd	Mg-10Gd
Roots	10.7±3.1	9.2±3.5
Crests	19.3±6.6	7.8±3.8
Sides	12±4.9	4.9±2

The corresponding EBSD image quality maps of each crest and root of Mg-5Gd and Mg-10Gd screws are presented in figure 4.2. EBSD maps show similar microstructural features to an optical micrograph, with grain and twin boundaries. Figure 4.2 also shows the quantification of these boundaries and the corresponding pole figures. The twin boundaries are marked with different colors corresponding to the misorientation relationships according to the twinning types, e.g. tensile, compression and secondary twins. It is obvious from the discrete pole figures, shown in figure 4.2D and E, that Mg-5Gd has a stronger texture than Mg-10Gd, with the basal poles perpendicular to the extrusion direction (ED). Mg-10Gd shows a more homogeneous distribution of the crystal orientations, which is clearly visible in the pole figure.

Tensile twinning is identified as the dominant mode in both alloys. The amount of the secondary twin boundaries is much smaller with 3.8% for Mg-5Gd and 5.9% for Mg-10Gd. For both alloys the smallest amount of boundaries are the compression twin boundaries, i.e. 1.5% for Mg-10Gd and 0.8% for Mg-10Gd. KAM are analyzed in three different areas, i.e. bulk, crest and root. The analyzed areas are depicted in figure 4.3. It is visible that Mg-5Gd shows a higher misorientation angle, especially at the crest and root of the screw, than Mg-10Gd (table 4.2). For a homogeneous plastic deformation the applied strain needs to be accommodated possibly equally in the material, while the dislocation slip and its accumulation result in a relatively high misorientation in the deformed microstructure due to the lattice distortion from the geometrically necessary dislocations. In the present study the area fraction of the deformed structure with a KAM of 4°to 5°at the 4th neighboring points, i.e. at a distance of 1.6 µm, is compared between the both alloys (table 4.2). The higher area fractions of the deformed structure are found at different areas in Mg-5Gd. The crest of Mg-5Gd shows about 50% more deformed area than that of Mg-10Gd, ca. 38% at the root and ca. 24% at the bulk. The difference in the fraction of the highly deformed area between the crest and the bulk of the implants is approximately 27% for Mg-5Gd and 13% for Mg-10Gd.

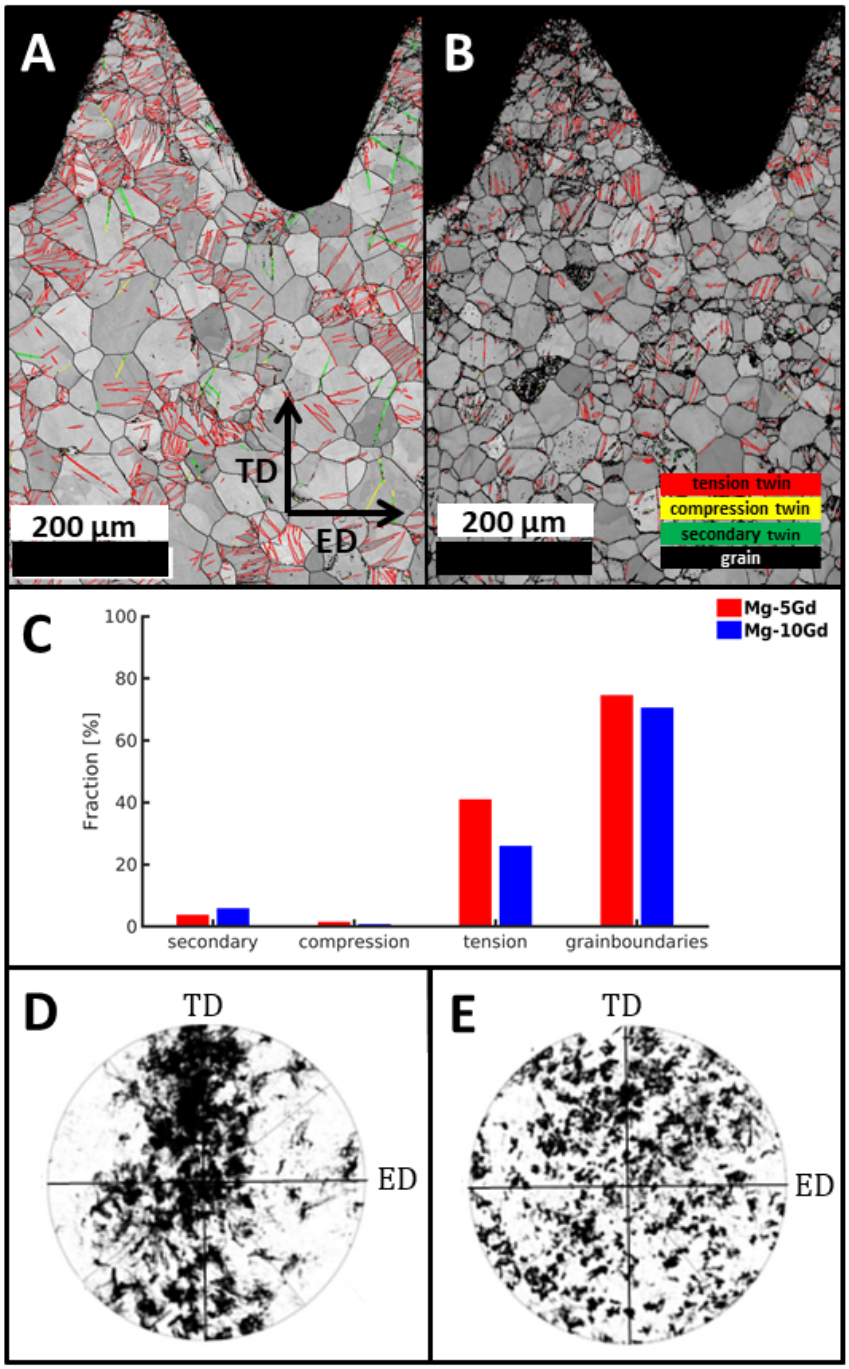

FIGURE 4.2: Quality images overlapped with the highlighted grain and deformation boundaries of A) Mg-5Gd and B) Mg-10Gd and with corresponding pole figures D) and E), respectively. The normal direction (ND) is perpendicular to the transverse direction (TD) and the extrusion direction (ED) of the sample, C) Surface fraction of each boundary from the total detected boundaries in the selected area [154]

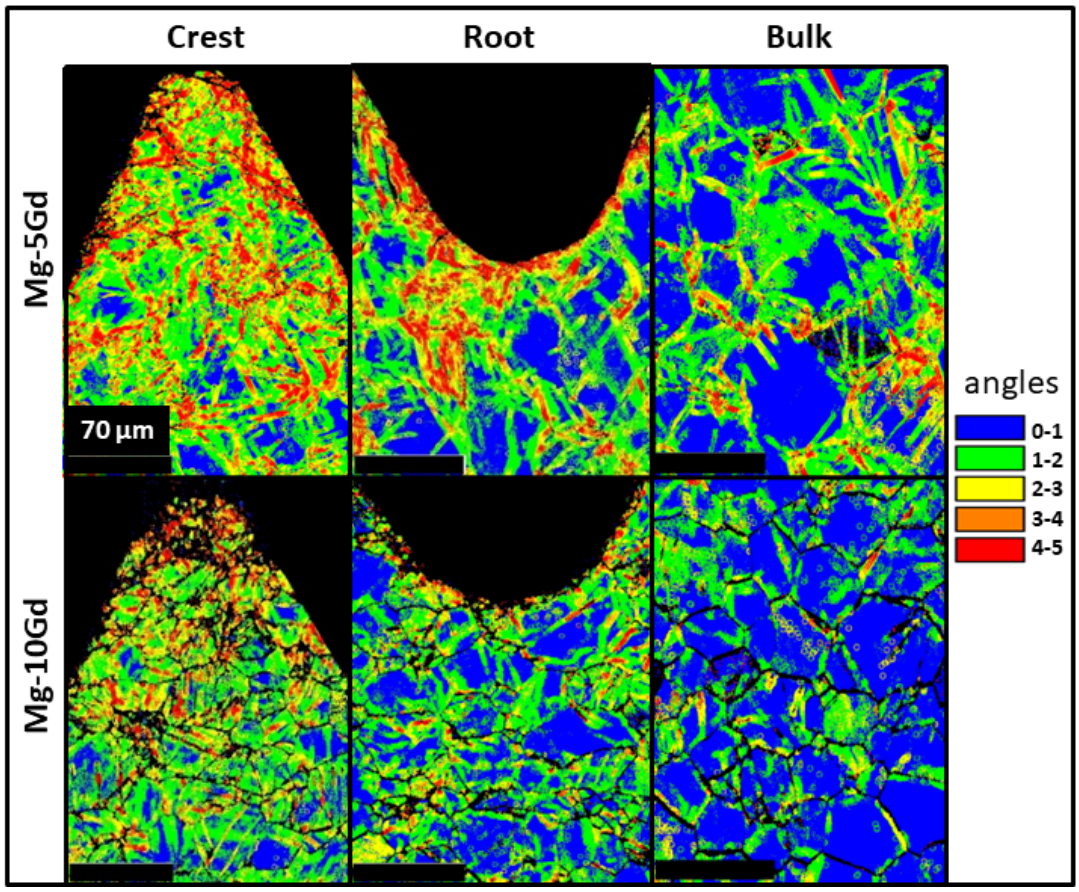

FIGURE 4.3: Kernel misorientation maps from EBSD measurements of Mg-5Gd and Mg-10Gd screws crest, root and bulk at 4th neighbor (distance = 1.6 µm) [154]

TABLE 4.2: Deformation layers thicknesses of processed Mg-xGd alloys in different areas of the screw [154]

Angle of misorientation	Alloy	Crest	Root	Bulk
4-5 degree	Mg-5Gd	0.123	0.063	0.033
	Mg-10Gd	0.060	0.024	0.008

Exemplary SRµCT slices and 3D renderings after segmentation of the Gd-rich particles in a volume-of-interest of Mg-5Gd (A, B) and Mg-10Gd (C, D) screws are shown in figure 4.4. The white dots in figure 4.4A and C are Gd-rich particles or agglomerations thereof, while the α-Mg matrix is depicted in grey. More Gd-rich particles are visible in Mg-10Gd than in Mg-5Gd, both in the slice and in the volume images. Agglomerations of Gd-rich particles in the extrusion direction are also visible in figure 4.4B and C.

The results of the quantitative analysis of agglomerations of Gd-rich particles from the SRµCT images are summarized in table 4.3. A significant difference is found in the overall volume of the agglomerations ($p<0.0005$) between Mg-5Gd and Mg-10Gd screws, where Mg-5Gd reveals a volume of agglomerations approximately half of that of Mg-10Gd. The observed smallest distance between two particles reveals that those agglomerations are less densely distributed (bigger distance between particles) in the matrix of Mg-5Gd than in Mg-10Gd, by nearly 35%. It is

visible from the volume distribution analysis that Mg-5Gd screws show smaller agglomerations than Mg-10Gd (volume outlier's and median: $p<0.0005$ and $p<0.05$, respectively). The high standard deviation of the Mg-5Gd agglomeration volume is due to one very big agglomeration." [154]

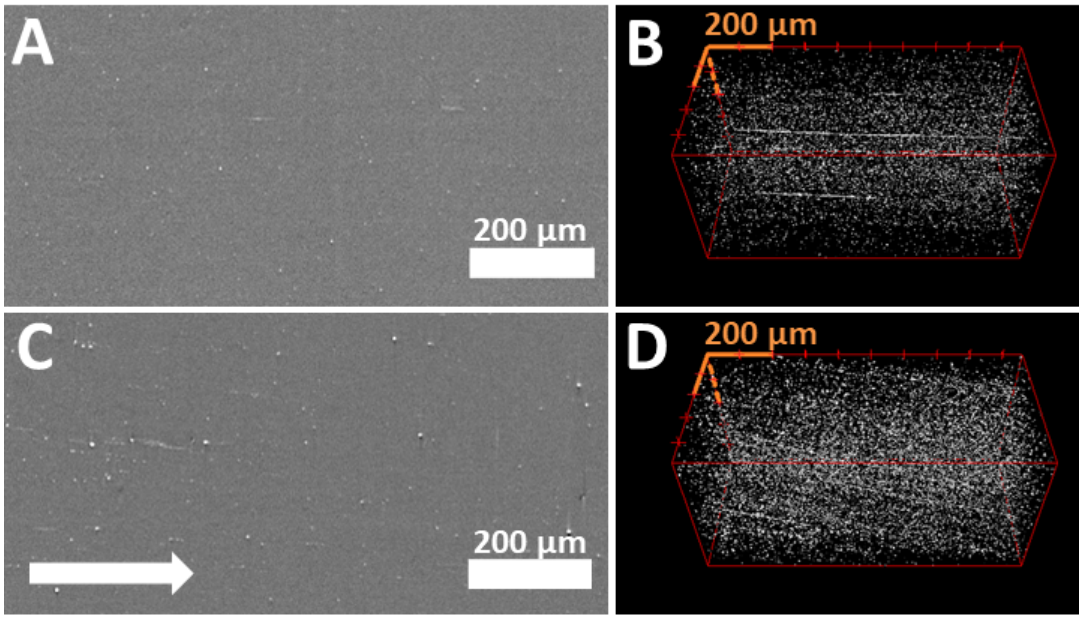

FIGURE 4.4: A, C) 2D tomography slice of Mg-5Gd and Mg-10Gd screws in the longitudinal direction of the screw (arrow: extrusion direction) B, D) Segmented Gd-rich particles (white dots) in a VOI (480x480x960 μm^3) of Mg-5Gd and Mg-10Gd, respectively; voxel size = 2.4 µm [154]

TABLE 4.3: Quantitative analysis of Gd-rich particle's volume, distribution, size in Mg-5Gd and Mg-10Gd screws (SRµCT n = 5) in a chosen volume-of-interest. *Calculation performed after removal of the very high outlier volume 10257 [μm^3] [154]

		Parameter	Mg-5Gd	Mg-10Gd	Statistical Significance
1	Number of detected Gd-rich particles	# particles	10038±1108	18293±2680	$p<0.005$
2	Total volume of the Gd-rich particles	Total volume [%]: mean±std	0.25±0.03	0.56±0.08	$p<0.0005$
3	Smallest distance between two Gd-rich particles	Smallest distance between two particles [µm]	17.15±0.88	11.11±2.18	no sig. diff.
4	Number of detected outliers	# outliers	590±369	986±92	no sig. diff.
5	Mean and std. size of the outlier Gd-rich particles from the volume distribution	Volume [μm^3]: outlier's mean±std	194.29±230.17 *(190.88±136.42)	252.53±230.08	$p<0.0005$
6	Median size of the Gd-rich particles from the volume distribution	Volume [μm^3]: median	41.47	55.30	$p<0.05$
7	Mean diameter of Gd-rich particles from the 2D slices	Mean feret diameter [µm]: mean±std	5.84±0.19	6.25±0.03	no sig. diff.
8	Max diameter of Gd-rich particles from the 2D slices	Max feret diameter [µm]: mean±std	204.58±218.77	126.68±55.22	no sig. diff.

4.1.2 Degradation Behavior *In Vitro*

For visualization, figure 3.7 shows 3D volume renderings of Mg-5Gd screw before and after 56 days *in vitro* degradation in DMEM+10% FBS medium. Figure 3.7C displays the deviation between the "difference layer" (layer between green and red dashed lines including also some black image background) and the "degradation layer" (layer between green and red dashed lines without black image backgrounds).

The following section has been published in [154].
"Results of *DR* calculations *via* weight loss (WL) and volume loss (VL) in *in vitro* experiments in different immersion solutions are plotted in figure 4.5, for comparison of the two measurement techniques (see also in Appendix). For both materials and techniques a high spread of the *DR*s is observed, more so for Mg-10Gd than for Mg-5Gd. It is recognizable that in comparison to Mg-5Gd, the DR_{WL} of Mg-10Gd in the beginning of the immersion period shows lower values than DR_{VL} measurements. Figure 4.5 shows that the degradation is faster at the beginning and decreases with immersion time for both materials.

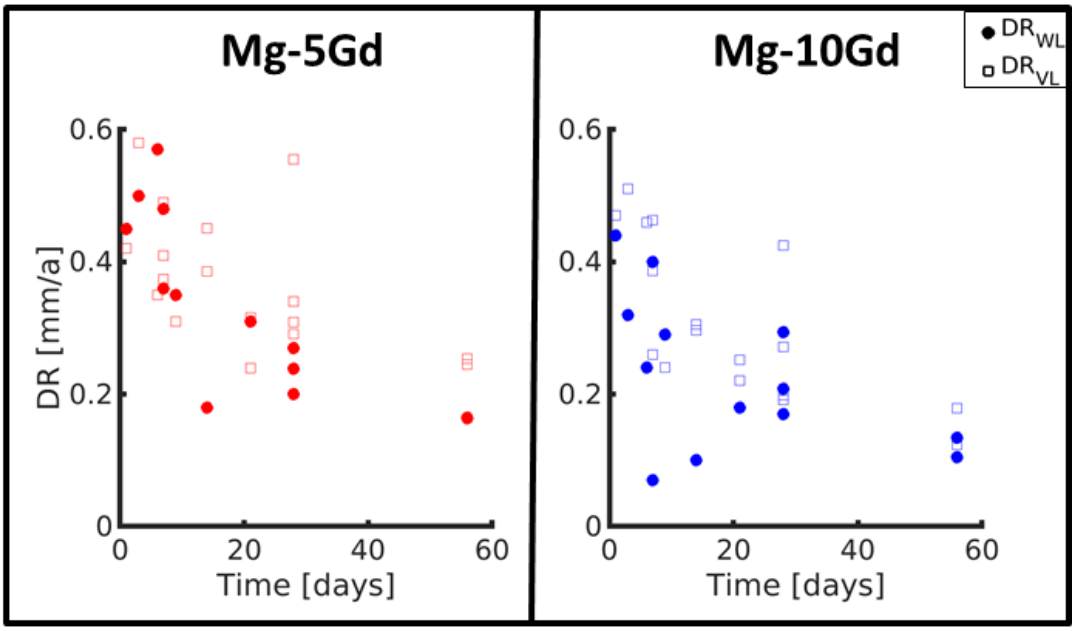

FIGURE 4.5: Degradation rates calculated *via* weight loss (DR_{WL}) and volume loss (DR_{VL}), respectively [154]

The DR_{VL} values of Mg-5Gd and Mg-10Gd screws degraded for 28 days in α-MEM or DMEM, respectively, reveal, that there is a little difference between the DR_{VL} values of Mg-5Gd (α-MEM: 0.30±0.013 vs. DMEM: 0.33±0.03), while the difference for Mg-10Gd is more than 50% (α-MEM: 0.19±0.01 vs. DMEM: 0.34±0.10).

The mean DR_{VL} of experiment (ii) and (iii) (7-56 days immersion time) are plotted again in figure 4.6A, for better comparison with other computed parameters. Both materials start nearly with the same *DR*, but Mg-10Gd shows a stronger reduction over time. The corresponding *MDD* is presented in figure 4.6B. From the fitting slope it is observed that Mg-5Gd reveals a higher *GDR* than Mg-10Gd (table 4.4), which agrees with the *DR* trend.

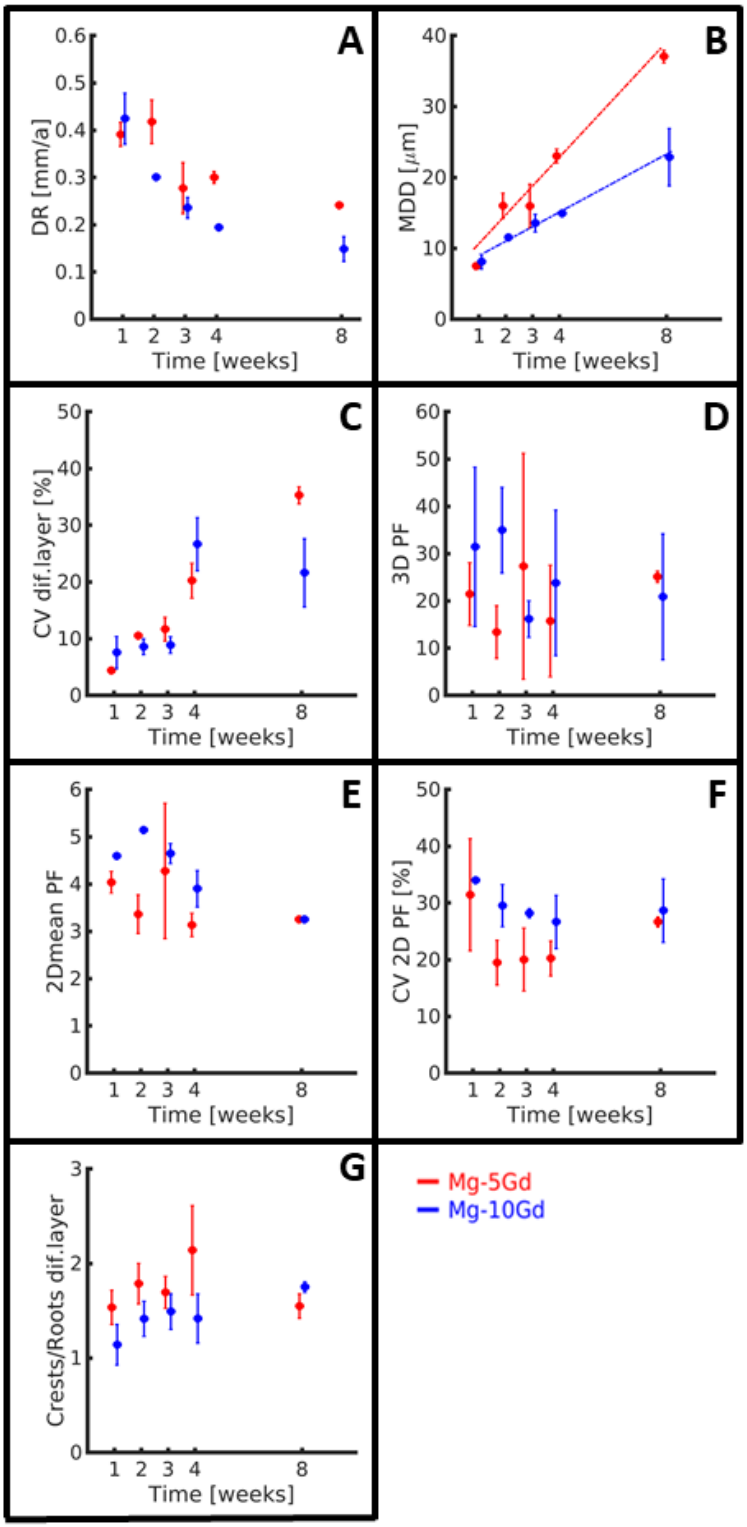

FIGURE 4.6: Results of semi static *in vitro* investigation of Mg-5Gd and Mg-10Gd screw implants over 7-56 days period (experiment (ii) + (iii)) from tomography images. A) Degradation rate, B) Mean degradation depth with linear regression fits (*GDR*: Mg-5Gd = 0.21 mm/a; Mg-10Gd= 0.11 mm/a), C) Coefficient of variation of the difference layer over the transversal slices of the 3D implant, D) 2D mean pitting factor, calculated for each slice with its *MDD*, E) Coefficient of variation from D), F) Ratio of the degradation layers at the crests and at the roots of the samples [154]

The *CV of the difference layer*, which is the ratio between the *2D-mean diff. layer* and the *2D-std diff. layer*, is presented in figure 4.6C and appendix. It shows that Mg-5Gd starts with a smaller CV, hence lower variation of the amount of difference layer along the screw and a very small standard variation between the samples in the 1st, 2nd weeks in comparison to than Mg-10Gd. It increases for both materials with immersion time, more for Mg-5Gd, which at the last time point is approximately 35%, and 25% for Mg-10Gd. The *3D-PF* represents the degradation homogeneity of the 3D dataset. In contrast, the *2D-PF*, being calculated slice-wise, represents the degradation homogeneity of the same dataset statistically. The *3D-PF* values, which are presented in figure 4.6D and appendix, are much higher than *2D-mean PF* values, (presented in figure 4.6E and in Appendix). There are no recognizable differences or tendencies in the *3D-PF* between both alloys and/or time points. With exception of the 1st week, Mg-10Gd shows a decreasing *2D-mean PF* reaching its maximum in the second week and a minimum in the 8th week. By contrast, Mg-5Gd does not show any tendency, but shows overall smaller mean values than Mg-10Gd, except for the 8th week, were they reach equity. The *CV of the 2D-PF* presented in figure 4.6F shows that there is a tendency of decreasing CV from the 1st to the 8th week in case of Mg-10Gd and. Mg-5Gd shows values like Mg-10Gd in the 1st and the 8th week and up to 10% lower CVs (meaning more homogeneous) values for 2nd, 3rd and 4th weeks. Figure 4.6G presents the ratio of the degradation between the crests and roots of the threads.

Both materials show *crest to root ratios* higher than 1, indicating faster degradation in crests compared to roots. It is visible that there is a tendency of increasing *crest to root ratio* of the degradation layer for Mg-10Gd from the 1st week to 8th week. Generally, Mg-5Gd shows higher values than Mg-10Gd. Until week 4, Mg-5Gd screws degrade up to 50% stronger at the crests than Mg-10Gd.

While the overall standard deviations are large, in particular for the degradation parameters, the observed differences between both materials are summarized in table 4.4." [154]

TABLE 4.4: Comparison of analyzed parameters for Mg-5Gd and Mg-10Gd screws [154]

	Parameter	**Mg-5Gd ... Mg-10Gd**
Microstructure	Grain size	>
	Deformation degree	>
Gd-rich particles	Volume	<
Degradation velocity	*DR*	>
	MDD	>
Degradation homogeneity	*CV diff. layer*	>
	2D mean PF	<
	CV 2D-PF	<
	Crests/roots	>

4.2 *Ex Vivo* Experiments

In the following the results from SRµCT and histological analysis of the *ex vivo* implants will be shown.

4.2.1 Degradation velocity and homogeneity from SRµCT analysis

Implant degradation rate and homogeneity from SRµCT analysis are presented figure 4.7. All values can also be found in the supplementary information. All the significant differences observed are given in table 4.5. The comparison of parameters between the *in vitro* volume loss measurements and *ex vivo* analysis are presented in figure 4.9 and the corresponding values can be found in the supplementary information.

4.2.1.1 Degradation Rate

The following has been published in [155].
"Both alloys revealed *DR*s below 1 mm/a for all time periods (figure 4.7A). There were no significant differences in the *DR*s of different materials for the same time points ($p>0.05$).

The *MDD* of the *in vivo* corroded implants is presented in figure 4.7B. The fitted lines in figure 4.7B represent the *GDR* (see Equation 2, supplementary information). The *GDR* of Mg-5Gd (0.18 mm/a) is more than twice as high as that of Mg-10Gd (0.077 mm/a)." [155]

4.2.1.2 Degradation Homogeneity

In the following section the implant's homogeneity analysis is presented *via* parameters *CV volume loss* and *PF*. It has been published in [155].

1. Coefficient of Variation of Volume Loss (*CV Volume Loss*)
   "The coefficients of variation of the volume loss (*CV volume loss*) are presented in figure 4.7C. High values for both alloys demonstrate high variability in the amount of degradation layer in different parts of each implant. This inhomogeneity of the degradation performance can be observed in figure 4.8, which shows different implant types after 12 weeks of degradation. Figure 4.8A in particular displays a Mg-10Gd screw. While in a region of the screw nearly all the threads were completely degraded (right hand-side in the figure 4.8A), in the bottom region, four threads appeared intact. When studying Mg-5Gd and Mg-10Gd alloys, we see that both alloys showed a decreasing tendency over time. Through all time points, Mg-10Gd showed a higher variation between the CV values. Mg-5Gd on the other hand revealed smaller variations and smaller mean values at 4 and 8 weeks than at 12 weeks. Therefore, Mg-10Gd degraded more inhomogeneously than Mg-5Gd until the 12 week time point. However, for *CV volume loss* there were no significant differences for the different materials at the same time points found ($p>0.05$)." [155]

2. Pitting Factor (*PF*)
   "*3D-, 2D-mean PF* and *CV PF* values are presented in figure 4.7D-F and in supplementary information. A tendency for *3D-PF* to decrease over time was observed for both materials. Mg-10Gd showed an overall higher *PF* and higher variations than Mg-5Gd at all time points, with the largest difference at 12

week (Mg-5Gd 12.3 and Mg-10Gd 15.4). No significant differences for the *3D-PF* of the different materials in the same time points could be found ($p<0.05$). There were no significant differences in the *2D mean PF*s and *CV 2D-PF*s neither between the alloys nor between the time points and the values were lower than the *3D-PF* values. Except for the 8 week time point, Mg-10Gd showed slightly higher mean values than Mg-5Gd. Hence, only the *3D-PF* indicated a slightly more inhomogeneous degradation performance of Mg-10Gd than of Mg-5Gd." [155]

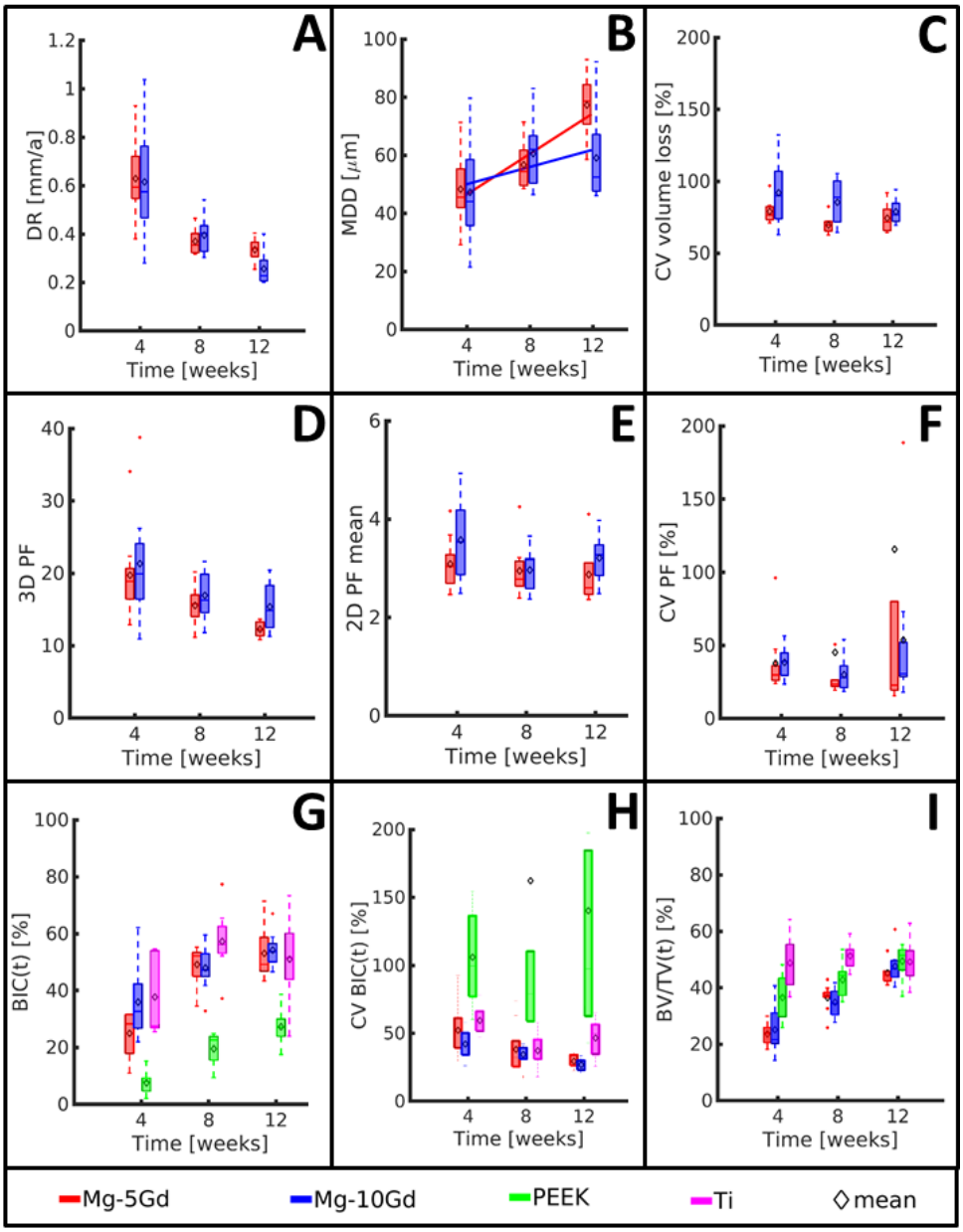

FIGURE 4.7: Results of *ex vivo* investigation of Mg-5Gd, Mg-10Gd, PEEK and Ti screw implants over 4,8,12 weeks healing period from SRµCT images. A) *MDD* with the fitted *GDR*, B) *DR*, C) *volume loss CV*, D) *3D-PF*, E) *2D-PF CV*, G) *3D-BIC(t)*, H) *2D-BIC(t) CV* , H) *BV/TV(t)* for 200 µm [155]

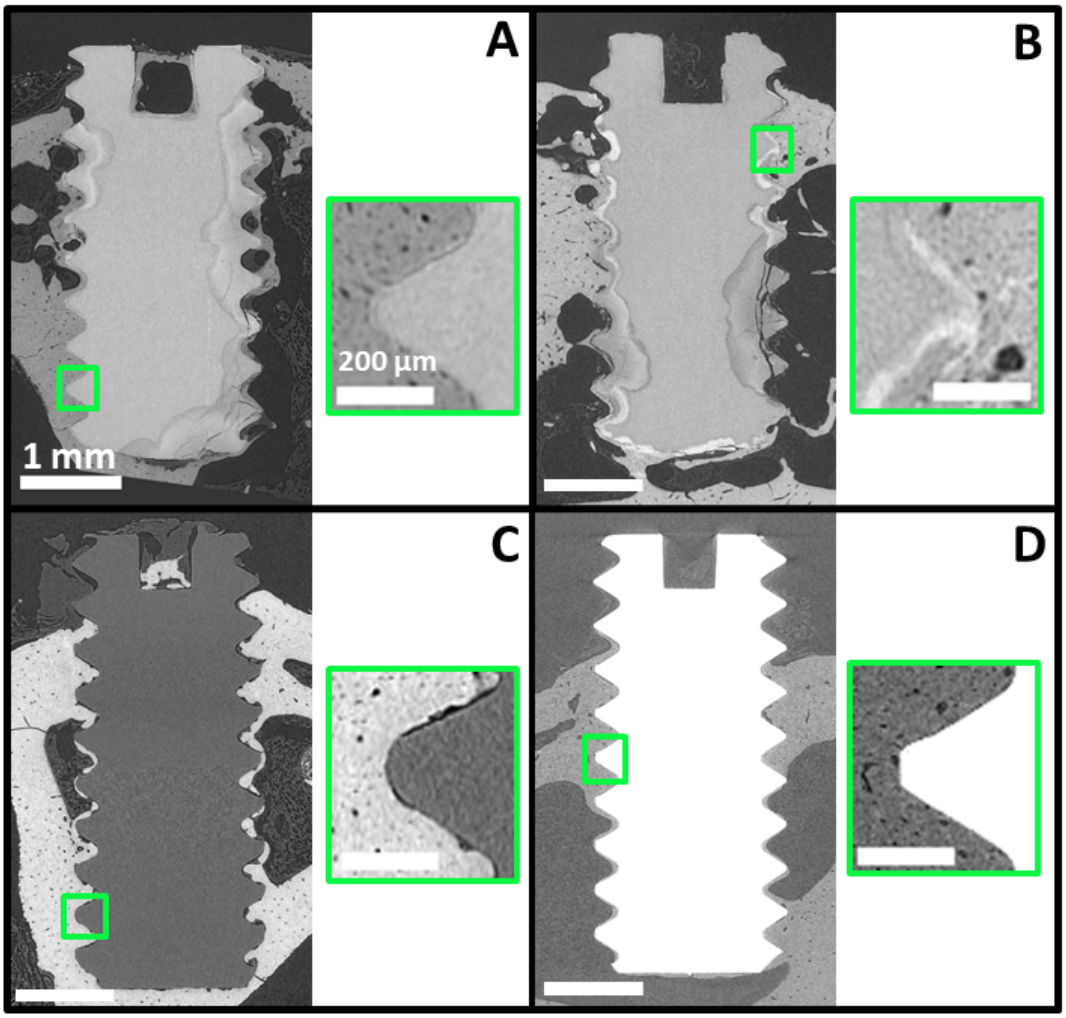

FIGURE 4.8: Representative slices of SRµCT *ex vivo* images after 12 weeks healing A) Mg-10Gd, B) Mg-5Gd, C) PEEK, D) Titan. The image contrast was adjusted for better visualization, which results in the different grey level appearances of the bone in the images. The scale bar applies to all images [155]

4.2.1.3 Comparison of *Ex Vivo* and *In Vitro* Results

The following section is cited from the publication [155], where the detailed comparison of *ex vivo* and *in vitro* results is presented.

In figure 4.9, the ratios between *ex vivo* and *in vitro* results for 5 selected parameters are displayed.

"The *DR*s observed *ex vivo* were higher than the *in vitro* ones for the same time points (4 and 8 weeks). The difference is notably higher for Mg-10Gd (2.8 and 2.6 times for 4 and 8 weeks, respectively) than for Mg-5Gd (2 and 1.5 times for 4 and 8 weeks, respectively).

The *CV volume loss* obtained *ex vivo* is almost 4 times higher compared to the one obtained in *in vitro* experiments, indicating a more inhomogeneous distribution of the degradation layer *ex vivo* (figure 4.9).

The comparison of *ex vivo* and *in vitro* homogeneity behavior reveals that *3D-PF*, *2D mean PF* and *CV 2D-PF* are similar for Mg-10Gd in both experiments (except *CV 2D-PF after* 4 weeks). For Mg-5Gd, the *2D mean PF* are similar in both experiments.

The mean ratios of the *CV PF* are between 1 and 2, meaning the *ex vivo* samples show higher overall inhomogeneity than the *in vitro* ones. This indicates that the degradation homogeneity of Mg-10Gd is similar for the *ex vivo* and *in vitro* experiments." [155]

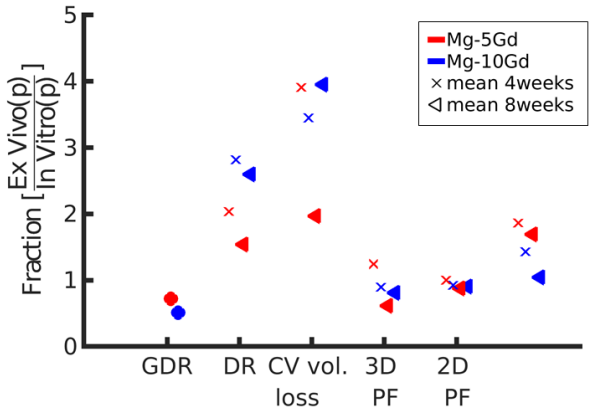

FIGURE 4.9: Factor (= ratio between mean *ex vivo* and mean *in vitro* analysis parameters (p), whereby the parameter is plotted on the x-axis [155]

4.2.2 Implant Integration into the Bone from SRµCT and Histology

The results of investigation about how well the 3D implant is integrated into the bone can be found in the following section (*3D-BIC(t)* and *3D-BV/TV(t)*). Also the results of the homogeneity of the integration is presented by use of the *CV BIC* parameter. The content of the following sections has been published in [155].

1. Bone-to-Implant Contact (*BIC*)
   "The results of osseointegration analyses of all four implant materials calculated on tomographic data are presented in figure 4.7G-I (Table 7 in Appendix). The *BIC(h)* values from the 2D histological analysis are shown figure 4.10 [155]. First, it can be observed that while all implants showed increasing *3D-BIC(t)* over time, PEEK implants displayed generally lower values than all other materials. Significant differences were found between PEEK and all other materials at all observation point. PEEK implants revealed on average between 25% and 50% less *BIC(t)* than the other materials at all time points. Figure 4.8 shows a magnification of an exemplary thread for each screw type to highlight this fact. After 12 weeks of implantation, a gap is still visible between PEEK surfaces and the surrounding bone, indicating a low osseointegration rate (4.8 C), in contrast to all other materials. Ti implants yielded the highest average *3D-BIC(t)* both at 4 and 8 weeks, but at 12 weeks both Mg alloys caught up, with Mg-10Gd having the highest average *3D-BIC(t)* at the longest follow-up time. In general, Mg-5Gd revealed lower (at 4 weeks) or similar (at 8 and 12 weeks) *3D-BIC(t)* values compared to Mg-10Gd. Furthermore, it appeared that Mg-xGd alloys implants exhibited smaller variations in *3D-BIC(t)* at 12 week than the titanium implants. Since the *2D-mean-BIC(t)* are nearly equal to the *3D-BIC* they are not presented in a graph or discussed. The results of *CV 2D-BIC(t)* are shown in figure 4.7H. The lowest variations were observed in Mg-xGd alloys implants, where Mg-10Gd revealed slightly lower values than Mg-5Gd. The highest variation values were observed in PEEK implants, which can be

related to the inhomogeneous distribution of bone-to-implant contact along the implants. Significant differences are found between PEEK after 8 weeks implantation and Mg-10Gd after 8 and 12 weeks implantation ($p<0.05$). Additionally, a significant difference is observed between PEEK implants after 8 weeks and titanium implant after 8 weeks degradation.

For three Mg-10Gd samples after 12 weeks *ex vivo* degradation the *3D-BIC(t)* was calculated once with the mineralized bone only resulting in *3D-BIC(t)*=48.1%±1.2%, once after adding the non-mineralized bone resulting in *3D-BIC(t)*=49.4%±1.6%." [155]

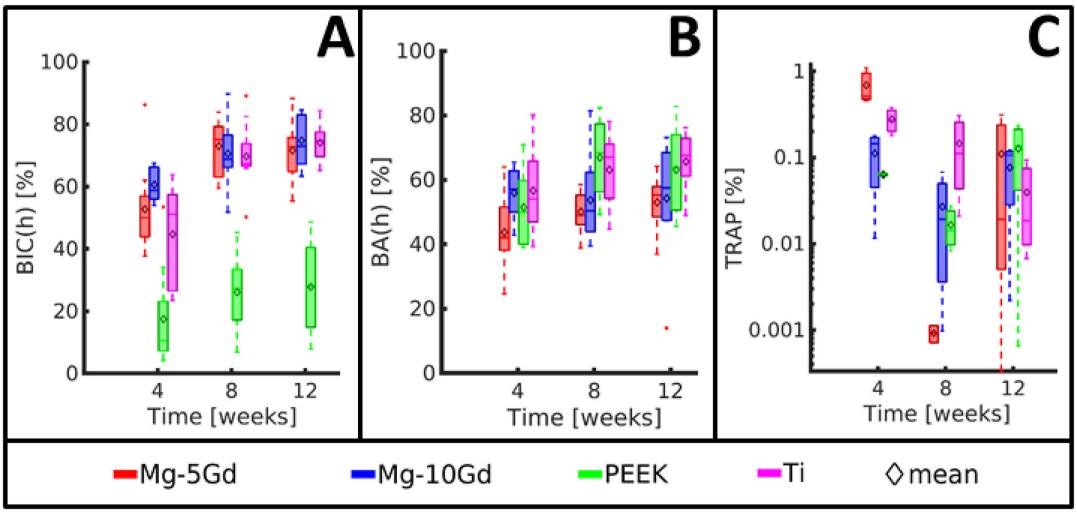

FIGURE 4.10: Results of *ex vivo* investigation of Mg-5Gd, Mg-10Gd, PEEK and Ti screw implants over 4, 8, 12 weeks healing period from histological analysis. (A) 2D Bone implant contact (*2D-BIC*), (B) 2D Bone area (*2D-BA*) for 200 µm, (C) Tartrate resistant acid phosphatase-positive area (TRAP) in a 200 µm ROI around the screw surfaces (Error bars correspond to 99% confidence interval) [155]

2. Bone Volume Fraction (*BV/TV(t)*)
The following section has been published in [155].
"Since the tendency for all materials' *BV/TV(t)* for all three VOIs were the same, only the results for the 200 µm VOI are discussed here and the values for the 100 µm and 300 µm VOIs are presented in the supplementary. Results of *BV/TV(t)* in the VOI of 200 µm around the screws are presented in figure 4.7I. Titanium samples revealed high *BV/TV* values at each time point. In particular, already after 4 weeks of implantation, the amount of bone around Ti implants was close to 50% and remained stable at longer time points (48.8% at 4 weeks, 51.3% at 8 weeks and 49.3% at 12 weeks). PEEK implants showed a *BV/TV* close to 40% at 4 weeks and it increased with time, with the highest average value for all material at 12 weeks (49.4%). At 4 weeks, both Mg alloys showed a *BV/TV* close to 20%, which raised to around 35% at 8 weeks. After 4 and 8 weeks of healing, Mg-xGd alloys exhibited significantly lower *BV/TV* values than titanium ($p<0.0001$) and PEEK implants ($p<0.0001$ and $p<0.006$ at 4 and 8 weeks respectively). Also for PEEK screws, the average values of *BV/TV* at 4 and 8 weeks were significantly lower than those of PEEK. However, at 12 weeks mark, all materials yielded similar *BV/TV* values, without statistically significant differences (between 45% and 49.3%).

For three Mg-10Gd samples after 12 weeks *ex vivo* degradation the *BV/TV* was calculated once only with the mineralized bone resulting in *BV/TV*=36.6±5.6%, once after adding the non-mineralized bone resulting in *BV/TV*=37.6±5.7%." [155]

4.2.2.1 Correlations

The content of the following section has been published in [155].
"The results of the Peason's R correlation of different parameters are presented in table 4.5 with the interpretation of the Pearson's R correlation coefficient from [171]. Only one very strong correlation between *3D-BIC(t)* and *3D-BV/TV(t)* was found, which was for Mg-5Gd. This suggests that there was a dependency between the amount of the bone growing in the surrounding of the screw and its connection to the bone for the Mg-5Gd alloys. For Mg-10Gd and PEEK the correlation was moderately strong. By contrast, there was no correlation for the titanium implants. A moderately strong inverse dependency was found between the *DR* and the *3D-BIC(t)* in Mg-5Gd implants, meaning that an increase of *3D-BIC(t)* can be correlated to a decrease of *DR*. The same dependency was weaker for Mg-10Gd, but close to moderately strong. Another moderately strong inverse correlation was found between the *3D-PF* and *3D-BV/TV(t)* of Mg-5Gd alloy implants. This dependency was just fair for Mg-10Gd. A fair inverse correlation was seen between *3D-BIC(t)* and *3D-PF* for Mg-5Gd, while there was a very poor, correlation for Mg-10Gd. For both alloys there was a very poor correlation found between *DR* and *3D-PF*." [155]

TABLE 4.5: Strength of the linear Pearson's R correlations, *BV/TV* and *BA* in 200 µm distance from implant surface (P1 and P2 correspond to Parameter1 and Parameter2): VS=very strong, MS=moderately strong, F=fair, P=poor [171] [155]

P1	P2	Mg-5Gd	Mg-5Gd	PEEK	Ti
3D-BIC	***DR***	MS: -0.76 (p=.000)	F: -0.58 (p=0.003)		
3D-BIC	***3D-PF***	F: -0.42 (p=.033)	P: -0.05 (p=.000)		
DR	***3D-PF***	P: 0.15 (p=.472)	P: -0.19 (p=.355)		
3D-PF	***3D-BV/TV***	MS: -0.60 (p=.001)	F: -0.37 (p=.065)		
3D-BIC	***3D-BV/TV***	VS: 0.86 (p=.000)	MS: 0.75 (p=.000)	MS: 0.73 (p=.000)	P: 0.05 (p=.831)

4.2.2.2 Qualitative Observations

The observations from the qualitative analysis are outlined in the following section, which has been published in [155].

1. **Degradation layers behaviour**
   "Some parts of the degraded screw threads were broken as observed on the tomography and histological data, which might indicate a brittle behaviour of the degradation layers (figure 4.8B). The amount of the degradation layer analysed on three Mg-10Gd screws after 12 weeks healing, which was fractured (which could be detected with the naked eye and segmented on tomographs) and fully isolated from the screw was 0.62±0.34%, of which (4.6 ± 1.34)% were surrounded by bone." [155]

   The majority of the degradation layer debris figure 4.8B) were surrounded by mineralized bone on the one side and by non-mineralized bone on the other

side. The bone seemed to be growing into the degradation layer, between the fracture lines of the degradation layer. Parts of degradation layer, which were surrounded by bone, are shown in figure 3.9A. The distance between the surface of the implant and the fractured pieces was 154 ± 4 µm for Mg-10Gd after 12 weeks *in vivo* degradation. In several areas of the screws, the original threaded shape was maintained intact, but the material was trasformed from the original metal to degradation layer that displayed a different grey values range in the tomographies and a different color in the histological slides.

2. **Tissue Integration and Tissue Reactions Around Different Materials**
The content of the following section has been published in [155].
"Bone tissue surrounded the implants of 4 materials already at 4 weeks, but it increased by week 12. The bone grew inside the thread spaces and a thin bundle of bone encapsulated most of the screws, extending even in those areas that initially where not facing bone surfaces (i.e. the medullar space of the tibia). However, differences appeared among the materials. The bone around PEEK implants was less often in direct contact with the surfaces, compared to the 3 metals.

   Newly formed bone was found predominantly facing regions of the implants that were more degraded, while more mature bone was observed incorporating areas of the implant with less corrosion. The newly formed bone looked sometimes detached from the surfaces of the degradation layers, especially in the 4 week samples, but that was likely an artefact of the critical drying process. The bone was in tight contact with the surface of the 3 metals tested here, especially after 12 weeks of healing. For many samples of the Mg alloy groups at 12 weeks, the bone and the degradation layers were so tightly connected that it was hard to distinguish between them, especially considering that the corrosion layers were stained in the same light purple colour of the bone. Osteocyte lacunae in the bone demarcating Mg alloys looked often oriented parallel to the implant surfaces. In general, no adverse reaction or excessive inflammatory infiltrate was noted around ay of the implants in this study." [155]

4.3 Image Processing and Analysis

Semi-automatically segmentation workflows made it possible to provide the needed amount of input data for the machine/deep learning approaches (training of neurons networks) in a reasonable time (segmentation of 3 samples in 2 days was possible). Overall 18 data sets (3 data sets x 2 material x 3 time point) were segmented semi-automatically.

4.3.1 "Difference" and "Corrosion" Layer

During the data analysis it was notable, that the borders of the pre-implantation screw did not match with the borders of the post-implantation screw (= residual + corrosion layer). This difference is visualized in figure 4.11. The layer between the pre-implantation and residual screw is defined as "difference layer". In case of a perfect registration process and if during the corrosion process no change of the screw dimensions would happen, this difference layer would theoretically be the corrosion layer.

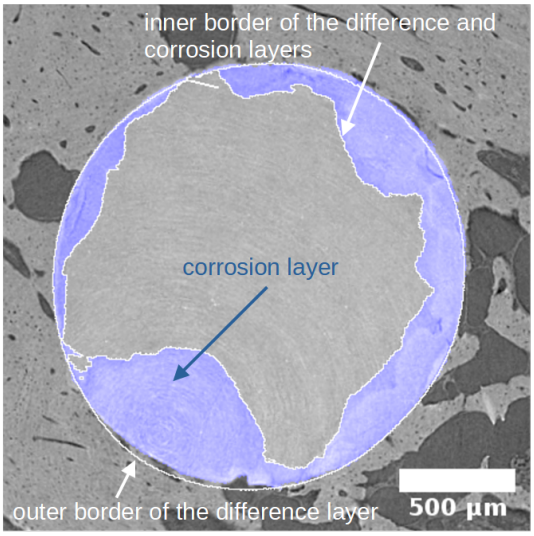

FIGURE 4.11: Cross sectional view of a Mg-10Gd screw in the bone after 12 weeks *in vivo* degradation. After registration, resampling and segmentaiton the white borders are identified as the borders of the difference layer, which results when subtracting the residual screw from the pre-implantation screw. The blue area is identified as the corrosion layer, which results when subtracting the residual screw from the not corroded screw from the *ex vivo data*. The pre-implantation screw, the not corroded screw and the residual screw are described and shown in chapter 3 in figure 3.2.

But since there is a change of the original screw borders during the corrosion process or/and because of the not perfect registration process, there is a small difference to detect between the "difference" and the "corrosion" layers volumes. Up to 14.8±7.6% for Mg-5Gd and 20.9±7.8% for Mg-10Gd after 4 weeks of *in vivo* degradation is noticeable. In case of longer *in vivo* degradation this difference decreases (after 8 weeks Mg-5gd and Mg-10Gd: 9.7±4.5% and 11.9±6.2% respectively; after 12 weeks Mg-5gd and Mg-10Gd: 11.1±3.1% and 8.7±2.6% respectively). But it doesn't necessarily mean, that the border is less changed, just that the change of the border in relation to the whole corrosion or difference layer is relatively small (since the volume of the corrosion or difference layer increases with the time). In general the tendency is visible, that the difference layer tends to have a slightly higher volume than the corrosion layer. If this difference just occurs because of a not completely perfect registration procedure, it should be kept in mind, that it can have an influence on the analyzed parameters. If, for the sake of simplification, one would consider the border of the pre-implantation screw and the bone as the bone-to-implant contact borders, this might result in false *BIC* values. Hence a very precise segmentation is necessary for an appropriate analysis.

4.3.2 Manual vs. Semi-Automatically Segmentation

A difference in the data was obtained, when segmented either manually or semi-automatically. This difference had an influence also on the results of the analyzed parameters. The magnitude of this segmentation influence on the analyzed parameters is shown in figure 4.12. It is obvious that some of the analyzed parameters are more and the others less sensitive towards the segmentation. The highest difference up to 325% is observed in the parameter *CV-PF*. The next highest difference (up to 50%) is found in the *BIC* between the same data once analyzed *via* manual once semi-automatically segmentation. Also *MDD* is with 46% difference between manual and

semi-automatic segmentation methods being sensitive towards data segmentation method.

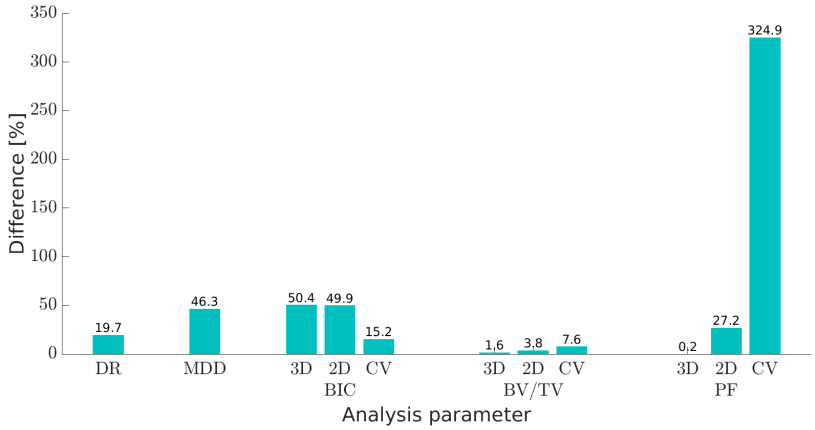

FIGURE 4.12: Differences of the parameters, once analyzed on the manually segmented data set and once on the semi-automatically. Mg-5Gd *ex vivo* sample after 12 weeks degradation from Paria Werner's master's thesis

4.3.3 Automatic Segmentation

The preliminary qualitative comparison between the semi-automatic and the automatic segmentation showed that the results of the automatic segmentation are more precise. The latter can be observed in figure 4.13 by comparing the areas marked with red arrows.

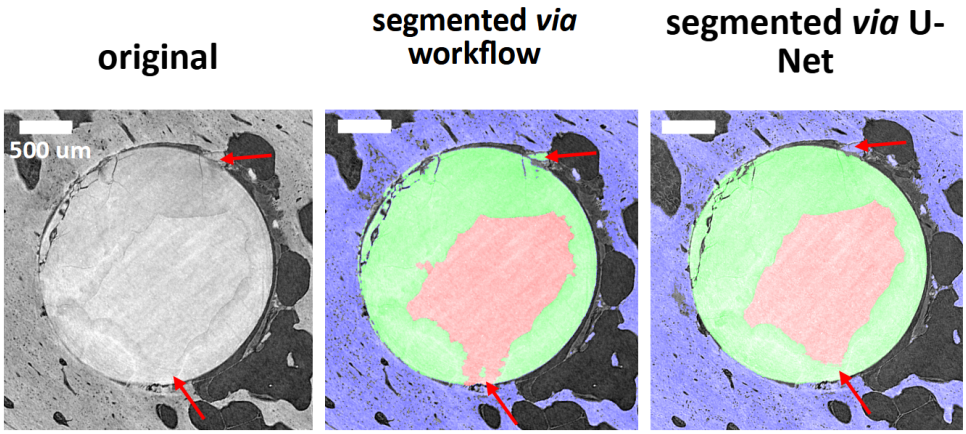

FIGURE 4.13: Mg-10Gd screw corroded *in vivo* for 12 weeks segmented semi-automatically (*via* workflow) and *via* U-Net deep learning approach [161].

The quantitative analysis of this difference is investigated and published in [161]. Overall more than 100 explants were segmented using the this automatic segmentation approach. For segmentation of each explant nearly 30 minutes are necessary. For the manual segmentation of the sample amount of explants several years would be needed.

4.3.4 Person-Dependent Segmentation

Differences in the segmentation result depending on the segmenting person were found. The selected slices for this person-dependent segmentation comparison are presented in figure 4.14. The white areas in this figure represent the areas where the difference in the segmentation appeared.

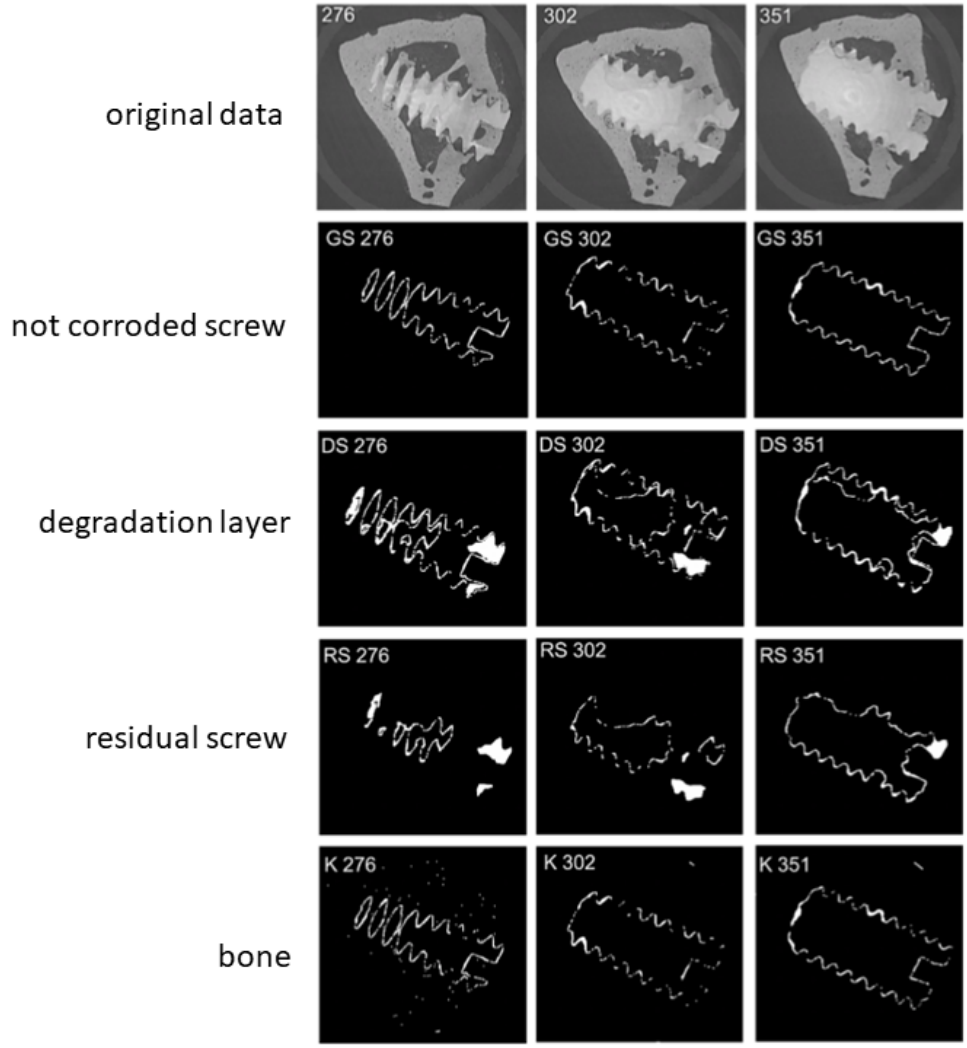

FIGURE 4.14: Person-dependent segmentation difference on three slices for the labels not corroded screw, degradation layer, residual screw and bone. Image is taken from master's thesis of Paria Werner

Visually, more inconsistency can be observed in the segmented labels "degradation layer" and "residual screw" (more white areas in figure 4.14). Up to $\approx 60\%$ coefficient of variation is found for the label degradation layer. The next very high coefficient of variation with $\approx 40\%$ is found for the label "residual screw". In contrast to the above mentioned, the labels "bone" and "not corroded screw" are with CVs of 2.5% and 10% much less.

4.3.5 Determination of Dissimilarities in Sample Dimensions

In figure 4.15, which shows the composition of the line profiles of the same metal ball once tomographed with the labor µCT device Nanotom (red outline) and once with the SRµCT at P05 (green outline), it is clearly visible that there is a difference in the metal ball diameter. This difference is ca. 8 µm. It occurs because of the less blurred borders of the ball imaged at the SRµCT compared to the one tomographed using laboratory µCT. Previous to analysis described above, this difference was compensated using a "correction factor", which was applied to the nanotom data (step 7 in the SOP of the workflow).

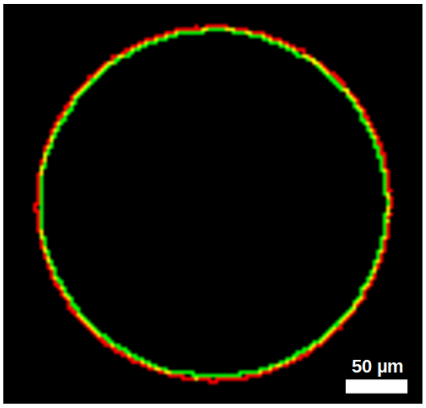

FIGURE 4.15: Composite of the line profiles of a metal ball imaged once with the laboratory µCT device Nanotom (red line) and once at the SRµCT at the IBL P05, DESY (green line). Yellow is the overlapped area of red and green lines.

4.3.6 Influence of Different Image Processing Methods on the Results

Table 4.6 summerizes the influence of different image processings on the final analysis parameter, explained in chapter 3, in subsection 3.4.3 (Nr. 5). The detailed information about the type and the extent of influence of each processing can be found in chapter 3, table 3.6. After calculating the coefficient of variation it is recognizable, that the most sensitive parameter is the *3D-BIC* (much more for the PEEK screw, but not for the Mg-5Gd screw) (4.6).

TABLE 4.6: Coefficients of variation (CV) for parameters degradation rate (*DR*), 3D pitting factor (*3D-PF*), 3D bone to implant contact (3D-*BIC*) and 3D bone volume density (*3D-BV/TV*) of a *ex vivo* degraded Mg-5Gd and PEEK implants after 12 weeks *in vivo* degradation and a Mg-10Gd screw after 8 weeks *in vitro* degradation. *BV/TV* is calculated at 200 µm distance from the implant's surface

CV	Mg-5Gd	Mg-10Gd	PEEK
DR [mm/a]	28.5%	0%	-
3D-PF	8.3%	0.6%	-
3D-BIC [%]	3.4%	-	63.0%
3D-BV/TV [%]	0.5%	-	10.2%

The next parameter that changed noticeably is the *DR* for the *in vivo* degraded Mg-5Gd screw. After the elimination of the outlier *DR* = 0.05 mm/a the *CV of DR* (Mg-5Gd) over the operations would be 11%. In contrast, the *CV of DR* of Mg-10Gd

is 0, which means, that there is no influence of the operation paramaters on the *DR* analysis of the *in vitro* data. *3D-PF* is 14 times more influenced by different operations in case of Mg-5Gd than of Mg-10Gd.

4.3.7 Influence of Different Implant Geometries on Analysis Parameters

To investigate the influence of the analyzed object's shape on the analyzed parameters *MDD* and *3D-PF*, the corrosion of two different objects was simulated. A homogeneous corrosion of a cylinder and a cuboid was simulated (figure 4.16A). The white area in figure 4.16A represents the simulated degradation layer.

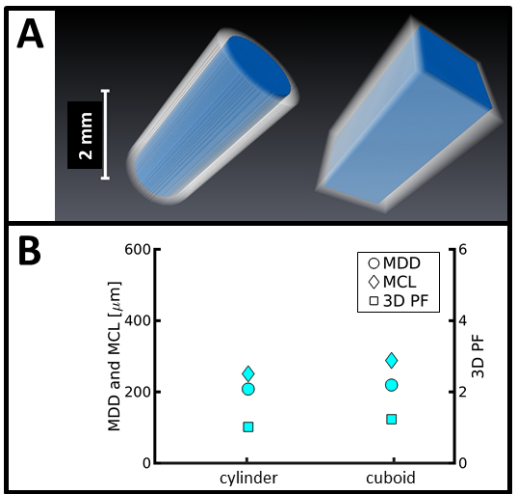

FIGURE 4.16: A) Visualization of homogeneously degraded cylinder and cuboid, B) Results of *MDD*, *MCL* and *3D-PF* calculation of the homogeneously degraded cylinder and cuboid

The comparison results are presented in figure 4.16B. As expected, the *MCL* for the homogeneous corrosion of the cylinder and cuboid is 250 µm. *MDD*, corrosion layer and *PF* calculations are performed on the part of the screw without the slit. *MDD*, which is calculated with the common formula out of the volume loss, is much less (ca. 200 µm for the cylinder and the cuboid). The homogeneously corroded cylinder (*PF*=1.02) and cuboid (*PF*=1.23) indicate, that the way of the *3D-PF* calculation is right.

4.4 Push-Out Experiments

The results of push-out experiments are preliminary as the study is ongoing. First outcomes of Mg-5Gd alloy and Ti explants after 12 weeks *in vivo* degradation are presented in figures 4.17 and 4.18. The comparison of first results showed that a crack first develops in the interface between the bone and the implant for both Mg-5Gd alloy and Ti implant. In case of the Mg-xGd alloys simultaneous cracks also occur in the degradation layer. In case of Ti implant the bone cracking is being the results of the increasing force on the implant.

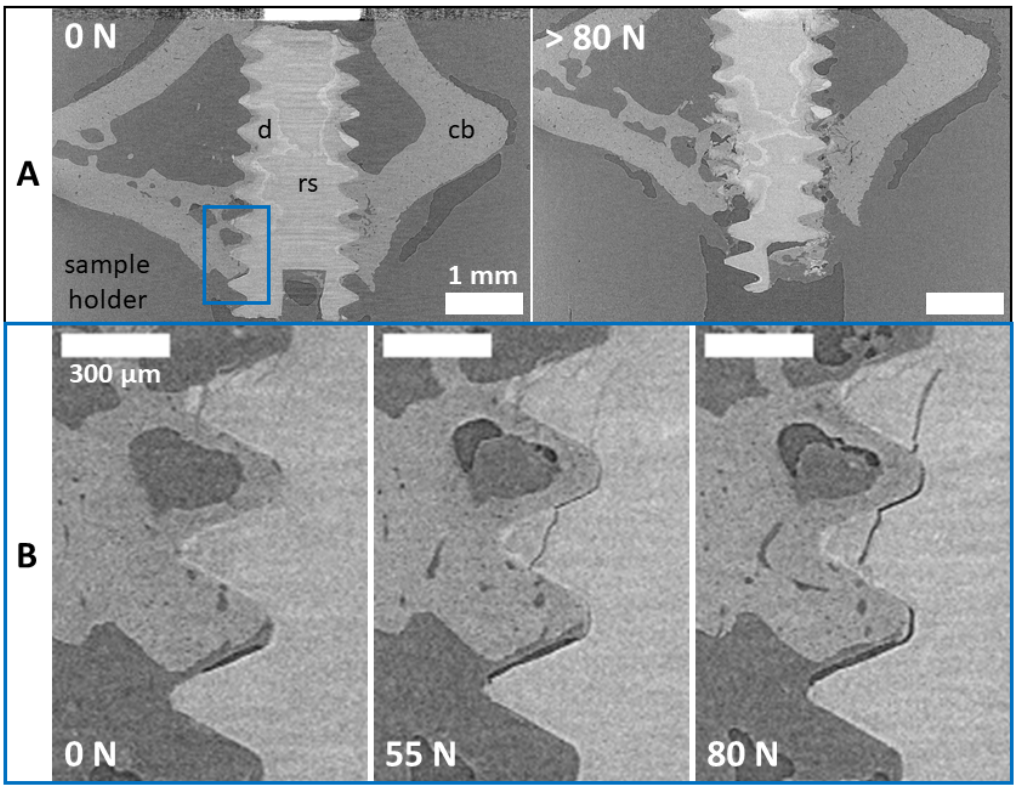

FIGURE 4.17: Mg-5Gd explant after 12 weeks *in vivo* degradation during the push-out test. A) A longitudinal slice of the explant when the screw is intact with the bone as long as no load is applied on the screw (left image) vs. implant failure in the bone after application of a force higher than 80N on the screw. B) Magnification of a chosen area of interest, showing the ongoing detachment of the screw from the bone and the crack development in the degradation layer with increasing applied force.

Plotting the applied force against the whole push-out experiment time one obtains curves, which correspond to the characterization of the implant stability and integration into the bone. Figure 4.19 shows the first results, which indicate, that Mg-5Gd explants fail at smaller load forces than Ti or PEEK implants. It is also visible, that the force the Ti explant can handle before breaking in the bone is twice as high (160N) as the force the Mg-5Gd can handle (80N). It is important to mention that the Mg-5Gd screw failed at much lower forces when tomographed with old, higher dosis. When the bone is being subjected to a high X-ray dose, it is turning more brittle, hence the failure of the implant is happening earlier. Although the modification of the X-ray dose does increase the maximum force before the failure of a Mg-xGd screw, it is still less stable in the bone than Ti or PEEK (figure 4.19).

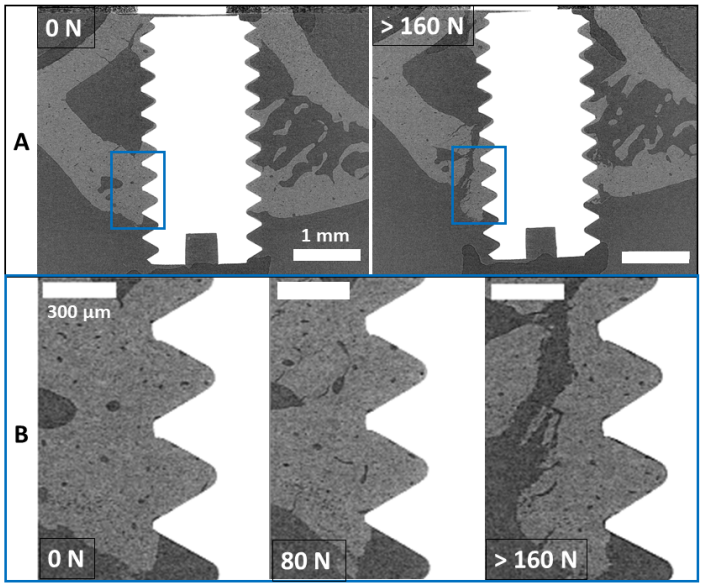

FIGURE 4.18: Ti explant after 12 weeks *in vivo* degradation during the push-out test. A) A longitudinal slice of the explant when the screw is intact with the bone as long as no load is applied on the screw (left image) vs. implant failure in the bone after application of a force higher than 160N on the screw. Several bone areas being broken are visible. B) Magnification of a chosen area of interest, showing the ongoing detachment of the Ti implant from the surrounding bone and the failure of bone with increasing applied force. However, no detachement and/or failure are yet visible at the 80N force.

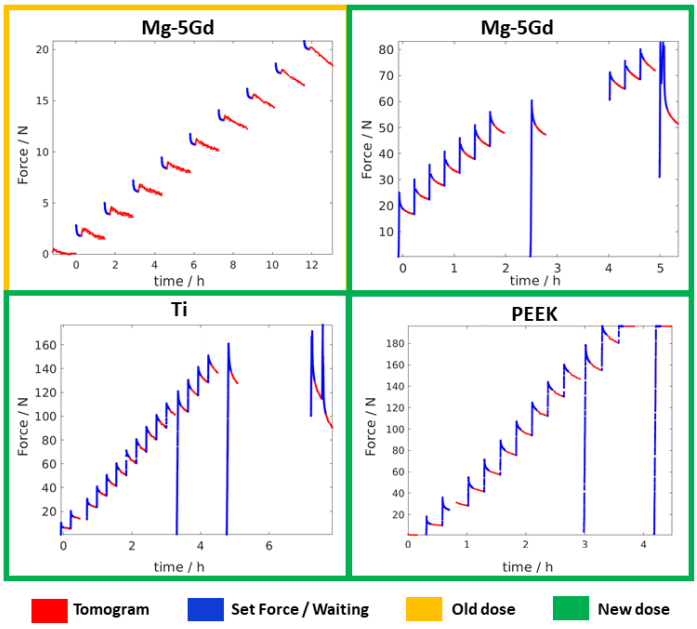

FIGURE 4.19: Push-out results of Mg-5Gd, Ti and PEEK samples after 12 weeks healing time. Yellow marked force-time plot: experiment with too high X-ray dose during the image acquisition. Green marked force-time plots: experiments with adjusted X-ray dose during the image acquisition.

Chapter 5

Discussion

A detailed discussion about the *in vitro*, *ex vivo* degradation rate and homogeneity of the investigated Mg-xGd alloys have been published in large parts in [154] and [155]. Hence some sections here are copied or paraphrased from that publications.

The subject of current thesis are Mg-5Gd and Mg-10Gd alloys in the shape of M2 screws. Their microstructure, *in vitro* and *ex vivo* degradation rate and homogeneity, as well as their integration into rat bone have been investigated. One of the intensively used investigation techniques was micro computed tomography, resulting in necessity of image processing and analysis. In the following are the results from the image processing and analysis, *in vitro*, *ex vivo* and push-out experiments discussed.

5.1 *In Vitro* Experiments

The following section has been published in [154].
"In the following, we will discuss the effect of the microstructure on the degradation behavior to highlight advantages and disadvantages of the Mg-5Gd and Mg-10Gd alloys for the use as implant material.

This study supports the tendency of higher extrusion speeds to result in bigger grain sizes as observed in [171]; Mg-5Gd with higher extrusion velocity revealed bigger grain sizes in comparison to Mg-10Gd. Additionally, a more homogeneous microstructure of Mg-10Gd samples in comparison to Mg-5Gd was observed.

The investigation of the influence of the machining on the near-surface microstructure of the screws revealed higher and regionally deeper microstructural deformations in coarse grained Mg-5Gd than Mg-10Gd. The latter is in agreement with previous findings of Gawlik *et al.* [172]. The Mg-5Gd matrix with coarse grain structure revealed also more tensile twins and tensile twin boundaries than the fine-grained Mg-10Gd alloys. This is in agreement with the fact that the growth of the twins is limited by the grain size, hence bigger grains produce bigger twins and consequently more twin boundaries [173].

Furthermore, Mg-5Gd reveals higher KAM values than Mg-10Gd, and hence has overall more deformed structures. It was previously discussed that the chemical activity at grain boundary regions increases the dissolution rate of fine grained alloys [174–176] and that more instable microstructural features have higher energies, which could accelerate the degradation process. We hypothesize that this process is responsible for the faster degradation speeds observed for Mg-5Gd. This is in contrast to the hypothesis of Gawlik *et al.* [172] that thicker twinning zones slow down the dissolution rate of the alloy, by acting as borders between the grains. Apart from having an influence on the *DR*, the deformation also has an impact on the mechanical properties of the material. Extension twinning occurs under tensile stress along the crystallographic c-axis, which results in a sudden re-orientation of parent grains by approximately 86.3° [177, 178]. When the tension twinning dominated deformation

exhausts, a fast strain hardening is happening, which later leads to an early fracture [179]. From this we conclude that the weaker texture of Mg-10Gd could be more beneficial for the deformation accommodation by the dislocation slip and for a more homogeneous deformation, thus lower risk for an early fracture can be expected for the Mg-10Gd alloys.

In addition to the deformations, the presence of metallic particles in the alloys may have an influence on the degradation behavior. The bright particles observed in the 3D volume are assumed to be agglomerations of GdH_2 particles, which is in agreement with the literature [180]. Under the assumption that these particles act as sites for galvanic corrosion, the smaller the particles and the more homogeneously distributed, the more homogeneous the degradation mechanism should be. Additionally, the more particles present in the alloy the faster the *DR* should be. Based on the observed degradation behavior it appears that the presence of these particles is negligible.

Based on the computed parameters, no clear conclusion can be drawn in terms of the homogeneity of the degradation of both materials. Similar to [25], the higher values of *2D mean PF* in the Mg-10Gd samples in this study are caused by the fact, that in relation to the lower average degradation depth the pit's depths are rather high. The deepest pits are approximately 632.5 µm in Mg-5Gd and 379.5 µm in Mg-10Gd and can be more than twice as deep as the screw thread. In general, the decrease of the *PF* values during longer degradation periods can have several reasons: i) several small pits could merge; ii) inhomogeneities, like GdH_2 particles, could fall out of the pits; iii) small pH differences between the surface and the deep pits, leading to slower degradation rates at the deeper pits than at the surface; iv) larger screw surface area at the top of the pit than at the bottom of the pit, hence less surface energy and slower degradation rates at the deeps of the pits as at the tops. The latter two points could also be a reason for the degradation rate differences at the roots and the crests of the screws.

In this study a larger decrease of *DR*s with the immersion duration of Mg-10Gd screws in comparison to Mg-5Gd could be detected. Kubásek *et al.* [12] discussed, that the Gd^{3+} cations substitute Mg^{2+} cations in the degradation layer, hence slowing down the degradation process. One of the reasons that Mg-5Gd screws degraded faster than Mg-10Gd could be the amount of Gd dissolved in the Mg-matrix. This difference becomes stronger for longer immersion times, which is consistent with Harmuth *et al.* [180] who did not find any significant correlation between the *DR* and the alloy composition in short time of 7 days corrosion tests of Mg-Gd alloys with 2, 5 and 10 wt.% Gd content.

With respect to the degradation rate both materials reveal a *DR* appropriate for orthopedic implants [6]. According to Rahim et. al. [6] the bone healing time can range from a month to 6 months in humans. By considering the calculated GDR_{VL} of 0.25 mm/a for Mg-5Gd after 56 days of degradation, the *MDD* of Mg-5Gd after 6 months is 115 µm. Performing the same *MDD* calculation for a degradation time of 6 months for Mg-10Gd one obtains a *MDD* of 69 µm (with GDR_{VL} = 0.15 mm/a). Therefore, for the given implant geometry, Mg-5Gd would remain in the body for 4.3 years and Mg-10Gd for 8.1 years, before dissolving completely (assuming *MDD*=radiusimplant = 0.9 mm). However, as we have shown that both materials degrade inhomogeneously, and given the sizes of the deepest pits, it is possible that the dissolution will occur faster *in vivo*. Based on this inhomogeneity, future tests must also take into account the change in mechanical stabilities of the implants over time.

Overall, in contrast to weight loss measurements, SRμCT measurements allow not only to assess the volume loss but also enable a description of the degradation homogeneity in a qualitative and quantitative way. Depending on the degradation period and image resolution volume loss measurements can give more precise results than the weight loss measurements of the degradation rate." [154]

5.2 *Ex Vivo* Experiments

An inescapably important comparison to the *in vitro* results are the results from *ex vivo* analysis, which were obtained *via* imaging techniques. At the same time, the osseointegration of the Mg-xGd alloys and the reaction of the surrounding tissue were studied and compared to control materials, Ti and PEEK, commonly used as orthopaedic implants.

Some parts of the following sections habe been published in [154] and [155].
"Previous research pointed out that the degradation rate of Mg alloys is usually faster *in vitro* than *in vivo* [125]. However, this was not confirmed by our study, where the opposite was found, with the *ex vivo* implants revealing higher *DR*s than the *in vitro* corroded ones (2 and 1.5 times for 4 and 8 weeks Mg-5Gd; 2.8 and 2.6 times for 4 and 8 weeks Mg-10Gd). A similar tendency was observed also in [126] on Mg-10Gd and Mg-2Ag alloys implants. As discussed in [126], the reasons for this tendency may be that the *in vitro* tests are mostly observed on disks instead of the actual implants. Moreover, SRμCT investigations of *ex vivo* data are conducted at significantly higher resolution than the *in vivo* imaging, which may result in significant differences. A possible explanation for the implants' degradation *in vivo* being faster than *in vitro* could be the influence of the mechanical stresses on the screws either due to the friction of the implant with the osteotomy walls during the insertion or due to the animal's movement during the implantation period in the animal, or a composition of both aspects [126]. Another possible reason for the faster degradation *in vivo* than *in vitro* is that in tissues the pH is efficiently buffered continuously and the degradation products as well as the Mg ions are quickly removed by the blood flow, while new electrolytes are fed to the corrosion sites, maintaining the local implantation environment propitious to continuous degradation [181]." [155]

"The Mg-10Gd implants in the current study degraded significantly slower than the alloy presented from Galli et al. [126] (ca. 50% and 33% lower after 4 and 8 weeks implantation respectively). However, despite the nominal alloys were the same in both studies, other factors were different. The microstructure of the alloy studied in the present study was more homogenous than the alloy investigated in the former study [126]. Our alloy showed smaller grain size (GS) standard deviation (GS = 26.67 ± 1.3 μm) in contrast to the one in [126] (GS = 21.9 ± 11 μm), and finer and better distributed Gd-rich particles. Hence, a more homogeneous degradation behaviour could be a reason for the enhanced degradation behaviour, and decreased degradation rates." [155]

A comparison of the *DR*s between the Mg-10Gd screw implants from this study and the Mg-10Gd pin implants from Myrissa et al. [125] after 4 weeks implantation reveal 0.1 mm/a slower *DR* of the allow from this study. In addition, Myrissa et al. were not able to observe the implants volume after 12 weeks degradation, due to its integrity loss and disintegration into small remnants of the material. In contrast, the observation of the post-implantation screw in our study was not a problem. In comparison to the Mg-2Ag and pure Mg pin implants after 12 weeks healing from

the same study [125] both Mg-xGd alloys from this study show higher *DR*s (Mg-5Gd 0.14 mm/a higher and Mg-10Gd 0.06 mm/a higher).

The homogeneity of degradation, which is an important characteristic for the mechanical integrity of the implants during healing, is mainly described by the *PF*, with a lower *PF* indicating a more homogenous corrosion behaviour. In our study, the *3D-PF* was higher for Mg-10Gd than Mg-5Gd and it tended to slightly decrease over time. It was interesting to compare the *3D-PF* observed in this study to the one resulted for the same alloys in an *in vitro* study. In general, the ratio between the *ex vivo 3D-PF* and *in vitro 3D-PF* is near 1 (with exception of Mg-5Gd after 8 weeks healing) for both materials 4 and 8 weeks. With a factor of 0.9 Mg-10Gd after 4 weeks healing shows the most *ex vivo* ad *in vitro* comparable 3D pitting. The *3D-PF* of Mg-10Gd implants was lower *ex vivo* than *in vitro*, after 4 and 8 weeks of degradation. Similarly, the *3D-PF* of Mg-5Gd in bone for 8 weeks was lower than that calculated *in vitro*. We can explain it partly by the increased *DR*s *in vivo* compared to *in vitro*, and since *DR* is the denominator of the formula to calculate the *PF*, a higher *DR* results in a smaller *PF* even with equal pits depth in the samples.

On the contrary, Mg-5Gd implants at 4 weeks revealed higher *3D-PF* values *in vivo*, while still having higher *DR*s *in vivo* than *in vitro*. This may indicate that the pitting corrosion for these material in bone was significant in the early stages of degradation.

The *2D-mean PF*s was slightly lower *ex vivo* than *in vitro*, both at 4 and 8 weeks for both materials. However, the coefficient of variation (CV) of the *2D-PF* was higher *in vivo* than *in vitro*. It describes the variation in *2D-PF* between different slices of the screws, as it is reconstructed on SRµCT. In addition, we observed a higher *CV of 2D volume loss* of the *in vivo* degraded screws for both materials and time points. This parameter again described the variation of volume loss in different slices of the screws. It revealed a relevant intra-implant variation, because different regions of a same screw corroded differently, but did not display higher pitting factors. In other words, the amount of material degraded is more or less homogeneous when calculated in each slice, without deeper pits, but slices at different height of the screws showed different amount degradation.

This phenomenon is not surprising, considering the composition of the bone tissue in which the screws were immersed. Some parts of the screws were in contact with the hard and compact bone of the cortical region of the tibia, while other parts were exposed to the trabecular bone with more marrow spaces or even the marrow cavity, and therefore the vascularization and fluid exchange was different in these different regions. That could have induced different environments for corrosion. Moreover, areas of the screws in contact with the cortical layer of the rat tibia could have been exposed to different levels of strain, due to the movement of the rats, and that might have triggered more degradation. The screws degraded *in vitro* were all immersed in the cell culture media and were therefore less affected by localised corrosion.

Another observation was that the screws were qualitatively more degraded at the bottom and at the top. An explanation for the latter could be the fact that at these areas there is more implant surface being exposed to the surrounding. One could also argue that the pitting corrosion would be mostly visible in the early implantation stages, when the *MDD* values in the *PF* formula are the highest. However, we found a poor correlation between the *DR* and *3D-PF* of both alloys, and for that we assumed that even in the early stages the degradation homogeneity is not influenced by the higher *DR*s.

What concerns the osseointegration, both Mg-xGd alloys performed as good as the Ti implants, at least in the healing times investigated here. The *BIC* studied with both imaging methods of tomography and histology, confirmed high values for the Mg alloys and the Ti.

"Comparisons of *BIC* among different studies should be done with caution, as there is a lot of variability among experiments (for example the shape of the implant, the implantation site, as well as the scanning parameters). However, it seems that the current results are in line with other results in literature. The *3D-BIC(t)* of the current Mg-xGd alloys are similar to the *3D-BIC(t)*s of an AZ31 alloy and pure Mg implants presented in [182] after 4 weeks. After 12 weeks of healing time however, Mg-xGd alloys show a lower *3D-BIC(t)* of approximately 5% and 20% for AZ31 and pure Mg, respectively." [155]

For 4 and 12 weeks implantation time periods, the *3D-BIC(t)*s of Ti implants in [126], which were implanted in rat tibia as in our study, were at least 30% higher than in the present study. By contrast, *the 3D-BIC(t)*s of Mg-10Gd in this study were 5-10% higher than in [126].

"The lower *DR*s observed in this study, which resulted in lower amounts of produced hydrogen gas, could explain the higher *BIC* values for the studied Mg-xGd alloys. The hydrogen gas formation during the initial fast degradation in tissues, could be the reason for the lower amount of bone found in the surroundings of the Mg-xGd screws compared to the Ti implants after 4 and 8 weeks implantation (*BV/TV* values). In a previous study of Marco et al. [124], the *DR* (1.11 ± 0.05 mm/a) of a Mg-10Gd pin implant was much higher than the one of pure Mg (0.15 ± 0.03 mm/a) and Mg-2Ag (0.13 ± 0.04 mm/a) from the same study. However, the number of gas pockets detected *via* µCT after 7 days post-implantation with Mg-10Gd (0.23 ± 0.32 mm^3) was much lower than with pure Mg (3.4 ± 1.93 mm^3) and Mg-2Ag (6.52 ± 8.41 mm^3). As a reason for it was suggested, that the Mg-RE alloys, e.g. Mg-10Gd, can form hydrides in cuboid shape absorbing hydrogen from the environment [183–185]." [155]

However, in many images, newly formed bone was seen in proximity of degradation layers, but detached from them buy a thin gap, with the gap being completely empty and not stained with cells or tissues. We thought this might be an artefact of the critical point drying procedure. This new bone was probably less mineralized, and it might in fact have shrunk during the drying process, resulting in a thin gap between the bone and the implant. That suggests that the real *BIC* for the Mg alloys was probably higher in the living animal than what we measured *ex vivo*.

"When correlating the *3D-BIC* and *DR*, we found a moderately strong inverse correlation for the Mg-5Gd screws and a fair inverse correlation for the Mg-10Gd implants. This can be interpreted in two ways. In the first, we hypothesised that Mg-5Gd degradation was affected by the amount of the bone attached to the implant, with a lower *DR* when more bone was in contact with the implant surface. The reverse hypothesis was that the formation of a close connection of bone to the Mg-5Gd was stronger when the degradation rate was lower, possibly due to the less gas formation interfering with the attachment of bone cells to the surface. Both these phenomena were for some reasons more accentuated for Mg-5Gd than for Mg-10Gd.

Previous *in vivo* investigation utilizing Mg implants have suggested that Mg enhances the bone formation and mineralization compared to permanent implants [29, 186, 187] and the possible reasons for that have been mentioned either the release of Mg ions or / and the alkalization of the local environment during the degradation [126, 188, 189]. In addition, the degradation layers of Mg-alloys are rich in Ca and P ions, which are the same components of hydroxyapatite, the bone mineral matrix,

and therefore might be osteoconductive. In fact, our observation of an increasing amount of *3D-BIC(t)* and *3D-BV/TV(t)* with ongoing healing time would support the latter suggestion.

Additionally, the fair and poor correlation of *3D-BIC* to *3D-PF* of Mg-5Gd and Mg-10Gd, respectively, indicate that a relatively high pitting factor does not interfere with the apposition of bone on the implant surfaces. Mg-10Gd are less vulnerable of degradation homogeneity from *BIC* in comparison to Mg-5Gd implants. However, the moderate strong and fair correlation of the *3D-PF* and *3D-BV/TV* for Mg-5Gd and Mg-10Gd implants could indicate the influence of the surrounding bone on the degradation homogeneity, more so for Mg-5Gd than for Mg-10Gd. Nevertheless, it has to be mentioned, that after elimination of the *3D-PF* outliers >30 of both materials, the correlations assimilated (correlation *3D-PF* to *3D-BIC*: -0.44 and -0.42 for Mg-5Gd and Mg-10Gd respectively; correlation *3D-PF* to *3D-BV/TV*: -0.55 and -0.45 for Mg-5Gd and Mg-10Gd respectively). The latter could indicate that the implant performance of both materials is more vulnerable for unexpected and/or different behaviour in the beginning of the implantation and are more similar in their performance after a certain period of implantation." [155]

"However, despite PEEK implants had significantly lower *BIC*s than the other materials, their *BV/TV*s and *BA*s were comparable and increased with the healing time. This suggested that all materials were gradually surrounded by bone, as a possible shielding form the richly vascularized medullar cavity. This bone was is tight contact with the 3 metals, including the areas of degradation layers for the Mg-alloys, but it was not with PEEK screws. This findings supports previous observations that PEEK does not support bone formation in direct contact with its surfaces as other implant materials like Ti do [190–193]. The strong and moderately strong correlation found between *3D-BIC* and *3D-BV/TV* for Mg-5Gd, Mg-10Gd suggested that for these materials the presence of more bone tissue in the proximity of the implants increased the probability that this bone was in contact with the implant surfaces.

However, the same moderate strong correlation is also found for the PEEK implants, which displayed overall low *3D-BIC*. The observed very poor correlation for the Ti implants, suggests there is no increasing implant stability over the implantation period for Ti screws, if high initial *3D-BIC* correlates to implant stability. The latter can be explained with the fact, that Ti has already very high *BV/TV* values after 4 weeks healing.

Additionally, the much more homogeneous distribution of the *BIC* in Mg-xGd and Ti implants (with increasing homogeneity with the implantation time period) in comparison to PEEK leads us to assume a more reliable and more homogeneous osseointegration of these implants." [155]

"The formation of the new bone and the ingrowth of the bone into the degradation layer, the complete bone integration of the detached debris of degradation layers for Mg-10Gd alloy, as well as the new bone formation in the environment of Ti implants have been already qualitatively observed in [126]. We confirmed this finding by a quantitative analysis of the distance and the integration of the fractured degradation layer into the bone. We could assume that the brittle behaviour of the degradation layers did not undermine the implant stability. In addition, the encapsulation of the newly formed degradation layers into bone suggest that the integrity and stability of the Mg-xGd implants did not decrease over time." [155]

Finally, it should be noted that SRμCT displays advantages in terms of the quantification of osseointegration over the gold-standard technique of histology, as it allows for a more comprehensive evaluation in 3D. A big advantage of the μCT investigation of the implant degradation in comparison to the histology is the possibility of gaining information on the degradation of the implant in 3D volume without the risk of the investigated 2D slice not being representative for the entire implant in case of histological investigation [194]. Additionally, the 3D volumetric data are opening possibilities for analysing the degradation homogeneity of the implant not just qualitatively, but also quantitatively over the whole implant, by parameters like pitting factor, which usually is being determined on the bulk material and not on the implant itself, which might be a reason for the differences in the results.

5.3 Image Processing and Analysis

One of the major parts of this work was the image segmentation as a part of image processing, which is a precondition to the image analysis. The duty of image segmentation in this work was the separation of the tomographed *in vitro* or *ex vivo* degraded screw and the degradation layer, as well as the the bone surrounding the *ex vivo* degraded screw. The most easy way of segmentation *via* thresholding technique couldn't be chosen as the only image segmentation in this work, due to the similarities of the linear attenuation coefficients of the bone, the degradation layer and the residual screw.

However, after evaluating a semi-automatic segmentation workflow, its efficiency and accuracy was not satisfying. For a proper segmentation of one data set at least 3 days of work were necessary.

The highest difference up to 325% is observed in the parameter *CV-PF*. A possible explanation for this high difference between the *PF* variations through the slices among the implant could be the following: during the manual segmentation on each third slice the deepest pit is being correctly segmented and the transition from slice to slice is being smooth. The smooth transition from slice to slice might be missing when segmenting only few (max. 10) slices semi-automatically and applying watershed on between the slices. Differences up to 50% for *BIC* and 46% for *MDD* were calculated when analyzed the same dataset once segmented completely manually (very time consuming, ca. 2 weeks, but precise) and than semi-automatically, *via* workflow. The explanation of this high difference in *BIC* might be found when thinking of the *BIC* definition: it is defined as one-pixel area between the bone and the implant. Hence a one pixel difference in the segmentations of the among the whole screw in all directions might result in a 100% difference in parameter *BIC*.

The next noticeably changed parameter is the *DR* for the *in vivo* degraded Mg-5Gd screw. The noticeable change of the *DR* of *in vivo* degraded Mg-5Gd screw when on the data then treated with different operatons could be the following: since the Mg-5Gd screw degraded 12 weeks, there might be several parts of the degradation layer, which might be easily encapsulated/attached from/to the residual screw *via* the shrinkage or the growing operations of the screw. By encapsulatind or attaching areas to or from the residual screw the calculated *DR* can be sctrongly effected. However, although these values are not being mathematically considered in the interpretation of the results, they should be kept in mind when making conclusions.

Additionally, differences in the analysis results were obtained depending on the person segmenting the data. A difference of up to $\approx 60\%$ for the label degradation layer in the coefficient of variation is found. This high difference can be expected

since the grey values between the residual screw and the corrosion layer are sometimes very similar and very subjective for different people to distinguish with their naked eye. The same reason might cause also the second high coefficient of variation in the "residual screw" ($\approx$ 40%). The effect is higher in the "degradation layer" since it has in overall less area than the "residual screw".

Furthermore, it was observed, that some analysis parameters are more sensitive towards the chosen image processing method. As the most sensitive parameter towards image processing method was noticed the *3D-BIC*. Interestingly, it was most influenced by the processind method change for the PEEK screw and not for the Mg-5Gd screw. This might be due to the fact, that PEEK implants had the lowest *BIC* values in comparison to the other implants. However, they had *BV/TV* comparable to the other implants. Hence, by small changes in the processing method (smoothing, growing or shrinking) the amount of contact between the bone and the implant can be easily changed.

After evaluating the importance of a good image segmentation to the analysis parameters a deep machine learning segmentation approach was found. Due to the huge amount of the samples, this machine learning segmentation was applied to all the Mg-Gd alloy datasets resulting in an enormous time saving and in an even more precise results than with manual segmentation.

5.4 Push-Out Experiments

The evaluation of the forces between the bone and the Mg-xGd alloy implants was performed *via* push-out experiments.

Already on the first push-out experiment on the influence of Mg^{2+} ions on the implant-bone interfacial shear strength was shown, that the intefacial shear strength was significantly higher in magnesium ion beam-embedded hydroxyapatite coated TiAlV rods than in ordinary hydroxyapatite controls 6 weeks after implantation in rabbits [195]. Also in the next push-out experiment of Mg and Ti alloy rods the same tendency was reported by Castellani et al. [196]. The latter research also indicated, that the increase of the maximum push-out force, ultimate shear strenth and energy absorption to failure was significant in Mg rods between 4 and 12 weeks, while *BIC* and *BV/TV*, which indicate the osseointegration, showed no significant changes.

The above observations of Castellani et al. [196] can not be confirmed by the preliminary push-out results of the current study. The maximum force for the failure of the Mg-5Gd implant after 12 weeks *in vivo* degradation was approx. 50% smaller than the maximum force for the failure of the Ti implant after 12 weeks *in vivo* degradation. On the other hand, *BIC* and *BV/TV* of Mg-5Gd and Ti alloy implants showed no significant differences after 12 weeks *in vivo* degradation. However, the reason for this disagreement can be the fact, that Castellani et al. [196] were investigating rods, but in this study actual screws were used. Further analysis of the push-out data is taking place and an extensive comparison of the results with the literature will be performed.

In this experiments special attention was paid to the X-ray dose, which was used for the explants tomography. Previously, Barth et al. [197, 198] showed, that at about 35 kGy irradiation dose the strength, ductility and fracture resistance of the human bone start to degrade and at ca. 70 kGy the bone plasticity is strongly reduced. Since a typical high quality tomogram acquired at synchrotron radiation facility easily reaches 1 MGy of irradiation dose (pixel size ca. 1 µm) the data acquisition had to be optimized for the push-out experiments to reduce the dose.

Chapter 6

Conclusions and Perspectives

In this study, two Mg-xGd alloys (Mg-5 wt.% Gd and Mg-10 wt.% Gd) were investigated *in vitro* and *ex vivo* in terms of their degradation rate and degradation homogeneity for short and long immersion times. We made use of a non-destructive 3D analysis using micro-computed tomography yielding not only the volume loss measurements but also allowing to access further parameters describing the homogeneity of the degradation in a qualitative and quantitative way. The multitude of the analyzed parameters allowed to investigate the degradation from various angles of vision.

With respect to the evaluation of the degradation and osseointegration of implants, SRµCT is advantageous over the standard technique of histology, as it allows for a more comprehensive and non-destructive evaluation. In general, SRµCT allows to assess parameters such as the degradation homogeneity or the pitting factor not only on a few, possibly not-representative slices, but throughout the entire sample qualitatively, quantitatively, and in 3D [194].

In particular the pitting factor calculations enable the quantitative analysis of the degradation homogeneity and are advantageous over sole weight or volume loss measurements. PEEK and Ti served as reference materials in the *ex vivo* experiments, hence it was possible to underline the material-dependent differences in the implants osseointegration, with parameters like bone to implant contact area and bone volume fraction around the implants.

Acceptable degradation rate and degradation homogeneity of the investigated Mg-xGd alloys was confirmed in the current study. Those Mg alloys reveal osseointegration similar to the golden standard Ti implants. On the other hand, the poor osseointegration of PEEK implants could also be confirmed. A clear assumption about the advantages or disadvantages of any of investigated Mg-xGd implants could not be made out of the results of this study. However, on balance, our study suggests Mg-10Gd to be the alloy of choice, since it has an overall lower degradation rate, more homogeneous microstructure and a weaker texture than Mg-5Gd.

Whether or not the high *BIC*s and *BV/TV*s of the observed Mg-xGd alloys are really indicators for more stable implants, is the topic of investigation as part of an ongoing study. In the mentioned study on the same four explant types investigated in current study are push-out experiments applied.

With respect to the methods, the importance of the propriate image processing was quantitatively highleted, the sensitive parameters were evaluated. Additionally, the significance of the automatic segmentation was underlined, which lead to successful development of machine learning approaches.

Chapter 7

Publications, Their Content and Own Contribution

1. Diana Krüger, Berit Zeller-Plumhoff, Björn Wiese, Sangbong Yi, Marcus Zuber, D C Florian Wieland, Julian Moosmann, and Regine Willumeit-Römer. "Assessing the microstructure and in vitro degradation behavior of Mg-xGd screw implants using µCT". in: *Journal of Magnesium and Alloys* (2021)
   Abstract: Biodegradable implants are taking an increasingly important role in the area of orthopaedic implants with the aim to replace permanent implants for temporary bone healing applications. During the implant preparation process the surface and microstructure of the material is being changed by forces and stresses induced by the machining. Hence degradable metal implants need to be fully characterized in terms of the influence of machining on the resulting microstructure and corrosion performance. In this study, micro computed tomography (µCT) is used for the quantification of the degradation rate of biodegradable implants. For the first time quantitative measures are introduced to describe the degradation homogeneity in 3D. Two magnesium gadolinium alloys, Mg-5Gd and Mg-10Gd (in weight %), in the shape of M2 headless screws have been investigated for their microstructure and their degradation performance over a 1 - 56 day period. For microstructure investigations optical microscopy, electron backscatter diffraction (EBSD) and µCT have been used. Particular attention was paid to the localized deformation of the alloys, due to the machining process. *In vitro* immersion testing has been performed to assess the degradation performance which was quantified by subsequent weight loss and by volume loss (using µCT) measurements. Furthermore, the influence of microstructure variation on localized degradation in implant screws has been determined. This enables a prediction in terms of implant stability during the degradation in the body. Due to its lower degradation rates, its more homogeneous microstructure and degradation performance, and because of its weaker texture, extruded Mg-10Gd emerges as a more suitable as implant material than Mg-5Gd.
   Own contribution: Data segmentation, Evaluation of analysis parameters, Data analysis, Participation in the beamtimes, Participation in the conceptual design of the experiments

2. Diana Krüger, Silvia Galli, Berit Zeller-Plumhoff, D C Florian Wieland, Niccolò Peruzzi, Björn Wiese, Philipp Heuser, Julian Moosmann, Ann Wennerberg, and Regine Willumeit-Römer. "High-resolution ex vivo analysis of the degradation and osseointegration of Mg-xGd implant screws in 3D". in: *Bioactive Materials* (2021)

Abstract: Biodegradable materials are getting more attention in the orthopaedic surgeries. Hence, it is essential to investigate the used alloys in terms of microstructure and corrosion performance both *in vitro* and *in vivo* due to the implants' performance differences in these different environments. In this regard, next to the degradation velocity, also the degradation homogeneity of the implants and their osseointegration into the host tissue are important parameters. Two magnesium gadolinium alloys (Mg-5 weight% Gd and Mg-10 weight% Gd) in the shape of M2 screws as implant materials and titanium and PEEK implants as references, have been investigated towards their *in vivo* degradation performance and bone to implant interaction *via* synchrotron radiation micro computed tomography and histology. Additional comparisons previously performed *in vitro* degradation investigations of the same implants are performed. Our results show, that Mg-5Gd is degrading faster and more inhomogeneously than Mg-10Gd. The implant to bone contact area of the Mg-xGd implants are likewise to the one of the golden standard titanium implants. In combination with the suggested implant stability over the time in the bone, it is concluded that the 2 Mg-xGd alloys are suitable as implant materials in bone. In contrast, the PEEK implants showed much lower bone to implant contact for all investigated time points than Mg-xGd and/or titanium implants.
Own contribution: Data segmentation, Evaluation of analysis parameters, Data analysis, Participation in the beamtimes, Participation in the conceptual design of the experiments

3. Julian Moosmann, D C Florian Wieland, Berit Zeller-Plumhoff, Silvia Galli, Diana Krüger, Alexey Ershov, Silke Lautner, Julian Sartori, Mason Dean, Sebastian Köhring, Hilmar Burmester, Thomas Dose, Niccoló Peruzzi, Ann Wennerberg, Regine Willumeit-Römer, Fabian Wilde, Philipp Heuser, Jörg U Hammel, and Felix Beckmann. "A load frame for in situ tomography at PETRA III". in: vol. 11113. 2019, p. 1111318
Abstract: A load frame for in situ mechanical testing is developed for the microtomography end stations at the imaging beamline P05 and the high-energy material science beamline P07 of PETRA III at DESY, both operated by the Helmholtz-Center Hereon. The load frame is fully integrated into the beamline control system and can be controlled *via* a feedback loop. All relevant parameters (load, displacement, temperature, etc.) are continuously logged. It can be operated in compression or tensile mode applying forces of up to 1 kN and is compatible with all contrast modalities available at IBL and HEMS i.e. conventional attenuation contrast, propagation based phase contrast and differential phase contrast using a grating interferometer. The modularity and flexibility of the load frame allows conducting a wide range of experiments. E.g. compression tests to understand the failure mechanisms in biodegradable implants in rat bone or to investigate the mechanics and kinematics of the tessellated cartilage skeleton of sharks and rays, or tensile tests to illuminate the structure-property relationship in poplar tension wood or to visualize the 3D deformation of the tendonbone insertion. We present recent results from the experiments described including machine-learning driven volume segmentation and digital volume correlation of load tomography sequences.
Own contribution: Preparation of the sample holders, Participation in the beamtimes

4. Berit Zeller-Plumhoff, Carina Malich, Diana Krüger, Graeme Campbell, Björn

Wiese, Silvia Galli, Ann Wennerberg, Regine Willumeit-Römer, and D C Florian Wieland. "Analysis of the bone ultrastructure around biodegradable Mg–xGd implants using small angle X-ray scattering and X-ray diffraction". In: *Acta biomaterialia* 101 (2020), pp. 637–645

Abstract: Magnesium alloys are increasingly researched as temporary biodegradable metal implants in bone applications due to their mechanical properties which are more similar to bone than conventional implant metals and the fact that Magnesium occurs naturally within the body. However, the degradation processes *in vivo* and in particular the interaction of the bone with the degrading material need to be further investigated. In this study we are presenting the first quantitative comparison of the bone ultrastructure formed at the interface of biodegradable Mg–5Gd and Mg–10Gd implants and titanium and PEEK implants after 4, 8 and 12 weeks healing time using two-dimensional small angle X-ray scattering and X-ray diffraction. Differences in mineralization, orientation and thickness of the hydroxyapatite are assessed. We find statistically significant ($p < 0.05$) differences for the lattice spacing of the (310)-reflex of hydroxyapatite between titanium and Mg–xGd materials, as well as for the (310) crystal size between titanium and Mg–5Gd, indicating a possible deposition of Mg within the bone matrix. The (310) lattice spacing and crystallite size further differ significantly between implant degradation layer and surrounding bone ($p < 0.001$ for Mg–10Gd), suggesting apatite formation with significant amounts of Gd and Mg within the degradation layer.

Own contribution: Participation in a beamtime

5. Niclas Bockelmann, Diana Krüger, D C Wieland, Berit Zeller-Plumhoff, Niccoló Peruzzi, Silvia Galli, Regine Willumeit-Römer, Fabian Wilde, Felix Beckmann, Jörg Hammel, Julian Moosmann, and Matthias P. Heinrich. "Sparse annotations with random walks for u-net segmentation of biodegradable bone implants in synchrotron microtomograms". In: *arXiv preprint arXiv:1908.04173* (2019)

   Abstract: Currently, most bone implants used in orthopedics and traumatology are non-degradable and may need to be surgically removed later on e.g. in the case of children. This removal is associated with health risks which could be minimized by using biodegradable implants. Therefore, research on magnesium-based implants is ongoing, which can be objectively quantified through synchrotron radiation microtomography and subsequent image analysis. In order to evaluate the suitability of these materials, e.g. their stability over time, accurate pixelwise segmentations of these high-resolution scans are necessary. The fully-convolutional U-Net architecture achieves a Dice coefficient of 0.750 ± 0.102 when trained with a small dataset with dense expert annotations. However, extending the learning to larger databases would require prohibitive annotation efforts. Hence, in this work we implemented and compared new training methods that require only a small fraction of manually annotated pixels. While directly training on these scribble annotation deteriorates the segmentation quality by 26.8 percentage points, our new random walk-based semi-automatic target achieves the same Dice overlap as a dense supervision, and thus offers a more promising approach for sparse annotations.

   Own contribution: Segmentation of the input data for machine learning approach

6. Eshwara Phani Shubhakar Nidadavolu, Diana Krüger, Berit Zeller-Plumhoff,

Domonkos Tolnai, Björn Wiese, Frank Feyerabend, Thomas Ebel, and Regine Willumeit-Römer. "Pore characterization of PM Mg–0.6 Ca alloy and its degradation behavior under physiological conditions". In: *Journal of Magnesium and Alloys* (2020)

Abstract: Several material parameters affect degradation characteristics of Mg and its alloys under physiological conditions. Porous Mg materials are interesting for their simultaneous degradation and drug delivery capabilities. However, an increase in pore surface area is detrimental to both degradation resistance and subsequent mechanical properties. The present work aims at determining the threshold porosity value in Mg–0.6Ca specimens produced by powder metallurgy (PM) below which low degradation rates persist with acceptable mechanical properties. Seven different porous Mg–0.6Ca specimens containing both closed and open pore structures were fabricated with porosities ranging from 3% to 21%. Degradation profiles were obtained *via* a semi static immersion test over 16 days under physiological conditions using Dulbecco's modified Eagle's medium with Glutamax and 10% fetal bovine serum as supplements. The results are related to morphological pore parameters like pore size distribution, pore interconnectivity and pore curvatures that were quantified using an ex situ µCT analysis. In general, with decreasing porosity a decrease in pore interconnectivity is seen followed by rounding of the pores. Low degradation rates (MDR < 0.3 mm/year) are observed in specimens until 10% porosity, however, the upper bound for reproducible degradation is observed to be in specimens until 12% porosity. This porosity level also marks the transition from closed to open pore nature with a simultaneous change in pore interconnectivity from less than 10% to greater than 95%, below and above this porosity level, respectively. The tensile strength and elongation to failure recorded for specimens with 10% porosity were 70 MPa and 2%, respectively displaying positive traits of both homogenous degradation and mechanical properties. The results suggest that high pore interconnectivity is the dominant factor controlling degradation and mechanical properties in porous Mg-0.6Ca specimens. The results also indicate a good sintering response of Mg-0.6Ca specimens providing further material development towards biomaterial applications.

Own contribution: Aquisition of tomographic data, Support in the segmentation of tomographic data, Support in the analysis of tomographic data

7. Mohammadreza Taale, Diana Krueger, Emmanuel Ossei-Wusu, Fabian Schuett, Muhammad Atiq Ur Rehman, Yogendra Kumar Mishra, Janik Marx, Norbert Stock, Bodo Fiedler, Aldo R Boccaccini, Regine Willumeit-Römer, Rainer Adelung, and Christine Selhuber-Unkel. "Systematically Designed Periodic Electrophoretic Deposition for Decorating 3D Carbon-Based Scaffolds with Bioactive Nanoparticles". In: *ACS Biomaterials Science and Engineering* 5 (9 2019), pp. 4393–4404

Abstract: The coating of porous scaffolds with nanoparticles is crucial in many applications, for example to generate scaffolds for catalysis or to make scaffolds bioactive. A standard and well-established method for coating surfaces with charged nanoparticles is electrophoresis, but when used on porous scaffolds, this method often leads to a blockage of the pores so that only the outermost layers of the scaffolds are coated. In this study, the electrophoretic coating process is monitored in situ and the kinetics of nanoparticle deposition are investigated. This concept can be extended to design a periodic

electrophoretic deposition (PEPD) strategy, thus avoiding the typical blockage of surface pores. In the present work we demonstrate successful and homogeneous electrophoretic deposition of hydroxyapatite nanoparticles (HAn, diameter $\leqslant$ 200 nm) on a fibrous graphitic 3D structure (ultralightweight aerographite) using the PEPD strategy. The microfilaments of the resulting scaffold are covered with HAn both internally and on the surface. Furthermore, protein adsorption assays and cell proliferation assays were carried out and revealed that the HAn-decorated aerographite scaffolds are biocompatible. The HAn decoration of the scaffolds also significantly increases the alkaline phosphatase activity of osteoblast cells, showing that the scaffolds are able to promote their osteoblastic activity.
Own contribution: Aquisition of tomographic data, Segentation of tomographic data, Analysis tomographic data

8. Ivo M Baltruschat, Hanna Cwieka, Diana Krüger, Berit Zeller-Plumhoff, Frank Schlünzen, Regine Willumeit-Römer, Julian Moosmann, and Philipp Heuser. "Scaling the U-net: segmentation of biodegradable bone implants in high-resolution synchrotron radiation microtomograms". In: *Scientific reports* 11 (1 2021), pp. 1–10
Abstract: Highly accurate segmentation of large 3D volumes is a demanding task. Challenging applications like the segmentation of synchrotron radiation microtomograms (SRµCT) at high-resolution, which suffer from low contrast, high spatial variability and measurement artifacts, readily exceed the capacities of conventional segmentation methods, including the manual segmentation by human experts. The quantitative characterization of the osseointegration and spatio-temporal biodegradation process of bone implants requires reliable, and very precise segmentation. We investigated the scaling of 2D U-net for high resolution grayscale volumes by three crucial model hyperparameters (i.e., the model width, depth, and input size). To leverage the 3D information of high-resolution SRµCT, common three axes prediction fusing is extended, investigating the effect of adding more than three axes prediction. In a systematic evaluation we compare the performance of scaling the U-net by intersection over union (IoU) and quantitative measurements of osseointegration and degradation parameters. Overall, we observe that a compound scaling of the U-net and multi-axes prediction fusing with soft voting yields the highest IoU for the class "degradation layer". Finally, the quantitative analysis showed that the parameters calculated with model segmentation deviated less from the high quality results than those obtained by a semi-automatic segmentation method.
Own contribution: Data segmentation, Development of the workflow, Participation in the beamtimes

Appendix A

Publications to *In Vitro* and *Ex Vivo* Experiments

Available online at www.sciencedirect.com

ScienceDirect

Journal of Magnesium and Alloys 9 (2021) 2207–2222

www.elsevier.com/locate/jma

Full Length Article

Assessing the microstructure and *in vitro* degradation behavior of Mg-xGd screw implants using μCT

Diana Krüger[a,*], Berit Zeller-Plumhoff[a], Björn Wiese[a], Sangbong Yi[b], Marcus Zuber[c,d], D.C. Florian Wieland[a], Julian Moosmann[e], Regine Willumeit-Römer[a]

[a] *Institute of Metallic Biomaterials, Helmholtz-Zentrum Hereon, Max-Planck-Str. 1, Geesthacht 21502, Germany*
[b] *Institute of Material and Process Design, Helmholtz-Zentrum Hereon, Max-Planck-Str. 1, Geesthacht 21502, Germany*
[c] *Institute for Photon Science and Synchrotron Radiation, Karlsruhe Institute of Technology, Herrmann-von-Helmholtz-Platz 1, Eggenstein-Leopoldshafen 76344, Germany*
[d] *Laboratory for Applications of Synchrotron Radiation, Karlsruhe Institute of Technology, Kaiserstr. 12, Karlsruhe, Germany*
[e] *Institute of Materials Physics, Helmholtz-Zentrum Hereon, Max-Planck-Str. 1, Geesthacht 21502, Germany*

Received 30 January 2021; received in revised form 29 June 2021; accepted 22 July 2021
Available online 25 September 2021

Abstract

Biodegradable implants are taking an increasingly important role in the area of orthopedic implants with the aim to replace permanent implants for temporary bone healing applications. During the implant preparation process, the material's surface and microstructure are being changed by stresses induced by machining. Hence degradable metal implants need to be fully characterized in terms of the influence of machining on the resulting microstructure and corrosion performance.

In this study, micro-computed tomography (μCT) is used for the quantification of the degradation rate of biodegradable implants. To our best knowledge, for the first time quantitative measures are introduced to describe the degradation homogeneity in 3D. This information enables a prediction in terms of implant stability during the degradation in the body.

Two magnesium gadolinium alloys, Mg-5Gd and Mg-10Gd (all alloy compositions are given in weight% unless otherwise stated), in the shape of M2 headless screws have been investigated for their microstructure and their degradation performance up to 56 days. During the microstructure investigations particular attention was paid to the localized deformation of the alloys, due to the machining process. *In vitro* immersion testing was performed to assess the degradation performance quantified by subsequent weight loss and volume loss (using μCT) measurements.

Although differences were observed in the degree of screw's near surface microstructure being influenced from machining, the degradation rates of both materials appeared to be suitable for application in orthopedic implants. From the degradation homogeneity point of view no obvious contrast was detected between both alloys. However, the higher degradation depth ratios between the crests and roots of Mg-5Gd ratios may indicated a less homogeneous degradation of the screws of these alloys on contract to the ones made of Mg-10Gd alloys. Due to its lower degradation rates, its more homogeneous microstructure, its weaker texture and better degradation performance extruded Mg-10Gd emerged more suitable as implant material than Mg-5Gd.

Keywords: Magnesium alloys; Biodegradable implant; Degradation rate; Degradation homogeneity; Micro-comptued tomography.

1. Introduction

Magnesium (Mg) and its alloys are already successfully introduced into the clinics for example by the company "Syntellix AG" [1] as biodegradable temporary orthopedic implants due to their optimal strength and adjustable corrosion rate

* Corresponding author.
E-mail address: diana.krueger@hereon.de (D. Krüger).

https://doi.org/10.1016/j.jma.2021.07.029

[2,3]. The biodegradation of such implants during the healing period [4] would prevent a second, costly, and risky implant removal surgery after the fracture has healed. The requirement of biodegradation is fulfilled both by biodegradable metals and biodegradable polymers. However, it has been proven that the mechanical properties of biodegradable polymeric implants significantly decrease in physiological environments, thus limiting them as load bearing implants [2]. In addition to available zinc or iron-based metallic degradable implants, implants made of Mg alloys exhibit better implant stability. Mg alloys possess an increased biocompatibility along with the suppression of inflammatory cascades, tissue loss [5] and stress shielding effects which reduces the bone growth stimulation and bone remodeling [5]. Mg ions released in the body do not cause cellular toxicity if they are below a critical concentration and are expelled along with urine [6]. In addition, Mg is essential to human metabolism as a cofactor of many enzymes and facilitates tissue-healing [7].

Since pure Mg alone does not provide sufficient strength for load-bearing applications, alloying elements are added such that the mechanical properties of the alloys are suitable for implant applications. As a consequence of the alloying, the implant's density, elastic modulus, and yield strength can be tailored close to those of human bone [7]. The addition of rare earth elements (REE) to a high purity Mg matrix results in promising biodegradable Mg alloys. Such alloys exhibit sufficient strength and toughness, rendering them useable for load-bearing applications [8,9]. Significant effects of solid solution strengthening have been observed in Mg-gadolinium (Gd) alloys in particular [10]. When alloying Gd to Mg for application as implants, the toxicity of Gd and its possible harm has to be taken into account, since it can accumulate in animal organs [11,12]. However, it was previously shown that the release of Gd from Mg-xGd alloys is below the critical toxicity level and these alloys are suitable candidate for medical usage [13–16]. Additionally, Mg-10Gd alloys have displayed good cytocompatibility and were shown to improve the osteoblast-induced mineralization [17]. Previously it has been shown that the addition of up to 10 wt% (wt.%) Gd to the Mg-matrix decreased the degradation rate [18]. The degradation rate increased again when increasing the Gd content in the alloy. One of the important effects of REE on the corrosion resistance of Mg is the so-called "scavenger effect", which means that the influence of impurities in the Mg matrix, like iron (Fe), can be suppressed due to the formation of the intermetallic phases between the REE and the impurity [19,20]. Previously, gadolinium hydride (GdH_2) particles have been observed in Mg-Gd alloys [10]. They are being formed in presence of a hydrogen containing medium and after a sample deformation has taken place [21]. During the alloy production, potential hydrogen sources are Mg with its high hydrogen storage capacity [22], and contaminations of Mg or Gd with H-containing compounds. The agglomerations of GdH_2 may serve as small galvanic cells in the alloy.

Recently, Mg has been investigated as an alloying element in Fe-based implant material, where Mg played the role of the degradation accelerator [23]. Although degradation rates suitable for bone implants were achieved for the Fe-20Gd solid solution, prepared by mechanically driven supersaturation, it is less conventional and more complicated, than the currently presented casting of Mg-xGd alloys. Casting is the most common approach in Mg bone implants fabrication, since it enables the easy control of the alloy composition, it is convenient to operate and it is not expensive [24].

Depending on their mechanical properties and microstructure, the investigated implants reveal deformation zones and twinning zones differing in thickness as a result of machining. Previously, Gawlik [25] reported that during acidic etching of Mg-xGd a tendency of increased material removal from the surface with increasing Gd (2, 5 and 10 wt.% Gd content) is observed. It was hypothesized that the alloys' thicker twinning zone with lower Gd content might have slowed down the dissolution rate at early stages. Since the twinning zone of Mg-10Gd was smaller, the un-twinned bulk material would have been reached much faster.

Due to the influences of the alloy's microstructure on the implant's degradation performance, we aim to link the microstructure of Mg-xGd (x = 5 or 10 wt.%) implants after fabrication into a screw shape to their degradation velocity over 1–56 days in cell culture media using the advantages of non-destructive 3D imaging *via* μCT. The microstructure itself is investigated *via* electron backscatter diffraction (EBSD) and optical microscopy (OM).

Commonly, the investigation of the biodegradation is performed using weight loss experiments. Weight loss is one of the most low-cost and simple experiments that provides accurate and clearly defined data that is simple to set up, perform, and control [33]. However, this method's disadvantages are that it does not provide any information on the corrosion mechanism, the time-dependent corrosion behavior, and multiple samples are needed to have a sufficiently low statistical error. Liu [34] have already shown that degradation rates of different materials measured *via* weight loss and volume loss using μCT are similar. We are additionally exploring the potential of μCT to determine degradation parameters such as the pitting factor by using the full three-dimensional information, as previously demonstrated [35]. By calculating parameters both in 2D and 3D, we are able to study the localized degradation of implant screws non-destructively. This may allow a prediction in terms of implant stability during the degradation in the body.

2. Materials and methods

2.1. Materials / samples

Two Mg alloys with 5 and 10 wt.% Gd (Mg-5Gd, Mg-10Gd) were investigated in the current study. Melting and casting were performed by permanent mold direct chill casting using Ar + 3 vol.% SF_6 as shielding gas in the induction furnace (Typ K 10/S 1, Nabertherm, Lilienthal, Germany). 5 or 10 wt.% Gd was added to the Mg melt at 700 °C and stirred for 20 min with a rotation speed of 150 min^{-1}. The molten materials were then poured into a permanent steel

mold (diameter 110 mm, height 230 mm), which was preheated up to 680 °C and kept for 15 min. Afterwards, the ingots were cooled down by water quenching. They were solution heat treated (T4) at 525 °C for 6 h and cooled down again by water quenching. Indirect extrusion was performed with an extrusion ratio of 84 to the final diameter of 12 mm. A ram speed of 0.7 mm/s for Mg-5Gd and 0.52 mm/s for Mg-10Gd and a temperature of 400 °C were used for extrusion. Rods with a diameter of 3 mm were cut from the extruded bars *via* wire electrical discharge cutting. Finally, headless screws were machined by turning and by milling the slit. The screws measured 4 mm in length, 2 mm in diameter, had an M2 thread and a 0.5 × 0.5 mm slot.

2.2. Microstructural observations

Bulk material and screws were cold embedded in an epoxy resin (Demotec 30®, Demotec Demel e.K, Nidderau, Germany), manually grinded and polished for the microstructure analysis. The grinding process was performed from 500 to 2500 grit SiC sandpapers. The polishing was performed in two steps. First by using SiO_2 (OPS^{TM}, Cloeren Technology GmbH, Wegberg, Germany) with water (H_2O), H_2O-free lubricant (ethylene glycol to ethanol in parts of 10:7) and sodium hydroxide (NaOH) for approximately 5 min. Second by using H_2O-free SiO_2 (OPS^{TM}, Cloeren Technology GmbH, Wegberg, Germany), diamond particle suspension with a 0.25 μm particle size with H_2O-free lubricant (ethylene glycol to ethanol in parts of 10:7) for 15–20 min.

Following picric acid solution sample etching [36], observation of the microstructure was performed using an optical microscope (DMI5000 M, Leica, Wetzlar, Germany). The calculation of the grain sizes was performed on the bulk material, in longitudinal (extraction direction) and transversal direction of extrusion as well as on transversal sections of the screw *via* the linear intercept method. As analysis software "analySIS Pro" (version 5, Olympus Soft Imaging Solutions GmbH, Münster, Germany) was used.

For the calculation of the deformation layer thickness on the optical micrographs three regions (root, flank, and crest) were defined (see Fig. 3A). In these regions, the region near the surface with no definable grains or twins was separated from areas with visible grains or twins (see Fig. 3C and D). The thickness measurement of the layer with no recognizable grains was performed in Fiji (ImageJ) [25].

Fig. 1 shows the areas chosen for the investigation of the microstructural differences between the bulk (210 × 195 μm^2) and surface near area of the screw, within the crests (310 × 200 μm^2) and the roots (310 × 200 μm^2) in particular. EBSD (SEM: Zeiss Crossbeam 550, EBSD detector: Oxford Symmetry) measurements were performed on one screw per material (1.5 pitches of the screws, whereby a pitch is the distance from the crest of one thread to the next crest). The EBSD image quality maps were used for the quantification of three different twin types (tensile, compression, and secondary twins). The twin type depends on its angle to the crystal's c-axis (tensile twins: ≈ 86°, compression twins: ≈ 56°, secondary twin: ≈ 38°) [37,38]. Also, the pole figure of each scanned area was obtained. The deformed microstructures' features were studied by analyzing boundary characteristics and misorientation among neighboring measuring points (pixel size or "step size" = 0.4 μm). The kernel average misorientation (KAM), which represents the average misorientation between each pixel and its nearest neighbors, was calculated to study the subgrain structures. These are indicators of the strain locally accumulated at the corresponding area.

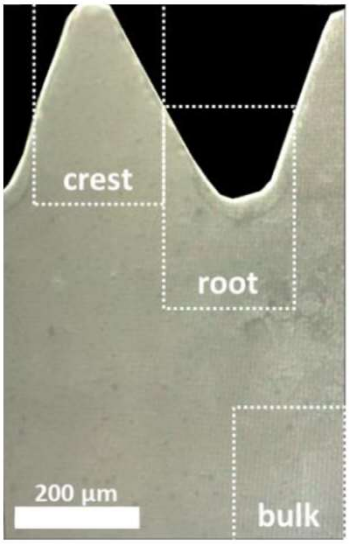

Fig. 1. Exemplary areas of bulk, crests and roots on a Mg-5Gd screw for the EBSD measurements.

2.3. Immersion tests

The degradation rate (*DR*) was determined over a (i) short durations (1, 3, 6, 7 and 9 days) and over two longer duration periods ((ii) 7, 14, 21, and 28 days and (iii) 28, 56 days) as a result of a semi-static immersion experiment. For experiments (i) and (ii) degradation medium α-Minimum Essential Medium (α-MEM; Thermo Fisher Scientific GmbH, Darmstadt, Germany) + 10% Fetal Bovine Serum (FBS; PAA Laboratories, Linz, Austria) + 1% Penicillin/Streptomycin (Thermo Fisher Scientific GmbH, Darmstadt, Germany) was used. For experiment (iii) the α-MEM was replaced with DMEM (Dulbecco's Modified Eagle's Medium) to verify the small difference in the implant's degradation behavior in these two media.

The immersion test was performed under cell culture conditions (37 °C, 5% CO_2, 20% O_2, 95% relative humidity). To avoid saturation, the medium was changed every 2–4 days. The number of samples used for the weight loss and volume loss measurements per time point can be found in Table 6.

2.4. Micro-computed tomography (μCT)

Prior to immersion testing, the screws were imaged using a laboratory μCT (Phoenix Nanotom GE inspection and

Table 1
Segmentation methods and used softwares.

Experiment	Immersion time	Tomography device / pixel size [μm]	Denoising	Denoising parameters	Segmentation method / software
i, ii, iii	0 time point	Nanotom / 2.5	No filter	–	Threshold / Fiji (ImageJ) [44]
i, ii	1–9 days, 7–28 days	DESY, IBL P05 / 2.6 KIT / 2.4	Non-local means [45,46]	sigma=15, smoothing factor=1	Watershed / Avizo version 9.4.2 (Thermo Fisher Scientific, Waltham, MA)
iii	28–56 days	Nanotom / 2.5	Mean 3D [47]	3 × 3 × 3	Threshold / Fiji (ImageJ) [44]

sensing technologies, Wunstorf, Germany) at an operating voltage of 100 kV at 70 µA current (binned pixel size: ≈ 2.5 µm). Following the immersion tests and removal of the degradation layer by chromic acid treatment, the degraded screws from immersion test (ii) have been imaged either at the imaging beamline (IBL) P05 [39], which is operated by the Helmholtz-Zentrum Hereon, at the PETRA III storage ring at the Deutsches Elektronen-Synchrotron (DESY) (energy: 25–30 keV, binned pixel size: ≈ 2.6 µm) or at the TOPO-TOMO beamline of the KARA synchrotron facility at the Karlsruhe Institute of Technology (KIT) (energy: filtered white beam - max. intensity at 16 keV), binned pixel size: ≈ 2.4 µm. The degraded screws from test (iii) have been imaged using the laboratory µCT after removing the degradation layer using the same treatment as described above. Additional information on the imaging parameters can be found in Table 9 in the appendices. For tomographic reconstruction at IBL, filtered backprojection (FBP) was used employing the ASTRA toolbox for the backprojection [40]. Data pre-processing and tomographic reconstruction was done using the tomographic reconstruction pipeline at IBL [41,42].

2.5. Image processing

Depending on the image quality, the segmentation was either performed on the original dataset or after the application of a filter. The chosen image filters, filter parameters, segmentation software, and method are presented in Table 1. Prior to the analysis registration of the corroded and not corroded implants on each other and an alignment to the z-axis of the 3D data parallel to the longitudinal axis of the screw were necessary; for an example of a transverse view see Fig. 7. The image registration procedure determines the parameter values of a rigid body transformation to match an image to a reference image [43]. The registered datasets are then resampled onto a common coordinate system with a voxel size of 5 µm. Resampling is the next step to the registration, which is the object's actual transformation according to the determined parameters. All registration and resampling steps were performed in Avizo.

The quantitative degradation parameters, as described in Sections 2.6 and 2.7, have been investigated in 2D and 3D, respectively. Degradation rate (*DR*) (described in Section 2.6) and mean degradation depth (*MDD*) (described in Section 2.7) were only calculated in 3D, volume loss only in 2D and pitting factor (*PF*) in 3D and in 2D . The same formulae of the 3D calculations were used in 2D calculations on each slice, resulting in statistical mean and standard deviation values for one sample.

2.6. Degradation rate (DR)

The *DR* for each immersion period was calculated with two methods: (1) weight loss and (2) volume loss measurements. The weight loss was measured *via* weighing the screws before immersion and after removal of the degradation layer with chromic acid. The volume loss, following µCT imaging, was determined *via* calculation of the screw volume before immersion and after removal of the degradation layer. Based on weight loss and volume loss measurements, the degradation rate was calculated as [48]:

$$DR\ [mm/a] = \frac{\Delta m}{A \cdot \rho \cdot t} = \frac{\Delta V}{A \cdot t} \quad (1)$$

where Δm [g] denotes the sample weight loss, ΔV the sample volume loss, A [cm^2] the initial surface area, ρ the material density ($\rho_{Mg-5Gd} = 1.81$ g/cm^3, $\rho_{Mg-10Gd} = 1.87$ g/cm^3), and t the immersion time. For the weight loss measurements, a high precision balance (MYA 2.4Y Microbalance, Radwag Balances and Scales, Radom, Poland) was used. The volume from the µCT investigations was calculated with software Fiji (ImageJ) [44] and Avizo version 9.4.2 (Thermo Fisher Scientific, Waltham, MA). For the weight loss (WL) calculations, the surface area of the screws was assumed to be the same for all screws and was theoretically calculated based on construction drawing ($A = 0.4125$ cm^2). For the volume loss (VL) measurements, the surface area of each screw was calculated with Avizo from the measured data.

For comparison with the literature, under the assumption of a uniform degradation, the mean degradation depth (*MDD*) for each immersion time was calculated by [48]:

$$MDD\ [\mu m] = DR \cdot t \quad (2)$$

It has been previously observed, that with increasing exposure times within one experimental setup the *DR* was always decreasing ([48,49,50]). Assuming a linear mean degradation depth increase with increasing exposure time a straight regression line was fitted to the *MDD* values. The slope of the fitted line is defined as the global degradation rate (*GDR* [mm/a]). The coefficient of determination (R^2), which is a measure of the proportion of variance of a predicted outcome [51], was determined for the fitted regression lines, *i.e. GDRs*. It reveals how well a linear regression model fits the experimental results, where the value 1 would correspond to a perfect fit of the data to the regression line.

2.7. Degradation homogeneity analysis

Pitting factor (in 2D and 3D), volume loss in 2D and crest/roots ratio were selected as analysis parameters describing the degradation homogeneity. These are described in more detail in the following and were calculated for samples degraded between 7 and 56 days.

Pitting factor (PF) in 2D and 3D

The pitting factor PF_i for a given slice i of a given volume of interest (VOI) is defined by [52]:

$$PF_i[a.u.] = \frac{DP_i}{MDD_i} \tag{3}$$

where DP_i and MDD_i are the deepest pit and the mean degradation depth within slice i, respectively, see Fig. 7C. Note that this calculation is only possible for the slices where the degradation layer does not reach the center of the screw. The mean and the standard deviation of the pitting factor in 2D is then calculated as:

$$2D\ mean\ PF\ [a.u.] = \overline{PF} = \frac{1}{N}\sum_{i=1}^{N} PF_i \tag{4}$$

$$2D\ std\ PF = \sqrt{\frac{1}{N-1}\sum_{i=1}^{N}\left(PF_i - \overline{PF}\right)^2} \tag{5}$$

where N is the number of analyzed image slices. For the calculation of the *3D-PF* Eq. (5) is used with *DP* [μm] being the deepest pit of the whole 3D implant and *MDD* that of the whole 3D implant. Compared to the other parameters describing degradation homogeneity, the 3D PF parameter depends only on the deepest pit along the whole screw. Thus, this parameter has a sensitivity to the global non-homogeneous degradation behavior among also the same alloys.

Volume loss

Volume loss defines the degraded volume per image slice and is the difference between the not-corroded and the corroded screw. It can differ from the "degradation layer", *i.e.* the layer of precipitates formed during the degradation process, since the volume of precipitates must not coincide with the degraded material, see Fig. 7. Volume loss is calculated for each slice i along the longitudinal axis of the screw as:

$$2D\ volume\ loss_i = (\#voxels_{ncs} - \#voxels_{rs})_i \cdot voxel\ size^3 \tag{6}$$

where the subscripts *ncs* and *rs* denote the not corroded screw and the residual screw, respectively (Fig. 7).

Gd-rich particles

To segment the Gd-rich particles in the 3D tomograms, automatic thresholding in Fiji (ImageJ) followed by removal of single-pixel large particles in Avizo was performed. The amount, size, and distribution of Gd-rich particles in both alloys was calculated with different parameters in the chosen volume-of-interest (VOI) measuring 480 × 480 × 960 μm^3: (1) the overall amount of detected Gd-rich particles; (2) overall volume of the Gd-rich particles [vol.%]; (3) smallest distance between two Gd-rich particles [μm]; (4) amount of detected outlier Gd-rich particles; (5) mean and standard deviation of the Gd-rich particles outliers from the 3D size distribution [μm^3], (6) median of the Gd-rich particles from the 3D size distribution [μm^3]; (7) mean Feret diameter [μm] and (8) max Feret diameter of the Gd-rich particles from the 2D size distribution. For the calculation of (3), a "Distance Transform 3D" was applied on the segmented 3D tomographic data in Fiji (ImageJ) [53]. As a result, each pixel of the image was labeled with the distance to the nearest obstacle pixel. After fitting a Poisson distribution to the histogram of the transformed images in MATLAB R2019b (The MathWorks Inc., USA), the minimum distance between two Gd-rich particles was determined. The outliers of the Gd-rich particles are determined in order to gain information about the largest Gd-rich particles. The calculation of the Feret diameter, which is a measure of an object's size along a specified direction [54] was performed in Fiji (ImageJ) using the "Particle Analyser" from Fiji (ImageJ)-Plugin BoneJ [55].

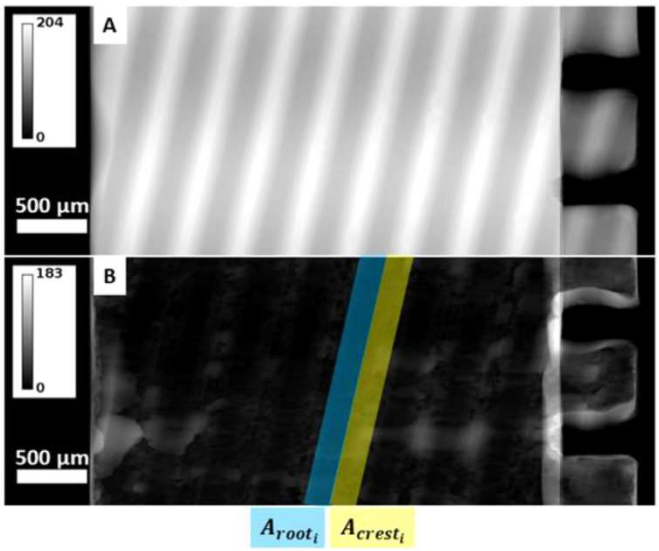

Fig. 2. 2D image of Mg-5Gd screw imaged using μCT (A) before degradation (not corroded screw), (B) difference layer thickness as defined in Eq. (7), after 56 days *in vitro* degradation; the color bar in the images shows the image depth in voxel.

Crest/Root ratio

In order to analyze the difference in localized degradation between crest and roots of the screw, the thickness variation of the difference layer was mapped to a 2D height profile using a customized Fiji script. Here, the difference layer thickness in voxels was encoded as a gray value, whereas the positions on the screw surface are given by x and y. For clarification, Fig. 2 shows a 2D height profile of a non-corroded Mg-5Gd screw (Fig. 2A) and difference layer (Fig. 2B) of the same screw after 56 days *in vitro* degradation. As illustrated in Fig. 2B, the ratio of difference layer thickness between crest and root areas (Eq. 8) was calculated:

$$\frac{Crests}{Roots} = \frac{G_{A_{crests}}}{G_{A_{roots}}} = \frac{\sum_1^N G_{A_{crests_i}}}{\sum_1^N G_{A_{roots_i}}} \tag{7}$$

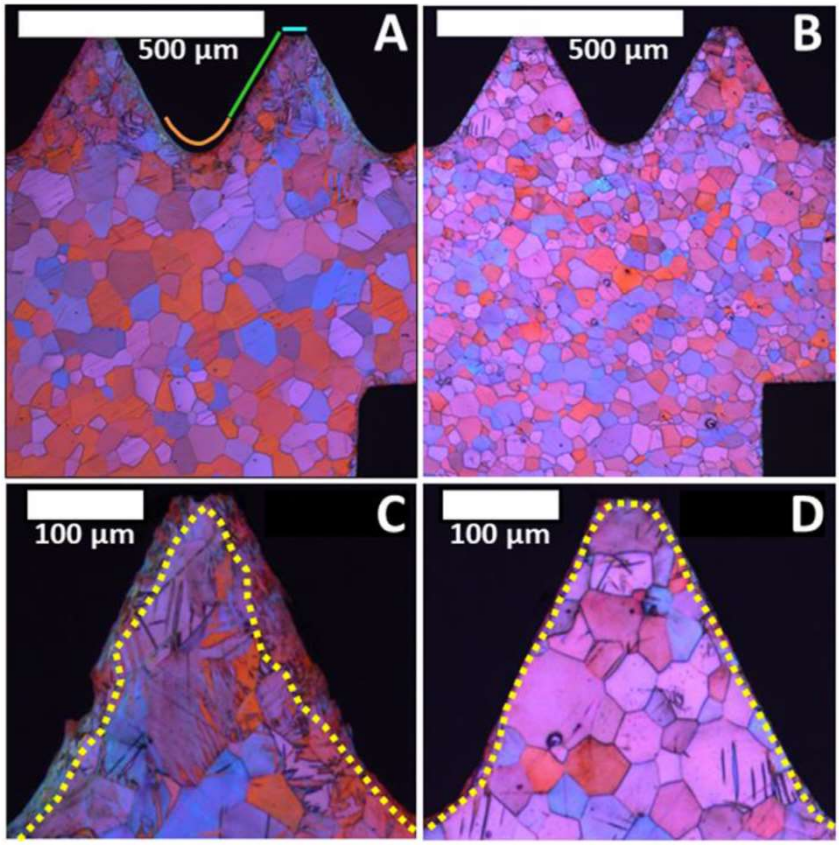

Fig. 3. Polarized optical micrographs of Mg-5Gd (A, C) and Mg-10Gd (D, B) screws, respectively. Markers in (A): orange - area of root, green - area of flank, blue - area of crest. Yellow dots in (C, D) separate the deformed layer from not deformed one.

where $G_{A_{crest_i}}$ and $G_{A_{root_i}}$ represent the sum of the gray values in one crest and root area, respectively (Fig. 2B). The determination of crests and roots was performed semi-automatically; the first crest area was determined manually (dimensions of A: $a = 43$ µm, $b = 365$ µm, $\alpha = 77°$) and all following crests and roots were defined automatically.

2.8. Statistical analysis

As a measure of the relative variation of the *PF* and the *volume loss* over the whole sample along its longitudinal axis the coefficient of variation (*CV*) of the *PF* for each sample was calculated *via* the division of the *2D-std PF* (Eq. (4)) ba the *2D-mean PF* (Eq. (3)) and *2D-std volume loss* by the *2D-mean volume loss* of each sample [56] in Fiji (ImageJ). A statistical significance *t*-test was performed on the results of Gd-rich particle's analysis. The volumetric size distribution was calculated using software package R 4.0.2 [57]. The calculations of the coefficient of determination (R^2) as well as all plots were also executed in MATLAB.

3. Results

3.1. Macro and microstructural analysis

The microstructure of Mg-5Gd and Mg-10Gd screws, obtained from polarized optical micrographs, are shown in Fig. 3. Mg-5Gd displays overall larger average grain size of 51.78 ± 10.91 µm and less homogeneous grain size distribution, whilst the average grain size of Mg-10Gd is significantly smaller and has a much narrower distribution (26.67 ± 1.30 µm) .

Table 2
Deformation layers thicknesses [µm] of processed Mg-xGd alloys in different areas of the screw.

	Deformation layer thickness [µm]	
	Mg-5Gd	Mg-10Gd
Roots	10.7 ± 3.1	9.2 ± 3.5
Crests	19.3 ± 6.6	7.8 ± 3.8
Flanks	12±4.9	4.9 ± 2

The deformation layer is defined as the near-surface region of the screw, where the machining process has influenced the microstructure and where no clear grain boundaries can be identified (Fig. 3C, D). Three threads (six flanks, three crests, and three roots – exemplarily marked in Fig. 3A) of one screw of each alloy were analyzed towards the deformation layer thickness. No noticeable difference is observed between the deformation layer thicknesses in the roots of both alloys, see Table 2. By contrast, Mg-5Gd reveals a deformation layer nearly 2.5 times as deep as Mg-10Gd on the crests and flanks of the threads as well as a significantly increased number of

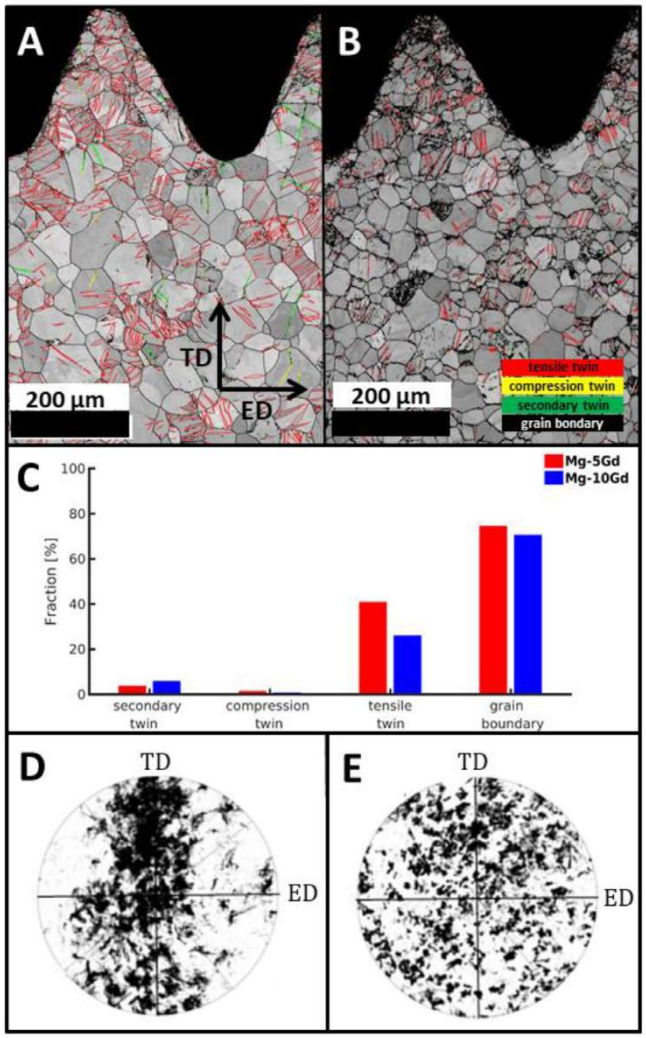

Fig. 4. EBSD IQ maps superimposed with the highlighted grain and twin boundaries of a Mg-5Gd (A) and a Mg-10Gd (B) screw and corresponding pole figures (D) and (E), respectively. The normal direction (ND) is perpendicular to the transverse direction (TD) and the extrusion direction (ED) of the sample. (C) Fraction of each type of boundary from the total detected boundaries in the selected area.

twins in the near-surface region of the threads compared to the Mg-10Gd screws.

Corresponding EBSD image quality (IQ) maps collected on representative crest and root areas of Mg-5Gd and Mg-10Gd screws are presented in Fig. 4. The EBSD IQ maps show similar microstructural features to the optical micrograph, with grain and twin boundaries. Fig. 4 also shows the quantification of these boundaries and the corresponding pole figures. According to the twinning types, the twin boundaries are marked with different colors corresponding to the misorientation relationships, *e.g.* tensile, compression and secondary twins. The discrete pole figures depicted in Fig. 4D and E, indicate that Mg-5Gd exhibit a stronger texture than Mg-10Gd, with the basal poles perpendicular to the extrusion direction (ED) and that Mg-10Gd shows a more homogeneous distribution of the crystal orientations.

Tensile twins are identified as the dominant mode in both alloys as the number of tensile twins is the greatest. The number of secondary twin boundaries is much smaller with 3.8% and 5.9% for Mg-5Gd and Mg-10Gd, respectively. For both alloys the smallest amount of boundaries are the compression twin boundaries, *i.e.* 1.5% for Mg-10Gd and 0.8% for Mg-10Gd.

The kernel average misorientation (KAM) is analyzed in three different areas, namely, bulk, crest and root as depicted in Fig. 5. Mg-5Gd shows a higher misorientation angle than Mg-10Gd, especially at the crest and root of the screw (see Table 3). The dislocation slip and its accumulation result in a relatively high misorientation in the deformed microstructure due to the lattice distortion from the geometrically necessary dislocations. In the present study, the area fraction of the deformed structure with a KAM of 4°∼5° at the 4th neighboring points, *i.e.* at a distance of 1.6 µm, is compared to both alloys (Table 3). The higher area fractions of the deformed structure are found in different areas in Mg-5Gd. The crest, root, and bulk of Mg-5Gd exhibit about 50%, 38%, and 24%, respectively, more deformed area than that of Mg-10Gd. The difference in the fraction of the highly deformed area between the crest and the implants' bulk is approximately 27% for Mg-5Gd and 13% for Mg-10Gd.

SRµCT slices and 3D renderings after segmentation of the Gd-rich particles in a volume-of-interest (VOI) of Mg-5Gd (A, B) and Mg-10Gd (C, D) screws are depicted in Fig. 6. The white dots in Fig. 6A and C are Gd-rich particles or agglomerations thereof, while the α-Mg matrix is depicted in gray. More Gd-rich particles are visible in Mg-10Gd than in Mg-5Gd, both in the slice and in the volume images. Agglomerations of Gd-rich particles in the extrusion direction are also visible in Fig. 6B and C.

The results of the quantitative analysis of agglomerations of Gd-rich particles from the SRµCT images are summarized in Table 4. A significant difference is found in the total volume of the agglomerations ($p < 0.0005$) between Mg-5Gd and Mg-10Gd screws, where Mg-5Gd shows a volume of agglomerations approximately half of that of Mg-10Gd. The observed smallest distance between two particles reveals that those agglomerations are less densely distributed in the matrix of Mg-5Gd than in Mg-10Gd, by nearly 35%. It is visible from the volume distribution analysis that Mg-5Gd screws show smaller agglomerations than Mg-10Gd (volume outlier's and median: $p < 0.0005$ and $p < 0.05$, respectively). The high standard deviation of the Mg-5Gd agglomeration volume is due to one very big agglomeration.

A table including the results of the chemical analysis from EDS and µXRF measurements can be found in Table 10. For the EDS analysis used images are presented in Fig. 11. The amount of Gd detected on the surface of the Mg-5Gd screw is 2.86 wt.% (Fig. 11A). Insignificantly less Gd content was detected inside the screw on a chosen area and a line (Fig. 11B). Nearly 5 times more Gd was observed from EDS measurement on a white spot, GdH_2 particle (Fig. 11B). The amount of Gd on the surface area of the screw is 6.14 wt.%. The EDS results of the screw surface analysis of a Mg-10Gd

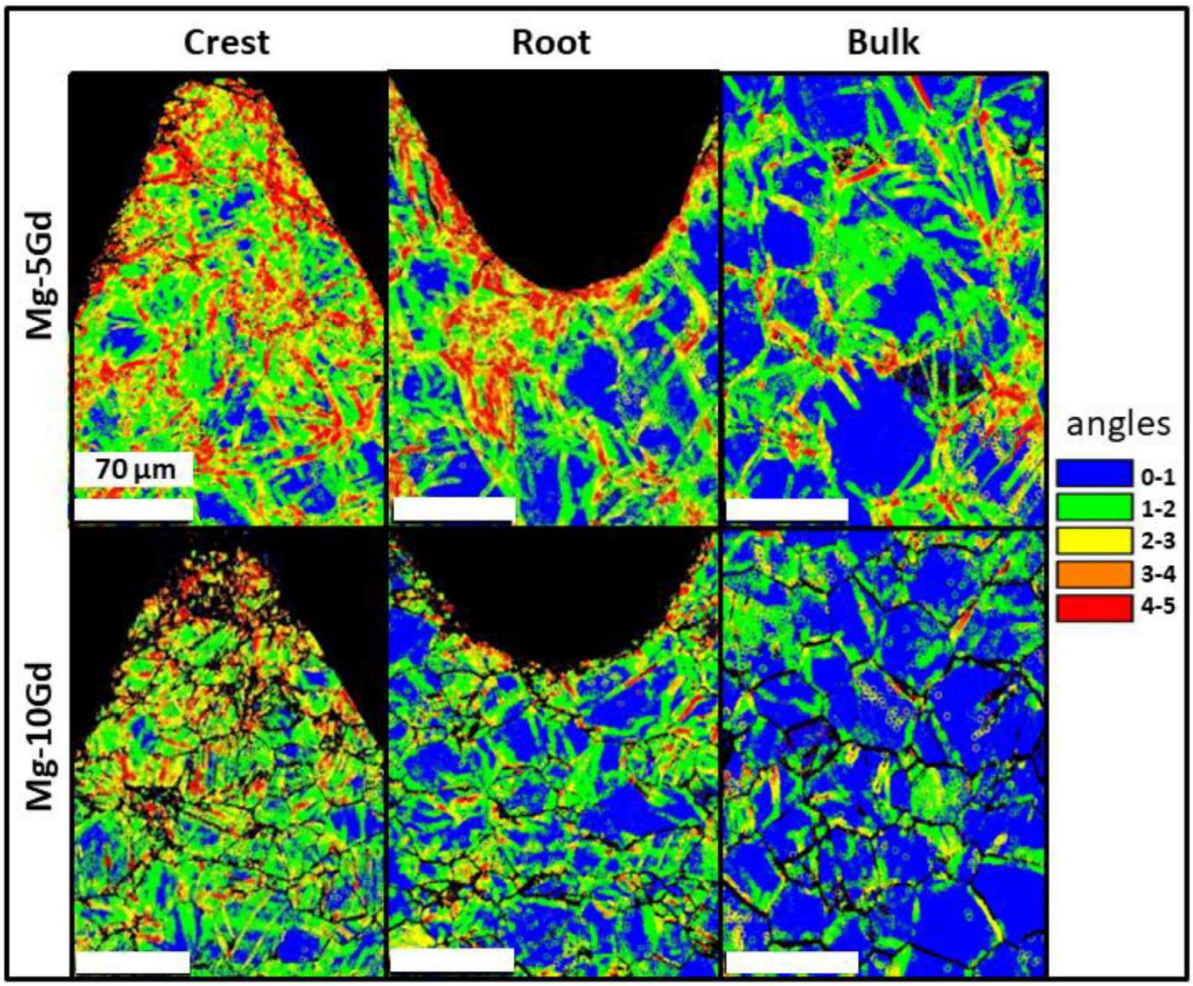

Fig. 5. Kernel average misorientation maps from EBSD measurements of Mg-5Gd and Mg-10Gd screws crest, root and bulk at 4th neighbor (distance = 1.6 µm).

Table 3
Area fractions from Kernel misorientation maps of Mg-5Gd and Mg-10Gd at 4th neighbor (distance = 1.6 µm).

Angle of misorientation	Alloy	Area fractions from Kernel misorientation maps at		
		Crest	Root	Bulk
4–5 °	Mg-5Gd	0.123	0.063	0.033
	Mg-10Gd	0.060	0.024	0.008

screw reveal Gd content of 6.14 wt.%, whereby the result of the µXRF analysis with 9.06 wt.% is much higher.

3.2. Degradation behavior

Fig. 7A and B depict 3D volume renderings of Mg-5Gd screw before and after 56 days of *in vitro* degradation in DMEM+10%FBS medium, respectively. Fig. 7C illustrates the deviation between the "difference layer" (layer between green and red dashed lines including also some black image background) and the "degradation layer" (layer between green and red dashed lines without black image backgrounds).

The results of the *DR* calculations *via* weight loss (WL), volume loss (VL) and for the different immersion solutions of all three experiments are compared in Fig. 8, in order to compare both measurement approaches (see also Table 7 in the Appendices). Due to the low sample numbers and high variability all measured data points are displayed instead of mean and standard deviation. For both materials and methods, a high spread of the *DR*s is observed; more for Mg-10Gd than for Mg-5Gd. In comparison to Mg-5Gd, the DR_{WL} of Mg-10Gd in the beginning of the immersion period shows lower values than DR_{VL} measurements. This trend is not seen in VL measurements. For both materials, the degradation is faster at the beginning and decreases with immersion time.

The DR_{VL} values of Mg-5Gd degraded in the different media for 28 days show little difference: α-MEM:

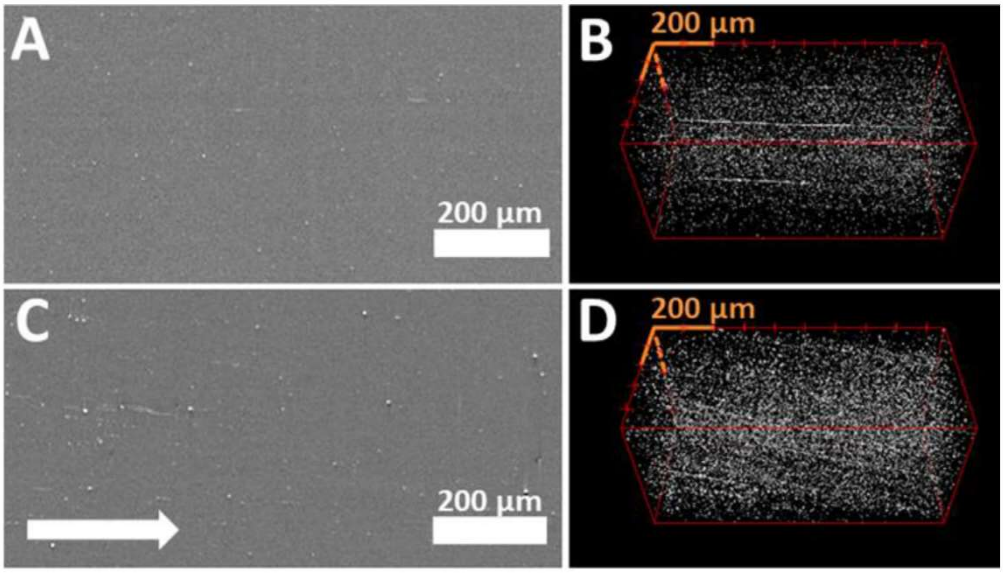

Fig. 6. (A, C) 2D tomographic slices of Mg-5Gd (A) and Mg-10Gd (C) screws in the longitudinal direction of the screw (arrow: extrusion direction). (B, D) Segmented Gd-rich particles (white dots) in a VOI (480 × 480 × 960 µm^3) of Mg-5Gd (B) and Mg-10Gd (C), respectively; voxel size=2.4 µm.

Table 4
Quantitative analysis of the volume, distribution and size of Gd-rich particles in Mg-5Gd and Mg-10Gd screws (SRμCT $n = 5$) in a chosen volume-of-interest. *Calculation performed after removal of the very high outlier volume 10257 [µm^3].

		Parameter	Mg-5Gd	Mg-10Gd	Statistical significance
1	Number of detected Gd-rich particles	# particles	10038 ± 1108	18293 ± 2680	$p < 0.005$
2	Total volume of the Gd-rich particles	Total volume [%]: mean±std	0.25 ± 0.03	0.56 ± 0.08	$p < 0.0005$
3	Smallest distance between two Gd-rich particles	Smallest distance between two particles [μm]	17.15 ± 0.88	11.11 ± 2.18	no sig. diff.
4	Number of detected outliers	# outliers	590 ± 369	986 ± 92	no sig. diff.
5	Mean and std. size of the outlier Gd-rich particles from the volume distribution	Volume [µm^3]: outlier's mean±std	194.29 ± 230.17 *(190.88 ± 136.42)	252.53 ± 230.08	$p < 0.0005$
6	Median size of the Gd-rich particles from the volume distribution	Volume [µm^3]: median	41.47	55.30	$p < 0.05$
7	Mean diameter of Gd-rich particles from the 2D slices	Mean feret diameter [µm]: mean±std	5.84 ± 0.19	6.25 ± 0.03	no sig. diff.
8	Max diameter of Gd-rich particles from the 2D slices	Max feret diameter [µm]: mean±std	204.58 ± 218.77	126.68 ± 55.22	no sig. diff.

Table 5
Wt.% Gd calculated with EDS as a function of the whole area (surface of the screw and the bulk), a line measurement (yellow line), a point measurement and μXRF-measurements. Reference Fig. 11.

Method	EDS					μXRF
Alloy	Mg-5Gd (Fig. 11B)			Mg-5Gd (Fig. 11A)	Mg-10Gd	Mg-10Gd
Analysis region	Area in bulk	Line in bulk	Point in bulk	Area on implant surface		In bulk
Gd [Wt.%]	2.7	2.63	13.86	2.86	6.14	9.09±0.6

0.30 ± 0.013 vs. DMEM: 0.33 ± 0.03. For Mg-10Gd after 28 days in the same media the DR_{VL} values vary more than 50% (α-MEM: 0.19 ± 0.01 vs. DMEM: 0.34 ± 0.10).

The mean DR_{VL} values of experiment (ii) and (iii) (7–56 days immersion time) are plotted again in Fig. 9A, with other computed parameters. Both materials start nearly with the same *DR*, but Mg-10Gd shows a stronger reduction over time. The corresponding *MDD* is presented in Fig. 9B. The fitted slope indicates that Mg-5Gd has a higher *GDR* than Mg-10Gd (Table 7), which agrees with the *DR* trend.

The *CV* of the *volume loss*, which is the ratio between the *2D-mean volume loss* and the *2D-std volume loss,* is presented in Fig. 9C and Table 8. It shows that Mg-5Gd starts with a smaller *CV,* hence a lower variation of the amount of

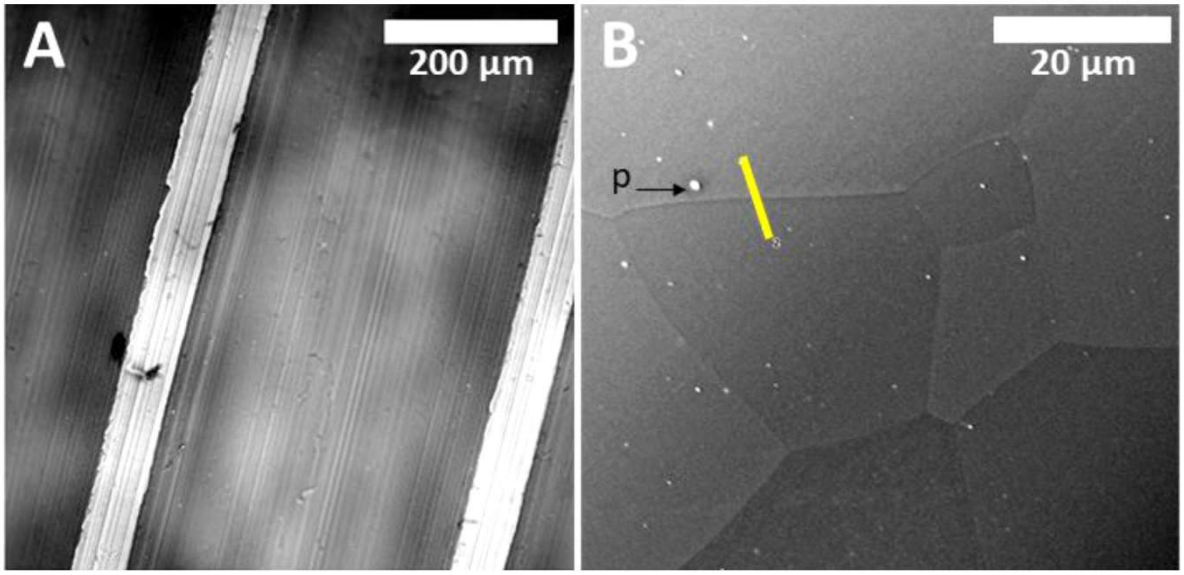

Fig. 7. (A) SEM image of the surface of an Mg-5Gd screw; (B) BSEM image of Mg-5Gd screw in the bulk. White dots represent either Mg5Gd intermetallic phases or GH_2 particles; Yellow line: Line crossing two grains.

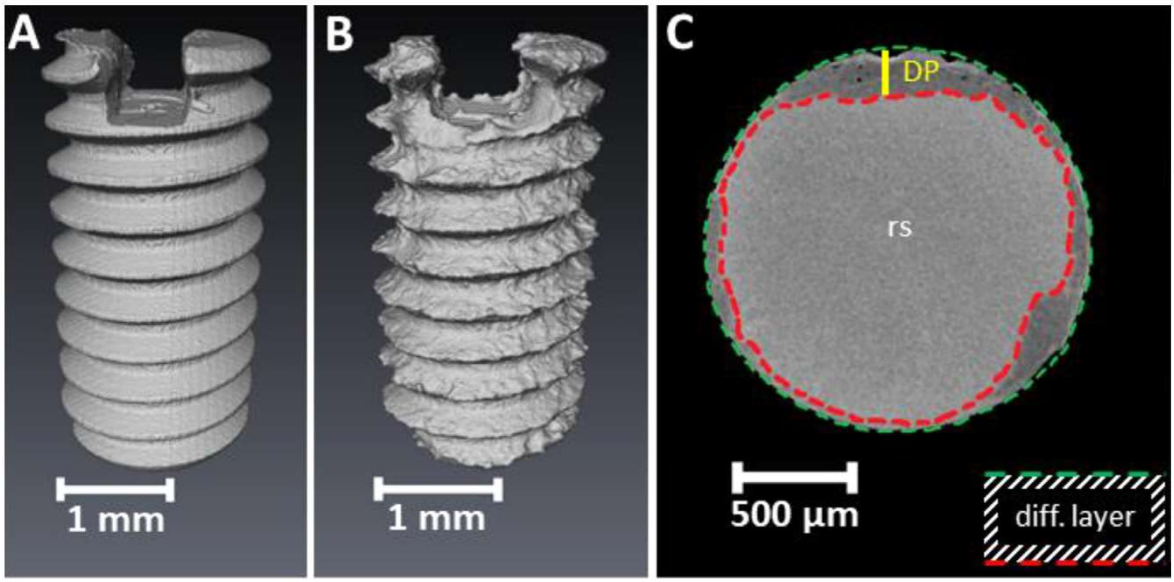

Fig. 8. Visualization of not corroded and corroded Mg screws. (A) 3D volume rendering after segmentation of a Mg-5Gd screw before immersion/degradation. (B) 3D volume rendering after segmentation of a Mg-5Gd screw after 56 days *in vitro* degradation and subsequent removal of the degradation layer. (C) A slice from the middle of the screw after degradation and before the removal of the degradation layer. The green line indicates the border between the preimplantation screw and the background. The red line indicates the border between the degradation layer and the residual *i.e.* not degraded material. The difference layer is given by the area between the green and the red line. The yellow line indicates the deepest pit (DP) within the depicted slice.

volume loss along the screw and a very small standard variation between the samples in the 1st, 2nd weeks compared to Mg-10Gd. It increases for both materials with immersion time, more for Mg-5Gd, which at the last time point is approximately 35, and 25% for Mg-10Gd.

The 3D-*PF* represents the degradation homogeneity of the 3D dataset. In contrast, the 2D-*PF*, being calculated slice-wise, represents the degradation homogeneity of the same dataset statistically. The *3D-PF* values presented in Fig. 9D and Table 8 are much higher than the *2D-mean PF* values (presented in Fig. 9E and Table 8). There are no recognizable differences or tendencies in the *3D-PF* between both alloys and/or time points. With the exception of the 1st week, Mg-10Gd shows a decreasing *2D-mean PF* reaching its maximum in the second week and a minimum in the 8th week. By contrast, Mg-5Gd does not show any tendency, but shows overall smaller mean values than Mg-10Gd, except for the 8th week, were they reach equity. The *CV* of the *2D-PF* presented in Fig. 9F shows that there is a tendency of decreasing *CV* from the 1st to the 8th week in case of Mg-10Gd and. Mg-5Gd

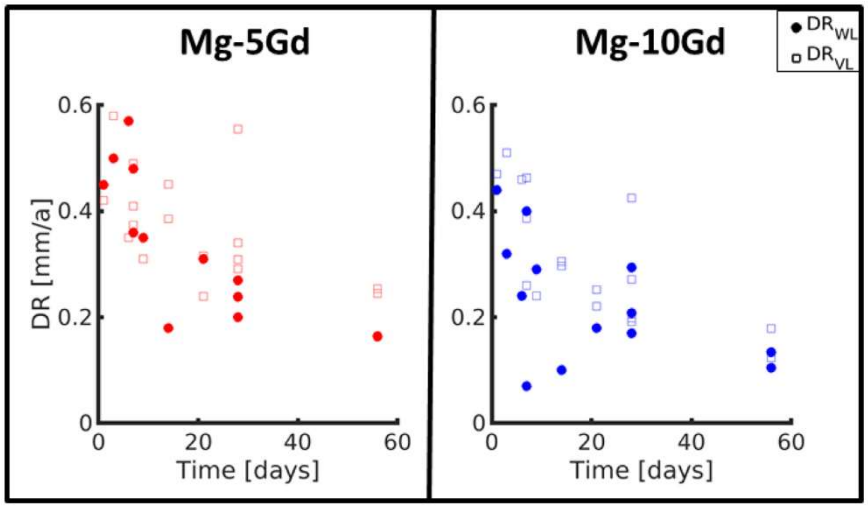

Fig. 9. Degradation rates calculated *via* weight loss (DR_{WL}) and volume loss (DR_{VL}), respectively.

Table 6
Comparison of analyzed parameters for Mg-5Gd and Mg-10Gd screws.

	Parameter	Mg-5Gd … Mg-10Gd
Microstructure	Grain size	>
	Deformation degree	>
Gd-rich particles	Volume	<
Degradation	DR	>
velocity	*MDD*	>
Degradation	*CV volume loss*	>
homogeneity	*2D mean PF*	<
	CV 2D PF	<
	Crests/Roots	>

shows values like Mg-10Gd in the 1st and the 8th week and up to 10% lower *CV*s (meaning more homogeneous) values for 2nd, 3rd, and 4th weeks.

Fig. 9G presents the ratio of the degradation between the crests and roots of the threads.

Both materials show crest-to-root ratios higher than 1, indicating faster degradation in crests compared to roots. It is visible that there is a tendency of increasing crest-to-root ratio of the degradation layer for Mg-10Gd from the 1st week to 8th week. Generally, Mg-5Gd shows higher values than Mg-10Gd. Until week 4, Mg-5Gd screws degrade up to 50% stronger at the crests than Mg-10Gd.

Although the overall standard deviations are large, in particular for the degradation parameters, the observed differences between both materials are summarized in Table 5.

4. Discussion

In the following, we will discuss the effect of the microstructure on the different degradation behaviors to highlight the advantages and disadvantages of the alloys for the use as an implant material (assuming a similar behavior to be observed *in vivo*).

This study supports the tendency of higher extrusion speeds to result in bigger grain sizes as observed in [10]; Mg-5Gd with higher extrusion velocity revealed bigger grain sizes in comparison to Mg-10Gd. Additionally, a more homogeneous microstructure of Mg-10Gd samples in comparison to Mg-5Gd was observed.

The investigation of the influence of the machining on the near-surface microstructure of the screws revealed higher and regionally deeper microstructural deformations in coarse grained Mg-5Gd than Mg-10Gd. The latter is in agreement with previous findings of Gawlik [25].

The Mg-5Gd matrix with a coarse grain structure revealed more tensile twins and tensile twin boundaries than the fine-grained Mg-10Gd alloys. This result is in agreement with the fact that the growth of the twins is limited by the grain size, hence bigger grains produce bigger twins and consequently, more twin boundaries [58].

Fig. 10, Table 10.

Furthermore, Mg-5Gd reveals higher kernel average misorientation values than Mg-10Gd, and hence has overall more deformed structures. Recently, intrinsic and extrinsic influences of the alloying elements on the microstructure and the degradation behavior of biodegradable implants has been reviewed by Bahmani et al. [59]. There, it has been concluded that in the case of single grains like single crystals or bicrystals, the corrosion rate increases with increasing grain size, while in very fine grains (< 50 μm), the corrosion rate decreases by decreasing the grain size. It was previously discussed that the chemical activity at grain boundary regions increases the dissolution rate of fine grained alloys [60,61,62] and that more unstable microstructural features have higher energies, which could accelerate the degradation process. We hypothesize that this process is responsible for the faster degradation speeds observed for Mg-5Gd. This is in contrast to the hypothesis of Gawlik [25] that thicker twinning zones slow down the dissolution rate of the alloy by acting as borders between the grains.

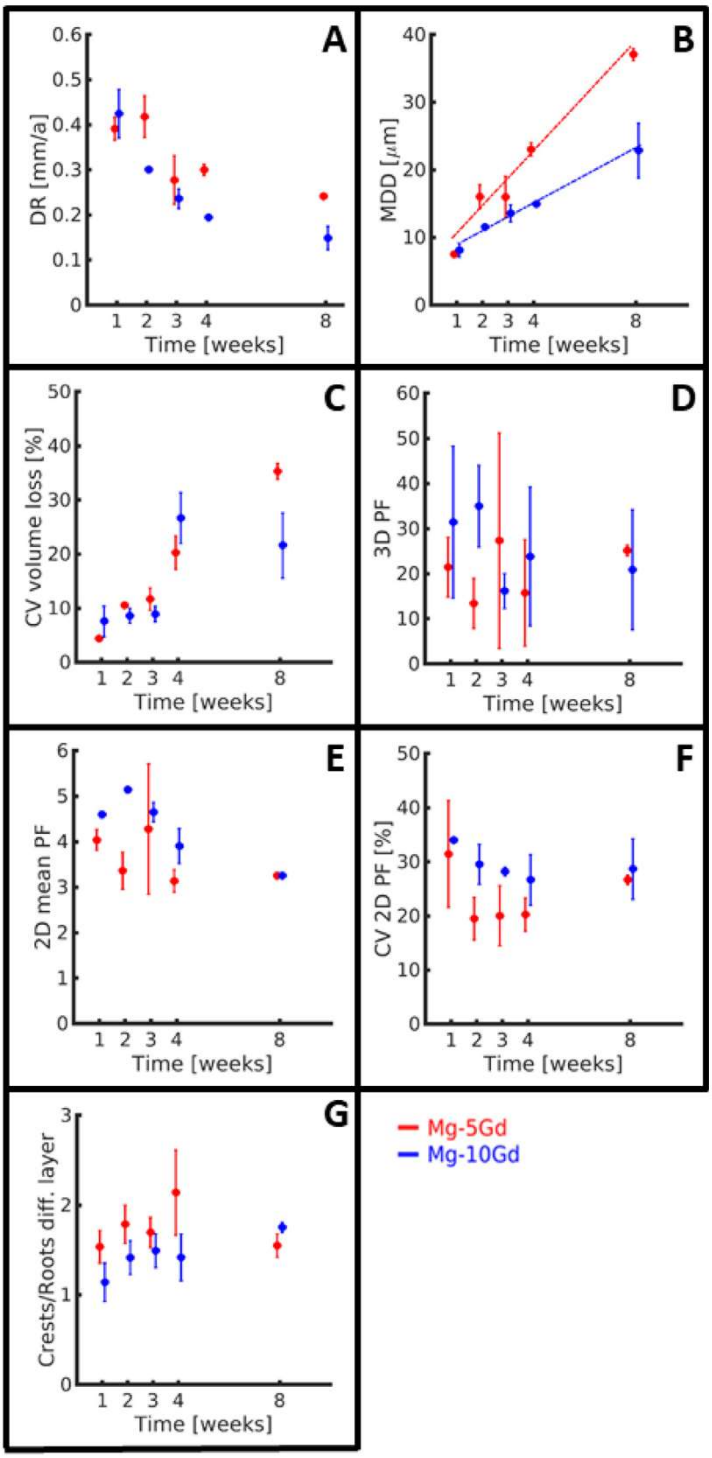

Fig. 10. Results of semi static *in vitro* investigation of Mg-5Gd and Mg-10Gd screw implants over 7–56 days period (experiment (ii) + (iii)) from tomography images. (A) Degradation rate, (B) Mean degradation depth with linear regression fits (*GDR*: Mg-5Gd = 0.21 mm/a; Mg-10Gd= 0.11 mm/a), (C) Coefficient of variation of the volume loss over the transversal slices of the 3D implant, (D) 2D mean pitting factor, calculated for each slice with its *MDD*, (E) Coefficient of variation from (D), (F) Ratio of the degradation layers at the crests and at the roots of the samples.

Apart from having an influence on the degradation rate, the deformation has also impacted the mechanical properties of the material. Extension twinning occurs under tensile stress along the crystallographic c-axis, which results in a sudden re-orientation of parent grains by approximately 86.3° [63,64]. When the tension twinning dominated deformation exhausts, a fast strain hardening is happening, which later leads to an early fracture [65]. From this, we conclude that the weaker texture of Mg-10Gd could be more beneficial for the deformation accommodation by the dislocation slip and more homogeneous deformation, thus lower risk for an early fracture can be expected for the Mg-10Gd alloys.

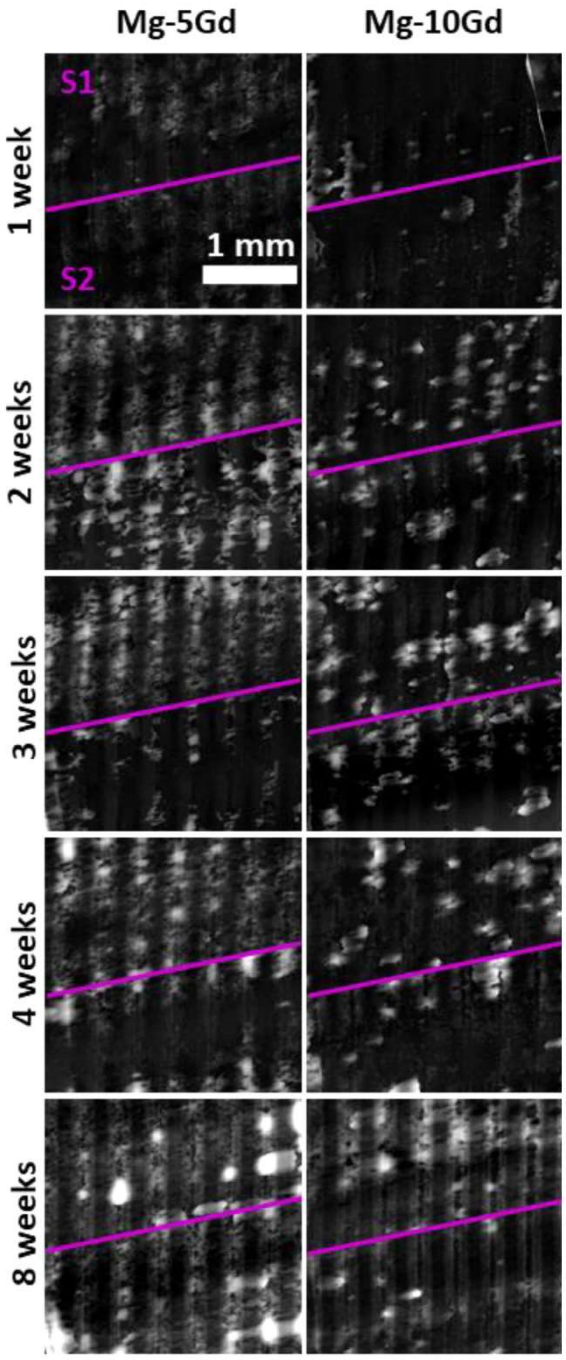

Fig. 11. 2D degradation layers of the investigated Mg-5Gd and Mg-10Gd from 7 to 56 days corroded screws. S1/S2 indicating Sample1/Sample2; Scale bar same for all images=1 mm; grey levels: brighter=more corroded, darker=less corroded. Mg-10Gd, 8 weeks, S2 (right bottom): yellow area=A_{crest}, green area=A_{root}.

In addition to the deformations, the presence of metallic particles in the alloys may have an influence on the degradation behavior. The bright particles observed in the 3D volume are assumed to be agglomerations of GdH_2 particles, which is in agreement with the literature [10,66]. Under the assumption that these particles act as sites for galvanic corrosion, the smaller the particles and the more homogeneously distributed, the more homogeneous the degradation mechanism should be.

Table 7
Number of samples used for *in vitro* investigation per measurement time point.

Exp.	Immersion days	Weight loss	Volume loss
i	1–9	1	1
ii	7–28	1	2
iii	28–56	2	2

Additionally, the more particles present in the alloy the faster the degradation rate should be. Based on the observed degradation behavior it appears that the presence of these particles is negligible.

Based on the computed parameters, no clear conclusion can be drawn in terms of the homogeneity of both materials' degradation. It can speculate on three different observed ways driving the implant's non-uniform degradation:

1. Localized non-uniform degradation in terms of the degradation depth differences on the screw's crest and root areas. This observation is made for both alloys, although in the first four weeks the effect is more visible in Mg-5Gd than in Mg-10Gd.
2. Localized non-uniform degradation in terms of the pitting corrosion described with the 3D and 2D mean PF values. Similar to [67], the higher values of 2D mean pitting factor in the Mg-10Gd samples are caused by a lower average degradation depth and rather high pits. This effect is even more visible in the parameter 3D PF. Instead of averaging the deepest pits along the screw's cross sectional slices only the deepest pit is considered in the calculation. The high variation of the 3D PF among all investigated samples indicates the sensitivity of this parameter. It also suggests the non-homogeneous degradation behavior of the samples among same alloy and/or probably the less significance of the 3D PF parameter. The deepest pits are approximately 632.5 μm in Mg-5Gd and 379.5 μm in Mg-10Gd and can be more than twice as deep as the screw thread. In general, the decrease of the pitting factor values during longer degradation periods can be due to several reasons: (i) several small pits could merge; (ii) inhomogeneities, like GdH_2 particles, could fall out of the pits; (iii) small pH differences between the surface and the deep pits, leading to slower degradation rates at the deeper pits than at the surface; (iv) larger screw surface area at the top of the pit than at the bottom of the pit, hence less surface energy and slower degradation rates at the depths of the pits than at the tops.
3. Non-localized non-uniform degradation increasing during the degradation time period. The latter two points of the localized non-uniform degradation (iii and iv) could also be a reason for the degradation rate differences at the roots and the crests of the screws.

In this study, a greater decrease of degradation rate with the immersion duration of Mg-10Gd screws in comparison to Mg-5Gd could be detected. Kubásek and Vojtěch [9] dis-

Table 8
Degradation rates (*DR*) [mm/a], α-MEM or DMEM +10%FBS+1% pen/strep, weight loss (WL), volume loss (VL).

Exp.	Immersion days	Mg-5Gd			Mg-10Gd			Solution	Samples
		DR_{WL}[mm/a]	DR_{VL}[mm/a]	DR_{WL}/DR_{VL}	DR_{WL}[mm/a]	DR_{VL}[mm/a]	DR_{WL}/DR_{VL}		
i	1	0.45	0.42	1.07	0.44	0.47	0.94	α-MEM	different
	3	0.50	0.58	0.86	0.32	0.51	0.63	α-MEM	different
	6	0.57	0.35	1.63	0.24	0.46	0.52	α-MEM	different
	7	0.48	0.49	0.98	0.40	0.26	1.54	α-MEM	different
	9	0.35	0.31	1.13	0.29	0.24	1.21	α-MEM	different
ii	7	0.36	0.39 ± 0.03	0.92	0.07	0.42 ± 0.05	0.17	α-MEM	different
	14	0.18	0.42 ± 0.05	0.43	0.10	0.30 ± 0.01	0.33	α-MEM	different
	21	0.31	0.28 ± 0.05	1.11	0.18	0.24 ± 0.02	0.75	α-MEM	different
	28	0.20	0.31 ± 0.02	0.65	0.17	0.22 ± 0.04	0.77	α-MEM	different
iii	28	0.25 ± 0.02	0.32 ± 0.03	0.59 ± 0.11	0.25 ± 0.06	0.34 ± 0.10	0.73 ± 0.04	DMEM	identical
	56	0.16 ± 0.01	0.24 ± 0.01	0.66 ± 0.01	0.12 ± 0.02	0.15 ± 0.03	0.84 ± 0.25	DMEM	identical

Table 9
All data to graphs.

	1 weeks		2 weeks		3 weeks		4 weeks		8 weeks	
	Mg-5Gd	Mg-10Gd	Mg-5Gd	Mg-10Gd	Mg-5Gd	Mg-10Gd	Mg-5Gd	Mg-10Gd	Mg-5Gd	Mg-10Gd
DR [mm/year]	0.39 ± 0.03	0.42 ± 0.05	0.42 ± 0.05	0.30 ± 0.01	0.28 ± 0.05	0.24 ± 0.02	0.31 ± 0.02	0.22 ± 0.04	0.24 ± 0.01	0.15 ± 0.03
MDD [μm]	7.5 ± 0.5	8.1 ± 1	16 ± 1.5	11 ± 0.2	16 ± 3.1	14 ± 1.3	24 ± 1.6	17 ± 3.1	37 ± 1	23 ± 4
3D-PF	21.4 ± 6.6	31.5 ± 16.8	13.4 ± 5.6	35.0 ± 9.1	27.4 ± 23.9	16.2 ± 3.8	15.8 ± 11.8	23.8 ± 15.4	25.1 ± 1.2	20.9 ± 13.3
2D-mean PF	4.0 ± 0.2	4.6 ± 0.1	3.4 ± 0.4	5.1	4.3 ± 1.4	4.6 ± 0.2	3.1 ± 0.2	3.9 ± 0.4	3.3 ± 0.0	3.3 ± 0.3
CV 2D PF [%]	31.5 ± 9.9	34.0 ± 0.0	19.5 ± 3.9	29.6 ± 3.7	20.0 ± 5.6	28.2 ± 0.8	20.2 ± 3.1	26.7 ± 4.7	26.7 ± 0.9	28.7 ± 5.6
CV dif. layer [%]	4.4 ± 0.2	7.6 ± 2.8	10.5 ± 0.1	8.6 ± 1.4	11.7 ± 2.1	8.9 ± 1.5	20.2 ± 3.1	26.7 ± 4.7	35.3 ± 1.5	21.6 ± 6.0
Amount of slices, where it is not possible to calculate PF [%]	0.5 ± 0.1	1.1 ± 1.1	0.7 ± 0.1	3.2 ± 1.0	0.7 ± 0.4	1.5 ± 1.5	1.8 ± 0.5	1.6 ± 0.2	4.0 ± 0	1.8 ± 1.3
Crests/roots dif. Layer	1.5 ± 0.2	1.1 ± 0.2	1.8 ± 0.2	1.4 ± 0.2	1.7 ± 0.2	1.5 ± 0.2	2.1 ± 0.5	1.4 ± 0.3	1.6 ± 0.1	1.7 ± 0.1

Table 10
μCT parameters.

Parameter	Laboratory μCT: Nanotom	SRμCT: IBL P05, DESY	TOPO-TOMO beamline, KARA
Amount of Projections	2700	1201	3000
Exposure time	1000 ms	300 ms	14.3 ms
Energy	–	25–30 keV	white beam- peak at 16 keV
Current	70 μA	–	–
Voltage	100 kV	–	–
Voxel size	2.5 μm	2.6 μm	2.4 μm

cussed that the Gd^{3+} cations substitute Mg^{2+} cations in the degradation layer, hence slowing down the degradation process. One of the reasons that Mg-5Gd screws degraded faster than Mg-10Gd could be the amount of Gd dissolved in the Mg-matrix. This difference becomes stronger for longer immersion times, consistent with Harmuth et al. [10] who did not find any significant correlation between the degradation rate and the alloy composition in a short time of 7 days corrosion tests of Mg-Gd alloys with 2, 5 and 10 wt.% Gd content.

The known fast degradation rate of Mg bone implants has also recently been mentioned by Yang et al. [24]. Mg-10Gd has been tested *in vivo* and *in vitro* by Marco et al. [68] over a short time period of up to 7 days. Myrissa et al. [66] and Galli et al. [69] tested Mg-10Gd *in vivo* over a time period of 12 weeks in a transcortical and monocortical rat femur model, respectively. Myrissa et al. [66] reported an initial low degradation rate without gas bubbles, but afterwards a very fast degradation rate with a high amount of gas bubbles visible. After 12 weeks of implantation nearly a complete dissolution of the implant in the bone was observed. This would not be acceptable for a fracture fixing implant, since it should provide structural stability at least for 12 weeks [66,70]. On the other hand Galli [69] concluded that Mg-10Gd showed a degradation behavior appropriate for bone formation and stable degradation layer. The different outcomes of experiments may be arising from different microstructures, differences in the production and manufacturing of the implant, place of implantation and different imaging modalities [69].With respect to the degradation velocity, both investigated materials reveal a degradation rate appropriate for orthopedic implants [3]. It was shown that degradation rates lower 0.5 and higher than 0.2 mm/a would match the

bone healing rates [71]. According to Rahim et al. [3] the bone healing time can range from a month to six months in humans. By considering the calculated global degradation $rate_{volume\ loss}$ of 0.25 mm/a for Mg-5Gd after 56 days of degradation, the mean degradation depth of Mg-5Gd after 6 months is 115 μm. Performing the same mean degradation rate calculation for 6 months for Mg-10Gd one obtains a mean degradation rate of 69 μm (with global degradation $rate_{volume\ loss}$= 0.15 mm/a). Therefore, for the given implant geometry, Mg-5Gd would remain in the body for 4.3 years and Mg-10Gd for 8.1 years, before dissolving completely (assuming mean degradation rate=$radius_{implant}$=0.9 mm). However, as we have shown that both materials degrade inhomogeneously, and given the sizes of the deepest pits, it is possible that the dissolution will occur faster *in vivo*. Based on this inhomogeneity, future tests must also consider the change in mechanical stabilities of the implants over time.

Overall, in contrast to weight loss measurements, SRμCT measurements allow to assess the volume loss and enable a description of the degradation homogeneity qualitatively and quantitatively. Depending on the degradation period and image resolution volume loss measurements can give more precise results than the weight loss measurements of the degradation rate.

5. Conclusions

In this study two Mg-xGd alloys (Mg-5 wt.% Gd and Mg-10 wt.% Gd) were investigated non-destructively in 3D in terms of their *in vitro* degradation velocity and homogeneity for short and long immersion times. Digital 3D analysis yields the volume loss measurements and allows to access further parameters describing the homogeneity of the degradation qualitatively and quantitatively. In particular, the pitting factor calculations, enable the quantitative analysis of the degradation homogeneity and are thus preferred over sole weight loss measurements.

Our analysis suggests that Mg-10Gd has an overall lower degradation rate, more homogeneous microstructure and a weaker texture than Mg-5Gd. Future *in vivo* tests need to be carried out to verify the degradation behavior *in vivo* and extrapolate the materials' suitability for implant materials.

Acknowledgements

This research was carried out within the SynchroLoad project (BMBF project number 05K16CGA) which is funded by the Röntgen-Ångström Cluster (RÅC), a bilateral research collaboration of the Swedish government and the German Federal Ministry of Education and Research (BMBF). We acknowledge also the project MgBone (BMBF project number 05K16CGB). We acknowledge DESY (Hamburg, Germany), a member of the Helmholtz Association HGF, for the provision of experimental facilities. We acknowledge provision of beamtime at beamline P05 at PETRA III at DESY related to the proposal I-20160104 and we would like to thank Felix Beckmann, Jörg Hammel and Fabian Wilde for assistance in using P05. We acknowledge the KIT light source for provision of instruments at their beamlines and we would like to thank the Institute for Beam Physics and Technology (IBPT) for the operation of the storage ring, the Karlsruhe Research Accelerator (KARA). We further thank Monika Luczak and Eshwara Nidadavolu for the help in performance of the immersion tests. This research was supported in part through the Maxwell computational resources operated at Deutsches Elektronen-Synchrotron DESY, Hamburg, Germany. We also acknowledge Sarkis Gavras for proofreading the article.

Appendix

In order to reveal best image quality some of scan parameters were varied (Table 9).

References

[1] *This metal implant turns into bone*, Syntellix A.G., viewed 22 September 2021, <https://www.syntellix.de/en/home.html>.
[2] N.M. Neves, A. Kouyumdzhiev, R.L. Reis, Mater. Sci. Eng. C 25 (2) (2005) 195–200.
[3] M.I. Rahim, S. Ullah, P.P. Mueller, Metals 8 (7) (2018) 532 (Basel).
[4] G.L. Song, Corrosion of Magnesium Alloys, Elsevier, 2011.
[5] M.P. Staiger, A.M. Pietak, J. Huadmai, G. Dias, Biomaterials 27 (9) (2006) 1728–1734.
[6] W. Jahnen-Dechent, M. Ketteler, Clin. Kidney J. 5 (Suppl_1) (2012) i3–i14 pp..
[7] P.C. Banerjee, S. Al-Saadi, L. Choudhary, S.E. Harandi, R. Singh, Materials 12 (1) (2019) 136 (Basel).
[8] R.K. Raman, S.E. Harandi, Materials 10 (11) (2017) 1316 (Basel).
[9] J. Kubásek, D. Vojtěch, Trans. Nonferrous Met. Soc. China 23 (5) (2013) 1215–1225.
[10] J. Harmuth, B. Wiese, J. Bohlen, T. Ebel, R. Willumeit-Römer, Front. Mater. 6 (2019) Aug., doi:10.3389/fmats.2019.00201.
[11] A. Myrissa, S. Braeuer, E. Martinelli, R. Willumeit-Roemer, W. Goessler, A.M. Weinberg, Acta Biomater. 48 (2017) 521–529.
[12] J. Ramalho, R.C. Semelka, M. Ramalho, R.H. Nunes, M. AlObaidy, M. Castillo, Am. J. Neuroradiol. 37 (7) (2016) 1192–1198.
[13] D.W. Bruce, B.E. Hietbrink, K.P. DuBois, Toxicol. Appl. Pharmacol. 5 (6) (1963) 750–759.
[14] F. Feyerabend, et al., Acta Biomater. 6 (5) (2010) 1834–1842.
[15] T.J. Haley, K. Raymond, N. Komesu, H.C. Upham, Br. J. Pharmacol. Chemother. 17 (3) (1961) 526–532.
[16] G.J. Strijkers, M. Mulder, J. Willem, F. Van Tilborg, A. Geralda, K. Nicolay, Anti Cancer Agents Med. Chem. (Formerly Curr. Med. Chem. Agents) 7 (3) (2007) 291–305.
[17] N.A. Agha, R. Willumeit-Römer, D. Laipple, B. Luthringer, F. Feyerabend, PLoS ONE 11 (6) (2016).
[18] N. Zidane, et al., Port. Electrochim. Acta 33 (5) (2015) 289–304.
[19] J.D. Hanawalt, C.E. Nelson, J.A. Peloubet, Trans. AIME 147 (1942) 273–299.
[20] T. Takenaka, T. Ono, Y. Narazaki, Y. Naka, M. Kawakami, Electrochim. Acta 53 (1) (2007) 117–121.
[21] Q. Peng, Y. Huang, J. Meng, Y. Li, K.U. Kainer, Intermetallics 19 (3) (2011) 382–389.
[22] I.P. Jain, C. Lal, A. Jain, Int. J. Hydrog. Energy 35 (10) (2010) 5133–5144.
[23] C. Shuai, et al., Compos. Part B Eng. 207 (2021) 108564.
[24] Y. Yang, et al., Mater. Des. 185 (2020) 108259.
[25] M.M. Gawlik, The Influence of Surface Defects on the Degradation Behaviour of Magnesium Alloys for Medical Applications, Christian-Albrechts Universität Kiel, 2019.
[33] N.T. Kirkland, N. Birbilis, M.P. Staiger, Acta Biomater. 8 (3) (2012) 925–936.

[34] L. Liu, et al., Appl. Sci. 8 (9) (2018) 1459.
[35] B. Zeller-Plumhoff, et al., Mater. Corros. 69 (3) (2018) 298–306.
[36] V. Kree, J. Bohlen, D. Letzig, K.U. Kainer, Prakt. Metallogr. 41 (5) (2004) 233–246.
[37] D. Drozdenko, J. Bohlen, S. Yi, P. Minárik, F. Chmel\'\ik, P. Dobro\vn, Acta Mater. 110 (2016) 103–113.
[38] S. Sandlöbes, S. Zaefferer, I. Schestakow, S. Yi, R. Gonzalez-Martinez, Acta Mater. 59 (2) (2011) 429–439.
[39] F. Wilde, et al., AIP Conf. Proc. 1741 (1) (2016) 30035.
[40] W. Van Aarle, et al., Ultramicroscopy 157 (2015) 35–47.
[41] J. Moosmann, et al., Nat. Protoc. 9 (2) (2014) 294–304.
[42] J. Moosmann, "Time-lapse X-ray phase-contrast microtomography for *in vivo* imaging and analysis of morphogenesis,". [Online]. Available: https://github.com/moosmann/matlab. [Accessed: 24-Jan-2021].
[43] J. Ashburner, K.J. Friston, Hum. Brain Funct. (1997) 43–58.
[44] J. Schindelin, et al., Nat. Methods 9 (7) (2012) 676–682.
[45] A. Buades, B. Coll, J.M. Morel, Image Process. Line 1 (2011) 208–212.
[46] J. Darbon, A. Cunha, T.F. Chan, S. Osher, G.J. Jensen, Fast nonlocal filtering applied to electron cryomicroscopy, in: Proceedings of the 5th IEEE International Symposium on Biomedical Imaging: From Nano to Macro, 2008, pp. 1331–1334.
[47] J. Ollion, J. Cochennec, F. Loll, C. Escudé, T. Boudier, Bioinformatics 29 (14) (2013) 1840–1841.
[48] E.P.S. Nidadavolu, F. Feyerabend, T. Ebel, R. Willumeit-Römer, M. Dahms, Materials 9 (8) (2016) 627 (Basel).
[49] I. Marco, F. Feyerabend, R. Willumeit-Römer, O. der Biest, Mater. Sci. Eng. C 62 (2016) 68–78.
[50] N.A. Agha, F. Feyerabend, B. Mihailova, S. Heidrich, U. Bismayer, R. Willumeit-Römer, Mater. Sci. Eng. C 58 (2016) 817–825.
[51] O.O.F.I. Cooperation "Correlation and regression Analysis".
[52] R.W. Revie, Corrosion and Corrosion Control: an Introduction to Corrosion Science and Engineering, John Wiley & Sons, 2008.
[53] G. Borgefors, Comput. Vis. Image Underst. 64 (3) (1996) 368–376.
[54] H.G. Merkus, Particle size Measurements: Fundamentals, Practice, Quality, 17, Springer Science & Business Media, 2009.
[55] M. Doube, et al., Bone 47 (6) (2010) 1076–1079.
[56] H. Abdi, Encycl. Res. Des. 1 (2010) 169–171.
[57] R. C. Team and othersR: A Language and Environment for Statistical Computing, Vienna, Austria, 2013.
[58] A. Ghaderi, M.R. Barnett, Acta Mater. 59 (20) (2011) 7824–7839.
[59] A. Bahmani, S. Arthanari, K.S. Shin, J. Magnes. Alloy. 8 (1) (2020) 134–149.
[60] U.C. Nwaogu, C. Blawert, N. Scharnagl, W. Dietzel, K.U. Kainer, Corros. Sci. 51 (11) (2009) 2544–2556.
[61] D. Song, A. Ma, J. Jiang, P. Lin, D. Yang, J. Fan, Corros. Sci. 52 (2) (2010) 481–490.
[62] W.R. Osório, C.M. Freire, A. Garcia, Mater. Sci. Eng. A 402 (1–2) (2005) 22–32.
[63] L. Wu, et al., Acta Mater. 56 (14) (2008) 3699–3707.
[64] L. Wu, et al., Acta Mater. 56 (4) (2008) 688–695.
[65] W. Wu, C.P. Chuang, D. Qiao, Y. Ren, K. An, J. Alloys Compd. 683 (2016) 619–633.
[66] A. Myrissa, et al., Mater. Sci. Eng. C 61 (2016) 865–874.
[67] P. Maier, F. Zimmermann, M. Rinne, G. Szakács, N. Hort, C. Vogt, Mater. Corros. 69 (2) (2018) 178–190.
[68] I. Marco, et al., Eur. Cell. Mater. 33 (2017) 90–104.
[69] S. Galli, Malmö University, Faculty of Odontology, 2016.
[70] S.F. Fischerauer, et al., Acta Biomater. 9 (2) (2013) 5411–5420.
[71] C. Shuai, S. Li, S. Peng, P. Feng, Y. Lai, C. Gao, Mater. Chem. Front. 3 (4) (2019) 544–562.

Bioactive Materials 13 (2022) 37–52

Contents lists available at ScienceDirect

Bioactive Materials

journal homepage: www.keaipublishing.com/en/journals/bioactive-materials

High-resolution *ex vivo* analysis of the degradation and osseointegration of Mg-xGd implant screws in 3D

Diana Krüger [a,*], Silvia Galli [b,**], Berit Zeller-Plumhoff [a,***], D.C. Florian Wieland [a], Niccolò Peruzzi [c], Björn Wiese [a], Philipp Heuser [d], Julian Moosmann [e], Ann Wennerberg [f], Regine Willumeit-Römer [a]

[a] Institute of Metallic Biomaterials, Helmholtz-Zentrum Hereon, Max-Planck-Str. 1, Geesthacht, 21502, Germany
[b] University of Malmö, Faculty of Odontology, Department of Prosthodontics, Carl Gustafs väg 34, Klerken, 20506, Malmö, Sweden
[c] Lund University, Department of Clinical Sciences Lund, Medical Radiation Physics, Barngatan 4, 22242, Lund, Sweden
[d] Deutsches Elektronen-Synchrotron (DESY), Notkestrasse 85, 22607, Hamburg, Germany
[e] Institute of Materials Physics, Helmholtz-Zentrum Hereon, Max-Planck-Str. 1, Geesthacht, 21502, Germany
[f] University of Gothenburg, Institute of Odontology, Department of Prosthodontics, Medicinaregatan 12 f, 41390, Göteborg, Sweden

ARTICLE INFO

Keywords:
Magnesium alloys
Biodegradable implant
Micro-computed tomography degradation rate
Degradation homogeneity
Ex vivo imaging
Ex vivo histology
Histology vs. tomography

ABSTRACT

Biodegradable magnesium (Mg) alloys can revolutionize osteosynthesis, because they have mechanical properties similar to those of the bone, and degrade over time, avoiding the need of removal surgery. However, they are not yet routinely applied because their degradation behavior is not fully understood.

In this study we have investigated and quantified the degradation and osseointegration behavior of two biodegradable Mg alloys based on gadolinium (Gd) at high resolution.

Mg-5Gd and Mg-10Gd screws were inserted in rat tibia for 4, 8 and 12 weeks. Afterward, the degradation rate and degradation homogeneity, as well as bone-to-implant interface, were studied with synchrotron radiation micro computed tomography and histology. Titanium (Ti) and polyether ether ketone (PEEK) were used as controls material to evaluate osseointegration.

Our results showed that Mg-5Gd degraded faster and less homogeneously than Mg-10Gd. Both alloys gradually form a stable degradation layer at the interface and were surrounded by new bone tissue. The results were correlated to *in vitro* data obtained from the same material and shape. The average bone-to-implant contact of the Mg-xGd implants was comparable to that of Ti and higher than for PEEK. The results suggest that both Mg-xGd alloys are suitable as materials for bone implants.

1. Introduction

Biodegradable implants emerged as a viable alternative to permanent orthopaedic implants as they eliminate the need for a second surgery to remove the implant, consequently reducing the chance of patients' harm as well as the financial burden. In comparison to permanent implants, e.g. joint implants, which substitute a missing function and are supposed to stay in the patient for decades, implants meant for osteosynthesis, such as screws, plates or nails, serve for bone support only temporarily [1]. Keeping these implants in the body for longer periods can lead to complications, especially for children, whose growth might be disturbed [1]. Additionally, the modulus of elasticity of conventional permanent implant materials, made of e.g. stainless steel, chrome-cobalt alloys and titanium, is much higher than that of cortical bone. This difference in the elasticity modulus leads to the implant carrying a greater portion of the load and can cause stress shielding effect [2].

Providing an elasticity modulus near to the one of cortical bone [2], being biodegradable and a natural part of the human body, magnesium (Mg) and its alloys are of particular interest as alternative materials for

Peer review under responsibility of KeAi Communications Co., Ltd.
* Corresponding author.
** Corresponding author.
*** Corresponding author.
E-mail addresses: diana.krueger@hereon.de (D. Krüger), silvia.galli@mau.se (S. Galli), berit.zeller-plumhoff@hereon.de (B. Zeller-Plumhoff).

https://doi.org/10.1016/j.bioactmat.2021.10.041
Received 29 August 2021; Received in revised form 22 October 2021; Accepted 28 October 2021
Available online 14 November 2021

temporary bone implants. The degradation of Mg leads to the formation of harmless corrosion products, which are removed through urine [2,3]. The major limitation of pure Mg is its low corrosion resistance, which can cause a reduction in the mechanical integrity of the implant before the bone or tissue is sufficiently healed. Additionally, a degradation occurring too fast results in the rapid production of hydrogen gas, which then leads to the formation of gas bubbles around the implant. The latter can cause separation of tissue layers from the implant and delays the healing of the tissue (necrosis of surrounding tissue might be the result) [3]. In the worst case, the evolution of gas bubbles may block the blood stream [4]. Another undesirable effect of a rapid degradation is the increase of the pH value in localized areas next to the implant, which can be harmful for the cells [1]. Thus, the degradation rate of the Mg implant must be such that the bone remodeling process occurs before the structural integrity of the implant is compromised.

One way to modulate the corrosion resistance and mechanical properties of Mg is alloying it with other elements. One candidate to improve the corrosion resistance of Mg is gadolinium (Gd), for example added as 5–10 wt percentage (wt. %) to Mg to form alloys [5]. Gd is a rare earth metal (RE), which is already used in medicine as contrast agent. The toxicity of Gd might be a concern, as it can accumulate in animal organs [6]. However, a systematic study on the toxicity and long-term effects of RE elements which are released as ions in the tissue is still missing. For the materials used in this study the release of Gd from Mg-xGd alloys has been shown to be below the toxicity level in cell culture [7–9]. In addition, Mg-10Gd showed in cell culture even an improved osteoblast-induced mineralization [10]. The cells grown on the Mg-10Gd alloy developed healthy cellular structures that allowed them to have good adhesion to the surface [11]. Thus, providing the essential requirements, such as initial mechanical stability, a suitable corrosion rate, and ensuring biocompatibility, Mg-Gd alloys are a possible choice as temporary implant material [12].

In addition to the general biodegradability of the material and its degradation velocity, the degradation homogeneity plays an important role for the performance as an implant material. Mg-based materials undergo galvanic, intergranular, pitting, or crevice corrosion, which all can occur in physiological environments [13,14]. Irregular, localized pitting corrosion may undermine the stability of the implant before the surrounding bone is sufficiently healed [15,16]. Hence, Mg alloys for orthopaedic use should not be subjected to pitting corrosion. To the best of our knowledge, up to now, the pitting behavior of Mg alloys is reported only in *in vitro* studies (e.g. Refs. [17,18]), and often it is only reported for bulk materials, instead that for the final implant design (e.g. Ref. [19]). The description and quantification of the degradation homogeneity of final osteofixation devices, such as pins or screws, is often missing in *ex vivo* or *in vivo* studies.

The *in vitro* degradation behavior of Mg-5Gd and Mg-10Gd screw implants has previously been presented [18]. In that study, Mg-10Gd revealed lower degradation rates, a more homogeneous microstructure degradation performance, and a weaker texture (i.e. orientation of the crystallographic poles in grains in a more random manner, which confers favorable mechanical properties), than Mg-5Gd and could therefore be more suitable as an alloy for load bearing implants. In addition, *Harmuth* et al. showed that it is possible to adjust the mechanical profile of Mg-Gd alloys to the medical requirements by tuning the extrusion process and the Gd content, without influencing the degradation rate [20].

However, the degradation performance of Mg-xGd alloys in bone requires further investigations. A recent publication showed the bone ultrastructure Mg-xGd implants, in comparison with that of more known materials as Ti and PEEK [21]. The bone at the interface with Mg-xGd screws differed significantly from that at the interface with Ti in terms of crystal lattice spacing, suggesting the Mg is potentially incorporated into the bone crystallites during implant degradation and bone healing. However, the crystal lattice spacing between the degradation layer and bone differed, which indicates that Gd potentially remains in the degradation layers and is not incorporated into the bone [21].

In the current work, we aimed to investigate the performance of the aforementioned Mg-xGd alloys with 5 and 10 wt% Gd in bone at high-resolution and over time. To this end, we have employed synchrotron-radiation micro computed tomography (SRμCT). SRμCT is a non-destructive 3D imaging technique with resolutions down to less than 1 μm. The technique enables the simultaneous assessment of the bone, the degraded implant and the degradation layer formed on the surface [22]. Due to the high resolution bone channels are visible, as well as larger secondary phases in the alloy. As the quantitative evaluation of SRμCT is time-consuming and greyscale differences between the degradation layer and bone are low, deep learning techniques can be used to speed up the segmentation process [23,24].

Using SRμCT followed by a segmentation *via* a U-Net convolutional neural network (CNN), we have assessed the bone microstructure and the *in vivo* degradation performance of Mg-xGd alloys. To this end, we implanted Mg-5Gd and Mg-10Gd screws and let them heal for 4, 8 and 12 weeks. After explantation, we studied the degradation rate (*DR*), mean degradation depth (*MDD*), pitting factor (*PF*), bone-to-implant contact (*BIC*) and bone volume fraction (*BV/TV*) and histomorphometrical parameters. Thus, we collected substantial information on the degradation behavior of the chosen materials. Screws of Ti and polyether ether ketone (PEEK) have been implanted as controls. In addition, we compared and correlated the current *ex vivo* results with data on the degradation of the same Mg-xGd alloys obtained previously *in vitro* over 4 and 8 weeks, to understand the prediction capability of *in vitro* testing of the *in vivo* behavior.

2. Materials and methods

The production procedure is described in detail in previous publications [18,23]. In brief, permanent mould direct chill casting was used for the melting and casting. The molten materials were then poured into a permanent steel mould. They were solution heat treated (T4) and indirect extrusion was performed with an extrusion ratio of 84 to the final diameter of 12 mm. Rods with a diameter of 3 mm were cut around the center (half radius) of the extruded rods by using wire erosion. The final screw shape was machined by turning and a slit head was formed by milling (4 mm length, 2 mm in diameter, thread M2 and a 0.5 × 0.5 mm slotted screw head). PEEK and Ti screws, purchased from Promimic AB (Mölndal, Sweden), were used as reference materials.

To check the alloys' homogeneity, the machining quality of the screws before implantation, and for a later comparison with the *ex vivo* results, all Mg-Gd screws were imaged by μCT using a Phoenix Nanotom benchtop μCT (GE inspection and sensing technologies, Wunstorf, Germany) at an operating voltage of 100 kV and a current of 70 μA (binned pixel size: ~2.5 μm). Screws with large Gd agglomerations or machining defects on the screw surface were discarded.

The Mg screws were cleaned in an ethanol bath, dried, and then packed in individual tubes and thereafter they were gamma-sterilized *via* gamma-irradiation sterilization at a minimum dosage of 27 kGy [25]. The Ti and PEEK screws were cleaned in ethanol bath, dried, then placed in glass vials and autoclaved.

2.1. Animal experiments

The animal experiments were conducted after ethical approval by the ethical committee at the Malmö/Lund regional board for animal research, Swedish Board of Agriculture, with the approval number DNR M 188-15. Sixty Sprague Dawley male adult rats with an average weight of 350 g were selected for the study. The rats were housed in cages of 2 or 3 animals each for at least 2 weeks before the beginning of the experiment. The implantation protocol was described in Ref. [21]. In brief, general anesthesia was administered to the rat before starting the surgical procedure and consisted in an intraperitoneal dose of Fentanyl 300 μg/kg + Dexmedetomidin 150 μg/kg. After shaving and disinfection

of the rats' legs (chlorhexidine ethanol solution 0.5 mg/ml, Klorhexidinsprit; Fresenius Kabi, Uppsala Sweden), local anesthetic was injected in the tibial area (1 ml xylocain, Aspen Nordic, Ballerup, Denmark) and a full thickness flap was created. The tibia metaphysis was exposed, and an osteotomy was drilled with a 1.4 mm round bur and then enlarged with a cylindrical bur of 1.6 mm diameter, under constant irrigation with sterile saline. After tapping, the screws were inserted with a manual screwdriver, one in each leg, leaving approximately 2–3 threads of the screw sticking out of the tibial plate, to avoid penetrating the lower cortical bone (monocortical implantation). Each rat received either 2 Mg-based screws (one Mg–10Gd and one Mg–5Gd) or two non-Mg screws (PEEK and Ti), with random allocation to the left and right leg. In total, 30 screws for each material were implanted in 60 rats. After screw insertion, the flaps were sutured. The rats received an analgesic dose of Buprenorfin of 0.01–0.05 mg/kg (Temgesic, Indivior Europe Limited, Dublin, Ireland). The rats were free to move in the cages and were fed *ad libitum*.

After 4, 8, and 12 weeks of healing, the rats were euthanized (20 rats per healing time) with a lethal dose of anesthetic. The legs were dissected, and bone was exposed around the implant area. The implants with bone around were explanted using a trephine bur of 6 mm diameter. The bone-implant blocks were fixed in 70% ethanol for at least 1 day and were then dehydrated in a graded series of ethanol. The samples were critically point dried.

2.2. SRμCT data acquisition and analysis

2.2.1. Synchrotron radiation based micro computed tomography (SRμCT)

Imaging of the critically point dried explants was performed at the P05 imaging beamline IBL, which is operated by the Helmholtz-Zentrum Hereon, at the PETRA III storage ring at the Deutsches Elektronen-Synchrotron (DESY) in Hamburg, Germany [26,27]. Samples were scanned during several beamtimes and with various settings due to technical problems with the monochromators and cameras. Various photon energies ranging from 25 to 45 keV were used employing a double crystal monochromator (DCM) or a double multilayer monochromator (DMM). The horizontal beam profile of both monochromators is about 6.5 mm. The vertical beam profile of the DMM is about 7 mm. This is due to an increased vertical divergence of the DMM caused by a slightly bent crystal introduced by its holder. The vertical beam profile of the DCM ranges from about 1.5 to 3.5 mm depending on the X-ray energy. When using the DCM, two height scans were necessary to image the sample. An indirect detector system was used where X-ray photons, which are transmitted by the sample, are converted to optical light by a cadmium tungstate (CdWO4) scintillator screen. The optical light is magnified by a microscope optic and detected by a camera. Two cameras were used: a camera with a CCD (charge-coupled device) sensor (KAF-09000) with 3056 × 3056 pixels, a 16-bit dynamic range and a pixel size of 12.0 μm, and a camera with a CMOS (Complementary metal–oxide–semiconductor) sensor (CMOSIS CMV 20000), which was developed in collaboration with KIT [28], with 5120 × 3840 pixels, a 12-bit dynamic range and a pixel size of 6.4 μm. An objective lens with a fivefold magnification was used resulting in an effective pixel size of 2.4 μm and 1.2 μm, respectively. All samples were imaged using attenuation contrast and a step-wise rotation. For the CCD camera 1200 projections were used. To account for the higher noise and the lower dynamics of the CMOS camera compared to the CCD, a higher number of projections was used from 2400 up to 3000 depending on the lateral extend of the sample and the X-ray energy. Data pre-processing (flat and dark field correction, pixel filtering, beam current normalization) and tomographic reconstruction was implemented in MATLAB (The MathWorks, Inc.) using the tomographic reconstruction pipeline at IBL [29,30]. For tomographic reconstruction the filtered back projection (FBP) algorithm was employed using the ASTRA toolbox for back projection [31,32].

2.2.2. Image segmentation of SRμCT data, registration and resampling of pre-implantation screw

The bone-implant interface exhibits a heterogeneous texture with a linear attenuation coefficient for the degradation layer that varies from the one of bone and the residual alloy, resulting in similar grey values for both materials. Therefore, automatic segmentation approaches failed when applied to the *ex vivo* datasets of the Mg-xGd screws [33]. Due to the fragmented texture of the bone-implant interface, the semi-manual segmentation using a watershed algorithm with an iterative refinement was very cumbersome and time-consuming. Hence, a deep learning based segmentation using a U-net convolutional neural network (CNN) was developed using the hitherto manually segmented annotations as training data [24]. In the segmentation process four labels were used: residual alloy, degradation layer, bone and background. The three-dimensional (3D) volume renderings of the labels are visualized in Fig. 1, while an example cross sectional slice of two Mg-10Gd implants showing the mixture of the materials and tissues with different X-ray attenuation is given in Fig. 2. The denotations used during the analysis process are listed and described in Table 1.

2.2.3. Image analysis of SRμCT data

After segmentation of the *ex vivo* image, the "pre-implantation screw" was registered and resampled on the "screw with degradation layer". All *ex vivo* data were resampled to a voxel size of 5 μm and the longitudinal axis of each screw was aligned parallel to the z-axis of the coordinate system (example of a transverse view in Figs. 1C and 2A) prior to the analysis. Here, a voxel size of 5 μm was chosen to accelerate the data processing. The parameters are investigated as 2D and 3D parameters and are summarized in Table 2 (with definitions following in subsequent sections).

The 3D calculations consisted in the calculation of the various parameters over the entire volume. The 2D calculations consisted in the calculation of the various parameters on each slice of each data-set and resulted in a statistical mean value and standard deviation for each parameter. The standard deviation of the certain parameter gives statistical information on the parameter's performance along the screw's height. Hence, the 2D calculations are beneficial, since more information with less samples can be gained.

The 2D and 3D calculations are described in details in another publication [18]

2.2.3.1. Degradation rate (DR), mean degradation depth (MDD), volume loss (ΔV) and pitting factor (PF). The degradation rate (*DR*), the mean degradation depth (*MDD*), the volume loss (Δ*V*) and the pitting factor (*PF*) are defined as

$$DR\ [mm\ a^{-1}] = \frac{\Delta V}{A \cdot t} \tag{1}$$

$$MDD\ [\mu m] = DR \cdot t \tag{2}$$

$$PF = \frac{DP}{MDD} \tag{3}$$

where denotes *A* the initial surface area, *t* the degradation time, and *DP* the depth of deepest pit. By fitting a line to the *MDD* values, the slope of the fitted line was calculated and defined as the global degradation rate (*GDR*) in mm a^{-1}. Details of the calculations are described in Ref. [18].

2.2.3.2. Bone to implant contact (BIC). In order to evaluate how well the implant is integrated into the bone (osseointegration), in the tomographic data the bone to implant contact *(BIC(t)*, where *t* stands for tomography*)*, which is the contact area of the screw (with the degradation layer) and the surrounding bone, is calculated (see Fig. 1B for the visualization of the *BIC(t)*). The normalized *BIC(t)* is given by:

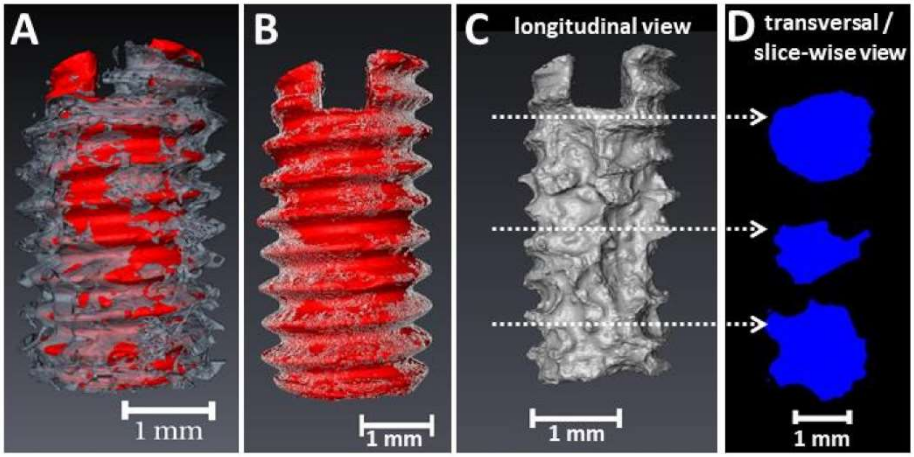

Fig. 1. Visualization of a SRμCT scan of a Mg-10Gd implant after 8 weeks *in vivo* using 3D volume renderings (A–C) and cross sections (D). (A) Screw with degradation layer (red) with 200 μm of surrounding bone (grey). (B) Visualization of the BIC (white) over the screw with degradation layer (red). (C) Residual alloy. (D) Transversal cross sections of the residual alloy as indicated in (C). (For interpretation of the references to color in this figure legend, the reader is referred to the Web version of this article).

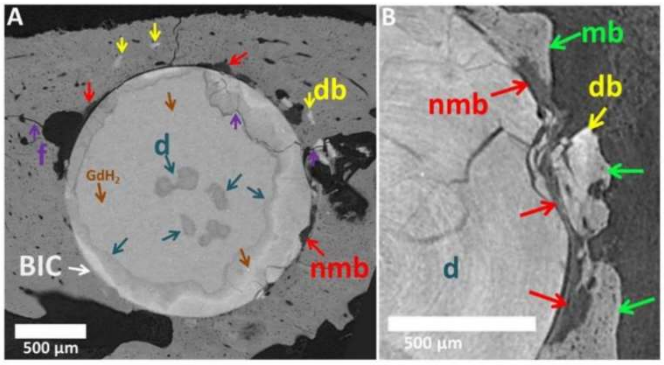

Fig. 2. Cross sections of SRμCT scans of two different Mg-10Gd implants after 12 weeks *in vivo* degradation; f = fracture, db = degradation layer in bone, nmb = non-mineralized bone (newly formed bone), mb = mineralized bone, d = degradation layer. Cross-sectional slices of Mg-5Gd, PEEK and Ti can be found in appendices, Fig. 10.The non-mineralized bone is referred as osteoid, because of its very low X-ray attenuation which indicates low levels of Ca. The lacunae and blood vessels are the pores within the mineralized and non-mineralized bone, which differ in size. Lacunae are ellipsoids with sizes smaller than approx. 15 μm. Bigger holes in the mineralized matrix are identified as vessels.

$$3D\text{–}BIC(t)\ [\%] = \frac{\#\ surface\ voxels\ of\ implant\ in\ contact\ with\ bone}{\#\ total\ surface\ voxels\ of\ ncs} \quad (4)$$

here, the implant stands for the *screw with degradation layer*, defined earlier in Table 1. To determine the contact voxels, the implant layer was dilated once using the image processing package Fiji/ImageJ [34,35] and added to the label bone. The voxels shared by the label "implant" and the label "bone" were defined as in bone-to-implant contact (BIC).

2.2.3.3. Bone volume fraction (BV/TV). In order to evaluate the influence of the materials on the surrounding bone formation and the extent of this influence at different distances from the screw, the bone volume (*BV*) normalized by the total volume (*TV*) was calculated in two different volumes of interest (VOIs) around the screws [36]. To two VOIs were obtained as subvolumes from the entire dataset volume by dilating the pre-implantation registered screw 20 and 40 times, respectively, to obtain a 100 μm (VOI1) and 200 μm (VOI2) volume of interest around each screw. The choice of these VOIs is based on the thread's depth of the M2 screws, which is 250 μm. VOI1 represent a volume in close proximity to the screw surfaces and VOI2 represents the volume inside the threads and around the thread tips (Fig. 1A). The number of voxels occupied by mineralized bone in the VOIs in the bone volume (BV) and is calculated as a ratio over the entire volume of the tissues in the VOIs

Table 1
Explanation of the denotations used during the μCT image analysis.

Name	Explanation
Pre-implantation screw	Volume of the screws prior to implantation measured on Nanotom lab-source μCT (applies only to the Mg-based screws, as the PEEK and Ti screws are expected not to change their shape during time)
Residual alloy	Volume of the screw in the explanted samples that did not corroded during the observation period. Calculated from the visible screw-shape implants without the degradation layer, on the basis of the absorption behavior.
Degradation layer	Corrosion products of Mg alloys in the explanted samples, remaining attached to the original metal, often maintaining the original threaded shape and distinguished from the original metal on the basis of the absorption behavior.
Screw with degradation layer ("degraded screw" or "implant")	Volume of the residual alloy and the attached corrosion layers, distinguished from the bone and the other surrounding tissues.
Bone	Volume of the mineralized tissue surrounding the implants in the explants.
Background	Volume of the all the remaining materials that were not assigned to the above labels (like soft tissues, air, water, etc.)

Table 2
Analysis parameters of the SRμCT *ex vivo* samples.

Parameter	Dimension of investigation	
	3D	2D
Degradation rate (DR)	✓	-
Mean degradation depth (MDD)	✓	-
Volume loss	-	✓
Pitting factor (PF)	✓	✓
Bone-to-implant contact (BIC)	✓	✓
Bone volume fraction (BV/TV)	✓	-

(*BV/TV*), following the formula:

$$3D - \frac{BV}{TV}[\%] = \frac{\#\ voxels\ of\ bone\ volume}{\#\ voxels\ of\ total\ volume\ of\ the\ VOI} \quad (5)$$

2.2.3.4. Additional segmentation. Due to the weak contrast between the non-mineralized bone and the background, the segmentation could not automatically discriminate the non-mineralized bone from the background in the SRμCT. Non-mineralized bone, present especially at the shorter healing times, was not segmented as bone, but was instead

included in the background layer as the soft tissues, and therefore it was excluded from the calculation of the *BIC* and *BV/TV* parameters.

However, on the SRμCT data it was possible to visually identify newly formed non-mineralized bone by the presence of the osteocytes lacunae, as seen in Fig. 2B [37].

To obviate to this problem and to try to quantify the amount of non-mineralized bone, 3 datasets of the Mg-10Gd after 12 weeks in bone were randomly selected and further segmented semi-automatically *via* a region growing algorithm using Avizo (version 9.4.2, Thermo Fisher Scientific, Waltham, MA), to identify and label the newly-formed non-mineralized bone.

Another aspect that was not possible to segment automatically with the deep learning segmentation method was the fragments of the degradation layer that occurred in some samples and were detached from the implants and integrated into the surrounding tissues (Fig. 2B). For that reason, on the same 3 datasets of Mg-10Gd at 12 weeks of healing, the fragments of the degradation layers were segmented semi-automatically *via* a region growing algorithm using Avizo and quantified.

The additional segmentation was not applied to all the dataset because it was greatly time-consuming.

2.2.3.5. Comparison of in vitro results from Ref. [18] with ex vivo results from this study. Because it is of great interest to understand the predictive capability of *in vitro* studies on the degradation behavior of Mg alloys in bone, the current data obtained by SRμCT in rats at 4, 8 and 12 weeks were compared to similar SRμCT data obtained from an *in vitro* study on the same alloys (Mg-5Gd and Mg-10Gd) in the same M2 screw shape, observed for 4 and 8 weeks. All the details of the *in vitro* experiment are reported in Ref. [18].

In brief, the correlation between and *ex vivo* and *in vitro* results was done by calculating the ratio between each *ex vivo* parameter and the *in vitro* parameter ($p_{ex\ vivo}/p_{in\ vitro}$) at 4 and 8 weeks (the common observation point between the 2 studies), where p is the parameter of the interest plotted on the x-axis. Both for $p_{ex\ vivo}$ and p_{in} *vitro* the mean value of the calculation is taken, since there were different amounts of samples in both experiments.

2.2.4. Histology

After SRμCT imaging, the explants were re-infiltrated in absolute ethanol and then embedded in methyl methacrylate resin by LLS Rowiak LaserLabSolutions GmbH (Hanover, Germany). Each sample was cut in half along the screw longitudinal axis with an Exakt saw. One half of each sample was then prepared for non-decalcified histology with the cutting-grinding technique *ad modum* Donath [38]. Sections of about 40 μm were obtained and stained with a solution of Toluidine Blue-Pyronine Y. The other halves of 36 samples (three per material and time point, randomly selected) were prepared for tartrate-resistant acid phosphatase (TRAP) staining, to identify osteoclasts activity in the proximity of the implants. These halves were laser cut with Tissue Surgeon by LLS Rowiak LaserLabSolutions GmbH (Hanover, Germany). Laser microtomy produced approximately 10 μm thick sections of the bone surrounding the implants (not including the implants but including some degradation layer) mounted on glass slides. The sections were then stained with TRAP using a modification of the protocol described in Ref. [39]. The modified protocol is proprietary by LLS Rowiak (Hanover, Germany). The reagents were purchased from Carl Roth (Karlsruhe, Germany). All stained sections were imaged with a white light optical microscope equipped with a camera (Nikon Eclipse Ci-L and DS-Fi3 camera, Tokyo, Japan). Automatic white-balance was performed on areas of non-tissue background and images were taken at the same exposure conditions. Quantitative histomorphometry was performed using the image analysis software Fiji/ImageJ [34,35] and the parameters defined in the following subsections were calculated.

2.2.4.1. Bone to implant contact (BIC(h)). The bone to implant contact from the histology images (*BIC(h),* where *h* stands for histology) was measured on toluidine blue stained sections at 200x magnification. *BIC* (*h*) was calculated as the percentage of the implant perimeter in direct contact with bone, versus the entire implant perimeter inserted in bone (therefore, the parts of the implants sticking out of bone and the implant perimeter inside the screw driver slot were not included in the analysis). For the Mg-based screws, as "screw" was considered the threaded-shaped implant, that included both residual alloy and degradation layers.

2.2.4.2. Bone area (BA(h)). Two regions of interests (ROIs) were designed around the screws on toluidine blue stained histological images at 200x magnification. The ROIs included an area of tissue enlarged orthogonally of 100 μm (ROI1) or 200 μm (ROI2) from the perimeter of the screw in each sample. These areas were chosen to describe the influence of the materials on the tissues in the immediate proximity of the implant surfaces (ROI1) and in an area included in the thread depth (ROI2). They overlapped with the selected VOIs.

Bone tissue was segmented from non-bone tissue in the histological images by manual segmentation. The bone area from the histology images (*BA(h)*, where *h* stands for histology) is defined as the area occupied by bone in each ROI, versus the entire area of each ROI. Again, only the area of the implants inserted in the bone was considered for the analysis.

2.2.4.3. Tartrate resistant acid phosphatase (TRAP)-positive area percentages (TRAP%). This parameter was measured on TRAP-stained sections at 200x magnification. Red-colored pixels were segmented with a color thresholding method in Image J from the non-colored background. The same ROI2 designed for the toluidine blue histological slides was employed also for the TRAP-stained slides. The TRAP-positive area percentage for each sample was calculated as the area stained in red in the ROI2 versus the entire area of ROI2.

2.2.5. Statistical analysis

The mean, median, and standard deviation of all analyzed parameters were calculated for each group. To measure the variation of the pitting factor (*PF*), the volume loss (*volume loss*) and the bone to implant contact (*BIC*) over the entire screw along its longitudinal axis, the coefficient of variation (CV) [40] were calculated. The latter is defined as the ratio of the 2D standard deviation to the 2D mean of the parameter of interest [18]. The *CV PF, CV volume loss* and *CV BIC* are used to assess the degradation homogeneity.

Pearson's R correlation (linear correlation) was used to calculate the dependency between the investigated parameters, assuming a normal distribution of the data (in MATLAB R2019b).

Bone-to-implant calculations obtained with histology and SRμCT were compared using a pair Person correlation (a pair being the results of the calculation with the two methods on the same sample). Both *3D BIC(t)* and the mean of *2D BIC(t)* for each sample were compared with the *BIC(h)*.

The mean values of all 2D and 3D parameters for each group (material, time point) were compared using a two-way analysis of variance (ANOVA) multiple comparison test in MATLAB R2019b (The MathWorks Inc., USA) and SPSS Software (IBM, Version 26 USA). Multiple testing correction was performed using the Bonferroni adjustment method [41]. A p-value below 0.05 was considered statistically significant.

3. Results

All 60 rats recovered from anesthesia and surgery, and completed the observation period. Nevertheless, not all scanned samples could be properly analyzed after SRμCT due to insufficient image quality and not

all samples could be processed for histology, due to technical problems.

The number of analyzed samples for each material and time is presented in Table 3.

3.1. Implant degradation velocity and homogeneity from SRμCT analysis

All parameters obtained from SRμCT data are presented in Fig. 3 as box plots, while exemplary longitudinal slices of the bone-implants samples are presented in Fig. 4. All values with details can be found as the supplementary information (Table 6 and Table 7). The significant differences observed are displayed in Table 4. The comparison between the *in vitro* volume loss measurements and *ex vivo* analyses is presented in Fig. 5, and the corresponding values can be found in Table 8.

3.1.1. Degradation rates

Both alloys revealed *DR*s below 1 mm a^{-1} at all time periods (Fig. 3A). There were no significant differences in the *DR*s of different materials for the same time points.

The *MDD* of the *in vivo* corroded implants is presented in 3B. The fitted lines in 3B represent the *GDR* (see Equation (2)). The *GDR* of Mg-5Gd (0.18 mm a^{-1}) is more than twice as high as that of Mg-10Gd (0.077 mm a^{-1}).

3.1.2. Coefficient of variation of volume loss (CV volume loss)

The coefficients of variation of the volume loss (*CV volume loss*) are presented in Fig. 3C. High values for both alloys indicate a high variability in the amount of the degradation layer in different parts of each implant. This inhomogeneity of the degradation performance can be observed in Fig. 4A where the Mg-10Gd screw displays regions with threads that appeared intact, while in most other region they are degraded entirely. When studying Mg-5Gd and Mg-10Gd alloys, we observe a decreasing tendency of *CV volume loss* over time for both alloys. At all time points, Mg-10Gd showed a higher variation between the *CV* values than Mg-5Gd. The latter further showed smaller values of the variation and mean at 4 and 8 weeks than at 12 weeks. This indicates, that Mg-10Gd degraded more inhomogeneously than Mg-5Gd until the 12-week time point. However, for the *CV volume loss*, no significant differences were found for the different materials at the same time points.

3.1.3. Pitting factor (PF)

The 3D pitting factor (*3D PF*), 2D pitting factor *(2D mean PF)*, and coefficient of variation of the 2D pitting factor (*CV 2D PF)* are represented in Fig. 3D–F and Table 6. A tendency for the *3D PF* to decrease over time was observed for both materials. No significant differences of the *3D PF* could be found for the two materials and at the same time points. No significant differences of the *2D mean PD*s and *2D CV PF*s were observed, neither between alloys nor time points, and the values were lower than the *3D PF* values.

3.2. Comparison ex vivo - in vitro

In Fig. 5, the ratios between *ex vivo* and *in vitro* results (*in vitro* results shown in Ref. [18]) for 5 selected parameters are displayed.

The DRs observed *ex vivo* were higher than the *in vitro* ones for the same time points (4 and 8 weeks). The difference is notably higher for Mg-10Gd (2.8 and 2.6 times for 4 and 8 weeks, respectively) than for Mg-5Gd (2 and 1.5 times for 4 and 8 weeks, respectively).

The CV volume loss obtained *ex vivo* is almost 4 times higher compared to the one obtained in *in vitro* experiments, indicating a more inhomogeneous distribution of the degradation layer *ex vivo* (Fig. 5).

The comparison of *ex vivo* and *in vitro* homogeneity behavior reveals that *3D PF*, *2D mean PF* and *CV 2D PF* are similar for Mg-10Gd in both experiments (except *CV 2D PF* after 4 weeks). For Mg-5Gd, the *2D mean PF* are similar in both experiments. The mean ratios of the *CV PF* are between 1 and 2, meaning the *ex vivo* samples show higher overall inhomogeneity than the *in vitro* ones. This indicates that the degradation homogeneity of Mg-10Gd is similar for the *ex vivo* and *in vitro* results.

Table 3
Amount of *ex vivo* samples investigated via SRμCT and histologically.

	SRμCT			Histology		
	4 weeks	8 weeks	12 weeks	4 weeks	8 weeks	12 weeks
Mg-5Gd	9	10	6	10	10	6
Mg-10Gd	8	9	8	7	10	9
Ti	5	8	8	9	9	10
PEEK	9	10	9	10	10	9

3.3. Implant integration into the bone from SRμCT and histology

3.3.1. Bone-to-implant contact (BIC)

The results of the osseointegration analyses of all four implant materials, calculated on tomographic data, are presented in Fig. 3G–I (Table 7 in appendix).

All implants showed increasing *3D BIC(t)* over time. Significant differences were found between PEEK and all other materials at all times points. PEEK implants showed on average between 25% and 50% lower *BIC(t)* than the other materials at all time points. This can also be observed in Fig. 6 showing magnifications of a thread for each material. After 12 weeks of implantation, a gap is still visible between the PEEK surface and the surrounding bone, indicating a low osseointegration (Fig. 6C), in contrast to all other materials. Ti implants yielded the highest average *3D BIC(t)* at 4 and 8 weeks. At 12 weeks both Mg alloys reached similar values as Ti, with Mg-10Gd having the highest average *3D BIC(t)* at the longest follow-up time. In general, Mg-5Gd revealed lower (4 weeks) or similar (8 and 12 weeks) *3D BIC(t)* values compared to Mg-10Gd. Both Mg-xGd implants showed smaller variations in *3D BIC (t)* at 12 weeks than the Ti implants.

Since the *2D mean BIC(t)* is nearly equal to the *3D BIC(t)*, it is neither presented in a graph nor discussed. The results of the *CV 2D BIC(t)* are shown in Fig. 3H. The lowest variations were observed in Mg-xGd implants, with Mg-10Gd having slightly lower values than Mg-5Gd. The highest variation was observed in PEEK implants, which can be related to the inhomogeneous distribution of bone-to-implant contact along the implants. Significant differences are found between PEEK after 8 weeks implantation and Mg-10Gd after 8 weeks of implantation. Additionally, a significant difference is observed between PEEK and Ti implants after 8 weeks of healing.

Three Mg-10Gd samples were analyzed after 12 weeks of implantation with respect to the non-mineralized, as well as the mineralized bone. The *3D BIC(t)* excluding the non-mineralized bone resulted 48.1% ± 1.2%, but after adding the non-mineralized bone it became 49.4% ± 1.6%.

The *BIC(h)* was calculated on histological slides stained with toluidine blue to recognize bone tissue. The results are displayed in Fig. 6A (and in Table 7 in the appendix). Exemplary slices of Ti, PEEK and Mg-5Gd explants can be found in Fig. 7.

For all materials, *BIC(h)* increased from 4 to 8 weeks but remained similar between 8 and 12 weeks. The lowest *BIC(h)* values were observed for PEEK at all time points and the difference was statistically significantly lower for PEEK compared to the other 3 materials at each time point. Both Mg alloys showed higher *BIC* than Ti at 4 weeks with a statistically significant difference between Mg-10Gd and Ti. The average *BIC(h)* values of Mg-5Gd and Mg-10Gd were slightly higher than those of Ti even at 8 and 12 weeks, but at this time point the difference was small and not statistically significant.

3.3.2. Bone volume fraction (BV/TV(t)) and bone area (BA(h))

The tendency of the bone volume fraction *BV/TV(t)* was the same for all materials and volumes of interest (VOIs). Therefore, only the results for the 200 μm VOI are discussed and the values for the 100 μm VOIs are

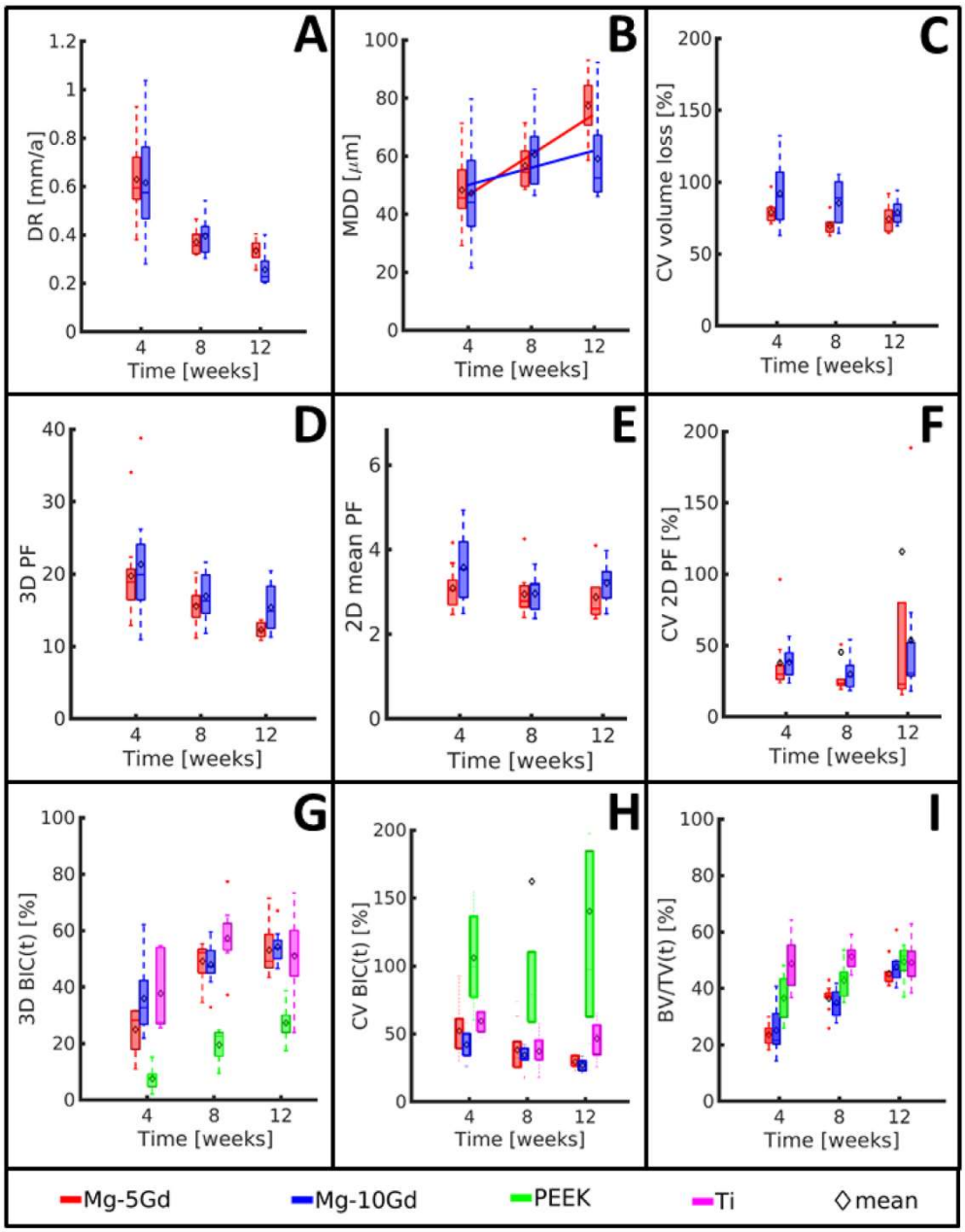

Fig. 3. Box plots of the results of the *ex vivo* investigation of Mg-5Gd, Mg-10Gd, PEEK and Ti screw implants over 4, 8, 12 weeks healing period from SRμCT images. (A) Mean degradation depth (*MDD*) with the fitted global degradation rate (*GDR)*, (B) Degradation rate (*DR*), (C) Coefficient of variation of the volume loss (*CV volume loss*), (D) 3D pitting factor (*3D PF*), (E) 2D pitting factor (*2D mean PF*), (F) Coefficient of variation of 2D pitting factor (*CV 2D PF*), (G) 3D Bone implant contact (*3D BIC*), (H) Coefficient of variation of 2D bone implant contact (*CV BIC*), (I) Bone volume density in a 200 μm VOI around the screw surfaces (*BV/TV*). (Middle line of box plot represents the median, ◇ represents the mean, whiskers correspond to 99% confidence interval. See Table 7 and Table 6 for numeric values).

presented in supplementary Table 7. The results of the *BV/TV(t)* for VOI2 are presented in Fig. 3I. Ti samples revealed high *BV/TV(t)* values at each time point. In particular, already after 4 weeks of implantation, the amount of bone around Ti implants was close to 50% and remained stable at longer time points. PEEK implants showed a *BV/TV* close to 40% at 4 weeks which increased with time, with the highest average value for all material at 12 weeks (49.4%). At 4 weeks, both Mg alloys showed a *BV/TV* close to 20%, which raised to around 35% at 8 weeks. After 4 and 8 weeks of healing, Mg-xGd implants exhibited significantly lower *BV/TV* values than Ti and PEEK implants. Similarly, for PEEK screws, the average values of *BV/TV* at 4 and 8 weeks were significantly lower than those of Ti. However, at the 12 weeks mark, all materials yielded similar *BV/TV* values, without statistically significant differences (between 45% and 49.3%).

For three Mg-10Gd samples after 12 weeks of *in vivo* degradation the *BV/TV(t)* was calculated including mineralized bone only resulting in a *BV/TV(t)* of 36.6% ± 5.6%, also including non-mineralized bone resulted in a *BV/TV(t)* of 37.6% ± 5.7%.

Bone area *(BA(h))* on the histological slides is the parameter to be compared to the bone volume density (*BV/TV(t))* on tomographic data. It was calculated on two ROIs of 100 and 200 μm from the screw surface. The results of *BA(h)* in the 200 μm ROI are displayed in Fig. 4B (and in Table 7 in the appendix) and discussed below. The results for the other ROI are presented as supplementary material in Table 7.

Ti implants showed a rather stable *BA(h)* over time, between 56.9% ± 13.6% at 4 weeks and 64.8% ± 8.9% at 12 weeks. The *BA(h)* of Ti was significantly higher than that of Mg-5Gd at all three times. The *BA(h)* of PEEK was the one that varied most over time, with an average value of 51.5% ± 11.6% at 4 weeks, which grew to 64.8% ± 11.5% at 8 weeks and 65.26% ± 14.6% at 12 weeks. Both values were the highest of all groups and the difference was statistically significant with Mg-5Gd and Mg-10Gd at 8 weeks, and Mg-5Gd at 12 weeks. The *BA(h)* of Mg-10Gd remained almost constant over time, while that of Mg-5Gd was lower at 4 weeks (44.7% ± 11.4%) and then increased to 53.0% ± 8.6% over time.

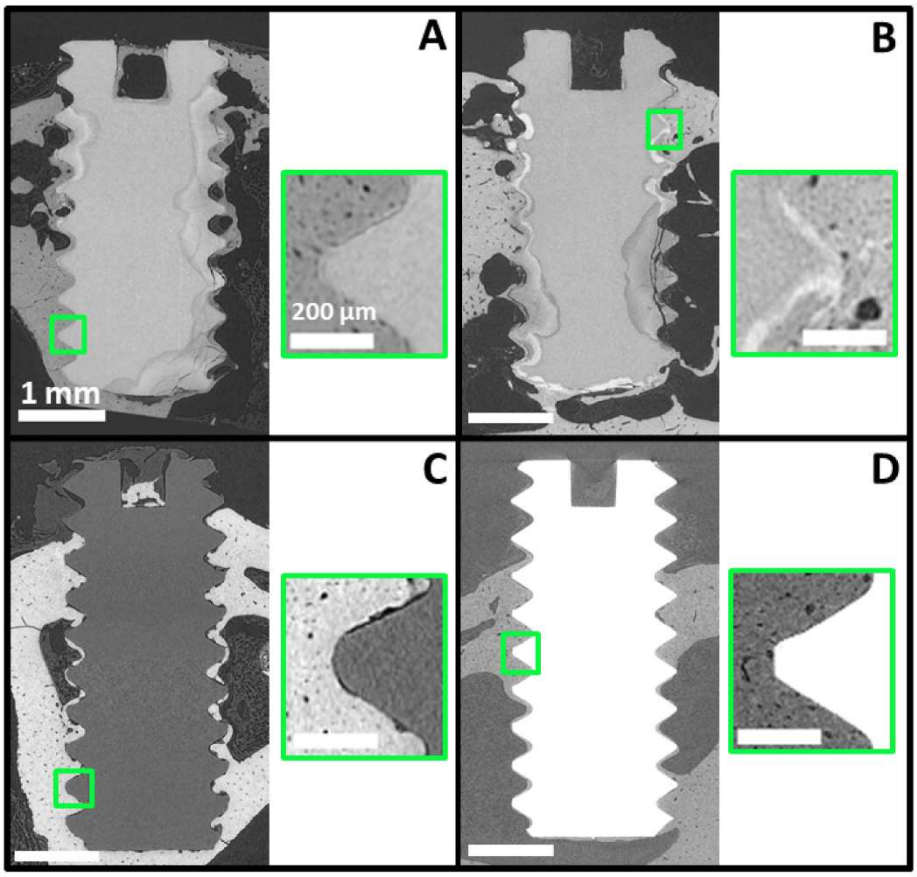

Fig. 4. Longitudinal slices of *ex vivo* SRµCT scans 12 weeks after implantation. (A) Mg-10Gd, (B) Mg-5Gd, (C) PEEK, (D) Ti. The image contrast was adjusted for better visualization, which results in the different grey level appearances of the bone in the images. The respective scale bars apply to all images. The thin black space between the bone (whiter) and the PEEK (darker grey) in (C) PEEK is the background, a small gap between the bone and the implant. Such gap is not visible in (A) Mg-10Gd, (B) Mg-5Gd or (D) Ti. This gap for PEEK can be found also in Fig. 10 in appendices.

Table 4
P-values; *DR ($p < 0.05$); ◊MDD ($p < 0.05$); +CV volume loss ($p < 0.05$); ○3D PF ($p < 0.05$); 2D mean PF ($p < 0.05$: no significant differences at all); CV PF ($p < 0.05$: no significant differences at all); ᵛ3D BIC ($p < 0.005$); □CV BIC ($p < 0.05$); ●BV/TV 200 µm ($p < 0.001$).

		Mg-5Gd			Mg-10Gd			PEEK			Ti		
		4	8	12	4	8	12	4	8	12	4	8	12
Mg-5Gd	4												
	8	*v											
	12	*◊v●											
Mg-10Gd	4		*+○	*◊●									
	8	*v											
	12	*v●			●								
PEEK	4		v	v	v	v	v						
	8	●	v□	v	●	v□	v□						
	12	v●			●			v	v				
Ti	4	●			●			v					
	8	v●	●		v ●	●		v●	v□				
	12	v●			●			v	v				

3.3.3. Tartrate resistant acid phosphatase (TRAP)-positive area percentages (TRAP%)

The presence of TRAP-positives regions in histological slides represents osteoclasts activated for bone resorption. There was a statistically significant difference in TRAP-positive regions among materials and at different healing times. The highest osteoclast activation for all materials was at 4 weeks, and the difference was statistically significantly higher compared to the other two time points. Then, for Ti sample, it decreased gradually with time, while for Mg-5Gd, Mg-10Gd and PEEK samples, it decreased from 4 to 8 weeks, then slightly increased between 8 and 12 weeks, but the difference between these two points was not statistically significant.

Mg-5Gd slides at 4 weeks showed the highest number of TRAP-positive locations among all materials, statistically significant higher than the other three materials. The differences among Mg-10Gd, PEEK and Ti were not statistically significant at any of the three time points.

In general, active osteoclasts were concentrated mostly on the surfaces of trabecular bone within the medullar regions of the tibia and less on the cortical regions. Osteoclasts were sporadically found directly on the surfaces of the degradation layer of Mg-5Gd samples (see Fig. 8).

Activated osteoclasts are visible as TRAP-positive pixels (grey arrows). At 4 weeks many TRAP-positive areas are present, especially in the trabecular bone and in regions very close to the implant surfaces. Some active osteoclasts are stained near the degradation layer (asterix). At 12 weeks, very few active osteoclasts could be observed.

Table 5
Strength and direction of the linear correlation between the investigated parameters [29].

P1	P2	Mg-5Gd	Mg-10Gd	PEEK	Ti
3D BIC (t) [%]	***DR [mm a^{-1}]***	MS: −0.76 (p = 0.000)	MS: −0.74 (p = 0.000)		
3D BIC (t) [%]	***3D PF [a. u.]***	F: −0.42 (p = 0.033)	P: −0.05 (p = 0.000)		
DR [mm a^{-1}]	***3D PF [a. u.]***	P: 0.15 (p = 0.472)	P: −0.19 (p = 0.355)		
3D PF [a.u.]	***3D BV/TV(t) [%]***	MS: −0.60 (p = 0.001)	F: −0.37 (p = 0.065)		
3D BIC (t) [%]	***3D BV/TV(t) [%]***	VS: 0.86 (p = 0.000)	MS: 0.75 (p = 0.000)	MS: 0.73 (p = 0.000)	P: 0.07 (p = 0.831)
BIC(h) [%]	***3D BIC (t) [%]***	MS: 0.74 (p = 0.000)	M: 0.554 (p = 0.008)	M: 0.56 (p = 0.002)	MS: 0.62 (p = 0.004)
BIC(h) [%]	***2D BIC (t) [%]***	MS: 0.74 (p = 0.000)	M: 0.53 (p = 0.01)	P: 0.32 (p = 0.1)	MS: 0.64 (p = 0.003)
BIC(h) [%]	***BA [%]***	P: 0.25 (p = 0.21)	P: 0.15 (p = 0.48)	M: 0.49 (p = 0.013)	M: 0.42 (p = 0.025)
BA [%]	***3D BV/TV(t) [%]***	M: 0.5 (p = 0.007)	P: 0.28 (p = 0.22)	MS: 0.60 (p = 0.002)	MS: 0.73 (p = 0.000)

Table legend: P1 and P2: parameters correlated; VS = very strong, MS = moderately strong, F = fair, P = poor; value: correlation coefficient; p-value: significance of the correlation; 3D BV/TV and BA values are those in the VOI2 and ROI2, within 200 μm from implant surface. The p-values represent the probability that the correlation between investigated parameters occurs by chance.

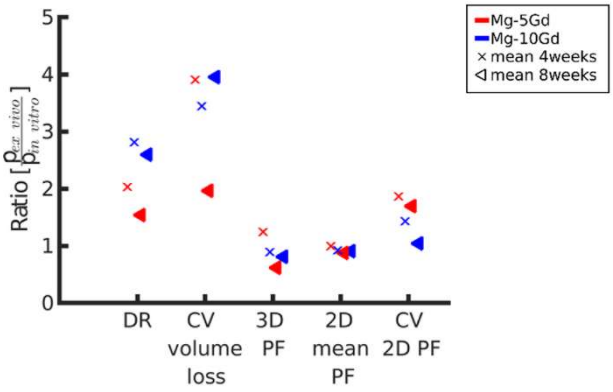

Fig. 5. Ratio between mean *ex vivo* and mean *in vitro* analysis parameters (p). The parameters plotted on the x-axis are degradation rate (*DR*), coefficient of variation of the volume loss (*CV volume loss*), 3D pitting factor (*3D PF*), 2D pitting factor (*2D mean PF*) and coefficient of variation of the 2D pitting factor (*CV 2D PF*). The *in vitro* analysis is published in Ref. [18]. The results are summarized in Table 8.

3.4. Correlations

The results of Pearson's correlation of different parameters are presented inTable 5 with the interpretation of the Pearson's correlation coefficient R from Ref. [42]. Only one very strong correlation between *3D BIC(t)* and *3D BV/TV(t)* was found for Mg-5Gd. This suggests a dependency between the amount of the bone growing in the surrounding of the screw and the bone in direct contact with the Mg-5Gd surfaces. For Mg-10Gd and PEEK the correlation was moderately strong. By contrast, there was no correlation for Ti implants. A moderately strong inverse correlation was found between the *DR* and the *3D BIC(t)* in Mg-5Gd and Mg-10Gd implants. Another moderately strong inverse correlation was found between the *3D PF* and *3D BV/TV(t)* of Mg-5Gd alloy implants. This dependency was just fair for Mg-10Gd. A fair inverse correlation was seen between *3D BIC(t)* and *3D PF* for Mg-5Gd, while there was a very poor, correlation for Mg-10Gd. For both alloys there was a very poor correlation found between *DR* and *3D PF*.

3.5. Qualitative observations

3.5.1. Degradation layer behavior

One characteristic aspect of the degraded Mg screws was that they maintained the original threaded shape while they transformed into degradation products. The degradation layers displayed a different grey values range in the tomograms and a different color in the histological slides compared to the original metal. In particular, on histological sections stained with toluidine blue, the degradation layers of Mg-xGd implants were stained in pale purple similarly to the surrounding bone (Fig. 7), but could be distinguished from the bone because they lacked the presence of cells.

The registration of the tomographic and histological images of the same samples confirmed that what was identified as degradation product on the basis of the grey value, was also stained in purple and identified as degradation layer in the histological images (Fig. 9). This observation validated our segmentation procedure (section 2.2.2).

Some parts of the degraded screw threads were broken, which might indicate a brittle behavior of the degradation layer (Figs. 2 and 6A and B). Tomograms of three Mg-10Gd screws after 12 weeks healing were visually inspected and segmented with respect to the amount of the degradation layer which was fractured and fully isolated from the screw. Averaged over three samples, 0.62% ± 0.34% of degradation layer was found to be fractured of which 4.6% ± 1.34% were surrounded by bone. The degradation layer debris were often surrounded by mineralized bone and sometimes newly formed non-mineralized bone grew into the fracture line between a detached debris and the implant (Fig. 2B). Cross-sectional SRμCT images of Mg-5Gd, PEEK and Ti as comparison to Fig. 2 after 12 weeks *in vivo* degradation can be found in appendices (Fig. 10).

3.5.2. Tissue integration and tissue reactions around different materials

Bone tissue surrounded the implants of all materials already at 4 weeks, and its amount increased continuous up to week 12. Bone grew into the screw threads, and a thin layer of bone encapsulated most of the screws extending even in those areas that initially were not in contact with bone surfaces (i.e. the medullar space of the tibia). We observed a higher amount of woven bone around the Mg alloys, especially at 4 weeks, while the bone around Ti and PEEK looked more mature. Woven bone was identified by its darker purple/blue color and the presence of larger osteocytes lacunae (magnifications in Fig. 9) with a round shape compared to mature bone that displayed a paler lilac/purple coloration and smaller and almond-shaped osteocyte spaces. Newly formed bone was found predominantly facing regions of the implants that were more degraded, while more mature bone was observed incorporating areas of the implant with less corrosion. Because of the extreme time consumption, quantification of that bone was not possible. The newly formed bone appeared sometimes detached from the surface of the degradation layer, especially in the 4-week samples, but that was likely an artefact of the critical point drying process. Bone was in tight contact with the screw surface of the three metallic materials tested, especially after 12 weeks of healing (Fig. 7). Many of the Mg screws at 12 weeks of healing showed a seamless connection of bone and degradation layers which was hard to distinguish on histological slices, especially considering that the corrosion layer was stained in the same light purple color of the bone (see Fig. 7, in particular the Mg-10Gd screw). Osteocyte lacunae in the bone demarcating Mg materials often appeared to be oriented parallel to the implant surfaces.

In general, no adverse reactions or excessive inflammatory infiltrates were noted around any of the implants in this study.

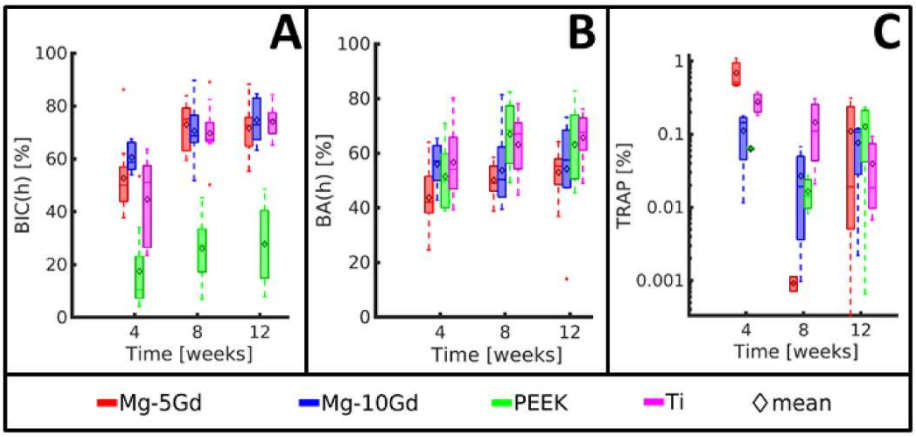

Fig. 6. Results of *ex vivo* investigation of Mg-5Gd, Mg-10Gd, PEEK and Ti screw implants over 4, 8, 12 weeks healing period from histological analysis. (A) 2D Bone implant contact (*2D BIC)*, (B) 2D Bone area (*2D BA)* for 200 μm, (C) Tartrate resistant acid phosphatase-positive area (*TRAP*) in a 200 μm ROI around the screw surfaces (Error bars correspond to 99% confidence interval). See Table 7 for numeric values.

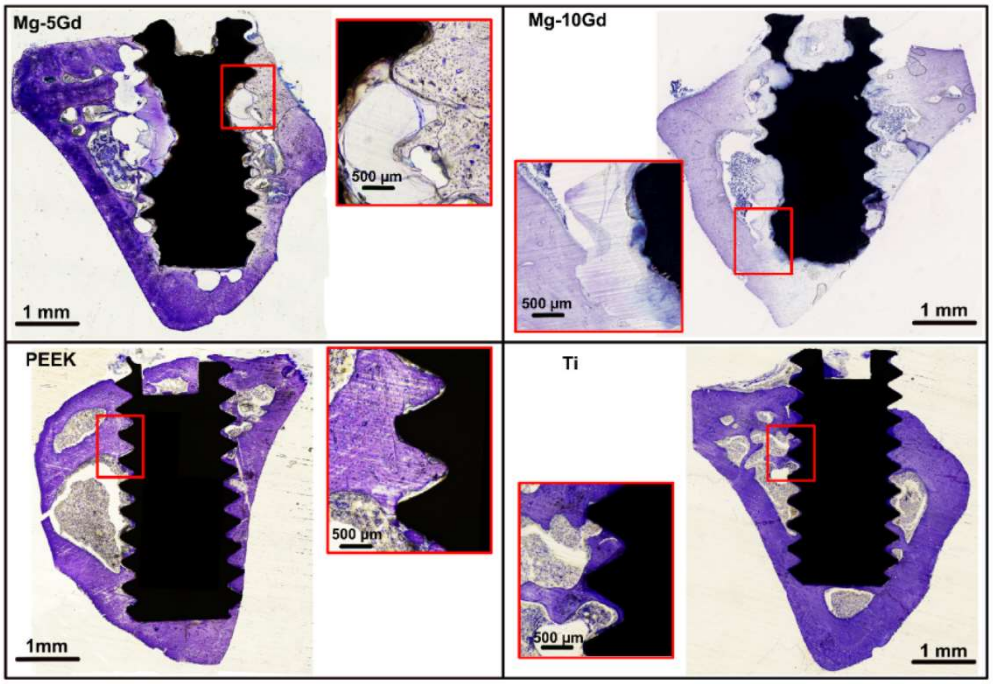

Fig. 7. *Ex vivo* histological slices of Mg-5Gd and Mg-10Gd, PEEK and Ti implants after 12 weeks of healing, stained with toluidine blue. (For interpretation of the references to color in this figure legend, the reader is referred to the Web version of this article).

4. Discussion

4.1. Degradation behavior

The Mg-10Gd implants in the current study degraded significantly slower than the alloy presented by Galli et al. [43] (ca. 50% and 33% lower after 4 and 12 weeks implantation respectively). However, while the nominal alloys were the same in both studies, other factors were different. The microstructure of the alloy, together with a thorough material characterization, was reported in a recently published paper, in which screws originating from the same batch as those used in the current experiment were examined [18]. In contrast to the screws of Galli et al. [43] the material in Ref. [18] and the current study was not taken from the center of the extruded bar, to avoid stronger galvanic effect by segregation processes from the casting. As one effect, the Gd-rich particles are smaller and more finely distributed in the Mg-xGd alloys of the study in Ref. [18] and the current one.

The study [18] showed that Mg-5Gd and Mg-10Gd had a grain size of 51.78 μm ± 10.91 μm and 26.67 μm ± 1.30 μm, respectively. Therefore, the grain sizes were larger than those reported by *Galli* et al. [43], but the standard deviation among samples were considerably smaller. Additionally, the Gd-rich particles of the alloys in our study were rather fine and homogeneously distributed, as shown in the metallographic examination [18] in contrast to what shown in *Galli* et al. for Mg-10Gd [43]. Another study from *Myrissa* et al. [44] investigated the degradation of Mg-10Gd in the form of pins for 4 weeks in rat femur. The authors reported nearly 0.1 mm a^{-1} slower degradation of the pins, compared to our screws. However, *Myrissa* et al. [44] observed substantial disintegration of the Mg-10Gd pins after 12 weeks in bone, and they could not calculate the degradation rate at that time point because it was not possible to segment all the small remnants of the implants from the bone. In contrast, both alloys in our study appeared manly intact for the

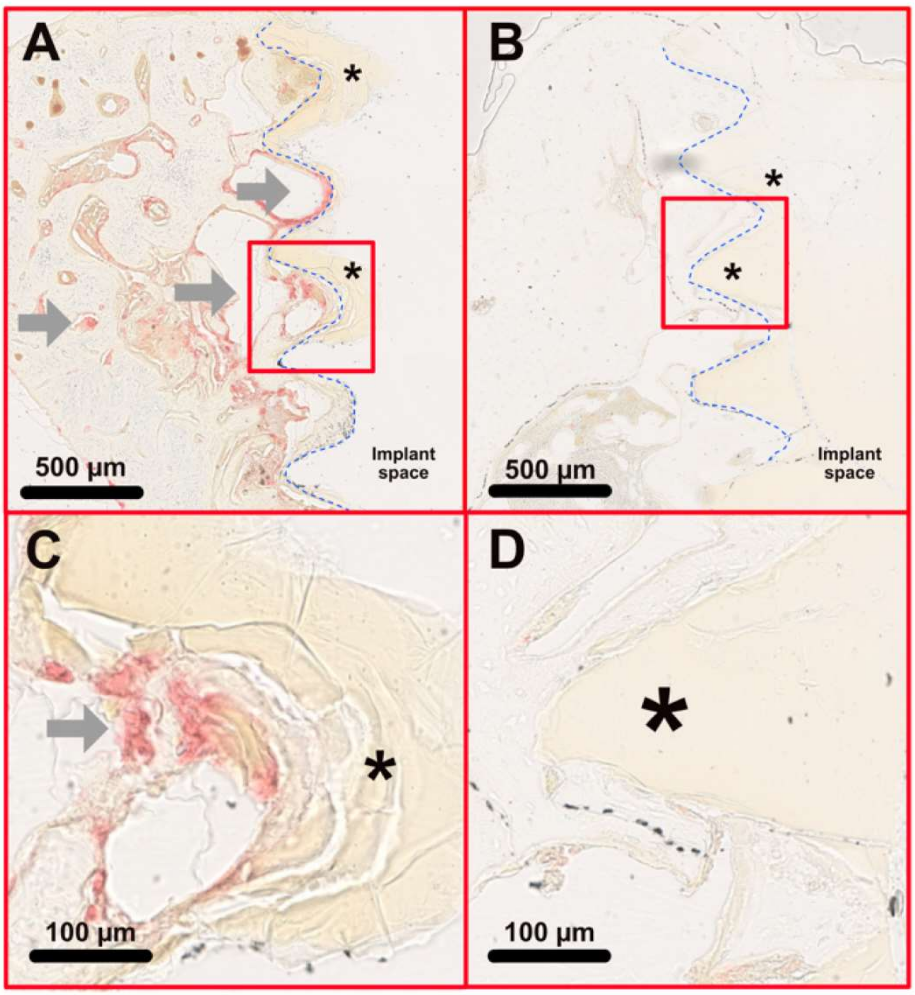

Fig. 8. Histological images with TRAP staining of (A) a Mg-5Gd screws after 4 weeks; (B) a Mg-5Gd after 12 weeks of degradation in rat bone. (C) and (D): magnified areas of the above images.

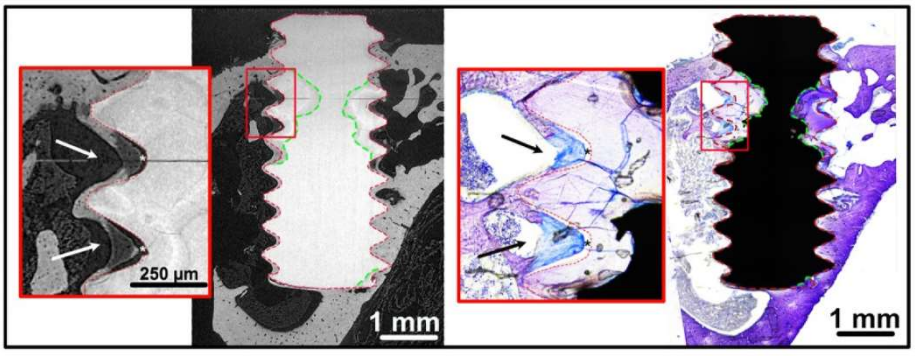

Fig. 9. A tomographic slice (left image) and histological slice (right image) of a Mg-10Gd screw after 8 weeks *in vivo*. The green line indicates the border between the residual alloy and the corrosion layer on the histological image. The red line indicates the borders between the corrosion layer and the bone from the tomographic image. The residual alloy appears black in the histology because it is made of the original metal and it does not allow light to pass through. It can be noted that the degradation layers identified on the histological image as part of the screws, but not made of metal, overlap with the same areas identified in the SRµCT as areas with a different absorption coefficient than the residual alloy. Higher magnifications of the µCT slice and of the histology (red square areas) show a region of woven bone, less mineralized. In the histology, the woven bone (black arrows) has a darker colour and rounder osteocites lacunea, compared to the mature bone. In the µCT, the woven bone (white arrows) is less absorbing than the mature bone, probably because it is less mineralized. In addition, this bone is slightly detached from the implant surface (asterixs), probably as an artefact due to the shrinkage occurred to this less mineralized tissue during critical point drying. (For interpretation of the references to color in this figure legend, the reader is referred to the Web version of this article.)

entire follow-up time.

The homogeneity of the degradation, which is an important characteristic for the mechanical integrity of the implants during healing, is mainly described by the *PF* with a lower *PF* indicating a more homogenous corrosion behavior. In our study, the *3D PF* was higher for Mg-10Gd than Mg-5Gd and it tended to decrease over time slightly.

One could argue that the pitting corrosion would be mostly visible in the early implantation stages, when the *MDD* values in the *PF* formula are lowest. However, we found a poor correlation between the *DR* and *3D PF* of both alloys, and for that we assumed that, even in the early

stages, the degradation homogeneity was not influenced by the higher *DR*s. However, other non-linear correlations could exist between the *DR* and *3D PF*, which were not investigated in this study.

4.2. Comparison of ex vivo and in vitro results

Previous research pointed out that the degradation rate of Mg alloys is usually faster *in vitro* than *in vivo* [44]. However, in our experiments, we observed degradation rates that were higher *in vivo* than *in vitro* (by a factor of 2 and 1.5 for Mg-5Gd and 2.8 and 2.6 for Mg-10Gd, both for 4 and 8 weeks of healing). A similar tendency was observed also in Ref. [43] on Mg-10Gd and Mg-2Ag alloy implants. As discussed in Ref. [43], the reason for this tendency may be that the *in vitro* tests are mostly observed on disks instead than of the actual implants. Moreover, the SRμCT investigations of *ex vivo* data we performed are conducted at a significantly higher resolution than the *in vivo* imaging usually found in literature, which may result in significant differences. A possible explanation for the implants' degradation being faster *in vivo* than *in vitro* could be the influence of the mechanical stresses on the screws either due to the friction of the implant with the osteotomy walls during the insertion or due to the animal's movement during the implantation period in the animal, or a combination of both aspects [43]. Another possible reason for the faster degradation *in vivo* than *in vitro* is that in tissues the pH is continuously buffered and the degradation products as well as Mg ions are quickly removed by the blood flow. Simultaneously new electrolytes are fed to the corrosion sites maintaining the local implantation environment propitious to continuous degradation [45].

We further compared the *PF* observed *in vivo* to the one observed *in vitro* for the same alloys [18]. The *3D PF* was very similar, but slightly lower for Mg-10Gd implants *in vivo* compared to *in vitro* at 4 and 8 weeks. In addition, *3D PF* was lower for Mg-5Gd *in vivo* than *in vitro*. This can be partly explained by the increased *DR in vivo* compared to *in vitro*, since the *PF* is inversely proportional to the *DR*. A higher *DR* can thus result in a smaller *PF* even at equal pits depth in the sample. However, Mg-5Gd implants at 4 weeks of degradation revealed on the contrary higher *3D PF* values *in vivo*, while still having higher *DR*s *in vivo* than *in vitro*. This may indicate that the pitting corrosion for these materials in bone was significant in the early stages of degradation.

The *2D mean PF* was slightly lower *in vivo* than *in vitro*, both at 4 and 8 weeks and for both materials. However, the coefficient of variation (*CV*) of the *2D PF*, which describes the variation between different slices of the screws, was higher *in vivo* than *in vitro*. In addition, we observed a higher *CV* of 2D *volume loss* of the *in vivo* degraded screws for both materials and time points. It revealed a relevant intra-implant variation, because different regions of the same screw corroded differently, but did not display higher pitting factors. In other words, the amount of material degraded is more or less homogeneous when calculated in each slice, without deeper pits, but slices at different heights of the screws showed different amounts of degradation. This is not surprising considering the bone tissue composition in which the screws were immersed. Some parts of the screws were in contact with the hard and compact bone of the cortical region of the tibia. In contrast, other parts were exposed to the trabecular bone with more marrow spaces or even the marrow cavity. Therefore, vascularization and fluid exchange are expected to be different in these regions, providing different environments for corrosion. Moreover, different areas of the screws in contact with the cortical bone of the rat tibia were likely to be exposed to different levels of movement-induced strain, which might have triggered a different degradation behavior. The screws degraded *in vitro* were all immersed in cell culture media and were, therefore, less affected by localized corrosion. Another qualitative observation was that the screws were more degraded at the bottom and at the top. This is likely to be attributed to the larger surface area of the screw which was exposed to the surrounding environment in these regions.

4.3. Bone response in relation to degradation

The *BIC,* studied with both imaging methods, tomography and histology, confirmed high values for the Mg materials and Ti and it suggested that both Mg-xGd alloys obtained comparable osseointegration as Ti implants, for the healing times investigated.

The comparisons of *BIC* among different studies should be done with caution, as there is a lot of variability among experiments (e.g. the shape of the implant, the implantation site, thickness of the histological sections as well as the scanning parameters). However, it seems that the current results are in line with other data in the literature. The *3D BIC(t)* of our Mg-xGd materials were similar to the *3D BIC(t)s* of pins made of AZ31 alloy and pure Mg, after 4 weeks of healing in rat bone, but after 12 weeks, Mg-xGd materials showed a lower *3D BIC(t)* of approximately 5% and 20% compared to AZ31 and pure Mg, respectively [46]. However, one reason for that could be that the AZ31 and pure Mg pins were studied with μCT from a lab source, with lower spatial and density resolution, compared to the SRμCT employed here.

Some studies discuss images of bone-implant samples obtained using both methods, showing that laboratory μCT is more prone than SRμCT to artefacts like beam-hardening [47]. Those artefacts affect especially the region of the edge between the metal implant and the bone, making it difficult when not impossible to correctly calculate the *BIC*. Neldam et al. [48] using SRμCT data around Ti implants in bone showed that the *BIC* calculated within 5 μm from the implant was tremendously different than the *BIC* calculated at 50 μm from the implant, arguing that the *BIC* results can vary a lot with the variation of the voxel size. In addition, in many images we found newly formed bone in the proximity of the degradation layers but detached from them and separated by a thin gap, which was completely empty and did not show staining for cells or tissues in histology (Fig. 9). This might be an artefact of the critical point drying procedure. The new bone was probably less mineralized, and it might in fact have shrunk during the drying process, resulting in a thin gap between the bone and the implant. That suggests that the real *BIC* for the Mg alloys was probably higher in the living animal than what we measured *ex vivo*.

One study, employing SRμCT as we did, showed *3D BIC(t)* values for Mg-10Gd screws after 4 and 12 weeks in rats that were 5–10% lower than what we found [43]. However, the *DR* of Mg-10Gd was also higher than what we reported, and that could explain the lower *BIC*, because of the greater surface degradation and formation of hydrogen gas during the early phases of degradation [43].

The *DR* could not be the only parameter that influences hydrogen gas formation and Mg-xGd alloys could have some advantages over pure Mg in that respect. Marco et al. [49] observed that the *DR* (1.11 mm a^{-1} ± 0.05 mm a^{-1}) of a Mg-10Gd pin implant was much higher than the one of pure Mg (0.15 mm a^{-1} ± 0.03 mm a^{-1}) and Mg-2Ag (0.13 mm a^{-1} ± 0.04 mm a^{-1}). However, the number of gas pockets detected with μCT after 7 days post-implantation for Mg-10Gd (0.23 mm^3 ± 0.32 mm^3) was much lower than with pure Mg (3.4 mm^3 ± 1.93 mm^3) and Mg-2Ag (6.52 mm^3 ± 8.41 mm^3). One reason for that is that Mg-RE alloys, such as Mg-10Gd, can absorb hydrogen from the environment and form hydrides in cuboid shape [50–52].

When correlating the *3D BIC* and *DR* of the Mg-xGd alloys, we found a moderately strong inverse correlation. This can be interpreted in two ways. We can hypothesize that when bone is in close contact with the surfaces of the Mg alloys, the *DR* slows down. But, the inverse hypothesis can also be true, which is that when the *DR* is lower, more bone can grow in direct contact with the screws (possibly due to a lower gas formation interfering with the attachment of bone cells to the surface).

Previous *in vivo* investigation utilizing Mg implants have suggested that Mg enhances the bone formation and mineralization compared to permanent implants [53–55] and the possible reasons for that is either the release of Mg ions and/or the alkalization of the local environment during the degradation [43,56,57]. In addition, the degradation layers of Mg materials are rich in calcium and phosphor ions, which are the

same components of hydroxyapatite, the bone mineral matrix, and therefore might be osteoconductive [58–60]. In fact, our observation of an increasing amount of *3D BIC(t)* and *3D BV/TV(t)* with ongoing healing time would support the latter suggestion.

Additionally, the fair and poor inverse correlation of *3D BIC* and *3D PF* of Mg-5Gd and Mg-10Gd, respectively, indicate that a relatively high pitting factor does not interfere with the apposition of bone on the implant surfaces. The moderately strong and fair inverse correlation of the *3D PF* and *3D BV/TV* for Mg-5Gd and Mg-10Gd implants could indicate the influence of the surrounding bone on the degradation homogeneity, more so for Mg-5Gd than for Mg-10Gd. Nevertheless, it has to be mentioned that after the elimination of *3D PF* outliers with values larger than 30 for both materials, the correlations assimilated (correlation *3D PF* and *3D BIC*: −0.44 and −0.42 for Mg-5Gd and Mg-10Gd, respectively; correlation *3D PF* and *3D BV/TV*: −0.55 and −0.45 for Mg-5Gd and Mg-10Gd respectively). This could indicate that the performance of both materials is more prone to unexpected and/or different behavior in the beginning of the implantation and is more comparable after a certain period of implantation. However, it is also suggested that in the presence of lower pitting factor there is more bone around the screws. Hence, the homogeneous degradation is in correlation with bone growth and/or the way around - the presence of bone induces homogeneous degradation.

Despite PEEK implants had significantly lower *BIC*s than the other materials, the lowest *BV/TV* was found for Mg-xGd. PEEK displayed a relatively high *BV/TV*s and *BA*s and both values increased with the healing time. This suggested that all materials were gradually surrounded by bone, possibly to shield the implanted material foreign to the body from the richly vascularized medullar cavity. The surrounding bone was in close contact with the three metallic implants including the areas of degradation of the Mg alloys, but it was often slightly detached from the PEEK screws. This finding supports previous observations that PEEK does not promote bone formation when in direct contact with bone, while other implant materials like Ti do [61–64].

The strong and moderately strong correlation found between *3D BIC* and *3D BV/TV* for Mg-5Gd and Mg-10Gd, respectively, suggests that for these materials the presence of more bone tissue in the proximity of the implants increased the probability that this bone was in contact with the implant surfaces. An equally strong correlation was also found for the PEEK implants which displayed overall low *3D BIC* values. For Ti, high values of the *3D BIC* and *3D BV/TV* were already observed after 4 weeks of healing. Assuming that the implant stability is correlated to the *3D BIC*, the very poor correlation observed for the Ti implants suggests that the implant stability of Ti screws did not increase over the implantation period.

A high variation of the *BIC* over slices, as described by the *CV BIC*, was observed for the PEEK implants in comparison to the metallic implants. We thus assume a more reliable and more homogeneous osseointegration of the metallic implants.

The formation of new bone in the environment of Mg-10Gd and Ti implants as well as the ingrowth of bone into the degradation layer and the complete encapsulation of the detached debris of the degradation layer by bone for Mg-10Gd material have already been observed qualitatively in Ref. [43]. We confirmed these findings by a quantitative analysis of the distance and the integration of the fractured degradation layer into the bone. We assume that the detachment of small fragments of the degradation layer from the bulk material did not affect the implant stability. The encapsulation of the newly formed degradation layer into bone suggests that the integrity and stability of the Mg-xGd implants did not decrease over time.

Simultaneous to our study, investigations were performed to track the Gd ions from Mg-xGd implants [3]. The main risk with Gd^{3+} ions is that they have a similar ionic radius to Ca^{2+}, and as such they might be accumulated in the bone. Peruzzi et al. [66] found no traceable amounts of Gd in the bone right next to the implants, neither with EDX nor with neutron tomography. Gd was not detected in the main excretory organs, which might mean that the Gd has remained in the implant site without any interaction. Of course, it could be that there is some Gd mobility, but it is below the detection limits of EDX, neutron tomography or XRF in the organs.

Moreover, using EDX, Peruzzi et al. [66] compared semi-quantitatively the bone in the proximity of the Mg-Gd implants versus the one in the proximity of Ti implants (for exact values Table 1 from Ref. [66]). No Gd was found anywhere, Mg was slightly higher in the bone next to Mg-Gd implants but not high enough to be statistically significant, Ca and P instead were significantly higher next to Ti than next to Mg-Gd. However, Ca and P were basically the same for Mg-5Gd and Mg-10Gd. This means that Mg-Gd implants indeed affects the mineralization of bone in their close proximity, when compared to controls, however a different concentration of Gd does not change this behavior. The latter might suggest, that the main responsible for this effect is probably Mg, rather than Gd.

With respect to the evaluation of the degradation and osseointegration of implants, SRμCT is advantageous over the standard technique of histology, as it allows for a more comprehensive and non-destructive evaluation. In general, SRμCT allows to assess parameters such as the degradation homogeneity or the pitting factor not only on a few, possibly not-representative slices, but throughout the entire sample qualitatively, quantitatively, and in 3D [65].

5. Summary and outlook

In the current study, the degradation behavior of two Mg materials containing Gd at different concentrations was investigated using *ex vivo* imaging techniques, SRμCT and histology. The degradation rate and degradation homogeneity were measured quantitatively with good statistics and high-resolution. PEEK and Ti, commonly used in orthopedics, were investigated as reference materials to assess the material-dependent differences in terms of osseointegration using parameters such as the bone-to-implant contact area and the bone volume fraction around the implants.

Acceptable degradation rates and degradation homogeneity of the investigated Mg-xGd materials were confirmed in the current study. The Mg materials displayed comparable osseointegration to the Ti controls. On the other hand, the poor osseointegration of PEEK implants could also be confirmed. A clear assumption about the advantages or disadvantages of any of the investigated Mg-xGd implants could not be made out of the is study's results.

Whether or not the observed high bone-to-implant contact area and bone volume fraction of the Mg-xGd materials are truly indicators for the implant stability needs to be investigated in the future.

CRediT authorship contribution statement

Diana Krüger: Methodology, Investigation, Formal analysis, Software, Writing – original draft, Writing – review & editing. **Silvia Galli:** Investigation, Formal analysis, Writing – original draft, Writing – review & editing. **Berit Zeller-Plumhoff:** Investigation, Supervision, Writing – review & editing. **D.C. Florian Wieland:** Investigation, Supervision, Writing – review & editing. **Niccolò Peruzzi:** Investigation, Writing – review & editing. **Björn Wiese:** Resources, Investigation, Supervision, Writing – review & editing. **Philipp Heuser:** Software, Writing – review & editing. **Julian Moosmann:** Investigation, Supervision, Software, Writing – review & editing. **Ann Wennerberg:** Funding acquisition, Conceptualization, Writing – review & editing. **Regine Willumeit-Römer:** Funding acquisition, Conceptualization, Supervision, Writing – review & editing.

Declaration of competing interest

The authors declare that they have no known competing financial interests or personal relationships that could have appeared to influence

the work reported in this paper.

Acknowledgements

This research was carried out within the SynchroLoad project (BMBF project number 05K16CGA) which is funded by the Röntgen-Ångström Cluster (RÅC), a bilateral research collaboration of the Swedish government and the German Federal Ministry of Education and Research (BMBF). We also acknowledge the project MgBone (BMBF project number 05K16CGB) and Swedish Research Council 2015-06109. Additionally, we acknowledge provision of beamtime by PETRA III DESY within the long-term Proposal II-20170009 and beamtimes related to following IDs: 11001978, 11003288, 11003440, 11003773, 11003950, 11004016, 11004263, 11005553, and 11005842. We thank the P05 beamline at PETRA III DESY, a member of the Helmholtz Association (HGF), and its staff, in particular Felix Beckmann, Jörg Hammel, Fabian Wilde, for the support. Also, we acknowledge the surgeons David Reinedahl, DDS, Pär Johansson, DDS, PhD, and Ricardo Trindade, DDS, PhD, for the help during the animal experiments. This research was supported in part through the Maxwell computational resources operated at Deutsches Elektronen-Synchrotron (DESY), Hamburg, Germany. The development of the automatic segmentation is supported by the Helmholtz Association Initiative and Networking Fund under project number ZT-I-0003 and by the Helmholtz Imaging Platform (HIP).

Appendices.

Table 6
Results (mean ± standard deviation) from SRμCT analysis of the *ex vivo* data and the comparison factor between the *ex vivo* and *in vitro* analysis – parameters related to the screw (FM = factor mean, which is the ratio between the mean *ex vivo* value and mean *in vitro* value; FS = factor standard deviation, which is the ratio between the standard deviation *ex vivo* value and standard deviation *in vitro* value).

		4weeks				8weeks				12weeks	
		Mg-5Gd		Mg-10Gd		Mg-5Gd		Mg-10Gd		Mg-5Gd	Mg-10Gd
DR [mm a^{-1}]	**FM|FS**	0.63± 0.16	2|8	0.62± 0.24	2.8|6	0.37± 0.05	1.5|5	0.39± 0.08	2.6|2.7	0.34± 0.05	0.26± 0.07
MDD [μm]	**FM|FS**	48.3± 12	2|7.5	47.3± 18.3	2.8|6	56.7± 8.3	1.5|9.2	60.6± 12.0	2.6|3.0	77.3± 12.0	59.1± 15.9
CV volume loss [%]	**FM|FS**	79.0 ± 8	3.9|2.5	92.1± 23.9	3.4|5.1	69.5± 5.4	2|3.6	85.4± 15.3	4|2.6	74.4± 10.9	78.9± 8.4
3D PF	**FM|FS**	19.7 ± 6	1.2|0.5	21.3± 8.4	0.9|0.5	15.5± 2.5	0.6|2.1	17.0± 3.3	0.8|0.2	12.3± 1.1	15.4± 3.4
2D mean PF	**FM|FS**	3.1 ± 0.5	1|2.5	3.6 ± 0.9	0.9|2.3	2.9 ± 0.5	0.9	3.0 ± 0.4	0.9|1.3	2.9 ± 0.7	3.2 ± 0.5
CV 2D PF [%]	**FM|FS**	38 ± 23	1.9|7.4	38 ± 11	1.4|2.3	45 ± 65	1.7|72.4	30 ± 11	1|2	116 ± 206	54 ± 57

Table 7
Results from the SRμCT and histomorphometrical analysis of the *ex vivo* data related to the bone and screw and bone interaction (mean ± standard deviation)

	4weeks				8weeks				12weeks			
	Mg-5Gd	Mg-10Gd	PEEK	Ti	Mg-5Gd	Mg-10Gd	PEEK	Ti	Mg-5Gd	Mg-10Gd	PEEK	Ti
3D BIC [%]	25.0 ± 7.7	36.0 ± 13.0	7.5 ± 3.8	37.7 ± 15.0	49.2 ± 6.3	48.0 ± 7.8	19.5 ± 5.5	57.3 ± 11.5	53.1 ± 10.4	54.3 ± 6.5	27.2 ± 5.8	51.1 ± 14.9
2D BIC mean [%]	25.8 ± 6.9	36.7 ± 13.4	7.2 ± 3.6	36.4 ± 14.3	50 ± 5.9	49.1 ± 7.9	26.4 ± 18	56.7 ± 12.6	54 ± 11.1	55 ± 6.6	34.7 ± 22.5	51.3 ± 14.6
CV BIC [%]	52.3 ± 20.9	42.1 ± 10.8	106.0 ± 36.1	59.3 ± 11.7	38.0 ± 17.1	34.4 ± 7.3	162.3 ± 200.6	37.2 ± 12.3	29.5 ± 5.2	26.8 ± 5.2	140.3 ± 119.7	46.5 ± 14.4
BV/TV [%] - 100 μm	23.5 ± 4.3	25.9 ± 10.1	33.5 ± 6.9	52.3 ± 7.9	40.5 ± 4.2	38.0 ± 4.5	45.5 ± 6.6	59.1 ± 4.6	49.5 ± 5.4	51.5 ± 5.8	59.1 ± 4.6	55.0 ± 6.9
BV/TV [%] - 200 μm	23.6 ± 3.9	25.1 ± 8.5	36.5 ± 7.7	48.8 ± 10.4	36.5 ± 4.3	34.9 ± 5.0	42.8 ± 5.8	51.3 ± 4.6	45.2 ± 4.3	47.6 ± 6.2	49.4 ± 5.7	49.1 ± 7.7
BV/TV [%] - 300 μm	24.8 ± 4.0	26.3 ± 8.2	38.3 ± 7.8	47.3 ± 10.9	35.9 ± 4.5	34.6 ± 5.0	41.3 ± 5.7	47.5 ± 4.3	44.4 ± 3.4	46.7 ± 6.3	47.5 ± 5.4	46.2 ± 7.8
CV BV/TV -200 μm [%]	60.8 ± 6.7	59.0 ± 7.7	98.2 ± 54.1	54.5 ± 9.3	48.0 ± 11.0	43.6 ± 12.7	171.2 ± 201.2	45.1 ± 13.7	36.3 ± 7.0	39.3 ± 7.0	240.1 ± 299.6	55.7 ± 11.1
2D BIC(h) [%]	52.8 ± 13.2	60.5 ± 5.6	17.5 ± 15.1	44.7 ± 16.8	73.0 ± 9.0	70.6 ± 10.3	26.1 ± 12.8	69.7 ± 16.8	71.6 ± 11.1	74.8 ± 8.6	27.8 ± 15.5	74.0 ± 5.7
2D BA(h) [%] – 100 μm	49.8 ± 12	58.6 ± 7.7	52.6 ± 12.8	61.9 ± 11.9	53.5 ± 7.9	59.6 ± 9.3	68 ± 8.2	67.6 ± 10.1	55.9 ± 9	58.5 ± 22.1	68.3 ± 14.6	69.8 ± 6.7
2D BA(h) [%] – 200 μm	43.7 ± 11.2	55.9 ± 8.2	51.5 ± 11.6	56.6 ± 12.2	50.2 ± 6.0	53.7 ± 13.2	67.0 ± 12.4	63.1 ± 11.5	53.0 ± 9.4	54.2 ± 19.0	63.1 ± 14.0	65.6 ± 9.1
TRAP at 200 μm [%]	0.7 ± 0.4	0.1 ± 0.1	0.1 ± 0.0	0.3 ± 0.1	0.0 ± 0.0	0.0 ± 0.0	0.0 ± 0.0	0.1 ± 0.1	0.1 ± 0.2	0.1 ± 0.1	0.1 ± 0.1	0.0 ± 0.0

Table 8
Results of different degradation parameters (mean ± standard deviation) of Mg-5Gd and Mg-10Gd screw implants obtained from the *in vitro* experiments, published in Ref. [18] and used for the comparison with the *ex vivo* results from this study

	4weeks		8weeks	
	Mg-5Gd	Mg-10Gd	Mg-5Gd	Mg-10Gd
DR [mm/year]	0.31 ± 0.02	0.22 ± 0.04	0.24 ± 0.01	0.15 ± 0.03
3D PF	15.8 ± 11.8	23.8 ± 15.4	25.1 ± 1.2	20.9 ± 13.3
2D mean PF	3.1 ± 0.2	3.9 ± 0.4	3.3 ± 0.0	3.3 ± 0.3
CV 2D PF [%]	20.2 ± 3.1	26.7 ± 4.7	26.7 ± 0.9	28.7 ± 5.6
CV dif. layer [%]	20.2 ± 3.1	26.7 ± 4.7	35.3 ± 1.5	21.6 ± 6.0

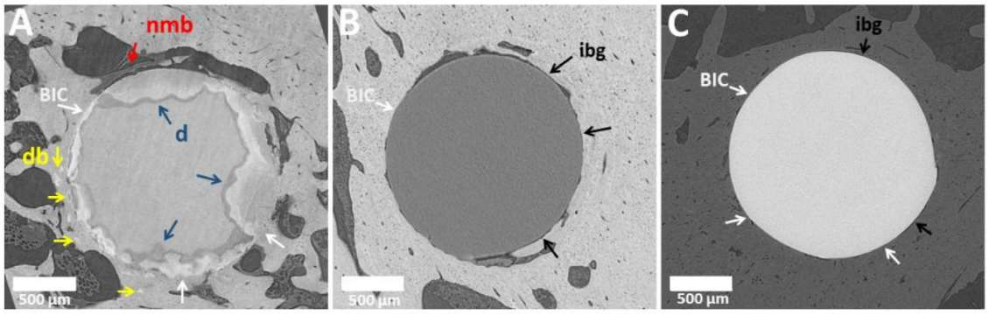

Fig. 10. Cross sections of SRµCT scans of implants after 12 weeks *in vivo* degradation;db = degradation layer in bone, nmb = non-mineralized bone (newly formed bone)d = degradation layer; ibg = implant bone gap; (A) Mg-5Gd, (B) PEEK, (C) Ti; The image contrast was adjusted for better visualization, which results in the different grey level appearances of the bone in the images.

References

[1] R. Willumeit-Römer, The interface between degradable Mg and tissue, JOM 71 (4) (2019) 1447–1455.
[2] C.K. Seal, K. Vince, M.A. Hodgson, Biodegradable surgical implants based on magnesium alloys–A review of current research, in: IOP conference series: materials science and engineering 4, 2009, p. 12011, 1.
[3] H.S. Brar, M.O. Platt, M. Sarntinoranont, P.I. Martin, M. V Manuel, Magnesium as a biodegradable and bioabsorbable material for medical implants, Jom 61 (9) (2009) 31–34.
[4] N.T. Kirkland, N. Birbilis, Magnesium Biomaterials: Design, Testing, and Best Practice, Springer, 2014.
[5] N. Hort, et al., Magnesium alloys as implant materials–Principles of property design for Mg–RE alloys, Acta Biomater. 6 (5) (2010) 1714–1725.
[6] A. Myrissa, S. Braeuer, E. Martinelli, R. Willumeit-Roemer, W. Goessler, A. M. Weinberg, Gadolinium accumulation in organs of Sprague–Dawley®rats after implantation of a biodegradable magnesium-gadolinium alloy, Acta Biomater. 48 (2017) 521–529.
[7] D.W. Bruce, B.E. Hietbrink, K.P. DuBois, The acute mammalian toxicity of rare earth nitrates and oxides, Toxicol. Appl. Pharmacol. 5 (6) (1963) 750–759.
[8] F. Feyerabend, et al., Evaluation of short-term effects of rare earth and other elements used in magnesium alloys on primary cells and cell lines, Acta Biomater. 6 (5) (2010) 1834–1842.
[9] T.J. Haley, K. Raymond, N. Komesu, H.C. Upham, Toxicological and pharmacological effects of gadolinium and samarium chlorides, Br. J. Pharmacol. Chemother. 17 (3) (1961) 526–532.
[10] N.A. Agha, R. Willumeit-Römer, D. Laipple, B. Luthringer, F. Feyerabend, The degradation interface of magnesium based alloys in direct contact with human primary osteoblast cells, PLoS One 11 (6) (2016).
[11] F. Cecchinato, et al., Influence of magnesium alloy degradation on undifferentiated human cells, PLoS One 10 (11) (2015).
[12] M.D. Costantino, A. Schuster, H. Helmholz, A. Meyer-Rachner, R. Willumeit-Römer, B.J.C. Luthringer-Feyerabend, Inflammatory response to magnesium-based biodegradable implant materials, Acta Biomater. 101 (2020) 598–608.
[13] N. Sezer, Z. Evis, S.M. Kayhan, A. Tahmasebifar, M. Koç, Review of magnesium-based biomaterials and their applications, J. Magnes. Alloy. 6 (1) (2018) 23–43.
[14] S. Bauer, P. Schmuki, K. Von Der Mark, J. Park, Engineering biocompatible implant surfaces: Part I: materials and surfaces, Prog. Mater. Sci. 58 (3) (2013) 261–326.
[15] R. Zeng, W. Dietzel, F. Witte, N. Hort, C. Blawert, Progress and challenge for magnesium alloys as biomaterials, Adv. Eng. Mater. 10 (8) (2008). B3–B14.
[16] N.T. Kirkland, J. Lespagnol, N. Birbilis, M.P. Staiger, A survey of bio-corrosion rates of magnesium alloys, Corrosion Sci. 52 (2) (2010) 287–291.
[17] P. Maier, F. Zimmermann, M. Rinne, G. Szakács, N. Hort, C. Vogt, Solid solution treatment on strength and corrosion of biodegradable Mg6Ag wires, Mater. Corros. 69 (2) (2018) 178–190.
[18] D. Krüger, B. Zeller-Plumhoff, B. Wiese, S. Yi, M. Zuber, D.C.F. Wieland, J. Moosmann, R. Willumeit-Römer, Assessing the microstructure and in vitro degradation behavior of Mg-xGd screw implants using µCT, J. Magnes. Alloys (2021), https://doi.org/10.1016/j.jma.2021.07.029.
[19] P. Maier, J. Gonzalez, R. Peters, F. Feyerabend, T. Ebel, N. Hort, Degradation morphology and pitting factor compared to degradation rate, Eur. Cell. Mater. 32 (6) (2016) 22.
[20] J. Harmuth, B. Wiese, J. Bohlen, T. Ebel, R. Willumeit-Römer, Wide range mechanical customization of Mg-Gd alloys with low degradation rates by extrusion, Front. Mater. 6 (Aug) (2019), https://doi.org/10.3389/fmats.2019.00201.
[21] B. Zeller-Plumhoff, et al., Analysis of the bone ultrastructure around biodegradable Mg–xGd implants using small angle X-ray scattering and X-ray diffraction, Acta Biomater. 101 (2020) 637–645.
[22] B. Zeller-Plumhoff, D. Tolnai, M. Wolff, I. Greving, N. Hort, R. Willumeit-Römer, Utilizing synchrotron radiation for the characterization of biodegradable magnesium alloys—from alloy development to the application as implant material, Adv. Eng. Mater. (2021) 2100197.
[23] J. Moosmann, et al., Biodegradable magnesium-based implants in bone studied by synchrotron radiation microtomography, in: Developments in X-Ray Tomography XI 10391, 2017, p. 103910O.
[24] J. Moosmann, et al., A load frame for in situ tomography at PETRA III, in: Developments in X-Ray Tomography XII 11113, 2019, p. 1111318.
[25] F. Feyerabend, M. Johannisson, Z. Liu, R. Willumeit-Römer, Influence of various sterilization methods on hardness, grain size and corrosion rate of a Mg6Ag-alloy, BioNanoMaterials 16 (1) (2015) 51–58.
[26] A. Haibel, et al., Micro-and nano-tomography at the GKSS imaging beamline at PETRA III, in: Developments in X-Ray Tomography VII 7804, 2010, p. 78040B.
[27] F. Wilde, et al., Micro-CT at the imaging beamline P05 at PETRA III, in: AIP conference Proceedings 1741, 2016, p. 30035, 1.
[28] S. Lautner, et al., Using SRuCT to define water transport capacity in Picea abies, in: Developments in X-Ray Tomography XI 10391, 2017, p. 1039118.
[29] J. Moosmann, et al., Time-lapse X-ray phase-contrast microtomography for in vivo imaging and analysis of morphogenesis, Nat. Protoc. 9 (2) (2014) 294–304.
[30] GitHub - moosmann/matlab: data reconstruction and analysis tools for tomography data acquired at the Imaging Beamline (IBL) at P05 and at the High-Energy Material Science (HEMS) beamline at P07 of PETRA III at DESY, both operated by HZG." [Online]. Available: Accessed: 15-Apr-2021, https://github.com/moosmann/matlab.
[31] W.J. Palenstijn, K.J. Batenburg, J. Sijbers, Performance improvements for iterative electron tomography reconstruction using graphics processing units (GPUs), J. Struct. Biol. 176 (2) (2011) 250–253.
[32] W. Van Aarle, et al., The ASTRA Toolbox: a platform for advanced algorithm development in electron tomography, Ultramicroscopy 157 (2015) 35–47.
[33] J.H. Hubbell, S.M. Seltzer, Tables of X-Ray Mass Attenuation Coefficients and Mass Energy-Absorption Coefficients 1 keV to 20 MeV for Elements Z= 1 to 92 and 48 Additional Substances of Dosimetric Interest, 1995.
[34] J. Schindelin, et al., Fiji: an open-source platform for biological-image analysis, Nat. Methods 9 (7) (2012) 676–682.
[35] C.T. Rueden, et al., ImageJ2: ImageJ for the next generation of scientific image data, BMC Bioinf. 18 (1) (2017) 1–26.

[36] M.L. Bouxsein, S.K. Boyd, B.A. Christiansen, R.E. Guldberg, K.J. Jepsen, R. Müller, Guidelines for assessment of bone microstructure in rodents using micro–computed tomography, J. Bone Miner. Res. 25 (7) (2010) 1468–1486.
[37] J.F. Griffith, H.K. Genant, "Imaging of Osteoporosis," in *Osteoporosis*, Elsevier, 2013, pp. 1505–1534.
[38] K. Donath, "Preparation of Histologic Sections by the Cutting-Grinding Technique for Hard Tissue and Other Material Not Suitable to Be Sectioned by Routine Methods," *Equip*, methodical Perform., 1988.
[39] A. Erlebacher, R. Derynck, Increased expression of TGF-beta 2 in osteoblasts results in an osteoporosis-like phenotype, J. Cell Biol. 132 (1) (1996) 195–210.
[40] H. Abdi, Coefficient of variation, Encycl. Res. Des. 1 (2010) 169–171.
[41] K.J. Blinowska, J. Zygierewicz, Practical Biomedical Signal Analysis Using MATLAB®, CRC Press, 2011.
[42] Y.H. Chan, Biostatistics 104: correlational analysis, Singap. Med. J. 44 (12) (2003) 614–619.
[43] S. Galli, On Magnesium-Containing Implants for Bone Applications, Malmö university, Faculty of Odontology, 2016.
[44] A. Myrissa, et al., In vitro and in vivo comparison of binary Mg alloys and pure Mg, Mater. Sci. Eng. C 61 (2016) 865–874.
[45] J. Wang, et al., Recommendation for modifying current cytotoxicity testing standards for biodegradable magnesium-based materials, Acta Biomater. 21 (2015) 237–249.
[46] N. Kawamura, Y. Nakao, R. Ishikawa, D. Tsuchida, M. Iijima, Degradation and biocompatibility of AZ31 magnesium alloy implants in vitro and in vivo: a micro-computed tomography study in rats, Materials 13 (2) (2020) 473.
[47] H. Sarve, Evaluation of Osseointegration Using Image Analysis and Visualization of 2D and 3D Image Data, 2011, 2011, p. 61, 2011.
[48] C.A. Neldam, et al., Application of high resolution synchrotron micro-CT radiation in dental implant osseointegration, J. Cranio-Maxillofacial Surg. 43 (5) (2015) 682–687.
[49] I. Marco, et al., In vivo and in vitro degradation comparison of pure Mg, Mg-10Gd and Mg-2Ag: a short term study, Eur. Cell. Mater. 33 (2017) 90–104.
[50] W. Gan, et al., Identification of unexpected hydrides in Mg–20 wt% Dy alloy by high-brilliance synchrotron radiation, J. Appl. Crystallogr. 45 (1) (2012) 17–21.
[51] I. Marco, F. Feyerabend, R. Willumeit-Römer, O. der Biest, Degradation testing of Mg alloys in Dulbecco's modified eagle medium: influence of medium sterilization, Mater. Sci. Eng. C 62 (2016) 68–78.
[52] Q. Peng, Y. Huang, J. Meng, Y. Li, K.U. Kainer, Strain induced GdH2 precipitate in Mg–Gd based alloys, Intermetallics 19 (3) (2011) 382–389.
[53] K. Jähn, et al., Intramedullary Mg2Ag nails augment callus formation during fracture healing in mice, Acta Biomater. 36 (2016) 350–360.
[54] C. Castellani, et al., Bone–implant interface strength and osseointegration: biodegradable magnesium alloy versus standard titanium control, Acta Biomater. 7 (1) (2011) 432–440.
[55] P. Cheng, et al., High-purity magnesium interference screws promote fibrocartilaginous entheses regeneration in the anterior cruciate ligament reconstruction rabbit model via accumulation of BMP-2 and VEGF, Biomaterials 81 (2016) 14–26.
[56] D.A. Bushinsky, Metabolic alkalosis decreases bone calcium efflux by suppressing osteoclasts and stimulating osteoblasts, Am. J. Physiol. Physiol. 271 (1) (1996) F216–F222.
[57] S. Yoshizawa, A. Brown, A. Barchowsky, C. Sfeir, Magnesium ion stimulation of bone marrow stromal cells enhances osteogenic activity, simulating the effect of magnesium alloy degradation, Acta Biomater. 10 (6) (2014) 2834–2842.
[58] F. Witte, et al., In vivo corrosion of four magnesium alloys and the associated bone response, Biomaterials 26 (17) (2005) 3557–3563.
[59] N.A. Agha, F. Feyerabend, B. Mihailova, S. Heidrich, U. Bismayer, R. Willumeit-Römer, Magnesium degradation influenced by buffering salts in concentrations typical of in vitro and in vivo models, Mater. Sci. Eng. C 58 (2016) 817–825.
[60] B. Zeller-Plumhoff, et al., Quantitative characterization of degradation processes in situ by means of a bioreactor coupled flow chamber under physiological conditions using time-lapse SRmicroCT, Mater. Corros. 69 (3) (2018) 298–306.
[61] P.J. Rao, M.H. Pelletier, W.R. Walsh, R.J. Mobbs, Spine interbody implants: material selection and modification, functionalization and bioactivation of surfaces to improve osseointegration, Orthop. Surg. 6 (2) (2014) 81–89.
[62] B.J.V. Yoon, F. Xavier, B.R. Walker, S. Grinberg, F.P. Cammisa, C. Abjornson, Optimizing surface characteristics for cell adhesion and proliferation on titanium plasma spray coatings on polyetheretherketone, Spine J. 16 (10) (2016) 1238–1243.
[63] R. Trindade, T. Albrektsson, S. Galli, Z. Prgomet, P. Tengvall, A. Wennerberg, Bone immune response to materials, Part II: copper and polyetheretherketone (PEEK) compared to titanium at 10 and 28 days in rabbit tibia, J. Clin. Med. 8 (6) (2019) 814.
[64] S. Barkarmo, et al., Enhanced bone healing around nanohydroxyapatite-coated polyetheretherketone implants: an experimental study in rabbit bone, J. Biomater. Appl. 29 (5) (2014) 737–747.
[65] W. Tjong, J. Nirody, A.J. Burghardt, J. Carballido-Gamio, G.J. Kazakia, Structural analysis of cortical porosity applied to HR-pQCT data, Med. Phys. 41 (1) (2014) 13701.
[66] N. Peruzzi, et al., Multimodal Ex Vivo Methods Reveal that Gd-Rich Corrosion Byproducts Remain at the Implant Site of Biodegradable Mg-Gd Screws, " *Acta Biomater.*, 2021.

Appendix B

Results Tables to all Analysis Parameters

Table 1: Degradation rates (DR) [mm/a], α-MEM or DMEM +10%FBS+1% pen/strep, weight loss (WL), volume loss (VL)

Exp.	Immersion days	Mg-5Gd			Mg-10Gd			Solution	Samples
		DR_{WL}[mm/a]	DR_{VL}[mm/a]	DR_{WL}/DR_{VL}	DR_{WL}[mm/a]	DR_{VL}[mm/a]	DR_{WL}/DR_{VL}		
i	1	0.45	0.42	1.07	0.44	0.47	0.94	α-MEM	different
	3	0.50	0.58	0.86	0.32	0.51	0.63	α-MEM	different
	6	0.57	0.35	1.63	0.24	0.46	0.52	α-MEM	different
	7	0.48	0.49	0.98	0.40	0.26	1.54	α-MEM	different
	9	0.35	0.31	1.13	0.29	0.24	1.21	α-MEM	different
ii	7	0.36	0.39±0.03	0.92	0.07	0.42±0.05	0.17	α-MEM	different
	14	0.18	0.42±0.05	0.43	0.10	0.30±0.01	0.33	α-MEM	different
	21	0.31	0.28±0.05	1.11	0.18	0.24±0.02	0.75	α-MEM	different
	28	0.20	0.31±0.02	0.65	0.17	0.22±0.04	0.77	α-MEM	different
iii	28	0.25±0.02	0.32±0.03	0.59±0.11	0.25±0.06	0.34±0.10	0.73±0.04	DMEM	identical
	56	0.16±0.01	0.24±0.01	0.66±0.01	0.12±0.02	0.15±0.03	0.84±0.25	DMEM	identical

Table 2: All data to graphs

	1 weeks		2 weeks		3 weeks		4 weeks		8 weeks	
	Mg-5Gd	Mg-10Gd	Mg-5Gd	Mg-10Gd	Mg-5Gd	Mg-10Gd	Mg-5Gd	Mg-10Gd	Mg-5Gd	Mg-10Gd
DR [mm/year]	0.39±0.03	0.42±0.05	0.42±0.05	0.30±0.01	0.28±0.05	0.24±0.02	0.31±0.02	0.22±0.04	0.24±0.01	0.15±0.03
MDD [µm]	7.5±0.5	8.1±1	16±1.5	11±0.2	16±3.1	14±1.3	24±1.6	17±3.1	37±1	23±4
3D-PF	21.4±6.6	31.5±16.8	13.4±5.6	35.0±9.1	27.4±23.9	16.2±3.8	15.8±11.8	23.8±15.4	25.1±1.2	20.9±13.3
2D-mean PF	4.0±0.2	4.6±0.1	3.4±0.4	5.1	4.3±1.4	4.6±0.2	3.1±0.2	3.9±0.4	3.3±0.0	3.3±0.3
CV 2D PF [%]	31.5±9.9	34.0±0.0	19.5±3.9	29.6±3.7	20.0±5.6	28.2±0.8	20.2±3.1	26.7±4.7	26.7±0.9	28.7±5.6
CV dif. layer [%]	4.4±0.2	7.6±2.8	10.5±0.1	8.6±1.4	11.7±2.1	8.9±1.5	20.2±3.1	26.7±4.7	35.3±1.5	21.6±6.0
Amount of slices, where it is not possible to calculate PF [%]	0.5±0.1	1.1±1.1	0.7±0.1	3.2±1.0	0.7±0.4	1.5±1.5	1.8±0.5	1.6±0.2	4.0±0	1.8±1.3
Crests/roots dif. Layer	1.5±0.2	1.1±0.2	1.8±0.2	1.4±0.2	1.7±0.2	1.5±0.2	2.1±0.5	1.4±0.3	1.6±0.1	1.7±0.1

Table 3: Resuls (mean ± standard deviation) from SRµCT analysis of the *ex vivo* data and the comparison factor between the *ex vivo* and *in vitro* analysis – parameters related to the screw (FM=factor mean, which is the ratio between the mean *ex vivo* value and mean *in vitro* value; FS=factor standard deviation, which is the ratio between the standard deviation *ex vivo* and standard deviation *in vitro* value)

		4weeks				8weeks				12weeks	
		Mg-5Gd		Mg-10Gd		Mg-5Gd		Mg-10Gd		Mg-5Gd	Mg-10Gd
DR [mm a^{-1}]	FM|FS	0.63± 0.16	2|8	0.62± 0.24	2.8|6	0.37± 0.05	1.5|5	0.39± 0.08	2.6|2.7	0.34± 0.05	0.26± 0.07
MDD [µm]	FM|FS	48.3± 12	2|7.5	47.3± 18.3	2.8|6	56.7± 8.3	1.5|9.2	60.6± 12.0	2.6|3.0	77.3± 12.0	59.1± 15.9
CV volume loss [%]	FM|FS	79.0±8	3.9|2.5	92.1± 23.9	3.4|5.1	69.5± 5.4	2|3.6	85.4± 15.3	4|2.6	74.4± 10.9	78.9± 8.4
3D PF	FM|FS	19.7±6	1.2|0.5	21.3± 8.4	0.9|0.5	15.5± 2.5	0.6|2.1	17.0± 3.3	0.8|0.2	12.3± 1.1	15.4± 3.4
2D mean PF	FM|FS	3.1±0.5	1|2.5	3.6±0.9	0.9|2.3	2.9±0.5	0.9	3.0±0.4	0.9|1.3	2.9±0.7	3.2±0.5
CV 2D PF [%]	FM|FS	38±23	1.9|7.4	38±11	1.4|2.3	45±65	1.7|72.4	30±11	1|2	116± 206	54±57

Table 4: Results from the SRµCT and histomorphometrical analysis of the *ex vivo* data related to the bone and screw and bone interaction

	4weeks				8weeks				12weeks			
	Mg-5Gd	Mg-10Gd	PEEK	Titan	Mg-5Gd	Mg-10Gd	PEEK	Titan	Mg-5Gd	Mg-10Gd	PEEK	Titan
3D BIC [%]	25.0±7.7	36.0±13.0	7.5±3.8	37.7± 15.0	49.2±6.3	48.0±7.8	19.5± 5.5	57.3± 11.5	53.1±10.4	54.3±6.5	27.2±5.8	51.1± 14.9
2D BIC mean [%]	25.8±6.9	36.7±13.4	7.2±3.6	36.4± 14.3	50±5.9	49.1±7.9	26.4± 18	56.7± 12.6	54±11.1	55±6.6	34.7±22.5	51.3± 14.6
CV BIC [%]	52.3±20.9	42.1±10.8	106.0± 36.1	59.3± 11.7	38.0± 17.1	34.4±7.3	162.3± 200.6	37.2± 12.3	29.5±5.2	26.8±5.2	140.3± 119.7	46.5± 14.4
BV/TV [%] - 100µm	23.5±4.3	25.9±10.1	33.5±6.9	52.3± 7.9	40.5±4.2	38.0±4.5	45.5± 6.6	59.1± 4.6	49.5±5.4	51.5±5.8	59.1±4.6	55.0± 6.9
BV/TV [%] - 200µm	23.6±3.9	25.1±8.5	36.5±7.7	48.8± 10.4	36.5±4.3	34.9±5.0	42.8± 5.8	51.3± 4.6	45.2±4.3	47.6±6.2	49.4±5.7	49.1± 7.7
BV/TV [%] - 300µm	24.8±4.0	26.3±8.2	38.3±7.8	47.3± 10.9	35.9±4.5	34.6±5.0	41.3± 5.7	47.5± 4.3	44.4±3.4	46.7±6.3	47.5±5.4	46.2± 7.8
CV BV/TV - 200 µm [%]	60.8±6.7	59.0±7.7	98.2± 54.1	54.5± 9.3	48.0± 11.0	43.6±12.7	171.2± 201.2	45.1± 13.7	36.3±7.0	39.3±7.0	240.1± 299.6	55.7± 11.1
2D BIC(h) [%]	52.8±13.2	60.5±5.6	17.5± 15.1	44.7± 16.8	73.0±9.0	70.6±10.3	26.1± 12.8	69.7± 16.8	71.6±11.1	74.8±8.6	27.8±15.5	74.0± 5.7
2D BA(h) [%]	43.7±11.2	55.9±8.2	51.5± 11.6	56.6± 12.2	50.2±6.0	53.7±13.2	67.0± 12.4	63.1± 11.5	53.0±9.4	54.2±19.0	63.1±14.0	65.6± 9.1
TRAP at 300 µm [%]	0.7±0.4	0.1±0.1	0.1±0.0	0.3± 0.1	0.0±0.0	0.0±0.0	0.0± 0.0	0.1±0.1	0.1±0.2	0.1±0.1	0.1±0.1	0.0± 0.0

Table 5: Strength and direction of the linear correlation between the investigated parameters

P1	P2	Mg-5Gd	Mg-10Gd	PEEK	Ti
3D BIC [%]	*DR [mm a^{-1}]*	MS: -0.76 (p=0.000)	MS: -0.74 (p=0.000)		
3D BIC [%]	*3D PF [a.u.]*	F: -0.42 (p=0.033)	P: -0.05 (p=0.000)		
DR [mm a^{-1}]	*3D PF [a.u.]*	P: 0.15 (p=0.472)	P: -0.19 (p=0.355)		
3D PF [a.u.]	*3D BV/TV [%]*	MS: -0.60 (p=0.001)	F: -0.37 (p=0.065)		
3D BIC [%]	*3D BV/TV [%]*	VS: 0.86 (p=0.000)	MS: 0.75 (p=0.000)	MS: 0.73 (p=0.000)	P: 0.07 (p=0.831)
BIC(h) [%]	*3D BIC(t) [%]*	MS: 0.74 (p=0.000)	M: 0.554 (p=0.008)	M: 0.56 (p=0.002)	MS: 0.62 (p=0.004)
BIC(h) [%]	*2D BIC(t) [%]*	MS: 0.74 (p=0.000)	M: 0.53 (p=0.01)	P: 0.32 (p=0.1)	MS: 0.64 (p=0.003)
BIC(h) [%]	*BA [%]*	P: 0.25 (p=0.21)	P: 0.15 (p=0.48)	M: 0.49 (p=0.013)	M: 0.42 (p=0.025)
BA [%]	*3D BV/TV(t) [%]*	M: 0.5 (p=0.007)	P: 0.28 (p=0.22)	MS: 0.60 (p=0.002)	MS: 0.73 (p=0.000)

Table legend: P1 and P2: parameters correlated; VS=very strong, MS=moderately strong, F=fair, P=poor; value: correlation coefficient; p-value: significance of the correlation; 3D BV/TV and BA values are those in ROI2, 200µm. The p-values represent the probability that the correlation between investigated parameters by chance.

Table 6: P-values; *DR (p<0.05); ◊MDD (p<0.05); +CV volume loss (p<0.05); ○3D PF (p<0.05); 2D mean PF (p<0.05: no significant differences at all); CV PF (p<0.05: no significant differences at all); ∨ 3D BIC (p<0.005); □CV BIC (p<0.05); ●BV/TV 200 µm (p<0.001)

		Mg-5Gd			Mg-10Gd			PEEK			Titan		
		4	8	12	4	8	12	4	8	12	4	8	12
Mg-5Gd	4												
	8	*∨											
	12	*◊∨●											
Mg-10Gd	4		*+○	*◊●									
	8	*∨											
	12	*∨●			●								
PEEK	4		∨	∨	∨	∨	∨						
	8	●	∨□	∨	●	∨□	∨□						
	12	∨●			●			∨	∨				
Ti	4	●			●			∨					
	8	∨●	●		∨ ●	●		∨●	∨□				
	12	∨●			●			∨	∨				

Appendix C

Detailed Results of Influence of Different Image Processing Methods on the Analysis Parameters

		DR [mm/a]		3D PF [u.a.]		3D BIC [%]		BV/TV [%]	
		Mg-5Gd	Mg-10Gd	Mg-5Gd	Mg-10Gd	Mg-5Gd	PEEK	Mg-5Gd	PEEK
1	nosmooth	0.40	0.17	10.91	34.79	71.35	23.33	46.04	46.78
2	smooth3with3	0.40	0.17	10.97	34.61	66.84	!	46.09	46.86
3	smooth3dwith3_smooth3dwith5	0.05		89.16		62.62	23.00	46.15	46.86
4	smooth3with5	0.40	0.17	10.86	34.52	63.47	22.24	46.14	46.86
5	smoothallsliceslongwith5	0.40	0.17	10.90	34.46	64.49	22.44	46.12	46.86
6	smoothallslicestranswith5	0.41	0.18	10.75	34.22	64.59	22.12	46.14	46.79
7	grow3donce	0.42		10.50		66.26		45.79	
8	grow3doncesmooth3dwith3	0.42		10.55		66.95		45.79	
9	grow3dtwice	0.44							
10	grow3dtwicesmooth3dwith3	0.43		10.21		65.38		45.36	
11	growallsliceslongonce	0.41		10.65		67.21		45.88	
12	growallsliceslongoncesmooth3dwith5	0.42		10.63		68.47		45.98	
13	growallsliceslongtwice	0.42		10.47		65.78		45.65	
14	growallsliceslongtwicesmooth3dwith5	0.57		7.76		66.74		45.70	
15	bone_growallsliceslongonce						27.20		45.54
16	bone_growallsliceslongtwice						29.54		43.57
17	bone_growvolume3donce						32.86		46.12
18	bone_growvolume3dtwice						35.08		45.23
19	bone_shrinkallsliceslongonce_growallsliceslongonce						21.71		46.81
20	bone_shrinkallsliceslongonce						5.14		43.36
21	bone_shrinkallsliceslongtwice						0		37.58
22	bone_shrinkvolume3donce						2.68		41.55
23	bone_shrinkvolume3dtwice						0		30.96
	Mean.	0.40	0.17	10.43	34.52	66.17	19.09	45.91	44.12
	Standard Deviation	0.11	0.00	0.87	0.21	2.25	12.04	0.24	4.49

Appendix D

Poor µCT Quality Images of Long Time *In Vitro* Immersion Tests on Mg-5Gd, Mg-10Gd and Pure Mg Pins and Screws

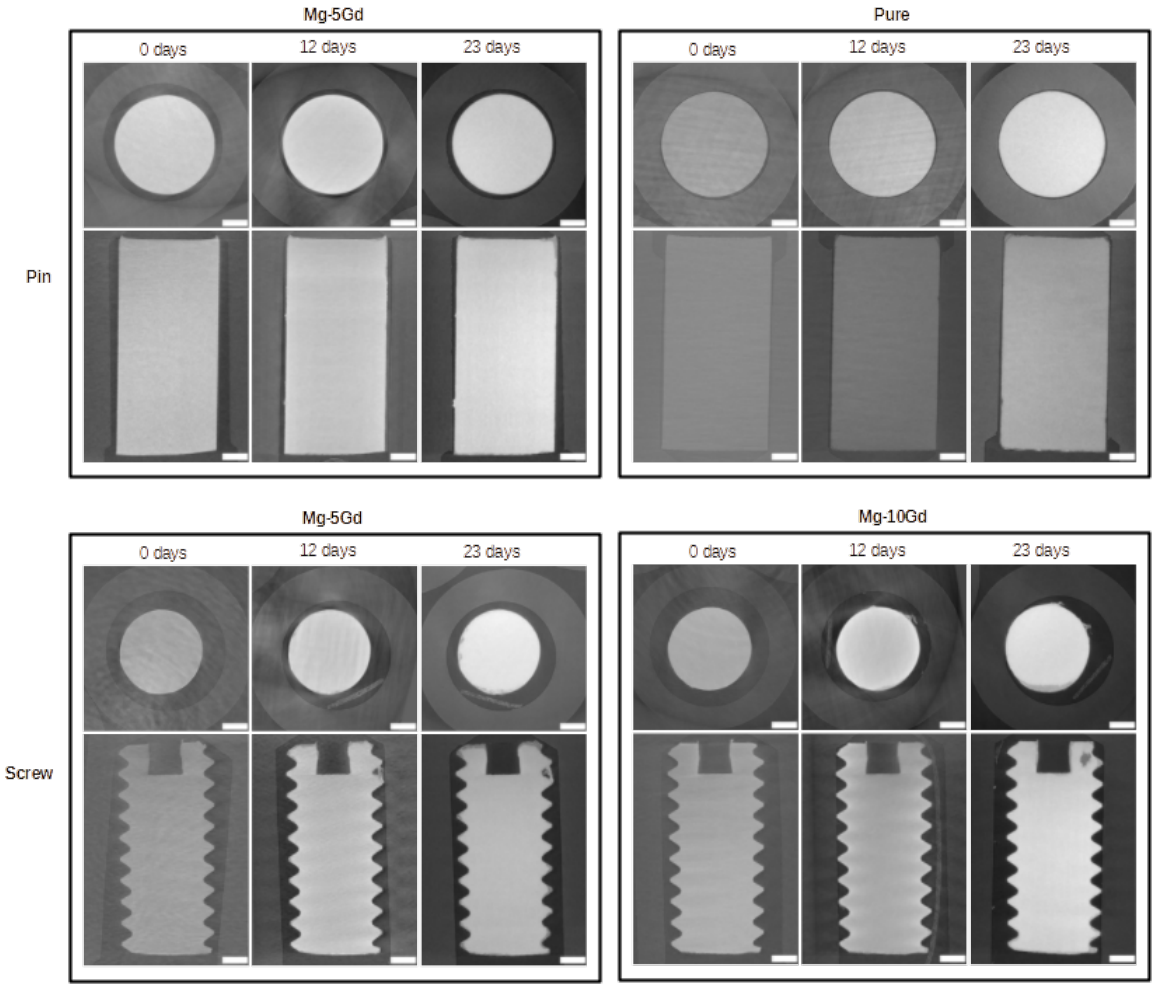

FIGURE D.1: Exemplary cross sectional and longitudinal slices from 3D SRµCT images of Mg-5Gd, Mg-10Gd and pure Mg pins and screws. The scale bar corresponds to 500 µm. The poor image quality made it impossible to do any qualitative or quantitative analysis on the current data.

Appendix E

Segmentation Workflows

Following are described the step-by-step instructions for the segmentation of the *ex vivo* data. As "reference screw" is meant the screw, which is used for the right orientation of the *ex vivo* data.

E.1 Segmentation Workflow of "not corroded screw"

1. Segmentation, registration and resampling of not corroded screw
   All the following steps described for segmentation of the not corroded screw are schematically shown in figure 3.3.

   (a) Import reference screw into Avizo with pixelsize 5x5x5 μm and 1200x1200x1000 pixel. Load the complete volume into the memory.

   (b) Import preimplantation screw (PS=preimplantation screw) (figure 3.2 A1) in Fiji. Segment preimplantation screw *via* thresholding in Fiji. At the end of the thresholding the screw should be white with value 255 and the background black with value 0. Save the segmented preimplantation screw (SPS) as image sequence.

   (c) Import the SPS into Avizo.

   (d) To make the reference and SPS visible right click on the reference data, find Isosurface and apply it.

   (e) Register (”Register images”) SPS on the reference screw by

      i. Click on align principal axis (”aligning”=matching the 2 screws in vertical direction) with rigid registration.

      ii. If the “Align principal axis” is not successful, align by hand (too precise alignment is not necessary).

      iii. Click “Apply”.

2. Resample the SPS on reference screw by ”Resample transformed image”.

3. Resize the voxel size of resampled SPS from 5 to 4.85. (in "crop editor"). This step is done because the preimplantation screws are imaged with Nanotom, which has a different calibration of the voxels compared to the synchtron CTs.

4. Afterwards again resample the resampled SPS on the reference screw. Export the result as 2D .tiff (figure 3.2 A3).

5. Import the corresponding explant into Fiji. Crop the data as much as possible without losing information and save as image sequence.

6. Convert the latter into 8-bit, filter either with “mean3D” or with "median3d” filter (voxel size 4x4x4) depending on the data quality. Save as image sequence (.tiff).

7. Import the filtered, 8-bit converted ex vivo image sequence into Avizo.

8. Roughly segment the not corroded screw, which is the corroded residual screw with the corrosion layer. For this rough segmentation use watershed. Hint: first mark only 3-4 slices with just 2 materials: ”screw” and ”background+bone”. Check for "Side-by-side" to be on and create a new labelfield and create a gradient image when applying the segmentation.

9. Check if the segmentation is sufficient enough. If not, roughly segment more slices and aaply the watershed segmentation again.

10. Import also the non-filtered ex vivo dataset into Avizo (figure 3.2 B1).

11. Connect the roughly segmented screw (label) obtained from watershed segmentation to the original dataset.

12. Register the label, which is now attached to the non-filtered original ex vivo data set on the resampled SPS.

13. To check if the registration went well apply "Volume Rendering" on the non-filtered original ex vivo data. Attach the "Orto Slice to resampled SPS (with Isosurface and Volume Rendering ON). To cut the data set into parts use "Clip" and switch the ortho slice off.

14. Import the as 2D-tiff exported resampled SPS into Avizo again. Convert to a 8-bit label (unclick "clean labels").

15. Attach the label of the registered SPS to the registered, resampled, non-filtered, original dataset.

16. Manually clean up the mistakes, where the resampled SPS doesn’t match to the borders of the non-corroded screw from the original data. You are free to use "grow", "smooth", "add", "subtract", etc. When the result is satisfying export the label as 2D .tiff.

17. Import the exported resampled non-filtered original data into Fiji. Also import the result from previous step, the non-corroded screw, into Fiji. The screw should have the value 1, background and the bone should be 0. Eliminate the bone and the background by multiplying this both data sets. Save the result as image sequence. This non-corroded screw is being called "screw" in the workflow chart (figure 3.2 B3.1).

E.2 Segmentation Workflow of "corroded screw"

1. Segmentation, registration and resampling of corroded screw
   All the following steps describe the segmentation of the corroded screw. The flowchart is shown in figure 3.4.

   (a) Import the dataset “screw” into Avizo (figure 3.2 B3.1).

(b) Perform watershed segmentation of the residual screw. Hereby create 2 materials: ”residual” and ”corrosion”. Mark inside the residual screw every 50 slice and add to “residual”, than mark the corrosion layer+background on the same slices. The marking of different labels can be performed very roughly.

(c) If you are happy with the result of the watershed save result as 2D .tiff ”residual_screw”. If not happy with the result perform some additional manual segmentation/cleaning and than save as 2D .tiff ”residual _screw” (figure 3.2 B3.2).

(d) In addition you might auto-threshold the corrosion layer in Fiji with the aim to remove the background from the corrosion layer.

E.3 Segmentation Workflow of "bone"

1. Segmentation, registration and resampling of bone
   All the following steps are described for segmentation of the bone. The schematics of the workflow is shown in figure 3.5.

   (a) Import the dataset “screw” into Fiji. Use mathematical operations to gain image stack with value 0 for screw and 1 for bone+background.

   (b) Import the registered, resampled, non-filtered original data into Fiji.

   (c) Multiply result from step 1 with step 2.

   (d) Perform automatic thresholding on the result from step 3. Save as 2D .tiff (figure 3.2 B3.3).

Appendix F

Fiji Script for the Conversion of the 3D Difference Layer of Mg-xGd Implant M2 Implant Screws to 2D Difference Layer

```
list=getList("window.titles");
        for(i=0; i<list.length; i++){
                winame=list[i];
                selectWindow(winame);
                run("Close");}

        run("Close All");
         if (isOpen("Log")){
        selectWindow("Log");
   run("Close");} //close the log datei
         if (isOpen("Results")){
        selectWindow("Results");
   run("Clear Results");} //close the results date

close("All");
run("Close All");


Dialog.create("All needed information for starting the analysis. Change all if neccessary!");
Dialog.addNumber("pixelsize in mm: x", 0.005);
Dialog.addNumber("pixelsize in mm: y", 0.005);
Dialog.addNumber("pixelsize in mm: z", 0.005);
Dialog.addNumber("Start of the data, which will be analysed (data saved in the excell table/.txt
file", 1);
Dialog.addNumber("End of the data, which will be analysed (data saved in the excell table/.txt file",
3);
Dialog.addString("Pfad of the .txt datei (allowed amount of characters: 300)",
"/asap3/petra3/gpfs/p05/2016/data/11001978/processed/Diana/invitroanalysis/
invitroanalysis_weeks/invitroanalysis_weeks_screwwithoutslit.txt", 150);

Dialog.show();
x_pixelsize = Dialog.getNumber();
y_pixelsize = Dialog.getNumber();
z_pixelsize = Dialog.getNumber();
start =Dialog.getNumber();
end = Dialog.getNumber();
pfad=Dialog.getString();

print("x_pixelsize (in mm) ="+x_pixelsize);
print("y_pixelsize (in mm) ="+y_pixelsize);
print("z_pixelsize (in mm) ="+z_pixelsize);
print("Start of the data, which will be analysed (data saved in the excell table/.txt file="+start);
print("End of the data, which will be analysed (data saved in the excell table/.txt file="+end);
print(pfad);

voxelsize=x_pixelsize*y_pixelsize*z_pixelsize;


filestring = File.openAsString(pfad);
```

```
rows = split(filestring, "\n");
id= newArray(rows.length);
openPfad= newArray(rows.length);
generalPfad = newArray(rows.length);
duration = newArray(rows.length);
alloy= newArray(rows.length);
hauptPfad= newArray(rows.length);
surface=newArray(rows.length);
volume=newArray(rows.length);
foldername=newArray(rows.length);


for(u=start; u<end; u++){
	IJ.log("Processing_file_" + u+"_of_"+end-1+";");
	corRate3D_nn=1;
	columns=split(rows[u],"\t");
	id[u]= columns[0];
	nameSample= id[u];
	name_sample= id[u];
	openPfad[u]=columns[1];
	generalPfad[u]= columns[2];
	duration[u]= columns[3];
	timepoint=duration[u]; //saved for the later naming of the last datei!
	alloy[u]=columns[4];
	legierung=alloy[u];
	hauptPfad[u]=columns[5];
	surface[u]=columns[6];
	surface_avizo=surface[u];
	volume[u]=columns[7];
	volume_avizo=volume[u];
	foldername[u]=columns[8];
	folder_name=foldername[u];
	inputCorrodedCropped=openPfad[u]+"/corroded/corroded0000.tif";
	//inputNotCorrodedCropped=openPfad[u]+"/preimplant/preimplant0000.tif";
	inputNotCorrodedCroppedExplant=openPfad[u]+"/notCorroded/notCorroded0000.tif";
	inputdifference=openPfad[u]+"/difference/difference000.tif";
	//inputBone=openPfad[u]+"/bone.am";

//inputNotCorrodedOriginal=generalPfad[u]+"/notcorroded_original/notcorroded_original0000.tif";
	savingPfad=generalPfad[u];
	savingHauptPfad=hauptPfad[u];
	mdd_oneSample=newArray;
   print(inputNotCorrodedCroppedExplant);
	//print(inputCorrodedCropped);


////////////////////////////////////////////////////////////OPEN NOTCORRODED////////////////////////////////////
```

```
checkreadyness=getBoolean("are u ready to analyse this sample? YOUR FULL ATTENTION
WILL BE NEEDED NOW!");
if (checkreadyness==1) {

opennotcorrodedresliced=generalPfad[u]+"/resliced_sum_notCorroded/"+name_sample+".tif";
run("Image Sequence...", "open=opennotcorrodedresliced sort");
print(opennotcorrodedresliced);
run("Select None");
//getSelectionCoordinates(x, z);
//x=x[0];
x=300;
y=getHeight();
width=getWidth();
makeRectangle(0, 0, width, y);
run("Measure");
areaimage=getResult("Area",0);
run("Clear Results");
print("areaimage="+areaimage);
makePolygon(x,        0,                x-80,y,          x-35,   y,                x+45,0);

checkpolygon=getBoolean("do u think the polygon covers one thread of the screw?");
if (checkpolygon==1) {
print("the given polygon with the coordinates BLA is ok. I am not going to change the coordinates -
> click 'yes'");
}
else {


checkreadytodothepolygon=getBoolean("are u ready to move the polygon NOW? After you click
'Yes', you just have 4000 ms to do so... please think of chosing the right thread before clicking 'yes'
");
if (checkreadytodothepolygon==1) {


print("the given polygon was not ok and i am going to move the polygon change the coordinates.
see log. datei for the coordinates ");
print("please move the polygon in such a way, that it covers one thread...");
wait(4000);
getSelectionCoordinates(xpoints, ypoints);
Array.print(xpoints);
x=xpoints[0];
makePolygon(x,        0,                x-80,y,          x-35,   y,                x+45,0);

checkpolygon2=getBoolean("do u think the polygon covers NOW one thread of the screw?");
if (checkpolygon2==1) {
print("the given polygon with the coordinates BLA is ok. I am not going to change the coordinates -
> click 'yes'");

x1=x-40;
print("x1="+x1);
```

```
x2=x1-40;
print("x2="+x2);
while (x2>0) {
x2=x2-80;
print("x2="+x2);
}


makePolygon(0,      0,          0,y,          x2-35, y,          x2+45,0);
run("Clear", "slice");


x3=x2+40;
print("x3="+x3);
makePolygon(x3,     0,          x3-80,y,          x3-35, y,          x3+45,0);
run("Clear", "slice");

wait(1000);
makePolygon(x3,     0,          x3-80,y,          x3-35, y,          x3+45,0);
run("Clear", "slice");


while (x3<width) {
x3=x3+80;

wait(1000);
makePolygon(x3,     0,          x3-80,y,          x3-35, y,          x3+45,0);
run("Clear", "slice");
}

}
}
run("Select None");
run("Clear Results");

////////////////GETTING HISTOGRAM OF NOT CORRODED/////////////////////////////////////////
   getStatistics(area, mean, min, max, std, histogram);
     if (bitDepth==8 || bitDepth==24) {
        for (i=0; i<histogram.length; i++) {
           setResult("Value", i, i);
           setResult("Count", i, histogram[i]);
         }
     } else {
        value = min;
        binWidth = (max-min)/255;
        for (i=0; i<histogram.length; i++) {
           setResult("Count", i, histogram[i]);
         }
     }
     updateResults();
```

```
      removedpixels=getResult("Count",0);
            pixelanalysedhills=(width*y)-removedpixels;
            print("removedpixels="+removedpixels);
            print("pixelanalysedhills="+pixelanalysedhills);
////////////////////////////////////////////////////////////OPEN DIFFERENCE////////////////////////////////////
opendifferenceresliced=generalPfad[u]+"/resliced_sum_difference/"+name_sample+".tif";
run("Image Sequence...", "open=opendifferenceresliced sort");
run("Select None");
imageCalculator("Multiply", "resliced_sum_notCorroded","resliced_sum_difference");
selectWindow("resliced_sum_difference");
close();
selectWindow("resliced_sum_notCorroded");
run("Select None");
rename("hills");
//////////////GETTING HISTOGRAM//////////////////////////////////////
   getStatistics(area, mean, min, max, std, histogram);
      if (bitDepth==8 || bitDepth==24) {
         for (i=0; i<histogram.length; i++) {
            setResult("Value", i, i);
            setResult("Count", i, histogram[i]);
         }
      } else {
         value = min;
         binWidth = (max-min)/255;
         for (i=0; i<histogram.length; i++) {
            setResult("Value", i, i);
            setResult("Count", i, histogram[i]);
         }
      }
      updateResults();
      differencevalueshill=0;
      for (i = 1; i <= 255; i++) {
          counts=getResult("Count",i);
          if (counts>0) {
          differencevalueshill=differencevalueshill+(counts*getResult("Value",i));
          }
      }
run("Clear Results");
run("Close All");
}

print("differencevalueshill="+differencevalueshill);
differencevalueshillnormed=differencevalueshill/pixelanalysedhills;


//////////////////////////////// DOING SAME FOR DALE!!!!!!////////////////////////////////////////////////////////
////////////////////////////////////////////////////////////OPEN NOTCORRODED////////////////////////////////////

opennotcorrodedresliced=generalPfad[u]+"/resliced_sum_notCorroded/"+name_sample+".tif";
run("Image Sequence...", "open=opennotcorrodedresliced sort");
```

```
print(opennotcorrodedresliced);
run("Select None");
//getSelectionCoordinates(x, z);
//x=x[0];


x1=x-40;
print("x1="+x1);
x2=x1-40;
print("x2="+x2);
while (x2>0) {
x2=x2-80;
print("x2="+x2);
}


makePolygon(0,	0,	0,y,	x2-35,	y,	x2+45,0);
run("Clear", "slice");


x3=x2;
print("x3="+x3);
makePolygon(x3,	0,	x3-80,y,	x3-35,	y,	x3+45,0);
run("Clear", "slice");

wait(1000);
makePolygon(x3,	0,	x3-80,y,	x3-35,	y,	x3+45,0);
run("Clear", "slice");


while (x3<width) {
x3=x3+80;

wait(1000);
makePolygon(x3,	0,	x3-80,y,	x3-35,	y,	x3+45,0);
run("Clear", "slice");
}

///////////////GETTING HISTOGRAM OF NOT CORRODED/////////////////////////////////////////
   getStatistics(area, mean, min, max, std, histogram);
      if (bitDepth==8 || bitDepth==24) {
         for (i=0; i<histogram.length; i++) {
            setResult("Value", i, i);
            setResult("Count", i, histogram[i]);
         }
      } else {
         value = min;
         binWidth = (max-min)/255;
         for (i=0; i<histogram.length; i++) {
            setResult("Count", i, histogram[i]);
```

```
        }
      }
      updateResults();
      removedpixels=getResult("Count",0);
      print("removedpixels="+removedpixels);
            pixelanalyseddales=(width*y)-removedpixels;
            print("pixelanalyseddales="+pixelanalyseddales);
run("Clear Results");
////////////////////////////////////////////////////////////OPEN DIFFERENCE////////////////////////////////////
opendifferencesresliced=generalPfad[u]+"/resliced_sum_difference/"+name_sample+".tif";
run("Image Sequence...", "open=opendifferencesresliced sort");
run("Select None");
imageCalculator("Multiply", "resliced_sum_notCorroded","resliced_sum_difference");
selectWindow("resliced_sum_difference");
close();
selectWindow("resliced_sum_notCorroded");
run("Select None");
rename("dales");
///////////////GETTING HISTOGRAM/////////////////////////////////////////
   getStatistics(area, mean, min, max, std, histogram);
      if (bitDepth==8 || bitDepth==24) {
         for (i=0; i<histogram.length; i++) {
            setResult("Value", i, i);
            setResult("Count", i, histogram[i]);
         }
      } else {
         value = min;
         binWidth = (max-min)/255;
         for (i=0; i<histogram.length; i++) {
          setResult("Value", i, i);
          setResult("Count", i, histogram[i]);
         }
      }
      updateResults();
      differencevaluesdale=0;
      for (i = 1; i <= 255; i++) {
          counts=getResult("Count",i);
          if (counts>0) {
          differencevaluesdale=differencevaluesdale+(counts*getResult("Value",i));
           }
      }

differencevaluesdalenormed=differencevaluesdale/pixelanalyseddales;
 //  run("Close All");
print("differencevalueshill="+differencevalueshill);
print("differencevaluesdale="+differencevaluesdale);
differencevaluesratio=differencevalueshillnormed/differencevaluesdalenormed;
print("differencevaluesratio="+differencevaluesratio);
          }
```

```
          if (isOpen("Log")){
         selectWindow("Log");

saveAs(savingHauptPfad+"/Log_"+nameSample+timepoint+"days_"+legierung+"_hillsdales.txt");
             if (isOpen("Log_"+nameSample+timepoint+"days_"+legierung+"_hillsdales.txt")){
         selectWindow("Log_"+nameSample+timepoint+"days_"+legierung+"_hillsdales.txt");
  run("Close");} //close the log datei



}; //end of all calculations for one data set

run("Close All");
run("Clear Results");
```

Appendix G

Workflow of the Sample Holder Preparation

The modified workflow of the sample holder preparation for the push-out experiments is described in the the following:

1. Export reconstruction as 16-bit Tiff files onto a distinct file folder
2. Import .tif files into ImageJ, crop to ROI and convert to 8-bit .raw file
3. If necessary to achieve better contrast between the bone and the implant filter the data.
4. Segment screw in one label field
5. Segment whole bone explant + screw into second label field
6. Import segmented bone+screw and screw into Avizo – enter voxel size (from .pcr file)
7. Import reference screw 1000x1000x917\asap3.desy.de\petra3-core\p05\2016\data\11001978\processed\SegmentationWorkflow \referencescrew\reference\1200x1200x1000\pixelsize5x5x5 with 0.005x0.005x0.005 voxel size
8. Align label with screw only with reference screw using "Register Images" module
9. Transform the bone+screw to same position as the registered screw (*via* copying the positions of the registered screw to the positions of the bone+screw)
10. Import holder bottom "\ \asap3.desy.de\petra3-core\p05\2016\data\ 11001978\processed\SynchroLoad\Holders\holder\bottom\holder\bottom.tif", voxel size 0.01132
11. Transform holder bottom by -7.49, -7.49 and z (minimum by -7.49), rotate holder by 180 on x-axis
12. Import Holder "\ \asap3.desy.de\petra3-core\p05\2016\data\11001978 \processed\SynchroLoad\Holders\ holder\top\holder\top.tif", voxel size 0.01132
13. Transform holder bottom by -7.49, -7.49 and z (according to the height of the holder bottom), rotate holder by 180 on x-axis
14. Resample transformed bone+screw on the holder bottom
15. Resample transformed bone+screw on the holder top

16. Morphological operations: Closing operation, cube, 2px, XY planes on the results from Step14
17. Morphological operations: Closing operation, cube, 2px, XY planes on the results from Step15
18. Export dataset from Step16 as .tif (2D)
19. Export dataset from Step17 as .tif (2D)
20. Open macro "\ \asap3.desy.de\petra3-core\p05\2016\data\11001978\processed \SynchroLoad\holder\macros\step20\top.ijm" in Fiji(ImageJ) and run on the top result from Step 18.
21. Open macro "\ \asap3.desy.de\petra3-core\p05\2016\data\11001978\processed \SynchroLoad\holder\macros\step20\bottom.ijm" in Fiji(ImageJ) and run on the bottom result from Step 19.
22. Adapt names in design\holder.pro for top holder and run for top holder
23. Adapt names in design\holder.pro for bottom holder and run for bottom holder
24. Open macro "\ \asap3.desy.de\petra3-core\p05\2016\data\11001978\processed \SynchroLoad\holder\macros\step24\top.ijm" in Fiji(ImageJ) and run on the top result from Step 22.
25. Open macro "\ \asap3.desy.de\petra3-core\p05\2016\data\11001978\processed \SynchroLoad\holder\macros\step24\24.ijm" in Fiji(ImageJ) and run on the bottom result from Step 23.
26. Import into Avizo with voxel size 0.02264 top sample holder
27. Import into Avizo with voxel size 0.02264 bottom sample holder
28. Extract surfaces of top sample holder from isosurface and simplify (until 1000000 faces, *via* 50000 steps), export as .stl
29. Extract surfaces of bottom sample holder from isosurface and simplify (until 1000000 faces, *via* 50000 steps), export as .stl

Appendix H

Customized Fiji-Scripts Used in the Sample Holder Preparation Workflow

In the following are the .ijm macros for the preparation of the sample holders presented. Their operation is described in the appendix G.

Step 13: top

```
dir = getDirectory( "Choose the Directory" );
list = getFileList( dir );
openimagepath=dir+list[0];
print(dir);
print(list[0]);
run("Image Sequence...", "open=openimagepath sort");
//run("Reverse");
run("Make Binary", "method=Default background=Dark");
run("Invert LUT");
setSlice(10);
run("Erode", "stack");
run("Erode", "stack");
run("Erode", "stack");
run("Erode", "stack");
run("Erode", "stack");
run("Erode", "stack");
//run("Dilate", "stack");
//run("Dilate", "stack");
//run("Dilate", "stack");
//run("Dilate", "stack");
//run("Dilate", "stack");
//run("Dilate", "stack");
makeRectangle(108, 144, 1251, 1221);
run("Clear Outside", "stack");
run("Select None");
wait(5000);
Dialog.create("Seed point coordinates");
Dialog.addNumber("x:", 0);
Dialog.addNumber("y:", 0);
Dialog.addNumber("z:", 199);
Dialog.show();
x = Dialog.getNumber();
y = Dialog.getNumber();
z = Dialog.getNumber();
run("Connected Threshold Grower ...", "x=x y=y z=z min=100 max=260");
run("Erode", "stack");
rename("step13_2");
newdir = dir+"\..";
File.makeDirectory(newdir+"/step13_2_holdertop/");
savingpath=newdir+"/step13_2_holdertop/step13_2_holdertop.tif";
saveAs("Tiff", savingpath);
```

Step 13: bottom

```
dir = getDirectory( "Choose the Directory" );
list = getFileList( dir );
openimagepath=dir+list[0];
print(dir);
print(list[0]);
run("Image Sequence...", "open=openimagepath sort");
```

```
run("Make Binary", "method=Default background=Dark");
run("Invert LUT");
run("Erode", "stack");
run("Erode", "stack");
run("Erode", "stack");
run("Erode", "stack");
run("Erode", "stack");
run("Erode", "stack");
run("Erode", "stack");
makeRectangle(108, 144, 1251, 1221);
run("Clear Outside", "stack");
run("Select None");
setSlice(2);
wait(5000);
Dialog.create("Seed point coordinates");
Dialog.addNumber("x:", 0);
Dialog.addNumber("y:", 0);
Dialog.addNumber("z:", 199);
Dialog.show();
x = Dialog.getNumber();
y = Dialog.getNumber();
z = Dialog.getNumber();
run("Connected Threshold Grower ...", "x=x y=y z=z min=100 max=300");
run("Erode", "stack");
rename("step13_2");
newdir = dir+"\..";
File.makeDirectory(newdir+"/step13_2_holderbottom/");
savingpath=newdir+"/step13_2_holderbottom/step13_2_holderbottom.tif";
saveAs("Tiff", savingpath);
```

Step 15: top

```
dir = getDirectory( "Choose the Directory" );
list = getFileList( dir );
openimagepath=dir+list[0];
print(dir);
print(list[0]);
run("Image Sequence...", "open=openimagepath sort");
setSlice(1);
run("Delete Slice");
run("Bin...", "x=2 y=2 z=2 bin=Min");
makeRectangle(102, 348, 31, 54);
run("Clear", "stack");
run("Image Sequence...",
"open=/asap3/petra3/gpfs/p05/2016/data/11001978/processed/SynchroLoad/Holders/
holders_archive/
CylinderForOrientierung_withHole_1500x1500x872_mitMarkierung_innerhole_2point25mm_onH
older_part2_binned2x2x2min/
CylinderForOrientierung_withHole_1500x1500x872_mitMarkierung_innerhole_2point25mm_onH
older_part20004.tif sort");
```

```
run("Concatenate...", "  title=[Concatenated Stacks] keep
image1=CylinderForOrientierung_withHole_1500x1500x872_mitMarkierung_innerhole_2point25
mm_onHolder_part2_binned2x2x2min image2=step14_holdertop image3=[-- None --]");
setSlice(nSlices);
run("Add Slice");
setSlice(nSlices-nSlices+1);
run("Add Slice");
setSlice(nSlices-nSlices+1);
run("Delete Slice");
rename("step15_holdertop");
newdir = dir+"\..";
savingpath=newdir+"/step15_holdertop/step15_holdertop.tif";
File.makeDirectory(newdir+"/step15_holdertop/");
for (i = 1; i < nSlices+1; i++) {
selectWindow("step15_holdertop");
setSlice(i);
run("Duplicate...", " ");
saveAs("Tiff", savingpath+"step15_holdertop_"+i+".tif");
close();
}
close();
close();
close();
```

Step 15: bottom

```
dir = getDirectory( "Choose the Directory" );
list = getFileList( dir );
openimagepath=dir+list[0];
print(dir);
print(list[0]);
run("Image Sequence...", "open=openimagepath sort");
run("Bin...", "x=2 y=2 z=2 bin=Min");
setSlice(nSlices);
run("Add Slice");
setSlice(nSlices-nSlices+1);
run("Add Slice");
setSlice(nSlices-nSlices+1);
run("Delete Slice");
rename("step15_holderbottom");
newdir = dir+"\..";
savingpath=newdir+"/step15_holderbottom/step15_holderbottom.tif";
File.makeDirectory(newdir+"/step15_holderbottom/");
for (i = 1; i < nSlices+1; i++) {
selectWindow("step15_holderbottom");
setSlice(i);
run("Duplicate...", " ");
saveAs("Tiff", savingpath+"step15_holderbottom_"+i+".tif");
close();
}
```

Appendix I

Fiji Script for the Analysis of *In Vivo* Degraded Mg-xGd, Ti and PEEK Implants in Rats Bone

Current Fiji script has been written as a part of my PhD thesis. It is an analysis script of tomographic data from synchrotron radiation micro-computed tomography station at DESY (Hamburg, Germany). The *ex vivo* data from *in vivo* corroded Mg-xGd implants in rats bone for 3 different time points (4, 8 and 12 weeks degradation) are analyzed regarding the degradation rate and the pitting factor of the screw formed implant. Additionally, implant's integration into the bone is also analyzed *via* parameters like bone to implant contact area and bone volume density of the bone surrounding the implant.

The script is published and can be found under https://zenodo.org/record/6481319#.YmWD2JFBxPY.

Bibliography

[1] Parama Chakraborty Banerjee, Saad Al-Saadi, Lokesh Choudhary, Shervin Eslami Harandi, and Raman Singh. "Magnesium implants: Prospects and challenges". In: *Materials* 12 (1 2019), p. 136.

[2] Regine Willumeit-Römer. "The interface between degradable Mg and tissue". In: *JOM* 71 (4 2019), pp. 1447–1455.

[3] Guang-Ling Song. *Corrosion of magnesium alloys*. Elsevier, 2011.

[4] Mark P Staiger, Alexis M Pietak, Jerawala Huadmai, and George Dias. "Magnesium and its alloys as orthopedic biomaterials: a review". In: *Biomaterials* 27 (9 2006), pp. 1728–1734.

[5] Nuno M Neves, A Kouyumdzhiev, and Rui L Reis. "The morphology, mechanical properties and ageing behavior of porous injection molded starch-based blends for tissue engineering scaffolding". In: *Materials Science and Engineering: C* 25 (2 2005), pp. 195–200.

[6] Muhammad Imran Rahim, Sami Ullah, and Peter P Mueller. "Advances and challenges of biodegradable implant materials with a focus on magnesium-alloys and bacterial infections". In: *Metals* 8 (7 2018), p. 532.

[7] Wilhelm Jahnen-Dechent and Markus Ketteler. "Magnesium basics". In: *Clinical kidney journal* 5 (Suppl_1 2012), pp. i3–i14.

[8] Harpreet S Brar, Manu O Platt, Malisa Sarntinoranont, Peter I Martin, and Michele V Manuel. "Magnesium as a biodegradable and bioabsorbable material for medical implants". In: *Jom* 61 (9 2009), pp. 31–34.

[9] Nicholas Travis Kirkland and Nick Birbilis. *Magnesium biomaterials: design, testing, and best practice*. Springer, 2014.

[10] R K Raman and Shervin Eslami Harandi. "Resistance of magnesium alloys to corrosion fatigue for biodegradable implant applications: Current status and challenges". In: *Materials* 10 (11 2017), p. 1316.

[11] N Hort, Y Huang, D Fechner, M Störmer, C Blawert, F Witte, C Vogt, H Drücker, R Willumeit, K U Kainer, et al. "Magnesium alloys as implant materials–Principles of property design for Mg–RE alloys". In: *Acta biomaterialia* 6 (5 2010), pp. 1714–1725.

[12] J Kubásek and D Vojtěch. "Structural and corrosion characterization of biodegradable Mg–RE (RE= Gd, Y, Nd) alloys". In: *Transactions of Nonferrous Metals Society of China* 23 (5 2013), pp. 1215–1225.

[13] Anastasia Myrissa, Simone Braeuer, Elisabeth Martinelli, Regine Willumeit-Roemer, Walter Goessler, and Annelie Martina Weinberg. "Gadolinium accumulation in organs of Sprague–Dawley®rats after implantation of a biodegradable magnesium-gadolinium alloy". In: *Acta biomaterialia* 48 (2017), pp. 521–529.

[14] J Ramalho, R C Semelka, M Ramalho, R H Nunes, M AlObaidy, and M Castillo. "Gadolinium-based contrast agent accumulation and toxicity: an update". In: *American Journal of Neuroradiology* 37 (7 2016), pp. 1192–1198.

[15] David W Bruce, Bernard E Hietbrink, and Kenneth P DuBois. "The acute mammalian toxicity of rare earth nitrates and oxides". In: *Toxicology and applied pharmacology* 5 (6 1963), pp. 750–759.

[16] Frank Feyerabend, Janine Fischer, Jakob Holtz, Frank Witte, Regine Willumeit, Heiko Drücker, Carla Vogt, and Norbert Hort. "Evaluation of short-term effects of rare earth and other elements used in magnesium alloys on primary cells and cell lines". In: *Acta biomaterialia* 6 (5 2010), pp. 1834–1842.

[17] T J Haley, K Raymond, N Komesu, and H C Upham. "Toxicological and pharmacological effects of gadolinium and samarium chlorides". In: *British journal of pharmacology and chemotherapy* 17 (3 1961), pp. 526–532.

[18] Nezha Ahmad Agha, Regine Willumeit-Römer, Daniel Laipple, Bérengère Luthringer, and Frank Feyerabend. "The degradation interface of magnesium based alloys in direct contact with human primary osteoblast cells". In: *PloS one* 11 (6 2016).

[19] Francesca Cecchinato, Nezha Ahmad Agha, Adela Helvia Martinez-Sanchez, Berengere Julie Christine Luthringer, Frank Feyerabend, Ryo Jimbo, Regine Willumeit-Römer, and Ann Wennerberg. "Influence of magnesium alloy degradation on undifferentiated human cells". In: *PloS one* 10 (11 2015).

[20] M D Costantino, A Schuster, H Helmholz, A Meyer-Rachner, R Willumeit-Römer, and B J C Luthringer-Feyerabend. "Inflammatory response to magnesium-based biodegradable implant materials". In: *Acta biomaterialia* 101 (2020), pp. 598–608.

[21] Nurettin Sezer, Zafer Evis, Said Murat Kayhan, Aydin Tahmasebifar, and Muammer Koç. "Review of magnesium-based biomaterials and their applications". In: *Journal of magnesium and alloys* 6 (1 2018), pp. 23–43.

[22] Sebastian Bauer, Patrik Schmuki, Klaus Von Der Mark, and Jung Park. "Engineering biocompatible implant surfaces: Part I: Materials and surfaces". In: *Progress in Materials Science* 58 (3 2013), pp. 261–326.

[23] Rongchang Zeng, Wolfgang Dietzel, Frank Witte, Norbert Hort, and Carsten Blawert. "Progress and challenge for magnesium alloys as biomaterials". In: *Advanced engineering materials* 10 (8 2008), B3–B14.

[24] N T Kirkland, Jeremy Lespagnol, Nick Birbilis, and M P Staiger. "A survey of bio-corrosion rates of magnesium alloys". In: *Corrosion science* 52 (2 2010), pp. 287–291.

[25] P Maier, F Zimmermann, M Rinne, G Szakács, N Hort, and C Vogt. "Solid solution treatment on strength and corrosion of biodegradable Mg6Ag wires". In: *Materials and Corrosion* 69 (2 2018), pp. 178–190.

[26] P Maier, J Gonzalez, R Peters, F Feyerabend, T Ebel, and N Hort. "Degradation morphology and pitting factor compared to degradation rate". In: *European Cells and Materials* 32 (6 2016), p. 22.

[27] Toshihide Takenaka, Takami Ono, Yuji Narazaki, Yusuke Naka, and Masahiro Kawakami. "Improvement of corrosion resistance of magnesium metal by rare earth elements". In: *Electrochimica Acta* 53 (1 2007), pp. 117–121.

[28] Berit Zeller-Plumhoff, Heike Helmholz, Frank Feyerabend, Thomas Dose, Fabian Wilde, Alexander Hipp, Felix Beckmann, Regine Willumeit-Römer, and Jörg U Hammel. "Quantitative characterization of degradation processes in situ by means of a bioreactor coupled flow chamber under physiological conditions using time-lapse SRmicroCT". In: *Materials and Corrosion* 69 (3 2018), pp. 298–306.

[29] Christoph Castellani, Richard A Lindtner, Peter Hausbrandt, Elmar Tschegg, Stefanie E Stanzl-Tschegg, Gerald Zanoni, Stefan Beck, and Annelie-Martina Weinberg. "Bone–implant interface strength and osseointegration: Biodegradable magnesium alloy versus standard titanium control". In: *Acta biomaterialia* 7 (1 2011), pp. 432–440.

[30] Martina Rauner, Nicola Stein, and Lorenz C Hofbauer. *Basics of bone biology*. Springer, 2012, pp. 1–26.

[31] Simón Méndez-Ferrer, Tatyana V Michurina, Francesca Ferraro, Amin R Mazloom, Ben D MacArthur, Sergio A Lira, David T Scadden, Avi Ma'ayan, Grigori N Enikolopov, and Paul S Frenette. "Mesenchymal and haematopoietic stem cells form a unique bone marrow niche". In: *Nature* 466 (7308 2010), pp. 829–834.

[32] Mone Zaidi. "Skeletal remodeling in health and disease". In: *Nature medicine* 13 (7 2007), pp. 791–801.

[33] Tim D White and Pieter A Folkens. *The human bone manual*. Elsevier, 2005.

[34] M Meskinfam. *Polymer scaffolds for bone regeneration*. Elsevier, 2017, pp. 441–475.

[35] E G Meinberg, J Agel, C S Roberts, Matthew D Karam, and J F Kellam. "Fracture and dislocation classification compendium—2018". In: *Journal of Orthopaedic trauma* 32 (2018), S1–S10.

[36] Lorenzo Marzona and Bernardo Pavolini. "Play and players in bone fracture healing match". In: *Clinical cases in mineral and bone metabolism* 6 (2 2009), p. 159.

[37] Thomas A Einhorn. "The cell and molecular biology of fracture healing". In: *Clinical Orthopaedics and Related Research®* 355 (1998), S7–S21.

[38] Richard Marsell and Thomas A Einhorn. "The biology of fracture healing". In: *Injury* 42 (6 2011), pp. 551–555.

[39] Michael Jagodzinski and Christian Krettek. "Effect of mechanical stability on fracture healing—an update". In: *Injury* 38 (1 2007), S3–S10.

[40] Paul Kostenuik and Faisal M Mirza. "Fracture healing physiology and the quest for therapies for delayed healing and nonunion". In: *Journal of Orthopaedic Research®* 35 (2 2017), pp. 213–223.

[41] Mark E Bolander. "Regulation of fracture repair by growth factors". In: *Proceedings of the Society for Experimental Biology and Medicine* 200 (2 1992), pp. 165–170.

[42] Jeffrey S Warren. "Interleukins and tumor necrosis factor in inflammation". In: *Critical reviews in clinical laboratory sciences* 28 (1 1990), pp. 37–59.

[43] Carol A Feghali, Timothy M Wright, et al. "Cytokines in acute and chronic inflammation". In: *Front Biosci* 2 (1 1997), pp. d12–d26.

[44] Brian McKibbin. "The biology of fracture healing in long bones". In: *The Journal of bone and joint surgery. British volume* 60 (2 1978), pp. 150–162.

[45] Francois N K Kwong and Mitchel B Harris. "Recent developments in the biology of fracture repair". In: *JAAOS-Journal of the American Academy of Orthopaedic Surgeons* 16 (11 2008), pp. 619–625.

[46] E Y Chao and Nozomu Inoue. "Biophysical stimulation of bone fracture repair, regeneration and remodelling". In: *Eur Cell Mater* 6 (2003), pp. 72–84.

[47] Thomas A Einhorn. "The science of fracture healing". In: *Journal of orthopaedic trauma* 19 (10 2005), S4–S6.

[48] Frank Bonnarens and Thomas A Einhorn. "Production of a standard closed fracture in laboratory animal bone". In: *Journal of orthopaedic research* 2 (1 1984), pp. 97–101.

[49] Carl T Brighton. "The biology of fracture repair." In: *Instructional course lectures* 33 (1984), pp. 60–82.

[50] Thomas A Einhorn, Cato T Laurencin, and Karen Lyons. "An AAOS-NIH Symposium: Fracture Repair: Challenges, Opportunities, and Directions for Future Research". In: *JBJS* 90 (2 2008), pp. 438–442.

[51] Donald R Peterson and Joseph D Bronzino. *Biomechanics: principles and practices*. CRC Press, 2014, p. 247.

[52] Michel Vert, Yoshiharu Doi, Karl-Heinz Hellwich, Michael Hess, Philip Hodge, Przemyslaw Kubisa, Marguerite Rinaudo, and François Schué. "Terminology for biorelated polymers and applications (IUPAC Recommendations 2012)". In: *Pure and Applied Chemistry* 84 (2 2012), pp. 377–410.

[53] Kenneth J Anusavice, Chiayi Shen, and H Ralph Rawls. *Phillips' science of dental materials*. Elsevier Health Sciences, 2012.

[54] Jürgen M Lackner and Wolfgang Waldhauser. "Diamond and diamond-like carbon coated surfaces as biomaterials". In: *BHM Berg-und Hüttenmännische Monatshefte* 155 (11 2010), pp. 528–533.

[55] Monika Saini, Yashpal Singh, Pooja Arora, Vipin Arora, and Krati Jain. "Implant biomaterials: A comprehensive review". In: *World Journal of Clinical Cases: WJCC* 3 (1 2015), p. 52.

[56] F Feyerabend. *In vitro analysis of magnesium corrosion in orthopaedic biomaterials*. Elsevier, 2014, pp. 225–269.

[57] E A Friis, T A DeCoster, and J C Thomas. *Mechanical testing of fracture fixation devices*. Elsevier, 2017, pp. 131–141.

[58] Radovan Zdero, Mina S R Aziz, and Bruce Nicayenzi. *Pullout force testing of cortical and cancellous screws in whole bone*. Elsevier, 2017, pp. 117–132.

[59] R M Slone, M M Heare, R A Vander Griend, and W J Montgomery. "Orthopedic fixation devices." In: *Radiographics* 11 (5 1991), pp. 823–847.

[60] S M Perren. "Technical and biomechanical aspects of screws used in bone surgery". In: *Int J Orthop Trauma* 2 (1992), pp. 31–48.

[61] Bérengère J C Luthringer, Frank Feyerabend, and Regine Willumeit-Römer. "Magnesium-based implants: a mini-review". In: *Magnesium research* 27 (4 2014), pp. 142–154.

[62] G Eddy Jai Poinern, Sridevi Brundavanam, and Derek Fawcett. "Biomedical magnesium alloys: a review of material properties, surface modifications and potential as a biodegradable orthopaedic implant". In: *American Journal of Biomedical Engineering* 2 (6 2012), pp. 218–240.

[63] Hamdy Ibrahim, Sajedeh Nasr Esfahani, Behrang Poorganji, David Dean, and Mohammad Elahinia. "Resorbable bone fixation alloys, forming, and post-fabrication treatments". In: *Materials Science and Engineering: C* 70 (2017), pp. 870–888.

[64] Dragos Apostu, Ondine Lucaciu, Cristian Berce, Dan Lucaciu, and Dan Cosma. "Current methods of preventing aseptic loosening and improving osseointegration of titanium implants in cementless total hip arthroplasty: a review". In: *Journal of International Medical Research* 46 (6 2018), pp. 2104–2119.

[65] C Shannon, R Thull, and A Von Recum. "Types I and III collagen in the tissue capsules of titanium and stainless-steel implants". In: *Journal of Biomedical Materials Research: An Official Journal of The Society for Biomaterials and The Japanese Society for Biomaterials* 34 (3 1997), pp. 401–408.

[66] Narges Shayesteh Moghaddam, Mohsen Taheri Andani, Amirhesam Amerinatanzi, Christoph Haberland, Scott Huff, Michael Miller, Mohammad Elahinia, and David Dean. "Metals for bone implants: Safety, design, and efficacy". In: *Biomanufacturing Reviews* 1 (1 2016), p. 1.

[67] Georg Reith, Vera Schmitz-Greven, Kai O Hensel, Marco M Schneider, Tibor Tinschmann, Bertil Bouillon, and Christian Probst. "Metal implant removal: benefits and drawbacks–a patient survey". In: *BMC surgery* 15 (1 2015), p. 96.

[68] Chunmei Li, Chengchen Guo, Vincent Fitzpatrick, Ahmed Ibrahim, Myrthe Jasmijn Zwierstra, Philip Hanna, Aron Lechtig, Ara Nazarian, Samuel J Lin, and David L Kaplan. "Design of biodegradable, implantable devices towards clinical translation". In: *Nature Reviews Materials* (2019), pp. 1–21.

[69] Rebecca Lensing, Peter Behrens, Peter Paul Müller, Thomas Lenarz, and Martin Stieve. "In vivo testing of a bioabsorbable magnesium alloy serving as total ossicular replacement prostheses". In: *Journal of biomaterials applications* 28 (5 2014), pp. 688–696.

[70] Frank Witte, V Kaese, H Haferkamp, E Switzer, A Meyer-Lindenberg, C J Wirth, and H Windhagen. "In vivo corrosion of four magnesium alloys and the associated bone response". In: *Biomaterials* 26 (17 2005), pp. 3557–3563.

[71] Sharookh P Vatchha, Amit Kohli, Sanjay Kumar Tripathi, Saurav Narayan Nanda, Prasant Pradhan, and Shaikh Muzammil Shiraz. "Biodegradable Implants in Orthopaedics". In: *Annals of International Medical and Dental Research* 1 (1 2015), pp. 3–8.

[72] H Sun, C F Luo, B Zhong, H P Shi, C Q Zhang, and B F Zeng. "A prospective, randomised trial comparing the use of absorbable and metallic screws in the fixation of distal tibiofibular syndesmosis injuries: mid-term follow-up". In: *The bone and joint journal* 96 (4 2014), pp. 548–554.

[73] Timothy R Arnett. "Extracellular pH regulates bone cell function". In: *The Journal of nutrition* 138 (2 2008), 415S–418S.

[74] R Swaminathan. "Magnesium metabolism and its disorders". In: *The Clinical Biochemist Reviews* 24 (2 2003), p. 47.

[75] Jerry Kazuo Aikawa. *The role of magnesium in biological processes*. Thomas (Charles), 1963.

[76] Housecroft Ce. "sharpe aG". In: *Inorganic Chemistry (3rd Ed) Prentice Hall, USA* (2008), pp. 305–306.

[77] J-M Seitz, R Eifler, Fr-W Bach, and H J Maier. "Magnesium degradation products: effects on tissue and human metabolism". In: *Journal of biomedical materials research Part A* 102 (10 2014), pp. 3744–3753.

[78] Uwe Gröber, Joachim Schmidt, and Klaus Kisters. "Magnesium in prevention and therapy". In: *Nutrients* 7 (9 2015), pp. 8199–8226.

[79] Stella Lucia Volpe. "Magnesium in disease prevention and overall health". In: *Advances in nutrition* 4 (3 2013), 378S–383S.

[80] Diane Haake. *Evaluation der Magnetresonaztomographie zur longitudinalen Untersuchung degradierbarer Magnesiumimplantate in vivo*. 2016.

[81] Jose R Weisinger and Ezequiel Bellorin-Font. "Magnesium and phosphorus". In: *The Lancet* 352 (9125 1998), pp. 391–396.

[82] Nils-Erik L Saris, Eero Mervaala, Heikki Karppanen, Jahangir A Khawaja, and Andrzei Lewenstam. "Magnesium: an update on physiological, clinical and analytical aspects". In: *Clinica chimica acta* 294 (1-2 2000), pp. 1–26.

[83] Jasmeet Soar, Gavin D Perkins, Gamal Abbas, Annette Alfonzo, Alessandro Barelli, Joost J L M Bierens, Hermann Brugger, Charles D Deakin, Joel Dunning, Marios Georgiou, et al. "European Resuscitation Council Guidelines for Resuscitation 2010 Section 8. Cardiac arrest in special circumstances: electrolyte abnormalities, poisoning, drowning, accidental hypothermia, hyperthermia, asthma, anaphylaxis, cardiac surgery, trauma, pregna". In: *Resuscitation* 81 (10 2010), p. 1400.

[84] Jeroen H F De Baaij, Joost G J Hoenderop, and René J M Bindels. "Magnesium in man: implications for health and disease". In: *Physiological reviews* 95 (1 2015), pp. 1–46.

[85] Lisanne M M Gommers, Joost G J Hoenderop, René J M Bindels, and Jeroen H F de Baaij. "Hypomagnesemia in type 2 diabetes: a vicious circle?" In: *Diabetes* 65 (1 2016), pp. 3–13.

[86] Josephine Chow. "Nephrology Secrets Third Edition". In: *Renal Society of Australasia Journal* 8 (1 2012), p. 38.

[87] Sara Castiglioni, Alessandra Cazzaniga, Walter Albisetti, and Jeanette A M Maier. "Magnesium and osteoporosis: current state of knowledge and future research directions". In: *Nutrients* 5 (8 2013), pp. 3022–3033.

[88] Allen C Alfrey and Nancy L Miller. "Bone magnesium pools in uremia". In: *The Journal of clinical investigation* 52 (12 1973), pp. 3019–3027.

[89] Stanley Wallach. "Effects of magnesium on skeletal metabolism." In: *Magnesium and trace elements* 9 (1 1990), pp. 1–14.

[90] Robert M McLean. "Magnesium and its therapeutic uses: a review". In: *The American journal of medicine* 96 (1 1994), pp. 63–76.

[91] Guangling Song and Andrej Atrens. "Understanding magnesium corrosion—a framework for improved alloy performance". In: *Advanced engineering materials* 5 (12 2003), pp. 837–858.

[92] Frank Witte, Norbert Hort, Carla Vogt, Smadar Cohen, Karl Ulrich Kainer, Regine Willumeit, and Frank Feyerabend. "Degradable biomaterials based on magnesium corrosion". In: *Current opinion in solid state and materials science* 12 (5-6 2008), pp. 63–72.

[93] Wolf-Dieter Mueller, M Lucia Nascimento, and Monica Fernandez Lorenzo De Mele. "Critical discussion of the results from different corrosion studies of Mg and Mg alloys for biomaterial applications". In: *Acta biomaterialia* 6 (5 2010), pp. 1749–1755.

[94] Liping Xu, Guoning Yu, Erlin Zhang, Feng Pan, and Ke Yang. "In vivo corrosion behavior of Mg-Mn-Zn alloy for bone implant application". In: *Journal of Biomedical Materials Research Part A: An Official Journal of The Society for Biomaterials, The Japanese Society for Biomaterials, and The Australian Society for Biomaterials and the Korean Society for Biomaterials* 83 (3 2007), pp. 703–711.

[95] Erlin Zhang, Liping Xu, Guoning Yu, Feng Pan, and Ke Yang. "In vivo evaluation of biodegradable magnesium alloy bone implant in the first 6 months implantation". In: *Journal of Biomedical Materials Research Part A: An Official Journal of The Society for Biomaterials, The Japanese Society for Biomaterials, and The Australian Society for Biomaterials and the Korean Society for Biomaterials* 90 (3 2009), pp. 882–893.

[96] L Yang, N Hort, R Willumeit, and F Feyerabend. "Effects of corrosion environment and proteins on magnesium corrosion". In: *Corrosion Engineering, Science and Technology* 47 (5 2012), pp. 335–339.

[97] Akiko Yamamoto and Sachiko Hiromoto. "Effect of inorganic salts, amino acids and proteins on the degradation of pure magnesium in vitro". In: *Materials Science and Engineering: C* 29 (5 2009), pp. 1559–1568.

[98] Regine Willumeit, Frank Feyerabend, and Norbert Huber. "Magnesium degradation as determined by artificial neural networks". In: *Acta biomaterialia* 9 (10 2013), pp. 8722–8729.

[99] Hazibullah Waizy, Andreas Weizbauer, Christian Modrejewski, Frank Witte, Henning Windhagen, Arne Lucas, Marc Kieke, Berend Denkena, Peter Behrens, Andrea Meyer-Lindenberg, et al. "In vitro corrosion of ZEK100 plates in Hank's Balanced Salt Solution". In: *Biomedical engineering online* 11 (1 2012), pp. 1–14.

[100] Marc Kieke, Frank Feyerabend, Jacques Lemaitre, Peter Behrens, and Regine Willumeit-Römer. "Degradation rates and products of pure magnesium exposed to different aqueous media under physiological conditions". In: *BioNanoMaterials* 17 (3-4 2016), pp. 131–143.

[101] Ralf Rettig and Sannakaisa Virtanen. "Composition of corrosion layers on a magnesium rare-earth alloy in simulated body fluids". In: *Journal of Biomedical Materials Research Part A: An Official Journal of The Society for Biomaterials, The Japanese Society for Biomaterials, and The Australian Society for Biomaterials and the Korean Society for Biomaterials* 88 (2 2009), pp. 359–369.

[102] Di Tie, Frank Feyerabend, Norbert Hort, Regine Willumeit, and Daniel Hoeche. "XPS studies of magnesium surfaces after exposure to Dulbecco's modified eagle medium, Hank's buffered salt solution, and simulated body fluid". In: *Advanced Engineering Materials* 12 (12 2010), B699–B704.

[103] Fusheng Pan, Xianhua Chen, Tao Yan, Tingting Liu, Jianjun Mao, Wei Luo, Qin Wang, Jian Peng, Aitao Tang, and Bin Jiang. "A novel approach to melt purification of magnesium alloys". In: *Journal of Magnesium and Alloys* 4 (1 2016), pp. 8–14.

[104] Marcjanna Maria Gawlik, Björn Wiese, Valérie Desharnais, Thomas Ebel, and Regine Willumeit-Römer. "The Effect of Surface Treatments on the Degradation of Biomedical Mg Alloys—A Review Paper". In: *Materials* 11 (12 2018), p. 2561.

[105] Nina Von Der Höh, Dirk Bormann, Arne Lucas, Berend Denkena, Christian Hackenbroich, and Andrea Meyer-Lindenberg. "Influence of different surface machining treatments of magnesium-based resorbable implants on the degradation behavior in rabbits". In: *Advanced Engineering Materials* 11 (5 2009), B47–B54.

[106] M Alvarez-Lopez, Maria Dolores Pereda, J A Del Valle, M Fernandez-Lorenzo, M C Garcia-Alonso, Oscar Antonio Ruano, and M L Escudero. "Corrosion behaviour of AZ31 magnesium alloy with different grain sizes in simulated biological fluids". In: *Acta biomaterialia* 6 (5 2010), pp. 1763–1771.

[107] R Walter and M Bobby Kannan. "Influence of surface roughness on the corrosion behaviour of magnesium alloy". In: *Materials and Design* 32 (4 2011), pp. 2350–2354.

[108] P Gunde, A C Hänzi, A S Sologubenko, and Peter J Uggowitzer. "High-strength magnesium alloys for degradable implant applications". In: *Materials Science and Engineering: A* 528 (3 2011), pp. 1047–1054.

[109] Jochen Harmuth, Björn Wiese, Jan Bohlen, Thomas Ebel, and Regine Willumeit-Römer. "Wide Range Mechanical Customization of Mg-Gd Alloys With Low Degradation Rates by Extrusion". In: *Frontiers in Materials* 6 (Aug. 2019). ISSN: 22968016. DOI: 10.3389/fmats.2019.00201.

[110] Alexander Feldhaus. "Wirkung von Seltenen Erden auf den osteoporotisch veränderten Knochen im Tiermodell der ovariektomierten Ratte". lmu, 2006.

[111] Christopher H Evans. *Biochemistry of the Lanthanides*. Vol. 8. Springer Science and Business Media, 2013.

[112] Thomas J Haley. "Toxicity". In: *Handbook on the Physics and chemistry of rare earths* 4 (1979), pp. 553–585.

[113] Richard C Semelka, Miguel Ramalho, Mamdoh AlObaidy, and Joana Ramalho. "Gadolinium in humans: a family of disorders". In: *American Journal of Roentgenology* 207 (2 2016), pp. 229–233.

[114] Rui Chen, Daishun Ling, Lin Zhao, Shuaifei Wang, Ying Liu, Ru Bai, Seungmin Baik, Yuliang Zhao, Chunying Chen, and Taeghwan Hyeon. "Parallel comparative studies on mouse toxicity of oxide nanoparticle- and gadolinium-based T1 MRI contrast agents". In: *ACS nano* 9 (12 2015), pp. 12425–12435.

[115] Tapan K Chaudhuri and Subhankar Paul. "Protein-misfolding diseases and chaperone-based therapeutic approaches". In: *The FEBS journal* 273 (7 2006), pp. 1331–1349.

[116] Henrik S Thomsen, Sameh K Morcos, Torsten Almén, Marie-France Bellin, Michele Bertolotto, Georg Bongartz, Olivier Clement, Peter Leander, Gertraud Heinz-Peer, Peter Reimer, et al. "Nephrogenic systemic fibrosis and gadolinium-based contrast media: updated ESUR Contrast Medium Safety Committee guidelines". In: *European radiology* 23 (2 2013), pp. 307–318.

[117] Henrik S Thomsen. "Nephrogenic systemic fibrosis: history and epidemiology". In: *Radiologic Clinics* 47 (5 2009), pp. 827–831.

[118] Ana Carolina de Souza Machado Igreja, Kleyton de Carvalho Mesquita, Shawn Edwin Cowper, and Izelda Maria Carvalho Costa. "Nephrogenic systemic fibrosis: concepts and perspectives". In: *Anais brasileiros de dermatologia* 87 (4 2012), pp. 597–607.

[119] I J Polmear. "Physical metallurgy of magnesium alloys". In: *DGM Informationsgesellschaft, Oberursel, Germany* 201 (1992).

[120] Karl Ulrich Kainer. *Magnesium-Eigen-Schaften*. Wiley-VCH, 2000.

[121] Indranil Basu, Günter Gottstein, and Brita Daniela Zander. *Recrystallization mechanisms in wrought magnesium alloys containing rare-earth elements*. Lehrstuhl für Korrosion und Korrosionsschutz, 2017.

[122] Lazar Leonovich Rokhlin. *Magnesium alloys containing rare earth metals: structure and properties*. Crc Press, 2003.

[123] Y Xin, Tao Hu, and P K Chu. "In vitro studies of biomedical magnesium alloys in a simulated physiological environment: a review". In: *Acta biomaterialia* 7 (4 2011), pp. 1452–1459.

[124] I Marco, A Myrissa, E Martinelli, F Feyerabend, R Willumeit-Römer, A M Weinberg, and Omer der Biest. "In vivo and in vitro degradation comparison of pure Mg, Mg-10Gd and Mg-2Ag: a short term study". In: *European cells and materials* 33 (2017), pp. 90–104.

[125] Anastasia Myrissa, Nezha Ahmad Agha, Yiyi Lu, Elisabeth Martinelli, Johannes Eichler, Gabor Szakacs, Claudia Kleinhans, Regine Willumeit-Römer, Ute Schäfer, and Annelie-Martina Weinberg. "In vitro and in vivo comparison of binary Mg alloys and pure Mg". In: *Materials Science and Engineering: C* 61 (2016), pp. 865–874.

[126] Silvia Galli. "On magnesium-containing implants for bone applications". Malmö university, Faculty of Odontology, 2016.

[127] S F Fischerauer, T Kraus, X Wu, Stefan Tangl, E Sorantin, A C Hänzi, Jörg F Löffler, Peter J Uggowitzer, and A M Weinberg. "In vivo degradation performance of micro-arc-oxidized magnesium implants: a micro-CT study in rats". In: *Acta biomaterialia* 9 (2 2013), pp. 5411–5420.

[128] Jorge Gonzalez, Rui Qing Hou, Eshwara P S Nidadavolu, Regine Willumeit-Römer, and Frank Feyerabend. "Magnesium degradation under physiological conditions–Best practice". In: *Bioactive materials* 3 (2 2018), pp. 174–185.

[129] Jorge Gonzalez, Rui Qing Hou, Eshwara P S Nidadavolu, Regine Willumeit-Römer, and Frank Feyerabend. "Magnesium degradation under physiological conditions–Best practice". In: *Bioactive materials* 3 (2 2018), pp. 174–185.

[130] R Willumeit, J Fischer, R PÖRTNER, T Di, N Hort, and K U Kainer. "Corrosion of magnesium in static and dynamic (bioreactor) systems". In: 2011.

[131] Zijian Li, Xunan Gu, Siquan Lou, and Yufeng Zheng. "The development of binary Mg–Ca alloys for use as biodegradable materials within bone". In: *Biomaterials* 29 (10 2008), pp. 1329–1344.

[132] Frank Witte, Jens Fischer, Jens Nellesen, Horst-Artur Crostack, Volker Kaese, Alexander Pisch, Felix Beckmann, and Henning Windhagen. "In vitro and in vivo corrosion measurements of magnesium alloys". In: *Biomaterials* 27 (7 2006), pp. 1013–1018.

[133] Angela S P Lin, Stuart R Stock, and Robert E Guldberg. *Microcomputed Tomography*. Springer, 2019, p. 2.

[134] Johann Kastner, Bernhard Harrer, Guillermo Requena, and Oliver Brunke. "A comparative study of high resolution cone beam X-ray tomography and synchrotron tomography applied to Fe-and Al-alloys". In: *Ndt and E International* 43 (7 2010), pp. 599–605.

[135] Hongchang Wang, Yogesh Kashyap, and Kawal Sawhney. "From synchrotron radiation to lab source: advanced speckle-based X-ray imaging using abrasive paper". In: *Scientific reports* 6 (2016), p. 20476.

[136] W Kockelmann, E Pantos, and A Kirfel. *Neutron and synchrotron radiation studies of archaeological objects*. Elsevier, 2000, pp. 347–377.

[137] Oliver Brunke, Kathleen Brockdorf, Susanne Drews, Bert Müller, Tilman Donath, Julia Herzen, and Felix Beckmann. "Comparison between x-ray tube-based and synchrotron radiation-based microCT". In: vol. 7078. 2008, 70780U.

[138] Anton Du Plessis, Chris Broeckhoven, Anina Guelpa, and Stephan Gerhard Le Roux. "Laboratory x-ray micro-computed tomography: a user guideline for biological samples". In: *Gigascience* 6 (6 2017), gix027.

[139] O Brunke. "High-resolution CT-based defect analysis and dimensional measurement". In: *Insight-Non-Destructive Testing and Condition Monitoring* 52 (2 2010), pp. 91–93.

[140] Anjali Singhal, James C Grande, and Ying Zhou. "Micro/nano-CT for visualization of internal structures". In: *Microscopy Today* 21 (2 2013), pp. 16–22.

[141] Lifeng Yu and Shuai Leng. "Image reconstruction techniques". In: *American College of Radiology* (2010).

[142] J C Jansen, M Stöcker, H G Karge, and J Weitkamp. *Advanced zeolite science and applications*. Vol. 85. Elsevier Amsterdam, 1994.

[143] Andreas Maier, Stefan Steidl, Vincent Christlein, and Joachim Hornegger. "Medical imaging systems: An introductory guide". In: (2018).

[144] Peter Staron, Andreas Schreyer, Helmut Clemens, and Svea Mayer. *Neutrons and synchrotron radiation in engineering materials science: From fundamentals to applications*. John Wiley and Sons, 2017.

[145] Samuel Krinsky, W Thomlinson, and A Van Steenbergen. *Overview of undulators and wigglers for the NSLS*. Brookhaven National Lab., Upton, NY (USA), 1982.

[146] Amardeep Bharti and Navdeep Goyal. *Fundamental of Synchrotron Radiations*. IntechOpen, 2019.

[147] Fabian Wilde, Malte Ogurreck, Imke Greving, Jörg U Hammel, Felix Beckmann, Alexander Hipp, Lars Lottermoser, Igor Khokhriakov, Pavel Lytaev, Thomas Dose, et al. "Micro-CT at the imaging beamline P05 at PETRA III". In: vol. 1741. 2016, p. 30035.

[148] Ruchika Chandel and Gaurav Gupta. "Image filtering algorithms and techniques: A review". In: *International Journal of Advanced Research in Computer Science and Software Engineering* 3 (10 2013).

[149] K Bhargavi and S Jyothi. "A survey on threshold based segmentation technique in image processing". In: *International Journal of Innovative Research and Development* 3 (12 2014), pp. 234–239.

[150] Bernhard Preim and D Bartz. "Image analysis for medical visualization". In: *visualization in medicine* (2007), pp. 83–131.

[151] Jadwiga Rogowska. "Overview and fundamentals of medical image segmentation". In: *Handbook of medical imaging, processing and analysis* (2000), pp. 69–85.

[152] John Ashburner and Karl J Friston. "Spatial transformation of images". In: *Human brain function* (1997), pp. 43–58.

[153] Lawrence A Ray. "Book Review: 2-D and 3-D Image Registration for Medical, Remote Sensing, and Industrial Applications". In: *Journal of Electronic Imaging* 14 (3 2005), p. 39901.

[154] Diana Krüger, Berit Zeller-Plumhoff, Björn Wiese, Sangbong Yi, Marcus Zuber, D C Florian Wieland, Julian Moosmann, and Regine Willumeit-Römer. "Assessing the microstructure and in vitro degradation behavior of Mg-xGd screw implants using µCT". In: *Journal of Magnesium and Alloys* (2021).

[155] Diana Krüger, Silvia Galli, Berit Zeller-Plumhoff, D C Florian Wieland, Niccolò Peruzzi, Björn Wiese, Philipp Heuser, Julian Moosmann, Ann Wennerberg, and Regine Willumeit-Römer. "High-resolution ex vivo analysis of the degradation and osseointegration of Mg-xGd implant screws in 3D". In: *Bioactive Materials* (2021).

[156] Berit Zeller-Plumhoff, Carina Malich, Diana Krüger, Graeme Campbell, Björn Wiese, Silvia Galli, Ann Wennerberg, Regine Willumeit-Römer, and D C Florian Wieland. "Analysis of the bone ultrastructure around biodegradable Mg–xGd implants using small angle X-ray scattering and X-ray diffraction". In: *Acta biomaterialia* 101 (2020), pp. 637–645.

[157] Volker KREE, Jan BOHLEN, Dietmar LETZIG, and Karl Ulrich KAINER. "Metallographische gefügeuntersuchungen von magnesium-legierungen". In: *Praktische Metallographie* 41 (5 2004), pp. 233–246.

[158] Antoni Buades, Bartomeu Coll, and Jean-Michel Morel. "Non-local means denoising". In: *Image Processing On Line* 1 (2011), pp. 208–212.

[159] Jérôme Darbon, Alexandre Cunha, Tony F Chan, Stanley Osher, and Grant J Jensen. "Fast nonlocal filtering applied to electron cryomicroscopy". In: 2008, pp. 1331–1334.

[160] Julian Moosmann, D C Florian Wieland, Berit Zeller-Plumhoff, Silvia Galli, Diana Krüger, Alexey Ershov, Silke Lautner, Julian Sartori, Mason Dean, Sebastian Köhring, Hilmar Burmester, Thomas Dose, Niccoló Peruzzi, Ann Wennerberg, Regine Willumeit-Römer, Fabian Wilde, Philipp Heuser, Jörg U Hammel, and Felix Beckmann. "A load frame for in situ tomography at PETRA III". In: vol. 11113. 2019, p. 1111318.

[161] Ivo M Baltruschat, Hanna Cwieka, Diana Krüger, Berit Zeller-Plumhoff, Frank Schlünzen, Regine Willumeit-Römer, Julian Moosmann, and Philipp Heuser. "Scaling the U-net: segmentation of biodegradable bone implants in high-resolution synchrotron radiation microtomograms". In: *Scientific reports* 11 (1 2021), pp. 1–10.

[162] Gunilla Borgefors. "On digital distance transforms in three dimensions". In: *Computer vision and image understanding* 64 (3 1996), pp. 368–376.

[163] Eshwara Phani Shubhakar Nidadavolu, Frank Feyerabend, Thomas Ebel, Regine Willumeit-Römer, and Michael Dahms. "On the determination of magnesium degradation rates under physiological conditions". In: *Materials* 9 (8 2016), p. 627.

[164] Johannes Schindelin, Ignacio Arganda-Carreras, Erwin Frise, Verena Kaynig, Mark Longair, Tobias Pietzsch, Stephan Preibisch, Curtis Rueden, Stephan Saalfeld, Benjamin Schmid, et al. "Fiji: an open-source platform for biological-image analysis". In: *Nature methods* 9 (7 2012), pp. 676–682.

[165] ORGANISATION O F ISLAMIC COOPERATION. "Correlation and Regression Analysis". In: ().

[166] R Winston Revie. *Corrosion and corrosion control: an introduction to corrosion science and engineering*. John Wiley and Sons, 2008, p. 17.

[167] Mary L Bouxsein, Stephen K Boyd, Blaine A Christiansen, Robert E Guldberg, Karl J Jepsen, and Ralph Müller. "Guidelines for assessment of bone microstructure in rodents using micro–computed tomography". In: *Journal of bone and mineral research* 25 (7 2010), pp. 1468–1486.

[168] James F Griffith and Harry K Genant. *Imaging of Osteoporosis*. Elsevier, 2013, pp. 1505–1534.

[169] Hervé Abdi. "Coefficient of variation". In: *Encyclopedia of research design* 1 (2010), pp. 169–171.

[170] Katarzyn J Blinowska and Jaroslaw Zygierewicz. *Practical Biomedical Signal Analysis Using MATLAB®*. CRC Press, 2011.

[171] Y H Chan. "Biostatistics 104: correlational analysis". In: *Singapore Med J* 44 (12 2003), pp. 614–619.

[172] Marcjanna Maria Gawlik. "The influence of surface defects on the degradation behaviour of magnesium alloys for medical applications". Christian-Albrechts Universität Kiel, 2019.

[173] Alireza Ghaderi and Matthew R Barnett. "Sensitivity of deformation twinning to grain size in titanium and magnesium". In: *Acta materialia* 59 (20 2011), pp. 7824–7839.

[174] Ugochukwu Chibuzoh Nwaogu, C Blawert, N Scharnagl, W Dietzel, and K U Kainer. "Influence of inorganic acid pickling on the corrosion resistance of magnesium alloy AZ31 sheet". In: *Corrosion Science* 51 (11 2009), pp. 2544–2556.

[175] Dan Song, AiBin Ma, Jinghua Jiang, Pinghua Lin, Donghui Yang, and Junfeng Fan. "Corrosion behavior of equal-channel-angular-pressed pure magnesium in NaCl aqueous solution". In: *Corrosion Science* 52 (2 2010), pp. 481–490.

[176] Wislei Riuper Osório, Célia Marina Freire, and Amauri Garcia. "The role of macrostructural morphology and grain size on the corrosion resistance of Zn and Al castings". In: *Materials Science and Engineering: A* 402 (1-2 2005), pp. 22–32.

[177] L Wu, S R Agnew, D W Brown, G M Stoica, B Clausen, A Jain, D E Fielden, and P K Liaw. "Internal stress relaxation and load redistribution during the twinning–detwinning-dominated cyclic deformation of a wrought magnesium alloy, ZK60A". In: *Acta Materialia* 56 (14 2008), pp. 3699–3707.

[178] L Wu, A Jain, D W Brown, G M Stoica, S R Agnew, B Clausen, D E Fielden, and P K Liaw. "Twinning–detwinning behavior during the strain-controlled low-cycle fatigue testing of a wrought magnesium alloy, ZK60A". In: *Acta Materialia* 56 (4 2008), pp. 688–695.

[179] Wei Wu, Chih-Pin Chuang, Dongxiao Qiao, Yang Ren, and Ke An. "Investigation of deformation twinning under complex stress states in a rolled magnesium alloy". In: *Journal of Alloys and Compounds* 683 (2016), pp. 619–633.

[180] K Donath. "Preparation of histologic sections by the cutting-grinding technique for hard tissue and other material not suitable to be sectioned by routine methods". In: *Equipment and methodical performance* (1988).

[181] Jiali Wang, Frank Witte, Tingfei Xi, Yufeng Zheng, Ke Yang, Yuansheng Yang, Dewei Zhao, Jian Meng, Yangde Li, Weirong Li, et al. "Recommendation for modifying current cytotoxicity testing standards for biodegradable magnesium-based materials". In: *Acta biomaterialia* 21 (2015), pp. 237–249.

[182] Naohiko Kawamura, Yuya Nakao, Rina Ishikawa, Dai Tsuchida, and Masahiro Iijima. "Degradation and Biocompatibility of AZ31 Magnesium Alloy Implants In Vitro and In Vivo: A Micro-Computed Tomography Study in Rats". In: *Materials* 13 (2 2020), p. 473.

[183] Weimin Gan, Yuanding Huang, Lei Yang, Karl Ulrich Kainer, Miao Jiang, H-G Brokmeier, and Norbert Hort. "Identification of unexpected hydrides in Mg–20 wtby high-brilliance synchrotron radiation". In: *Journal of Applied Crystallography* 45 (1 2012), pp. 17–21.

[184] Iñigo Marco, Frank Feyerabend, Regine Willumeit-Römer, and Omer der Biest. "Degradation testing of Mg alloys in Dulbecco's modified eagle medium: Influence of medium sterilization". In: *Materials Science and Engineering: C* 62 (2016), pp. 68–78.

[185] Qiuming Peng, Yuanding Huang, Jian Meng, Yangde Li, and Karl Ulrich Kainer. "Strain induced GdH2 precipitate in Mg–Gd based alloys". In: *Intermetallics* 19 (3 2011), pp. 382–389.

[186] Katharina Jähn, Hiroaki Saito, Hanna Taipaleenmäki, Andreas Gasser, Norbert Hort, Frank Feyerabend, Hartmut Schlüter, Johannes M Rueger, Wolfgang Lehmann, Regine Willumeit-Römer, et al. "Intramedullary Mg2Ag nails augment callus formation during fracture healing in mice". In: *Acta biomaterialia* 36 (2016), pp. 350–360.

[187] Pengfei Cheng, Pei Han, Changli Zhao, Shaoxiang Zhang, Hongliu Wu, Jiahua Ni, Peng Hou, Yuanzhuang Zhang, Jingyi Liu, Haidong Xu, et al. "High-purity magnesium interference screws promote fibrocartilaginous entheses regeneration in the anterior cruciate ligament reconstruction rabbit model via accumulation of BMP-2 and VEGF". In: *Biomaterials* 81 (2016), pp. 14–26.

[188] DAVID A Bushinsky. "Metabolic alkalosis decreases bone calcium efflux by suppressing osteoclasts and stimulating osteoblasts". In: *American Journal of Physiology-Renal Physiology* 271 (1 1996), F216–F222.

[189] Sayuri Yoshizawa, Andrew Brown, Aaron Barchowsky, and Charles Sfeir. "Magnesium ion stimulation of bone marrow stromal cells enhances osteogenic activity, simulating the effect of magnesium alloy degradation". In: *Acta biomaterialia* 10 (6 2014), pp. 2834–2842.

[190] Prashanth J Rao, Matthew H Pelletier, William R Walsh, and Ralph J Mobbs. "Spine interbody implants: material selection and modification, functionalization and bioactivation of surfaces to improve osseointegration". In: *Orthopaedic surgery* 6 (2 2014), pp. 81–89.

[191] Byung Jo Victor Yoon, Fred Xavier, Brendon R Walker, Samuel Grinberg, Frank P Cammisa, and Celeste Abjornson. "Optimizing surface characteristics for cell adhesion and proliferation on titanium plasma spray coatings on polyetheretherketone". In: *The Spine Journal* 16 (10 2016), pp. 1238–1243.

[192] Ricardo Trindade, Tomas Albrektsson, Silvia Galli, Zdenka Prgomet, Pentti Tengvall, and Ann Wennerberg. "Bone immune response to materials, Part II: Copper and polyetheretherketone (PEEK) compared to titanium at 10 and 28 days in rabbit tibia". In: *Journal of clinical medicine* 8 (6 2019), p. 814.

[193] Sargon Barkarmo, Martin Andersson, Fredrik Currie, Per Kjellin, Ryo Jimbo, Carina B Johansson, and V Stenport. "Enhanced bone healing around nanohydroxyapatite-coated polyetheretherketone implants: an experimental study in rabbit bone". In: *Journal of biomaterials applications* 29 (5 2014), pp. 737–747.

[194] Willy Tjong, Jasmine Nirody, Andrew J Burghardt, Julio Carballido-Gamio, and Galateia J Kazakia. "Structural analysis of cortical porosity applied to HR-pQCT data". In: *Medical physics* 41 (1 2014), p. 13701.

[195] Peter A Revell, Elsie Damien, X S Zhang, P Evans, and C Rolfe Howlett. "The effect of magnesium ions on bone bonding to hydroxyapatite coating on titanium alloy implants". In: vol. 254. 2004, pp. 447–450.

[196] Christoph Castellani, Richard A Lindtner, Peter Hausbrandt, Elmar Tschegg, Stefanie E Stanzl-Tschegg, Gerald Zanoni, Stefan Beck, and Annelie-Martina Weinberg. "Bone–implant interface strength and osseointegration: Biodegradable magnesium alloy versus standard titanium control". In: *Acta biomaterialia* 7 (1 2011), pp. 432–440.

[197] Holly D Barth, Maximilien E Launey, Alastair A MacDowell, Joel W Ager III, and Robert O Ritchie. "On the effect of X-ray irradiation on the deformation and fracture behavior of human cortical bone". In: *Bone* 46 (6 2010), pp. 1475–1485.

[198] Holly D Barth, Elizabeth A Zimmermann, Eric Schaible, Simon Y Tang, Tamara Alliston, and Robert O Ritchie. "Characterization of the effects of x-ray irradiation on the hierarchical structure and mechanical properties of human cortical bone". In: *Biomaterials* 32 (34 2011), pp. 8892–8904.

[199] Niclas Bockelmann, Diana Krüger, D C Wieland, Berit Zeller-Plumhoff, Niccoló Peruzzi, Silvia Galli, Regine Willumeit-Römer, Fabian Wilde, Felix Beckmann, Jörg Hammel, Julian Moosmann, and Matthias P. Heinrich. "Sparse annotations with random walks for u-net segmentation of biodegradable bone implants in synchrotron microtomograms". In: *arXiv preprint arXiv:1908.04173* (2019).

[200] Eshwara Phani Shubhakar Nidadavolu, Diana Krüger, Berit Zeller-Plumhoff, Domonkos Tolnai, Björn Wiese, Frank Feyerabend, Thomas Ebel, and Regine Willumeit-Römer. "Pore characterization of PM Mg–0.6 Ca alloy and its degradation behavior under physiological conditions". In: *Journal of Magnesium and Alloys* (2020).

[201] Mohammadreza Taale, Diana Krueger, Emmanuel Ossei-Wusu, Fabian Schuett, Muhammad Atiq Ur Rehman, Yogendra Kumar Mishra, Janik Marx, Norbert Stock, Bodo Fiedler, Aldo R Boccaccini, Regine Willumeit-Römer, Rainer Adelung, and Christine Selhuber-Unkel. "Systematically Designed Periodic Electrophoretic Deposition for Decorating 3D Carbon-Based Scaffolds with Bioactive Nanoparticles". In: *ACS Biomaterials Science and Engineering* 5 (9 2019), pp. 4393–4404.